NEURO-IMMUNE AXIS IN WHITE MATTER AGING

CHARACTERIZING THE INTERPLAY BETWEEN MICROGLIA, OLIGODENDROCYTES, AND CD8+ T CELLS

Tuğberk Kaya

Graduate School of Systemic Neurosciences

LMU Munich

Dissertation at the

Graduate School of Systemic Neurosciences

Ludwig-Maximilians-Universität München

May, 2024

Supervisor
Prof. Dr. Mikael Simons
Institute of Neuronal Cell Biology,
Technical University Munich
German Centre for Neurodegenerative Diseases (DZNE)

First Reviewer: Prof. Dr. Mikael Simons
Second Reviewer: Dr. Sarah Jaekel

Date of Submission: May 16, 2024
Date of Defense : Feb 11, 2025

ABSTRACT

In the past decade, the advancement and adoption of innovative methods for generating sequencing libraries at the single-cell resolution have deepened our grasp on biological mechanisms. Simultaneously, breakthrough computational analysis techniques have emerged, expanding our reach within the field even more. The breadth and intricacy of systemic approaches have greatly profited from these advancements. These technological innovations have not only changed the narrative in scientific literature but also brought about a paradigm shift in numerous disciplines, redefining the way we approach and understand the complexities of life at a cellular level. Identifying the diversity among individual cell identities is crucial to understand their state changes and their reciprocal influence concerning the host phenotype.

This dissertation encompasses two studies elucidating the link between white matter aging and the immune system. In the first study, we explored the alterations in microglia cell states due to aging and identified a distinct population specific to white matter, termed white-matter associated microglia (WAM). Our objective was to comprehend why white matter aging specifically modifies microglial identity. We characterized WAMs, finding that they are not only exclusive to white matter but also age-dependent and reliant on TREM2 signaling for their formation. WAMs form small nodules and are instrumental in clearing myelin debris that accumulates with age.

Despite oligodendrocytes being the myelin-producing cells, our understanding is limited regarding their responses to myelin pathology driven by aging. In our subsequent study, we examined aging-related changes in oligodendrocytes and identified a novel interferon-responsive oligodendrocyte population. The identification of these IFN-responsive cells prompted us to explore the role of the adaptive immune system in white-matter loss during normal aging. We established a connection between CD8+ T cells, IFN-responsive oligodendrocytes, and microglia.

Our results underscore the less explored yet increasingly recognized association between CD8+ T cells and neurodegeneration. In the discussion section, I reflect on our findings and those of others, and contemplate the future of this research area as more sophisticated tools and techniques become widely available.

ZUSAMMENFASSUNG

In den letzten zehn Jahren haben neue Entwicklungen in der Einzelzelltechnologie unser Verständnis von biologischen Systemen erheblich verändert. Der Fortschritt und die Übernahme von innovativen Methoden zur Erzeugung von Sequenzierbibliotheken auf Einzelzellebene haben unser Verständnis für biologische Mechanismen vertieft. Gleichzeitig sind bahnbrechende Techniken der Datenanalyse entstanden, die unseren Handlungsspielraum in diesem Bereich noch weiter ausgedehnt haben. Die Breite und Komplexität systemischer Ansätze haben stark von diesen Fortschritten profitiert. Diese technologischen Innovationen haben nicht nur die Erzählung in der wissenschaftlichen Literatur verändert, sondern auch einen Paradigmenwechsel in zahlreichen Disziplinen herbeigeführt, indem sie die Art und Weise, wie wir die Komplexitäten des Lebens auf zellulärer Ebene angehen und verstehen, neu definiert haben. Die Identifizierung der Vielfalt unter einzelnen Zellidentitäten ist entscheidend, um ihre Zustandsveränderungen und ihren gegenseitigen Einfluss auf den Wirtsphänotyp zu verstehen.

Diese Dissertation umfasst zwei Studien, die den Zusammenhang zwischen der Alterung der weißen Substanz und dem Immunsystem klären. In der ersten Studie haben wir die Veränderungen der Mikroglia-Zellzustände aufgrund des Alterns untersucht und eine spezifische Population identifiziert, die wir als mit weißer Substanz assoziierte Mikroglia (WAM) bezeichnen. Unser Ziel war es zu verstehen, warum das Altern der weißen Substanz speziell die Mikroglia-Identität verändert. Wir charakterisierten WAMs und fanden heraus, dass sie nicht nur ausschließlich in der weißen Substanz vorkommen, sondern auch altersabhängig sind und auf TREM2-Signalgebung für ihre Bildung angewiesen sind. WAMs bilden kleine Knötchen und spielen eine entscheidende Rolle bei der Beseitigung von Myelin-Ablagerungen, die sich mit dem Alter ansammeln.

Obwohl Oligodendrozyten die Myelin-produzierenden Zellen sind, ist unser Verständnis ihrer Reaktionen auf durch das Altern bedingte Myelin-Pathologie begrenzt. In unserer anschließenden Studie haben wir altersbedingte Veränderungen in Oligodendrozyten untersucht und eine neue Interferon-ansprechende Oligodendrozyten-Population identifiziert. Die Identifizierung dieser IFN-ansprechenden Zellen veranlasste uns, die Rolle des adaptiven Immunsystems bei dem Verlust von weißer Substanz während des normalen Alterns zu

untersuchen. Wir stellten eine Verbindung zwischen CD8+ T-Zellen, IFN-ansprechenden Oligodendrozyten und Mikroglia her.

Unsere Ergebnisse unterstreichen die weniger erforschte, aber zunehmend anerkannte Assoziation zwischen CD8+ T-Zellen und Neurodegeneration. Im Diskussionsteil reflektiere ich unsere Befunde und die anderer und denke über die Zukunft dieses Forschungsbereichs nach, während immer ausgefeiltere Werkzeuge und Techniken weit verbreitet zur Verfügung stehen.

CONTENTS

LIST OF FIGURES

1. INTRODUCTION

1.1 Aging as a Risk Factor

Ageing is a natural process that is linked to physical decline, increasing the likelihood of disease and mortality (Rose, 2009). This process varies across species, individuals within a species, and even different tissues within an individual. Biomarkers of ageing are closely tied to the fundamental molecular mechanisms of ageing (Carmona & Michan, 2016). Among the numerous risk factors for neurodegeneration, ageing is the most influential. Therefore, understanding the basic mechanisms of ageing is crucial for developing effective interventions for neurodegenerative diseases.

A 2015 report by the United Nations on global population ageing predicts that the number of individuals aged 60 and above across the world will more than double over the next 35 years, reaching nearly 2.1 billion people (Wyss-Coray, 2016). The majority of this increase will be seen in developing regions of the world. However, the segment of the population aged over 80, often referred to as the "oldest old," is expanding most rapidly in developed regions. As this demographic expands, the financial strain of age-related health disorders will also increase, necessitating effective preventative measures and treatments. Neurodegeneration and the resulting cognitive decline are particularly noteworthy among age-related diseases due to their substantial impact on health span and quality of life.

In the elderly population, neurodegenerative diseases are prevalent, and disease-free brains are rare, especially among the very old (Wyss-Coray, 2016). This suggests that brain aging might be on a continuum with neurodegeneration (Figure 1). Both genetic and environmental factors influence the progression of neurodegenerative diseases. Hence, it's plausible to view neurodegenerative diseases as an accelerated form of aging. Aging, in turn, is a major risk factor for neurodegeneration. The most common

neurodegenerative diseases, Alzheimer's and Parkinson's, are primarily observed in the elderly, and the risk for these diseases escalates with age.

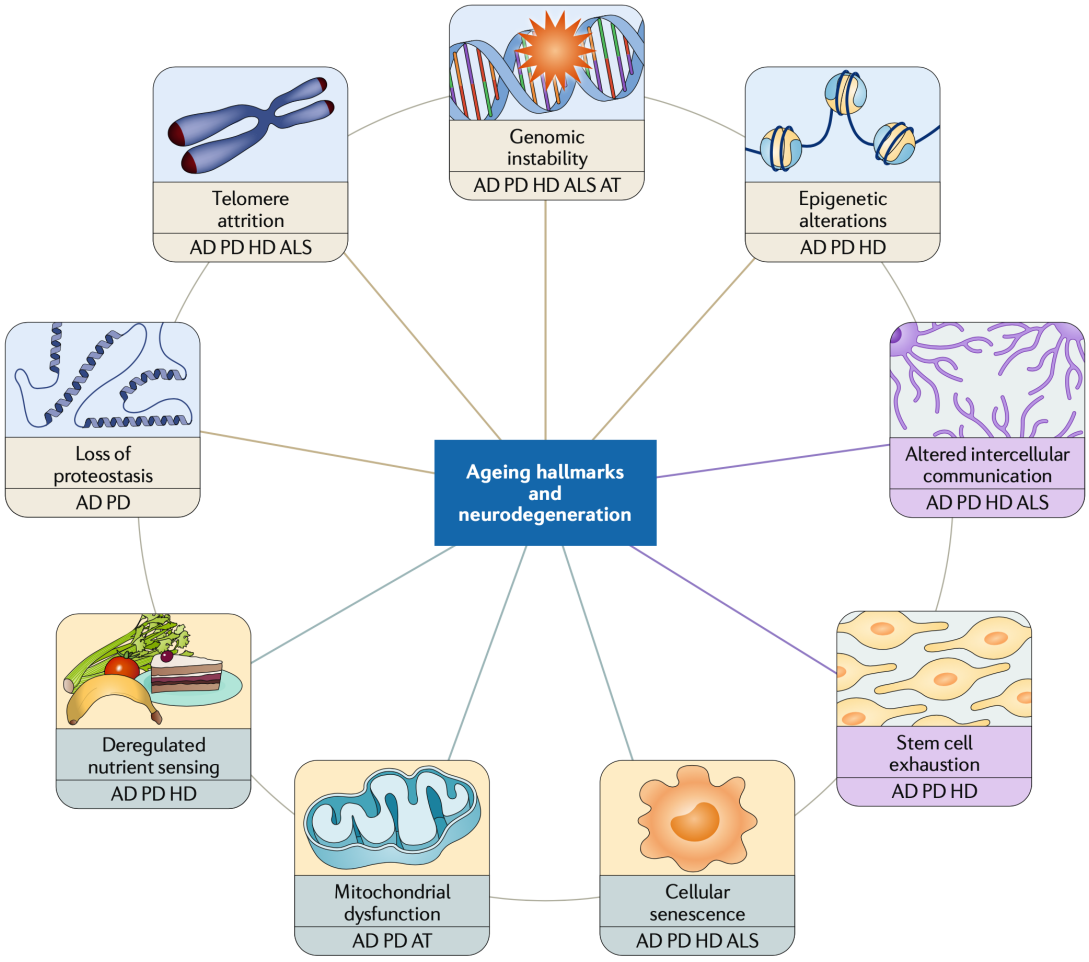

Figure 1: Hallmarks of aging (Hou et al., 2019)

Molecular studies have shown that brain tissue from older individuals contains abnormal deposits of aggregated proteins, such as hyperphosphorylated tau, amyloid-beta, and alpha-synuclein (Elobeid et al., 2016). However, it's still unclear whether the levels of these deposits correlate with the degree of cognitive impairment. Some re-

search suggests that the risk of neurodegenerative disease is linked with early developmental defects, implying that brain structural changes might occur much earlier than cognitive impairment. For instance, MRI measurements of white matter myelin water fraction and grey matter volume in various brain regions of infants carrying the apolipoprotein E (APOE) ε4 allele, a major susceptibility gene for sporadic (late-onset) Alzheimer's, were significantly different from measurements in non-carriers (Dean et al., 2014). Exposure to adverse environmental stimuli during development, such as trauma, drugs, or environmental toxins, could have long-term effects, potentially impacting neuroplasticity.

1.2 The Myelinated Brain

White matter's characteristic light color is primarily attributed to the high lipid content found in myelin, a complex, multilayered membrane structure that envelops axons and contributes to nearly half of the white matter's dry weight (Rockland & Defelipe, 2011). Oligodendrocytes create numerous layers of this myelin membrane around the axons within the central nervous system, thereby enhancing the speed and effectiveness of nerve conduction (Guan & Kong, 2015; McKenzie et al., 2014).

Historically, the sole function ascribed to myelin was the facilitation of saltatory nerve conduction. However, recent findings suggest a broader role for myelin and oligodendrocytes (Nave & Ehrenreich, 2014; Nave & Werner, 2014; Simons & Nave, 2016). Indeed, oligodendrocytes that produce myelin are integral to a broad network of interconnected glial and neuronal cells, with an expanding body of evidence supporting their active involvement in this network. Specifically, oligodendrocytes provide metabolic support to neurons, regulate ion and water homeostasis, and respond to neuronal signals that are dependent on activity levels (Bradl & Lassmann, 2010; Kato & Wake, 2019).

Magnetic resonance imaging (MRI) studies have identified various white matter alterations that occur during the normal aging process. For instance, it's been reported that from the age of 45, the volume of white matter begins to decrease gradually (Bethlehem et al., 2022). Furthermore, white matter lesions often appear as hyperintensities on T2-weighted MRI images (Prins & Scheltens, 2015; Salat et al., 2005).

Deep white matter regions, located at the ends of arterial circulation, are particularly vulnerable to decreases in blood flow and oxygenation. Moreover, some white matter regions reside in watershed zones between the anterior and middle cerebral arteries, and between the middle and posterior cerebral arteries (Dogariu et al., 2023; Wardlaw et al., 2015). These anatomical characteristics could contribute to the increased vulnerability of aged white matter to hypoperfusion (Martinez Sosa & Smith, 2017; Montagne et al., 2015), possibly triggered by age-related vascular changes (Alber et al., 2019; Hase et al., 2018; Kalaria & Hase, 2019).

Electron microscopy studies conducted on non-human primates, have shown that the primary changes observed during normal aging are not a loss of neurons, but rather alterations in the morphology of myelinated nerve fibers (Peters, 2002). Aging is associated with substantial degenerative changes in myelin sheaths, such as splitting at the major dense line leading to an accumulation of dense cytoplasm with vesicular inclusions (Correale & Ysrraelit, 2022; Peters et al., 2000; Safaiyan et al., 2016).

Additionally, aged brains often exhibit myelin out-foldings containing multiple layers of compacted myelin lamellae, and the number of lamellae appears to increase in some of the old brain's sheaths. In studies involving older mice, multilamellar myelin fragments have been observed (Safaiyan et al., 2016). Some fragments represent myelin out-foldings, while others are seen engulfed by microglia, suggesting a possible active role of microglia in stripping off damaged myelin.

In the aged brain of mice, there's almost a twofold increase in the number of microglia with expanded lysosomal compartments. These aged microglia accumulate autofluo-

rescent material reminiscent of lipofuscin (Safaiyan et al., 2016). This lipofuscin contains nondegradable oxidized lipids, some of which are likely remnants of indigestible myelin (Marschallinger et al., 2020; Thériault & Rivest, 2016). Therefore, it is plausible that the increased burden of myelin clearance in the older brain could contribute not only to an increase in microglia with lysosomal inclusions but also potentially to age-associated microglial dysfunction (Pluvinage et al., 2019).

1.3 The Neuro-Immune Axis

1.3.1 The not so immune-privileged organ: The brain

The central nervous system is protected from potential threats by the cerebrospinal fluid (CSF), the meninges, and a physical blood-brain barrier (BBB). The meninges are populated by various immune cells, providing a level of immune surveillance (Engelhardt & Coisne, 2011; Ousman & Kubes, 2012; Pachter et al., 2003). However, the exact mechanisms by which these cells and antigens from the CNS trigger immune responses have remained unclear (Alves de Lima et al., 2020; Ayub & Bae, 2021; Louveau, Harris, et al., 2015).

Early research involving the transplantation of tumors (Murphy & Sturm, 1923) or fetal tissue (Willis & Keith, 1935) into the brain parenchyma showed successful growth, suggesting the brain as a potential site for studying embryonic and tumor development. The tolerance of these transplants, in contrast to their rejection in peripheral areas, indicated the brain's unique immunological status. Seminal experiments by Medawar in the 1940s (Medawar, 1948) further reinforced this concept, contributing to the understanding of the brain as an 'immune privileged' site. This immune privilege was thought to arise from several physiological characteristics of the CNS, including the presence of the blood-brain barrier (BBB), the lack of professional antigen-presenting cells in brain tissue, low expression of MHC class I and II, and the perceived absence of traditional lymphatic drainage (Brent, 2016; Medawar, 1996; Simpson, 2004). These

factors were believed to contribute to the slow immune reactions observed in the brain. However, despite these barriers, interactions between the CNS and the immune system were found to occur, extending beyond pathological conditions to include homeostatic functions (Carson et al., 2006; Galea et al., 2007; Louveau, Harris, et al., 2015).

Significant progress has been made since these initial studies, with key findings demonstrating that CNS-derived antigens can induce an immune response in the deep cervical lymph nodes (Cserr et al., 1992), that the immune response in the CNS can have both positive and negative effects on brain function (Walsh et al., 2014), and that the CNS houses a functional lymphatic system within the meninges (Louveau, Smirnov, et al., 2015).

However, the concept of the CNS as immune privileged continues to evolve as our understanding of complex neuroimmune interactions expands. One of the early mechanisms suggested to underlie immune privilege was the perceived absence of classical lymphatic drainage of CNS antigens (Burnet, 1970; Galea et al., 2007). Despite this, it's now known that soluble constituents from the brain tissue and the CSF do drain into the deep cervical lymph nodes, albeit via a different route (Harling-Berg et al., 1989; Laman & Weller, 2013; Weller et al., 2010).

1.3.2 Variability of immune privilege

The central nervous system (CNS) is divided into several compartments: the parenchyma, the subarachnoid space which contains the choroid plexus and cerebrospinal fluid (CSF), the meninges, and the brain skull bone marrow (Louveau, Harris, et al., 2015). The state of immune privilege in these areas is not absolute but rather conditional and varies regionally.

It's now widely accepted that both innate and adaptive immune system cells are present in the CNS under normal conditions. In a healthy brain, microglia continually

monitor the brain parenchyma. There are also small amounts of both adaptive and innate immune cells, such as T cells, B cells, neutrophils, monocytes, and macrophages derived from them. These cells can enter the brain, especially the meninges, and contribute to brain development and learning (Alves de Lima et al., 2020).

Recent research has revealed that adaptive and innate immune cells can populate the dura through channels in the skull that connect the skull bone marrow to the dura (Louveau, Smirnov, et al., 2015). Therefore, under normal conditions, immune cells can access, especially, the border regions of the brain and potentially interact with cell populations within the parenchyma. The fact that most adaptive immune cells in the CNS under normal conditions are located at its borders allows the brain and spinal cord to detect and respond to disturbances while simultaneously maintaining neuronal function through immunological protection.

1.3.3 Compartmentalization of CNS Immunity

Vertebrates' immunological defenses are made up of two subsystems: the innate and adaptive immune responses (Vivier & Malissen, 2005). The innate immune system reacts to pathogens through receptors that are encoded in the germline and are particularly expressed in non-clonally distributed cell types. During an innate immune response, pattern-recognition receptors like Toll-like receptors (TLRs) identify microbial pathogens and damage-associated molecular patterns (such as misfolded proteins, denatured DNA, and lipopolysaccharide [LPS]), triggering the activation of NF-kB signaling and inflammation (Medzhitov, 2001). The cellular components of the innate immune system include dendritic cells, monocytes, macrophages (including microglia in the brain), and natural killer T cells. The innate immunity response is quick and somewhat nonspecific.

On the other hand, adaptive immune responses can be highly specific, relying on the vast array of antigen receptors on T and B cells (TCR and BCR), which are the cellular elements of the adaptive immune system (Clark & Kupper, 2005). The diversity of TCR and BCR is generated somatically through site-specific DNA recombination, and each receptor of a particular specificity is expressed clonally. This repertoire of receptors enhances the adaptive immune response's ability to detect a wide range of potential antigens encountered throughout life. Thus, the nature of the innate and adaptive repertoire is a key difference between these two types of immunity.

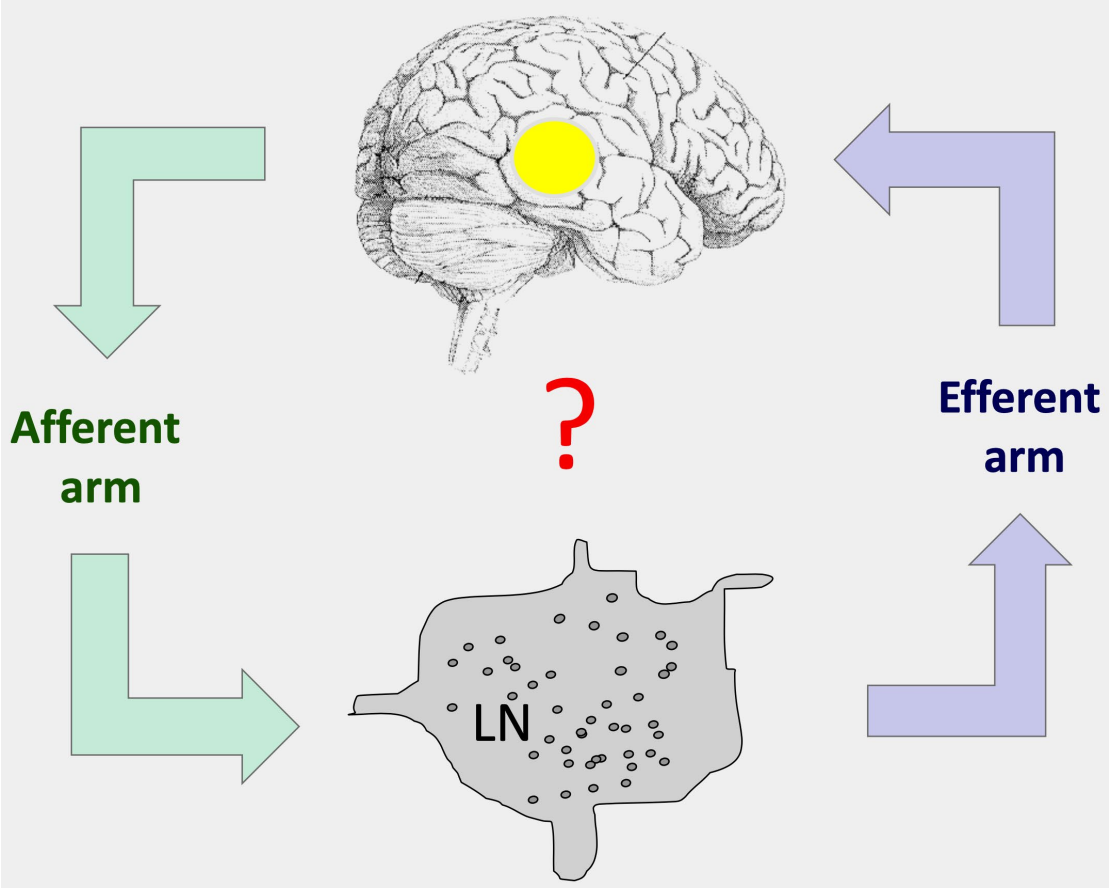

Figure 2: Elements of CNS Immunity

The immune responses are divided into afferent and efferent arms, in line with the two cellular composition arms of the immune systems. The afferent arm of the adaptive

immune response involves antigen presentation to naive T cells, leading to their priming and activation. Soluble antigens and immune cells carrying antigens from the brain are transported to the deep cervical lymph nodes (dCLNs), where these antigens are presented to naive T cells and B cells by professional antigen-presenting cells (APCs), such as mature dendritic cells (Papadopoulos et al., 2020). Antigen-specific T cells and B cells become activated and undergo clonal expansion after returning to the brain. Under disease conditions, APCs accumulate in the inflamed brain (Garber et al., 2019). It remains unclear whether endogenous or infiltrated APCs in the brain parenchyma function as antigen presenters in situ, leading to an adaptive immune response. The entry of new APCs, T cells, and B cells into the brain, along with the local response of resident microglia to local disease pathology, results in an altered immune state in the brain parenchyma that differs from that in the homeostatic brain.

The efferent arm of the adaptive immune response begins when antigen-specific T cells reach the brain parenchyma and exert their effector function. However, before that, these cells need to cross either the blood-brain barrier or from brain borders to the parenchyma, where they encounter a unique brain niche, including neurons, microglia, astrocytes, oligodendrocytes, endothelial cells, extracellular matrix, and brain fluids.

Both the immune system and the central nervous system continuously monitor the environment and make necessary adjustments to maintain homeostasis.

1.4 Interferon Signaling

The immune response to pathogenic stimuli is an incredibly complex, multi-layered process. In our studies, we explore one of the components of this response: Interferon signaling.

The interferon (IFN)-mediated innate immune response, a product of evolutionary selection, is intrinsically encoded within genomes and acts as a formidable initial barrier against invading pathogens. Upon the detection of a pathogen and the subsequent

synthesis of IFN, these molecules attach to receptors on the cell surface, instigating a signaling sequence via the Janus kinase signal transducer and activator of transcription (JAK-STAT) pathway. This results in the transcriptional control of a multitude of IFN-regulated genes (IRGs), culminating in a potent antiviral state that is effective against various RNA viruses (positive-, negative-, and double-stranded), DNA viruses, and intracellular bacteria and parasites (Stark & Darnell, 2012). Moreover, IFN signaling is instrumental in molding the adaptive immune response (Platanias, 2005; Schoenborn & Wilson, 2007).

Years of meticulous research have allowed scientists to delineate the mediators of signal transduction and the DNA response elements that participate in JAK-STAT signaling. However, the functions of only a small number of IRGs have been extensively examined. Studies into the mechanisms governing IRGs are beginning to shed light on how the IFN-induced state alters cellular biology, priming cells for heightened pathogen detection, facilitating effective defense against pathogens, and aiding in the restoration of normal cellular function. Furthermore, the discovery of abnormal IFN signatures in various autoimmune diseases emphasizes the critical need for rigorous regulation of IFN signaling (Crow & Manel, 2015).

1.4.1 A Brief History

In the early 1950s, the scientific community recognized that virus-infected cells could exhibit resistance to subsequent viral infections under specific conditions, indicating that viruses could mutually interfere (Henle, 1950). This phenomenon was also observed with inactivated influenza virus, which could hinder the activity of live influenza virus, although the agent causing this interference remained unidentified at that time. In 1957, Isaacs & Lindenmann coined the term "interferon" (Isaacs et al., 1957; Isaacs & Lindenmann, 1957) to describe a likely cellular substance that obstructed influenza infection. Subsequent research identified interferon (IFN) as a small protein,

secreted by cells in response to the detection of pathogen-associated molecular patterns (PAMPs) via pattern-recognition receptors (PRRs) (J. Wu & Chen, 2014).

Following these foundational discoveries, IFN was extracted from crude protein fractions of stimulated human or nonhuman primate white blood cells, serving as a primary source of the substance (Cantell, Hirvonen, Kauppinen, et al., 1981; Cantell, Hirvonen, & Koistinen, 1981). Nearly twenty years after IFN's initial description, methodologies were developed for its purification and detailed characterization (Pestka, 2007). During this refinement process, it was revealed that IFN was not a singular entity but a family of unique proteins, categorized into three distinct classes based on their receptor complexes (Knight, 1975; Rubinstein et al., 1981). These classes of IFN, along with their subtypes, trigger signaling pathways leading to diverse and significant effects, including variations in ISG profiles, induction kinetics, antiviral and antiproliferative activities, and immunomodulatory capacities. This dissertation focuses more on Type I and II interferons.

1.4.2 Type I and II Interferons

Type I IFNs represent the most extensive class of interferons in humans, encompassing IFN-α, IFN-β, IFN-ε, IFN-κ, and IFN-ω. These are all located on chromosome 9 and signal via the type I IFN receptor complex, which consists of IFN-α receptor 1 (IFNAR1) and IFNAR2 subunits (Figure 3). Except for IFN-α, which includes 13 human subtypes, each type I IFN is encoded by an individual gene. Almost all cells have the ability to produce IFN-α/β, but plasmacytoid dendritic cells, specialized immune cells, are responsible for the majority of IFN-α production during an infection (Siegal et al., 1999). The type I IFNs exhibit varying tissue expression and binding affinities to the IFNAR1/2 receptor complex (Lee & Ashkar, 2018; Pestka, 2007), leading to diverse effects in terms of antiviral, antiproliferative, and immunomodulatory functions (Jaitin et al., 2006; Moraga et al., 2009).

IFN-γ, the only member of the type II IFN class, forms a homodimer and signals through the IFN-γ receptor complex (IFNGR; Figure 3), which is activated by the interaction with two IFNGR1 subunits, followed by the binding of two more IFNGR2 subunits (Walter et al., 1995). The production of IFN-γ is mainly confined to immune system cells, but since the IFNGR1/2 proteins are broadly expressed, nearly all cell types can respond to IFN-γ (Valente et al., 1992). The resulting signaling plays a crucial role in shaping cellular immunity and also triggers gene products that enhance the type I IFN response (Levy et al., 1990; Lew et al., 1989). In a reciprocal manner, type I IFN signaling also augments IFN-γ signaling (Fujimoto & Naka, 2010; Linossi et al., 2013).

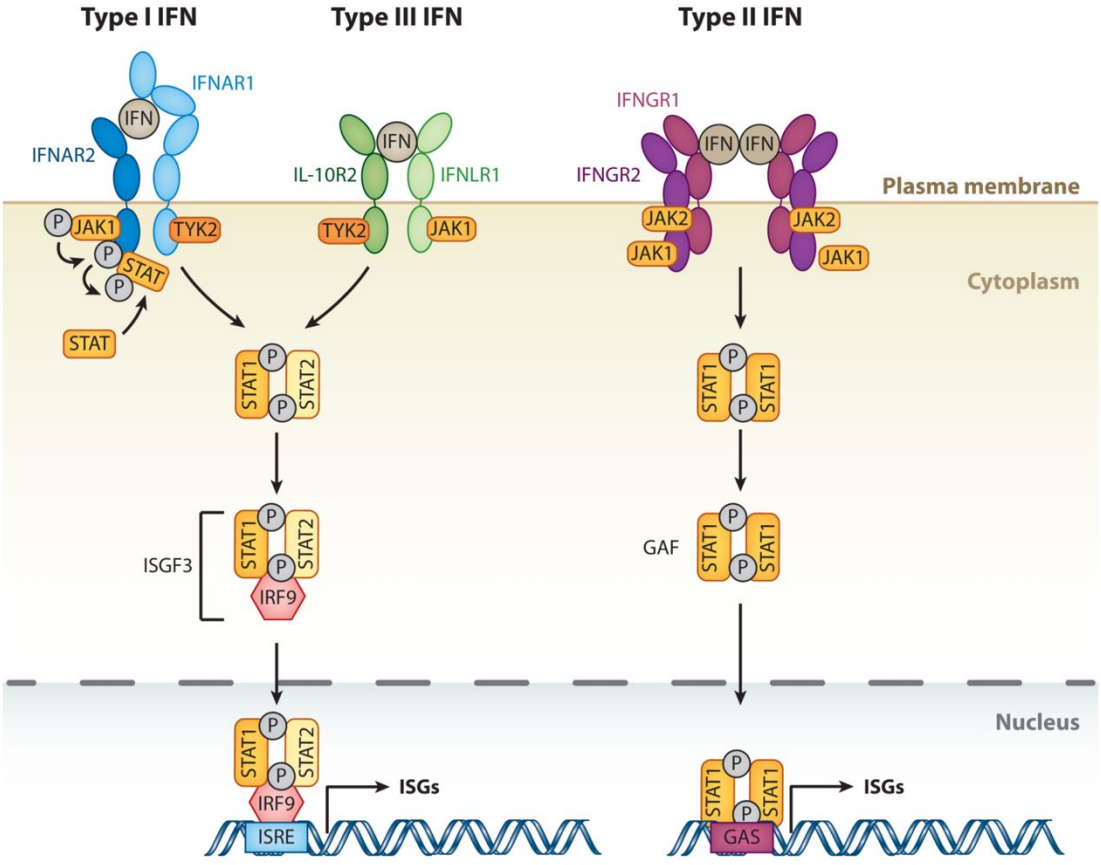

Figure 3: Overview of the interferon signaling cascade

1.4.3 JAK-STAT Pathway

When IFNs attach to cell surface receptors, a signal is propagated across the membrane and into the cell, resulting in significant alterations in cellular characteristics. A remarkable aspect of IFN signaling is the rapidity with which it takes place, a feature enabled by the fact that the creation of new proteins is unnecessary—all the required components are already present at baseline levels (Larner et al., 1984, 1986). JAK-STAT signaling pathway is the universal conduit through which all IFNs transmit their signals.

When a pathogen is detected, IFNs are produced and secreted by the infected cells. These IFNs then bind to specific receptors on the surface of neighboring cells, triggering the activation of associated Janus kinases (JAKs). The activated JAKs, in turn, phosphorylate the receptor, creating docking sites for the STAT proteins (Kawamura et al., 1994).

Once the STAT proteins are recruited to the receptor, they too are phosphorylated by the JAKs (Schindler et al., 1992). This phosphorylation causes them to dimerize, forming active STAT complexes that translocate into the nucleus. Inside the nucleus, these STAT complexes bind to specific DNA response elements, initiating the transcription of IFN-regulated genes (IRGs) (Haan et al., 2006; Kawamura et al., 1994). The expression of these IRGs leads to a wide array of cellular responses, including the establishment of an antiviral state, modulation of cell growth, and regulation of apoptosis.

The JAK-STAT pathway is highly regulated, with numerous checkpoints and modulators ensuring that the signaling is tightly controlled. This is essential, as excessive or prolonged activation can lead to pathological conditions, including autoimmune disorders (Lee-Kirsch, 2017) and certain cancers (Louveau, Harris, et al., 2015). Conversely, deficiencies in JAK-STAT signaling can result in immunodeficiency. The specificity and diversity of the responses are determined by the particular combination of JAKs and STATs involved, as well as the type of IFN and the cellular context (Haan et al., 2006;

Stark & Darnell, 2012). This intricate and highly coordinated signaling pathway exemplifies the complexity of the immune response, allowing for both sound protection against pathogens and fine-tuned regulation of cellular functions (Schindler et al., 2007).

1.4.4 Interferon-γ Signaling

Interferon gamma (IFN-γ) is identified as a pro-inflammatory cytokine, synthesized by a specific subset of peripheral cells, including T lymphocytes, natural killer (NK), and NKT cells, as well as by cells within the central nervous system (CNS) in reaction to particular stimuli (Kasahara et al., 1983; Ye et al., 1995).

Initially characterized as an inhibitor of viral replication, IFN-γ's role has expanded to encompass a multitude of functions in the immune response, particularly against intracellular pathogens and in anti-tumoral defense. This cytokine is now acknowledged as vital for both the innate and adaptive branches of the immune system. Its involvement spans various immune responses, such as macrophage activation, enhancement of major histocompatibility complex (MHC) expression (Giroux et al., 2003), and the modulation of T helper (Th) response types (Bradley et al., 1996; Smeltz et al., 2002).

In the context of healthy brain parenchyma, where T, NK, and NKT cells are typically minimal, IFN-γ's role was believed to be confined to pathological scenarios. These include CNS infections, inflammatory diseases (Olsson et al., 1990; Panitch et al., 1987; Traugott and Lebon, 1988), trauma (Lau and Yu, 2001), and stroke (Seifert et al., 2014; Yilmaz et al., 2006). More recent research has linked IFN-γ to various neuropsychiatric and neurodegenerative disorders where inflammation is considered a key factor. Furthermore, IFN-γ's influence on neural cell genesis and synaptic plasticity, essential for standard brain physiology, indicates that its biological functions may indeed transcend the confines of the immune response (Monteiro et al., 2017).

In Manuscript 2. (Kaya et al., 2022), we suggest that a key pathogenic mediator of brain-resident CD8+ T cells during aging is IFNγ production. IFNγ initiates multiple neurodegenerative pathways, including the suppression of neural stem-cell proliferation (Dulken et al., 2019), the direct cytotoxic elimination of oligodendrocytes by CD8+ T cells^5, and the targeting of neuronal axonal connections by CD8+ T cells^6. Another study presented IFNγ as a regulating component of neuronal connectivity and social behavior in mice (Filiano et al., 2016).

The complex interplay between interferon-gamma signaling and microglia activation form a vital axis (Alspach et al., 2019). Historically, lymphocytic IFN-γ was perceived just as an enhancer of proinflammatory reactions by microglia in the context of bacterial or viral infections. However, recent in situ slice culture studies and in vivo investigations have revealed a more complex and specialized role for IFN-γ in the activation of microglia (Filiano et al., 2016; Ivashkiv, 2018; Prinz & Priller, 2017).

The priming of microglia by IFN-γ leads to a series of responses, including proliferation (microgliosis), increased elimination of synapses, and a moderate release of nitric oxide. These actions are sufficient to disrupt synaptic transmission, gamma rhythm activity, and cognitive functions (Escoubas et al., 2023; Ta et al., 2019). Furthermore, IFN-γ is instrumental in steering Toll-like receptor (TLR)-activated microglia towards neurotoxic phenotypes (Chausse et al., 2020; Papageorgiou et al., 2016), resulting in energetic and oxidative stress, significant network dysfunction, and ultimately, neuronal death.

Pharmacological interventions targeting activated microglia may prove beneficial in conditions characterized by elevated IFN-γ levels, loss of blood–brain barrier integrity, and infiltration of parenchymal T lymphocytes. Such conditions include, but are not limited to, encephalitis (Waltl & Kalinke, 2022), multiple sclerosis (Takeuchi et al.,

2006), and Alzheimer's disease (Chakrabarty et al., 2010; He et al., 2020; Unger et al., 2020).

1.5 Gene Expression: DNA to Phenotype

The fundamental principle of genetics revolves around gene expression, which determines an organism's biological function (Crick, 1958; Roeder & Rutter, 1969). Genes, the basic building blocks of heredity, are composed of nucleotide sequences that create a gene product upon expression. Typically in eukaryotes, a gene, made up of DNA, undergoes transcription into mRNA, which then translates into a protein (Roeder & Rutter, 1969). However, in certain scenarios, RNA is the ultimate gene product, including instances of transfer RNA and microRNA.

The process of gene expression is highly regulated at various stages, involving factors like chromatin accessibility (Kornberg, 1974), DNA silencing (Hotchkiss, 1948), and mRNA processing. These multiple regulatory points are encapsulated within the central dogma of molecular biology (Crick, 1958), further establishing the significance of gene expression in biological studies, as it decisively influences the organism's phenotype.

The transition from genotype to phenotype is a multi-faceted process that initiates from a gene (Allfrey et al., 1964; Luger et al., 1997). For gene expression to occur, the gene must be accessible, which is strictly controlled through post-transcriptional modifications to histones and DNA methylation in vertebrates. With the correct modifications in place, histones will initiate the unwinding of certain regions of the DNA, rendering the gene accessible and ready to serve as a template for RNA polymerase (Holliday & Pugh, 1975). During transcription, RNA polymerase traverses the DNA, attaching a complementary ribonucleotide to the growing RNA strand, thereby gener-

ating an RNA molecule that mirrors the DNA, with the exception of thymine, which is replaced by uracil in RNA.

In eukaryotes, three distinct RNA polymerases exist, among which RNA polymerase II is primarily accountable for the synthesis of protein-coding mRNA. Once the pre-mRNA has been synthesized, it undergoes processing and exportation (Köhler & Hurt, 2007). A crucial aspect of mRNA processing is alternative splicing, which enables the removal of introns or non-coding regions of the pre-mRNA, leading to the production of multiple transcript variants from a single gene. Moreover, the pre-mRNA undergoes capping at the 5' end and polyadenylation at the 3' end for molecule stabilization and protection (Shatkin & Manley, 2000). The processed mRNA is subsequently transported from the nucleus to the cell's cytoplasm.

Once in the cytoplasm, ribosomes bind to the mRNA, guiding the transfer RNAs (tRNAs) to the mRNA. Contrasting the process of transcription where each nucleotide is individually read, during translation, a set of three nucleotides forms a reading unit, or codon (Grunberger et al., 1969). When the anticodon tRNAs, carrying specific amino acids, match a codon, the ribosome links the amino acid to the expanding amino acid chain. The final gene products, proteins, each with a unique function, determine the organism's observed phenotype.

1.6 Capturing the mRNA Signal

Messenger RNA (mRNA) serves as a vital intermediary in the process of gene expression. The first successful methodology for quantifying mRNA was established in 1977 via northern blotting (Alwine et al., 1977). The northern blotting technique necessitates the separation of RNA molecules by gel electrophoresis, their subsequent transfer to a nylon membrane, and their hybridization with either radioactively or chemiluminescent probes. The resultant gel was traditionally imaged using autoradiography, although more contemporary approaches utilize chemiluminescence detection.

Northern blotting, however, requires substantial amounts of mRNA, necessitating the development of more sensitive procedures. Quantitative polymerase chain reaction (qPCR), initially designed for DNA quantification, was adapted to measure gene expression (A. M. Wang et al., 1989). This technique employs either intercalating dyes or hybridizing probes to generate a fluorescent signal during each PCR cycle, which can then be quantified to represent the number of detected mRNA copies in the sample. While qPCR addresses the RNA input limitation of northern blots, it is best suited for the analysis of a limited number of genes and is therefore not suitable for high throughput gene expression studies.

To enable the simultaneous detection and quantification of numerous genes, methodologies like microarrays (Schena et al., 1995), and RNA sequencing (RNA-seq) (Z. Wang et al., 2009) were devised. Microarray technology employs a chip furnished with surface-bound probes that can target numerous genes. The RNA is reverse transcribed, labelled, and then binds to complementary probes on the microarray surface. The degree of binding, quantified by fluorescence intensity, provides comparative data: the signal of a given gene under one condition is juxtaposed with the same gene under a different condition.

1.6.1 The NGS Revolution

Lastly, RNA-seq involves reverse transcribing the RNA and sequencing the cDNA using high-throughput next-generation sequencing (NGS) (Head et al., 2014; Nagalakshmi et al., 2010; Z. Wang et al., 2009). The resulting data are typically mapped to a reference genome, and the total number of detected reads provides information about gene expression (Dobin et al., 2013; Dobin & Gingeras, 2015; Mortazavi et al., 2008). Notably, unlike microarrays, RNA-seq does not necessitate prior sequence knowledge, making it applicable to non-model organisms and de novo genes (Schena et al., 1995; Z. Wang et al., 2009; Wilhelm & Landry, 2009). Furthermore, it provides information not just

about gene expression levels, but also splicing, mutations, and other post-transcriptional modifications (Ozsolak & Milos, 2011; Trapnell et al., 2009; E. T. Wang et al., 2008).

It's worth noting that despite these advancements, bulk RNA sequencing approaches do present limitations, notably in their inability to detect heterogeneity within tissue samples, as the signal represents an average of all cells within the sample (X. Li & Wang, 2021; Nguyen et al., 2018). Newer single-cell RNA sequencing methods are beginning to overcome these limitations, providing a more detailed, cell-by-cell view of gene expression (Nguyen et al., 2018; A. R. Wu et al., 2014; Ziegenhain et al., 2017).

1.6.2 The Ascent of the Single-cell

The advent of single-cell RNA sequencing (scRNA-seq) has revolutionized the field of genomics, offering an unprecedented level of resolution in gene expression profiling (Regev et al., 2017). Unlike traditional bulk RNA-seq technologies, which average gene expression across thousands of cells, scRNA-seq allows for the exploration of gene expression at the individual cell level. This has proven particularly useful in the study of cellular heterogeneity and early embryonic development, where only a few cells are present.

Single-cell RNA-seq has been successfully applied across a range of species, including various human tissues, both normal and diseased. These studies have uncovered significant variability in gene expression between individual cells (Lafzi et al., 2018). The development of different scRNA-seq protocols, driven by technological advancements, has greatly enhanced our understanding of gene expression dynamics at the single-cell level (Mereu et al., 2020).

However, scRNA-seq is not without its challenges. The low amount of starting material can lead to low capture efficiency and high dropout rates. Furthermore, scRNA-seq data is inherently noisier and more variable than bulk RNA-seq data, due to both technical noise and biological variation. This presents substantial challenges for the computational analysis of scRNA-seq data.

Current scRNA-seq protocols can be broadly divided into two categories based on the coverage of the captured transcript: full-length transcript sequencing approaches (Smart-seq2 (Picelli et al., 2013)) and 3' or 5' end transcript sequencing technologies (10X Chromium). Each of these protocols has its own strengths and weaknesses, and the choice of protocol can significantly impact the results of the study (Ziegenhain et al., 2017).

1.7 Smart-seq2 and 10X Chromium Workflows

The initial step in single-cell RNA sequencing (scRNA-seq) is the isolation of individual cells, a process that presents a significant challenge due to the need for high capture efficiency. Among the various techniques available for this purpose, Flow-Activated Cell Sorting (FACS) is a widely adopted method. The sorting experiments in the studies detailed here were conducted using FACS. This technique uses the principles of fluid dynamics and optics to sort a heterogeneous mixture of cells into two or more containers, one cell at a time. The cells are first suspended in a fluid and then passed through a detection apparatus at high speed. As the cells pass through a laser beam, the light scattered by each cell and any fluorescence emitted from the cell is collected and analyzed. Based on the light scattering and fluorescence characteristics, the system can rapidly sort and separate cells into different populations. This method requires a large starting volume of cells in suspension and is capable of high-throughput cell sorting (Gross et al., 2015).

In the articles described here, two different platforms were used to generate scRNA-seq datasets; Smart-seq2 (Picelli et al., 2013) and 10X Genomics Chromium. Each platform utilizes a unique approach to single-cell transcriptomics, offering distinct advantages and potential limitations.

The 10X Genomics Chromium platform is a high-throughput system that leverages a unique barcoding strategy to simultaneously analyze thousands to tens of thousands of cells. This platform operates on the principle of droplet-based partitioning, where individual cells are encapsulated in droplets along with a gel bead carrying a unique barcode (Zheng et al., 2017). The cell's mRNA is then reverse transcribed within the droplet, with the unique barcode (Figure 3) incorporated into the cDNA. This allows for the pooling and simultaneous sequencing of a multitude of cells, with the barcode serving to link each sequence read back to its cell of origin.

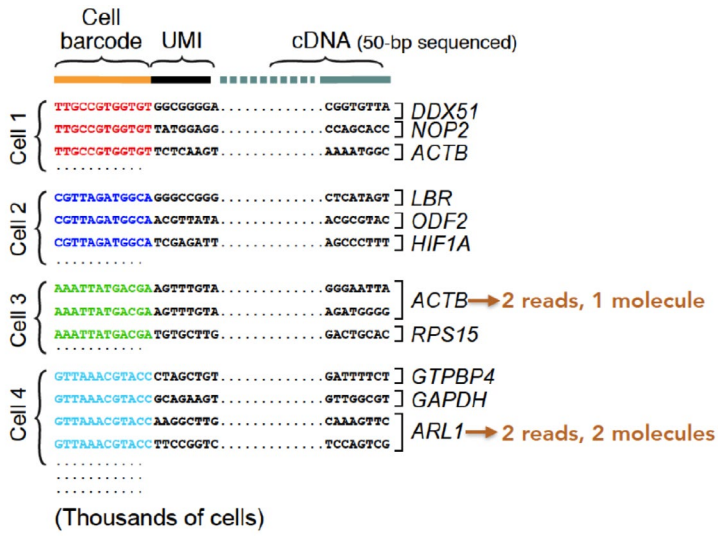

Figure 4: The UMI principle

However, the Chromium platform captures only the 3' or 5' ends of transcripts, limiting the resolution of gene expression analysis. This is a trade-off for the high-throughput nature of the platform, which allows for a broad snapshot of cellular heterogeneity. Additionally, the platform's high-throughput nature can introduce noise

and increase the dropout ratio, which refers to the failure to detect a gene that is expressed in a cell.

On the other hand, Smart-seq2 offers a more detailed view of gene expression by providing full-length transcript coverage. This platform operates on a plate-based system, where individual cells are isolated in wells of a microtiter plate (Picelli et al., 2013). Each cell's mRNA is then reverse transcribed to cDNA within its respective well, allowing for the capture of the entire transcript. This full-length coverage enables the detection of alternative splicing events and allele-specific expression, offering a more in-depth characterization of individual cells.

The sensitivity of Smart-seq2 is also higher than that of the Chromium platform, making it a better choice for detecting low-abundance transcripts (Figure 4). However, the Smart-seq2 platform is a low-throughput method, making it less suitable for studies requiring the analysis of large numbers of cells. Additionally, the protocol is more technically demanding and time-consuming than the Chromium platform, which can increase the potential for technical variability, in turn introducing batch specific artefacts.

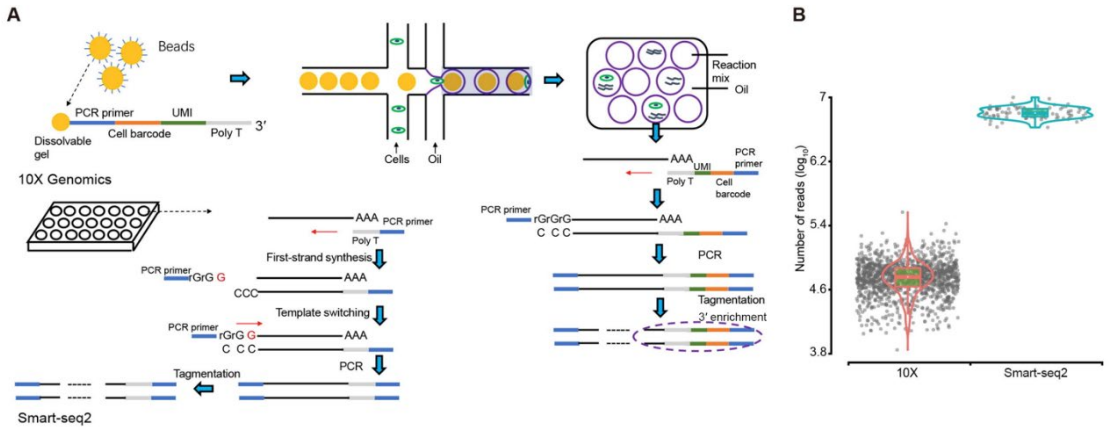

Figure 5: Plate- and droplet-based scRNA-seq platforms

A. The step-wise diagrams of the 10X Chromium and Smart-seq2. **B.** The total read number of each cell using a liver tumor dataset, taken from Wang et al., Figure 1 (X. Wang et al., 2021).

In conclusion, both the 10X Genomics Chromium and Smart-seq2 platforms offer powerful tools for scRNA-seq. The 10X Chromium platform excels in high-throughput analysis, capturing a broad view of cellular heterogeneity, while the Smart-seq2 platform provides a more detailed and sensitive analysis of individual cells. We used both platforms to generate datasets to ensure the validity and reproducibility of our findings.

1.8 Thesis Focus

This dissertation encompasses two studies elucidating the link between white matter aging and the immune system. To characterize the transcriptional profiles of seemingly homogenous yet distinct sub-populations of glial cell types, we established an optimized single-cell RNA-sequencing pipeline, spanning from cell isolation to data analysis.

In the first study (Safaiyan et al., 2021), we identified a distinct microglial population localized to white matter, which appears to adopt a protective cellular state against myelin-related pathologies prevalent in aging. However, the underlying mechanisms driving these myelin pathologies remained unaddressed. To explore this further, in our subsequent study, in which I was a co-first author (Kaya et al., 2022), we employed single-cell RNA sequencing (scRNA-seq) to investigate the cellular states of oligodendrocytes, the myelin-producing cells of the central nervous system. We hypothesized that elucidating oligodendrocyte aging trajectories and their interactions with other glial populations could provide insights into the origins of myelin dysfunction. This approach led to the identification of a novel interferon-responsive oligodendrocyte population, prompting further investigation into the relationship between aging and the adaptive immune system. Taken together, these studies provide

a characterization of certain glial cell state dynamics and their interplay with the adaptive immune system in the context of white matter aging.

2. RESULTS

2.1 White Matter Aging Drives Microglial Diversity

Abstract

Aging results in gray and white matter degeneration, but the specific microglial responses are unknown. Using single-cell RNA sequencing from white and gray matter separately, we identified white matter-associated microglia (WAMs), which share parts of the disease-associated microglia (DAM) gene signature and are characterized by activation of genes implicated in phagocytic activity and lipid metabolism. WAMs depend on triggering receptor expressed on myeloid cells 2 (TREM2) signaling and are aging dependent. In the aged brain, WAMs form independent of apolipoprotein E (APOE), in contrast to mouse models of Alzheimer's disease, in which microglia with the WAM gene signature are generated prematurely and in an APOE-dependent pathway similar to DAMs. Within the white matter, microglia frequently cluster in nodules, where they are engaged in clearing degenerated myelin. Thus, WAMs may represent a potentially protective response required to clear degenerated myelin accumulating during white matter aging and disease.

Declaration of Contribution

M. Simons and O.G. conceived and supervised the project. S.S., S.B.-G., **T.K.**, M. Schifferer, L.L., N.K., O.G., H.J., F.U., L.C.-C., M.J.R., R.P., G.G., M.B., D.F., and X.X. performed experiments and analyzed the data. S.B.-G. and **T.K.** developed software and curated and visualized the scRNA-seq data. O.G., M.R., and M. Simons analyzed the data or supervised data acquisition. M. Simons and O.G. wrote the manuscript with input from all authors.

Neuron

Article

White matter aging drives microglial diversity

Graphical Abstract

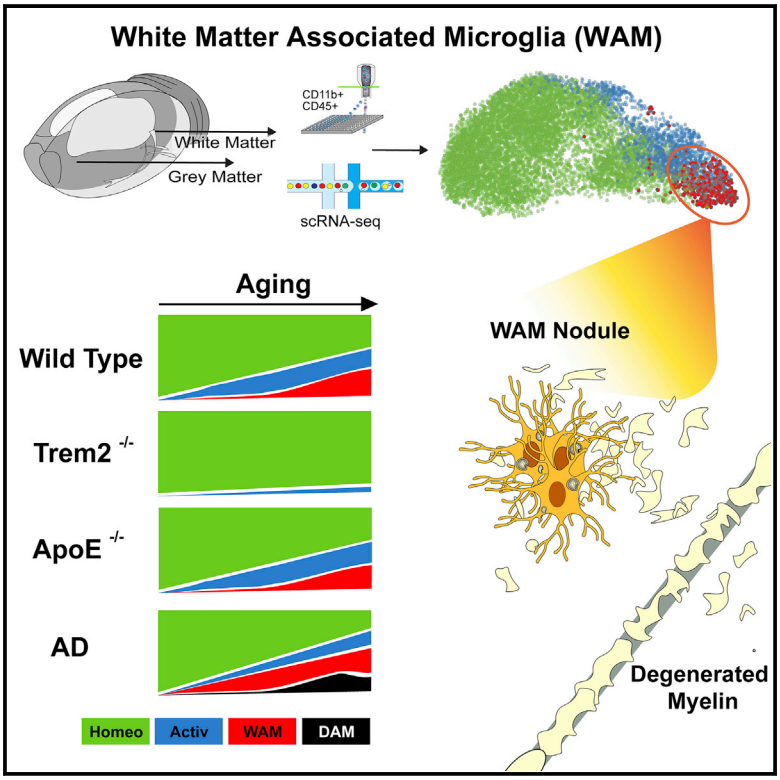

Authors

Shima Safaiyan, Simon Besson-Girard, Tuğberk Kaya, ..., Matthias Brendel, Ozgun Gokce, Mikael Simons

Correspondence

oezguen.goekce@med.uni-muenchen.de (O.G.),
msimons@gwdg.de (M.S.)

In Brief

Safaiyan et al. identify white matter-associated microglia (WAMs), which form in a TREM2-dependent but APOE-independent manner in aging white matter, where they form nodules that are engaged in phagocytosing damaged myelin. Thus, WAMs represents a response required to clear degenerated myelin that accumulates during white matter aging and disease.

Highlights

- scRNA-seq identifies age-dependent white matter-associated microglia (WAMs)
- WAMs form nodules that are engaged in clearing degenerated myelin
- WAM formation depends on TREM2 but not on APOE signaling
- In mouse models of Alzheimer's disease, the WAM response occurs before DAM

Safaiyan et al., 2021, Neuron *109*, 1100–1117
April 7, 2021
https://doi.org/10.1016/j.neuron.2021.01.027

CellPress

CellPress

Neuron

Article

White matter aging drives microglial diversity

Shima Safaiyan,[1,2,9] Simon Besson-Girard,[3,9] Tuğberk Kaya,[1,2,3] Ludovico Cantuti-Castelvetri,[1,2] Lu Liu,[3] Hao Ji,[3] Martina Schifferer,[2] Garyfallia Gouna,[1,2] Fumere Usifo,[3] Nirmal Kannaiyan,[4] Dirk Fitzner,[5] Xianyuan Xiang,[6] Moritz J. Rossner,[4] Matthias Brendel,[7,8] Ozgun Gokce,[3,8,10,*] and Mikael Simons[1,2,8,10,11,*]

[1]Institute of Neuronal Cell Biology, Technical University Munich, 80802 Munich, Germany
[2]German Center for Neurodegenerative Diseases (DZNE), 81377 Munich, Germany
[3]Institute for Stroke and Dementia Research, University Hospital of Munich, LMU Munich, 81377 Munich, Germany
[4]Department of Psychiatry, Ludwig-Maximilians-Universität, 80336 Munich, Germany
[5]Department of Neurology, University of Göttingen, 37075 Göttingen, Germany
[6]Metabolic Biochemistry, Biomedical Center (BMC), Faculty of Medicine, Ludwig-Maximilians-Universität Munich, 81377 Munich, Germany
[7]Department of Nuclear Medicine, University Hospital of Munich, LMU Munich, 81377 Munich, Germany
[8]Munich Cluster of Systems Neurology (SyNergy), 81377 Munich, Germany
[9]These authors contributed equally
[10]Senior author
[11]Lead contact
*Correspondence: oezguen.goekce@med.uni-muenchen.de (O.G.), msimons@gwdg.de (M.S.)
https://doi.org/10.1016/j.neuron.2021.01.027

SUMMARY

Aging results in gray and white matter degeneration, but the specific microglial responses are unknown. Using single-cell RNA sequencing from white and gray matter separately, we identified white matter-associated microglia (WAMs), which share parts of the disease-associated microglia (DAM) gene signature and are characterized by activation of genes implicated in phagocytic activity and lipid metabolism. WAMs depend on triggering receptor expressed on myeloid cells 2 (TREM2) signaling and are aging dependent. In the aged brain, WAMs form independent of apolipoprotein E (APOE), in contrast to mouse models of Alzheimer's disease, in which microglia with the WAM gene signature are generated prematurely and in an APOE-dependent pathway similar to DAMs. Within the white matter, microglia frequently cluster in nodules, where they are engaged in clearing degenerated myelin. Thus, WAMs may represent a potentially protective response required to clear degenerated myelin accumulating during white matter aging and disease.

INTRODUCTION

White matter is composed of mostly myelinated axons that connect neurons from different brain regions into functional circuits. The light appearance of white matter results from the high lipid content of myelin, a multilamellar membrane structure that coats axons and constitutes almost half of the dry weight of white matter (Stadelmann et al., 2019). Long thought to be a passive part of the brain, it is now clear that dynamic, experience-dependent generation of white matter myelin content by oligodendrocytes affects learning and brain function (McKenzie et al., 2014; Mount and Monje, 2017; Pan et al., 2020; Wang et al., 2020; Steadman et al., 2020). In humans, white matter volume reaches its peak at around 40–50 years of age, after which it declines continuously (Sowell et al., 2003). White matter aging is not only associated with tissue shrinkage but also frequently with focal lesions seen upon magnetic resonance imaging (MRI) as hyperintensities related to cognitive impairment and increased risk of stroke and dementia (Prins and Scheltens, 2015). Electron microscopy studies performed in non-human primates have revealed that major pathological alterations that occur during aging are found in white but not gray matter (Peters, 2002), consisting of myelin outfolding, splitting, and accumulation of multilamellar fragments (Peters, 2002; Safaiyan et al., 2016). A better understanding of such age-related white matter pathology and its associated cellular responses is essential because aging is a major risk factor for the most prevalent neurodegenerative diseases. One cell population that responds to aging is microglia, long-lived, self-renewing cells with phagocytic scavenging and immune surveillance functions (Grabert et al., 2016; Füger et al., 2017; Salter and Stevens, 2017; Prinz et al., 2019). Gene expression studies have shown that aged microglia develop a more inflammatory phenotype, particularly in white matter (Poliani et al., 2015; Safaiyan et al., 2016). Age-dependent increase in inflammatory status of microglia is often referred to as primed or sensitized, but the nature of this response is only partially understood (Perry and Holmes, 2014). Several groups have applied single-cell genomics approaches to characterize the shift in microglial states after various pathological insults (Keren-Shaul et al., 2017; Mathys et al., 2017; Friedman et al., 2018; Hammond et al., 2019). This work has established that microglia undergo a relatively stereotypical conversion into disease-associated

microglia (DAM) with a microglia-neurodegenerative (MGnD) or activated response microglia (ARM) phenotype (Keren-Shaul et al., 2017; Krasemann et al., 2017; Sala Frigerio et al., 2019). This conversion is dependent on TREM2 (triggering receptor expressed on myeloid cells 2) activity, which increases phagocytosis and lipid metabolism. DAMs have the potential to restrict pathology by enhancing clearance of misfolded and aggregated proteins that commonly accumulate in neurodegenerative diseases, but to what extent DAMs/MGnD/ARMs are also generated during normal aging is under debate (Keren-Shaul et al., 2017; Friedman et al., 2018; Hammond et al., 2019; Sala Frigerio et al., 2019). Because aging-induced damage to the brain involves degeneration of myelinated nerve fibers, not characterized by protein aggregates but by release of lipid-rich, tightly compacted, and difficult-to-digest myelin debris, we hypothesized that microglial responses should differ between aged gray and white matter. To characterize this microglial response, we combined genetic perturbation, single-cell RNA sequencing (scRNA-seq), immunohistochemistry, and functional assays to comprehensively characterize microglial responses that occur in aged white matter.

RESULTS

TREM2- and age-dependent formation of white-matter associated microglia

To characterize this microglial response, we took advantage of scRNA-seq, a powerful and sensitive technique to reveal transcriptomic cell-to-cell variation of microglia in the normal and diseased brain (Hammond et al., 2019; Keren-Shaul et al., 2017; Krasemann et al., 2017; Masuda et al., 2019; Mathys et al., 2019; Van Hove et al., 2019; Chen et al., 2020). However, transcriptional responses to dissociation have also been shown to alter microglial scRNA-seq analysis (Ayata et al., 2018; Haimon et al., 2018; Hammond et al., 2019; Li et al., 2019). To avoid isolation artifacts, we established an automated dissociation protocol for microglia that inhibits *ex vivo* transcription by addition of actinomycin D (ActD) (Wu et al., 2017). Using scRNA-seq, we tested the effect of ActD addition, which was able to prevent significant induction of four genes (*Jun*, *Lars2, Gm23935*, and *CT010467.1*) and of average expression of immediate-early genes known to respond to brain dissociation (Wu et al., 2017; Figures S1A–S1C; STAR methods). Using this optimized protocol, we dissociated gray matter from the frontal cortex and white matter tracts from the *corpus callosum* as well as the optical tracts and the *medial lemniscus* from wild-type aged mice (18–20 months old; Figure 1A). To compare aging and neurodegeneration effects on microglia, we also isolated microglia from a transgenic Alzheimer's disease (AD) mouse model that expresses five human familial AD gene mutations (5×FAD) (Oakley et al., 2006). Because activation of the DAM gene expression profile depends on TREM2 signaling (Keren-Shaul et al., 2017), we included aged *Trem2* knockout mice (*Trem2*$^{-/-}$) in the analysis. We performed Smart-seq2 (SS2), which has a high transcript capture rate that produces biologically meaningful clusters even for a small number of cells (Picelli et al., 2014; Gokce et al., 2016; Li et al., 2019). After eliminating low-quality SS2 libraries, we included 1,038 microglia from 16 mice. Analysis of sorting data showed that aged wild-type white matter immune cells had significantly increased levels of CD45^{+} and CD11b^{+} labeling compared with gray matter, which was not observed in aged *Trem2*$^{-/-}$ animals (Figures S1D–S1F). Based on known immune cell markers, we identified 847 high-quality SS2 scRNA-seq microglia from aged mice and cells expressing markers for granulocytes, perivascular macrophages, and oligodendrocytes, which were excluded from downstream analyses (Figures S1I and S1J). Next we analyzed the transcriptomes of single cells using unsupervised uniform manifold approximation and projection (UMAP) analysis, a dimension reduction method, which separated aged white matter from aged gray matter microglia (Figure S1K). This white matter microglia-specific cluster was defined by a specific gene signature (STAR methods; Figure S1K; Table S2). Using this white matter microglia gene signature, we distinguished four distinct populations: two white matter-specific clusters, which we called white matter associated microglia (WAMs) and activated microglia, and two additional clusters found in gray and white matter, which we called homeostatic microglia 1 and 2 (Figures 1B–1E; Figure S2A; Table S2). Comparing wild-type with *Trem2*$^{-/-}$ mice revealed that WAMs and activated microglia are TREM2 dependent (Figure 1E; Figure S2A). WAMs are characterized by downregulation of homeostatic genes (set 4 genes; Figure 1C; Figure S3A), such as purinergic receptor (*P2ry12* and *P2ry13*) and checkpoint genes (*Csfr1r*, *Cx3cr1*, *Hexb*, and *Tmem119*) and by upregulation of DAM-associated genes (set 1 genes; Figure 1C; Figure S2A), such as lipid metabolism and phagosome-related genes (*ApoE*, *Cst7*, *Bm2*, *Lyz2*, *Cd63*, and *Clec7a*), cathepsins (*Ctsb*, *Ctss*, and *Ctsz*), and major histocompatibility complex (MHC) class II-related genes (*H2-D1* and *H2-K1*). Activated microglia are marked by upregulation of genes encoding many metabolic genes, mostly ribosomal subunits and mitochondrial genes (set 2 genes), many of which are part of the microglial response to aging (Ximerakis et al., 2019) (set 2 genes; Figures 1C and 1D; Figure S2A). Homeostatic microglia 1 and 2 were detected in white and gray matter and differed from WAMs by higher expression of homeostatic genes such as *Tmem119*, *Csf1r*, *Cx3cr1*, *Hexb*, and *Tmem119* (set 4 genes; Figure 1C; Figure S2A) and lower expression of genes linked to the DAM signature, such as *ApoE*, *Cst7*, *Bm2*, *Lyz2*, *Cd63*, *Clec7a*, *Ctsb*, *Ctss*, *Ctsz*, *H2-D1*, and *H2-K1* (set 1 genes; Figure 1C; Figure S2A).

To validate our results, we performed droplet-based scRNA-seq (Drop-seq) on 24-month-old mice (21,197 high-quality cells from 17 mice used in five Drop-seq runs; Figures 2A and 2B; Figures S2B and S2C; Table S1, tab "Current Study-10X"). We partitioned cells into major cell types (Figure 2B), revealing the white and gray matter cellular landscapes (Figure 2C). The distribution of ciliated and secretary ependymal cells between white and gray matter validated our microdissection because these cells were located on the *corpus callosum* surface. Using the white matter signature genes, we again identified a continuous range of microglia that reproduced the four microglia clusters of the SS2 scRNA-seq dataset (Figure 2D). The gene expression profiles of all four microglia clusters were very similar in both scRNA-seq datasets. None of the 5,991 microglia from the frontal cortex were identified as WAMs, validating allocation of WAMs to aged white matter (Figures 2E–2G). The activated

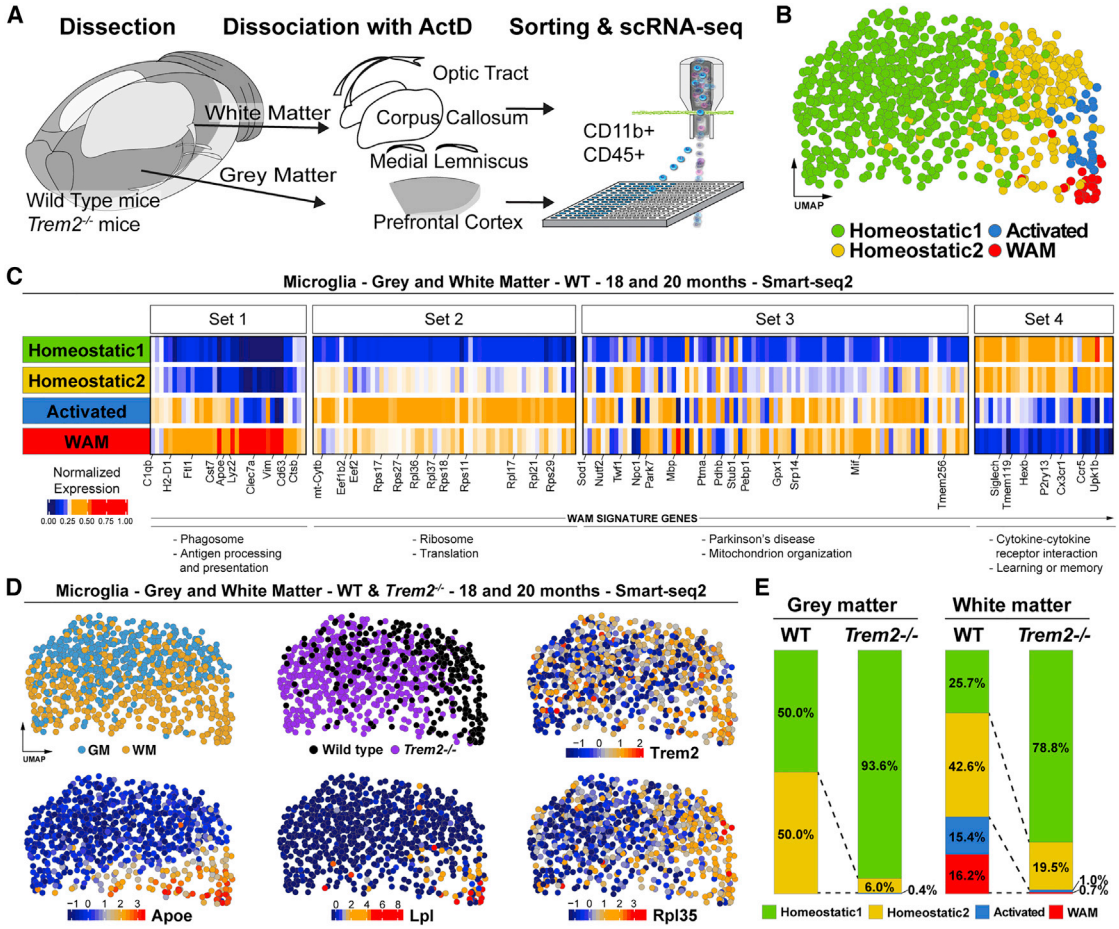

Figure 1. White matter-associated microglia (WAMs) are specific to white matter and exhibit a differential gene expression signature

(A) Experimental design from dissection to cell sorting for the SS2 pipeline (STAR methods).

(B) UMAP of microglia, colored by populations after identification of the white matter activated microglia signature. SS2 dataset, gray matter (GM) and white matter (WM), wild-type (WT), and *Trem2*$^{-/-}$, 18–20 months old (Table S1).

(C) Heatmap of the average expression of differentially expressed genes, comparing the 4 populations of microglia (WAM signature). Values are normalized per gene, showing gene expression across the populations. The gene sets (1–4) were identified by hierarchical clustering of the differentially expressed genes of each population (STAR methods). Gene Ontology analysis pathways are shown below each set of genes. A single-cell version of this heatmap is available in Figure S2A. A list of differentially expressed genes (WAM signature) is shown in Table S2.

(D) UMAP of microglia in WAM signature genes (Table S2). Gene expression is the scaled value.

(E) Bar plot showing the relative distribution of each microglia population in WT GM, *Trem2*$^{-/-}$ GM, WT WM, and *Trem2*$^{-/-}$ WM.

microglia population was enriched in white matter but was also detected in gray matter. The difference in activated microglia distribution in the SS2 and Drop-seq datasets might be due to the different age points analyzed (18–20 versus 24 months) or the higher cell number in the Drop-seq dataset (Figure 2G). Using the Drop-seq dataset, we compared activated microglia with WAMs (Figures 2H and 2I) and identified 428 transcripts that were differentially expressed (Figure 2H). Kyoto Encyclopedia of Genes and Genomes (KEGG) pathway enrichment analysis of the upregulated genes showed that ribosomes were the top enriched pathway in activated microglia. The most enriched pathway in WAMs was hypoxia-inducible factor (HIF-1) signaling, lysosomal, and cholesterol pathways (Figure 2I).

To address whether the WAM signature is aging dependent, we isolated microglia and other myeloid cells from the *corpus callosum* (white matter) and frontal cortex (gray matter) of 4- and 21-month-old wild-type mice using CD11b microbeads and performed bulk RNA-seq analysis. Pathway analysis showed that genes involved in immune cell function were among the most upregulated pathways in aged white matter (Figure S2E). Microglia in aging gray matter did not show these changes in immune cell function but instead exhibited alterations in pathways involved in ion channel activity (Figure S2F). When comparing the genes expressed differentially in aged white matter compared with young white matter or aged gray matter CD11b^{+} cells, 39 transcripts were identified that overlapped with WAM signature genes, such as *Lgals3*, *Spp1*, *Cst7*, *Lpl*, *Clec7a*, *Itgax*, and *ApoE* (Figures S2G and S2H; Table S3), suggesting that WAM marker genes increase with aging in the white matter. Because recent scRNA-seq studies have analyzed microglia during

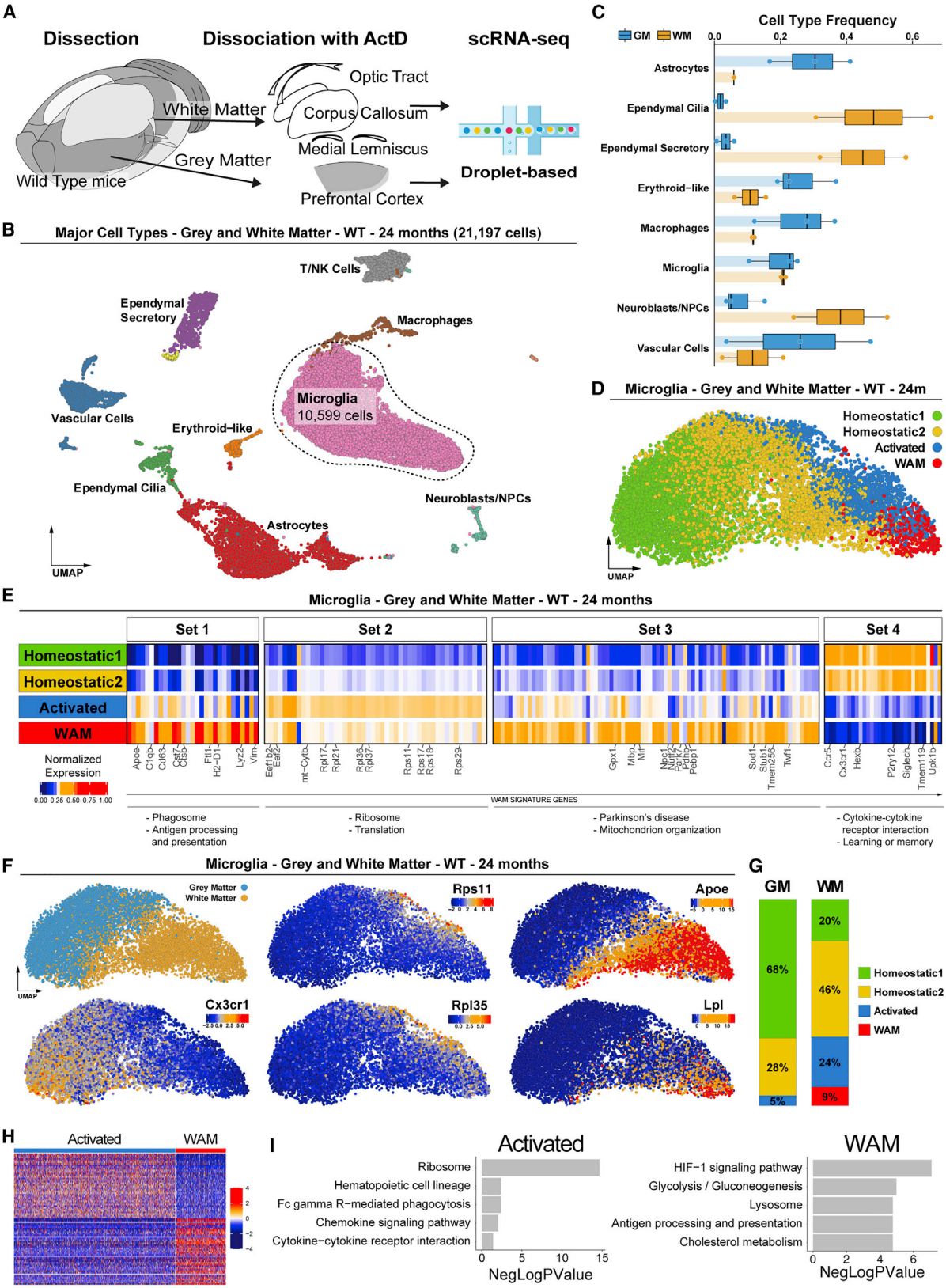

(legend on next page)

normal brain aging without reporting WAMs, we re-analyzed these existing datasets (Hammond et al., 2019; Sala Frigerio et al., 2019). We first analyzed the microglia scRNA-seq by Sala Frigerio et al., 2019, which used cold dissociation to avoid *ex-vivo*-induced transcriptional activity artifacts with the SS2 protocol. We identified microglia with gene expression patterns nearly identical to WAMs (Figure 3A). Already at 3 months of age, microglia with WAM expression patterns could be identified, and the number of these microglia with the WAM gene signature increased with aging (Figure 3B; Figure S3A). Furthermore, when we integrated our dataset with that of Sala Frigerio et al., 2019, we found that the microglial states cluster together (Figure S3B). Similarly, we identified microglia with the WAM gene signature in the Drop-seq dataset from Hammond et al. (2019), which also used cold-dissociated animals to collect cells (Figures 3A–3D; STAR methods). In both datasets, we observed an increase in microglia with the WAM gene signature during aging (Figure 3B). Microglia with the WAM gene signature were characterized by downregulation of homeostatic genes (set 4 genes, *P2ry12*) and upregulation of DAM-associated genes (set 1 genes, *Cd63*). In all three datasets, the activated microglia were marked by upregulation of translation-related gene set 2 (*Rpl37* and *Rpl41*) (Figures 3A, 3C, and 3D). WAMs appear to be present in different datasets with very similar expression profiles.

WAMs cluster in nodules in a TREM2-dependent pathway

To determine the localization of reactive microglia in the brain, we co-stained ionized calsium-binding adaptor 1 (IBA1)$^+$ microglia with activated microglia and WAM markers (Figure S3C) using antibodies against CRYBA4, CLEC7A, AXL, and LGALS3 (Galectin-3) and RNA *in situ* probes against *Itgax* (Figure 4; Figures S4A and S4B). Consistent with the scRNA-seq data, we found that antibodies against the activated microglia marker CRYBA4 (Figure S4B) marked IBA1$^+$ cells in young (2 months old) and old (24 months old) white matter tracts (~15%–20% of IBA1$^+$ cells; Figure S4C). This was in contrast to the WAM markers CLEC7A, AXL, LGALS3 (Galectin-3), and *Itgax*, which labeled IBA1$^+$ cells in old but not young white matter (Figure 4A; Figure S4A). Quantification revealed that ~10%–30% of IBA1$^+$ cells in the *corpus callosum* were positive for the respective WAM markers in 24-month-old mice (20.75% ± 9.67% CLEC7A$^+$IBA1$^+$ cells/area, 14.44% ± 5.05% AXL$^+$IBA1$^+$ cells/area, 31.64% ± 11.68% LGALS3$^+$IBA1$^+$ cells/area, and 9.64% ± 6.46% *Itgax*$^+$IBA1$^+$ cells/area) (Figure 4A). Notably, and in agreement with our RNA-seq data, we found that these cells were almost absent from cortical areas of the aged brain (Figure 4B). Analysis of the localization of double-positive microglia in the white matter showed that they were not distributed evenly but often found in clusters consisting of 3–5 cells with large cell bodies and thick processes (Figure 4C; Figure S4E). Microglia clusters were only found in white matter, where they increased with age (Figure 4C). Such clusters of activated microglia have previously been called microglial "nodules" and are found with a number of different brain diseases, including brain trauma, multiple sclerosis, and viral encephalitis (Rock et al., 2004). To determine the ultrastructure of these nodules, we performed correlated light and electron microscopy using an antibody against IBA1. We found myelin debris in microglia nodules and degenerated myelin in the direct vicinity of the cells, suggesting that microglia nodules are engaged in myelin phagocytosis (Figure 4D; Figure S4F). We performed immunohistochemistry using antibodies against myelin basic protein (MBP), the main structural protein of myelin, to quantify the amount of microglia containing MBP, and found that almost half of the IBA1$^+$ cells with internalized MBP$^+$ particles localized to nodules (Figure 4E; Figure S4G). Microglia in nodules were positive for WAM markers, and we did not detect any activated microglia defined as CRYBA4$^+$/Galectin-3$^-$/IBA1$^+$ cells in nodules (Figure S4D). These data suggest that WAMs actively digest myelin debris in aging white matter, possibly deriving from degenerated myelin sheaths that accumulate over time during aging. If this is the case, then triggering myelin degeneration should induce premature clustering of microglia into nodules. To test this prediction, we used a mouse model for Pelizaeus-Merzbacher disease (PMD mice), a leukodystrophy with extra copies of the proteolipid protein gene (Readhead et al., 1994). These mice initially develop relatively normal myelin, but within weeks, myelin sheaths are broken down gradually (Readhead et al., 1994). We co-stained IBA1$^+$ microglia using antibodies against CLEC7A, AXL, and LGALS3 together with antibodies against MBP to detect myelin particles in microglia. Strikingly, at 2 months of age, when the demyelinating phenotype of these mice starts, microglia nodules appeared in the *corpus callosum* (Figure S5A). These IBA1$^+$ cells in nodules contained MBP$^+$ intracellular particles and increased in number with time (Figures S5B–S5E). Such nodules were not observed in cortical areas. Quantification revealed that ~9%–40% of IBA1$^+$ cells in the *corpus callosum* were already positive for CLEC7A, AXL, or LGALS3 in 2-month-old PMD mice. Similar results were obtained in 7- and 10-month-old PMD mice (Figures S5F–S5H).

These data provide evidence that WAMs in nodules are engaged in clearing degenerated myelin in aging or diseased

Figure 2. Drop-seq validates that WAMs are specific to WM

(A) Experimental design from dissection to cell loading for the Drop-seq pipeline (STAR methods).
(B) UMAP of 21,197 single-cell transcriptomes, colored by major cell type clusters.
(C) GM and WM proportions in major cell type clusters.
(D) UMAP of microglia, colored by populations after identification of the WM microglia signature. Drop-seq dataset, GM and WM, 24 months old (Table S1).
(E) Heatmap of the average expression of differentially expressed genes, comparing the 4 populations of microglia (WAM signature). Values are normalized per gene, showing gene expression across the populations. Gene Ontology analysis pathways are shown below each set of genes.
(F) UMAP colored by tissue annotation and expression of selected marker genes. Gene expression is the scaled value.
(G) Bar plot showing the relative distribution of each microglia population in WT GM and WT WM.
(H) Activated and WAM populations were analyzed separately. Shown is a heatmap with the top 40 differentially expressed genes for activated and WAM populations. Each row represents a gene and each column a single cell.
(I) KEGG pathway enrichment for activated and WAM upregulated differential expression analysis (DEGs).

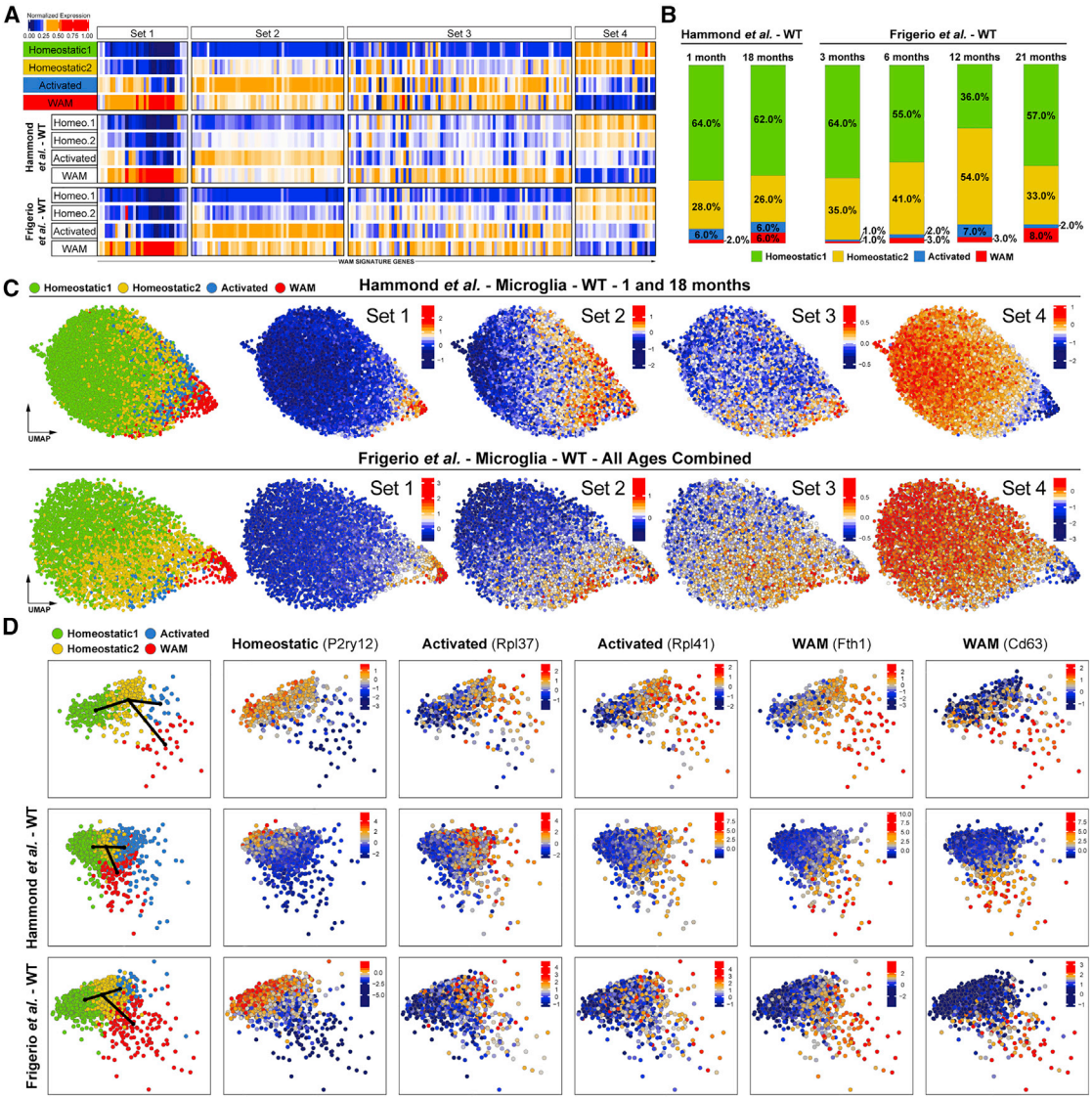

Figure 3. The WAM signature is consistent across multiple datasets

(A) Heatmaps of the average expression of WAM signature gene sets (sets 1–4) for each population, aligned with the four populations identified in data from Hammond et al. (2019) and Sala Frigerio et al. (2019). Values are normalized per gene. The first heatmap is identical to Figure 1C and is reported here for easier comparison. All age groups are pooled within the respective datasets (Table S1).

(B) Cell population ratios by age groups. Shown are data from 1- to 18-month-old WT mice and from 3-, 6-, 12-, and 21-month-old WT mice data from Hammond et al. (2019) and Sala Frigerio et al. (2019), respectively.

(C) UMAPs showing the 4 identified populations and the average scaled expression of each gene set per cell. The first row shows data from Hammond et al. (2019), young and old mouse data combined, 9,558 microglia. The second row shows data from Sala Frigerio et al. (2019), all age groups combined, 5,093 microglia (Table S1).

(D) Principal-component analyses (PCAs) based on the WAM signature genes and overlay with Slingshot plots colored by microglia populations (left), the homeostatic marker *P2ry12*, the activated markers *Rpl37* and *Rpl41* (center), and the WAM markers *Fth1* and *Cd63* (right). Rows 1–3 correspond to data from this study, Hammond et al. (2019), and Sala Frigerio et al. (2019), respectively. Gene expression is the scaled value.

white matter. Because our scRNA-seq data indicated a function of TREM2 in this process, we used antibodies and *in situ* probes to visualize microglia in *Trem2*$^{-/-}$ mice. Consistent with our scRNA-seq data, we failed to detect CLEC7A, AXL, *Itgax*, or LGALS3 (Galectin-3) in the *corpus callosum* of aged *Trem2*$^{-/-}$ mice (Figure 5A). Next we determined the number of homeostatic microglia using antibodies against TMEM119 and P2RY12 and found that the number of TMEM119^{+}IBA1^{+} or P2RY12^{+}IBA1^{+} decreased with age in the white matter of wild-type mice (Figures 5B–5D; Figure S4H). This was in contrast to *Trem2*$^{-/-}$ mice, in which the numbers remained unchanged in 6-, 12-, and 18-month-old mice (Figures 5B–5D; Figure S4H). In addition, and

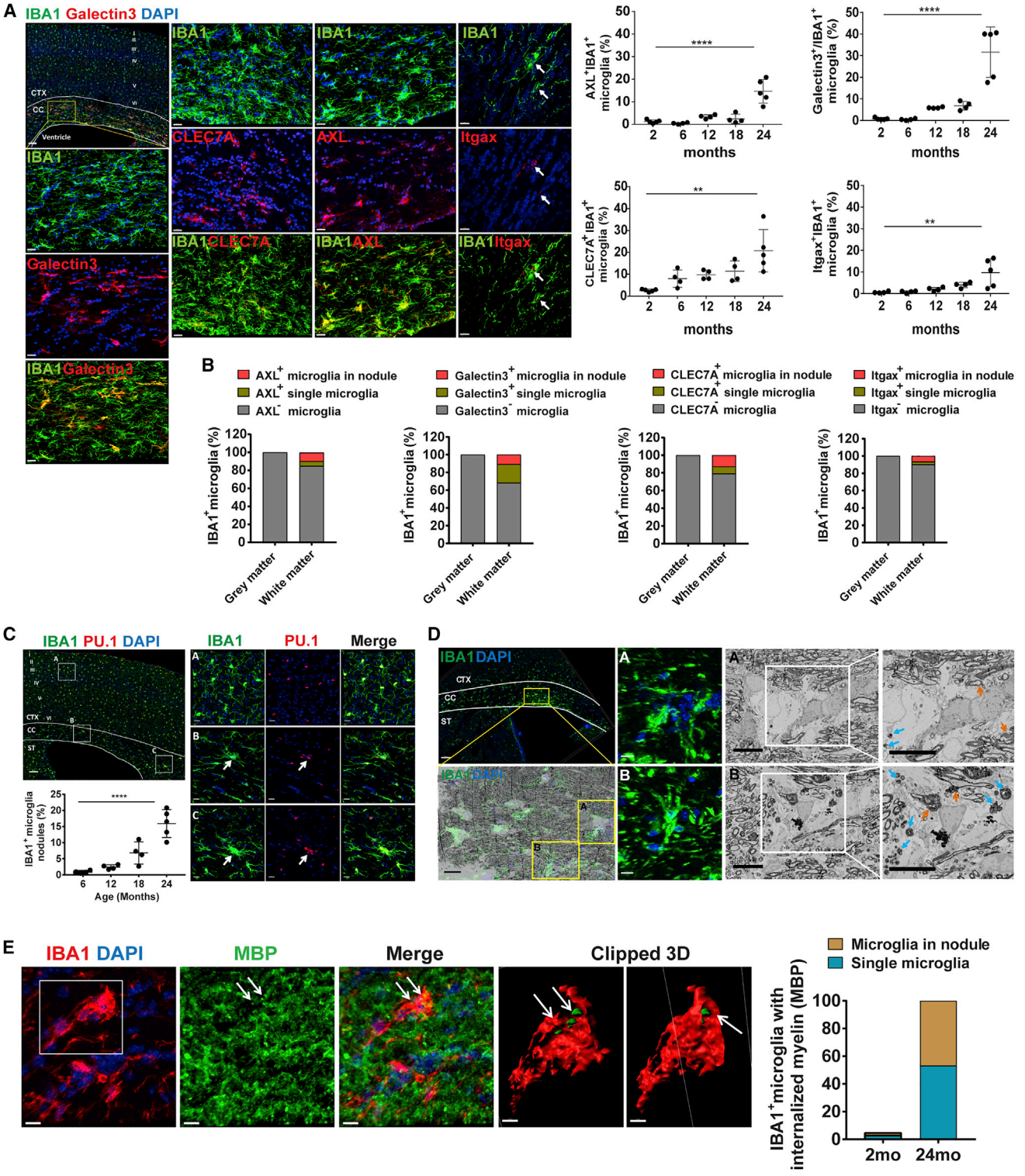

Figure 4. WAM are localized in microglia nodules and contain myelin fragments

(A) Confocal images of CLEC7A, AXL, Galectin-3, and *Itgax* (red) co-localization with IBA1$^+$ microglia (green) in 24-month-old mice using immunohistochemistry and RNAScope *in situ* hybridization. Scale bars, 100 μm (overview) and 20 μm (magnification). Also shown is quantification of CLEC7A, AXL, Galectin-3, and *Itgax* expression in 2-, 6-, 12-, 18-, and 24-month-old mice in WM (*corpus callosum*; n = 4–5 mice per group, mean ± SD, one-way ANOVA followed by Bonferroni's post hoc test; AXL, ****$p < 0.0001$; Galectin-3, ****$p < 0.0001$; CLEC7A, **$p = 0.0013$; *Itgax*, **$p = 0.0039$).

(legend continued on next page)

consistent with previous results (Poliani et al., 2015; Kleinberger et al., 2017), we found that the increase in the number of microglia that occurs during normal aging in wild-type white matter was abolished in *Trem2*$^{-/-}$ mice (Figure S4I). Although nodules increased during aging in white matter of wild-type mice, they were almost undetectable in *Trem2*$^{-/-}$ mice at all time points analyzed (Figure 5E). We also examined microglia in the cortex of *Trem2*$^{-/-}$ and wild-type mice but were unable to detect changes in cell density (Figure S4I) or in the proportion of homeostatic IBA1^{+} cells (Figure 5B–5D; Figure S4H), further suggesting that age-related and DAM-associated changes are mainly confined to the white matter of the brain.

WAMs are engaged in clearing myelin debris

Because the WAM response and generation of nodules is abolished in *Trem2*$^{-/-}$ mice, this mouse model provides a means to investigate the biological function of WAMs. We used electron microscopy to visualize possible differences in the ultrastructure of aged white matter in wild-type and *Trem2*$^{-/-}$ mice. We found enhanced accumulation of myelin whorls (not associated with axons) in the *corpus callosum* of aged *Trem2*$^{-/-}$ compared with wild-type control mice (Figure 5F). In addition, an increased number of cells with electron-dense intracellular inclusions were detected in *Trem2*$^{-/-}$ mice, and, using correlated light-electron microscopy, we found that these cells were microglia (Figure 5G). With light microscopy, MBP^{+}, proteolipid protein (PLP)$^{+}$, and FluoroMyelin^{+} intracellular particles were noticed in microglia of aged *Trem2*$^{-/-}$ in white matter to the same extent as in wild-type mice (Figures S4J–S4L). Furthermore, using light microscopy, microglia with irregular processes were detected, as described previously in the context of human brain aging and particularly in neurodegenerative human diseases (Streit et al., 2004). By double immunostaining, using antibodies against IBA1 and CD68 to visualize microglia process morphology (Tischer et al., 2016), we found a dramatic increase in the number of microglia with irregular processes in the *corpus callosum* of 18-month-old *Trem2*$^{-/-}$ compared with wild-type mice. Strikingly, microglia with irregular processes appeared to be restricted to white matter regions; microglia were of ramified morphology in cortical areas (Figure 5H). Thus, TREM2-dependent WAM activity may be a protective response against damaged myelin, possibly to enhance its uptake and breakdown during white matter aging.

To directly assess whether TREM2 is required for uptake and/or breakdown of myelin debris, we performed *in vitro* experiments with cultured primary microglia. CD11b^{+} cells were prepared from wild-type and *Trem2*$^{-/-}$ mice by magnetic-activated cell sorting (MACS), and myelin debris binding, uptake, and degradation were examined. First, we explored the interaction of myelin debris with the cell surface by performing cell surface binding assays at 4°C, which revealed that similar amounts of myelin debris attached to the surface of wild-type and *Trem2*$^{-/-}$ microglia (Figure 6A). In addition, phagocytic uptake of myelin debris occurred to the same extent in wild-type and *Trem2*$^{-/-}$ microglia (Figure 6B). However, differences were detected when cells were chased for 24 h and immunostained for PLP to determine degradation of the ingested myelin (Figure 6B). These experiments demonstrated that myelin debris degradation occurred less efficiently in *Trem2*$^{-/-}$ microglia compared with the wild type, similar to what occurs when microglia are treated with inhibitors of lysosomal function (leupeptin or bafilomycin A; Figure S6A). We used qRT-PCR to examine whether the impaired degradation was due to an inability to induce expression of lysosomal enzymes and found that expression of *cathepsinL*, *beta-galactosidase1*, and *N-acetylglucosamine-6-sulfatase*, but not *hexoaminidase*, were upregulated upon myelin debris uptake in wild-type but not *Trem2*$^{-/-}$ microglia (Figure 6C). Failure of *Trem2*$^{-/-}$ microglia to upregulate Cathepsin L upon myelin debris treatment was confirmed at the protein level by western blotting (Figure 6D). To determine whether myelin debris degradation was also impaired *in vivo* in *Trem2*$^{-/-}$ mice, we employed a toxin-induced model in which a single injection of lysolecithin was injected into the *corpus callosum* to induce a focal demyelinating lesion in the white matter. Removal of damaged myelin debris occurs mainly by microglia because only relatively few monocyte-derived macrophages enter lesions from the periphery (Lloyd et al., 2019; Plemel et al., 2020). We used fluorescent myelin staining (FluoroMyelin) to determine the amount of myelin debris in LAMP1^{+} degradative compartments in IBA1^{+} cells and found that clearance of internalized myelin debris was delayed in *Trem2*$^{-/-}$ mice (Figure 6E).

Next we established a cell culture-based uptake assay to systematically explore the requirements for myelin debris phagocytosis. We used HeLa cells for this assay because only small amounts of myelin debris are taken up by these cells. This allowed us to transiently express a number of different phagocytic

(B) Bar plots showing the fraction of IBA1^{+} microglia found as single cells or in nodules co-localizing with Galectin-3, CLEC7A, AXL, and *Itgax* in WM (*corpus callosum*) and GM (cortical layers I–V) of 24-month-old WT mice (n = 5 mice per group, each fraction represents the mean value of 5 mice).

(C) Confocal image of IBA1^{+} microglia nodules (green) co-labeled with PU.1 (red) in the *corpus callosum* and cortex of 24-month-old WT mice. Scale bars, 50 μm (overview) and 15 μm (magnification). Also shown is quantification of the number of microglia nodules in 6-, 12-, 18-, and 24-month-old WT male mice (n = 4–5 mice per group, mean ± SD, one-way ANOVA, ****p < 0.0001).

(D) Correlative light and electron microscopy of microglia in the *corpus callosum*. Top left: confocal image of a whole section as a guide map for correlation. Bottom left: scanning electron microscopy (SEM) serial section (100 × 100 × 100 nm) overlaid with a confocal image (transparent, IBA1 in green, and DAPI in blue). Two microglia nodules are relocated on this SEM serial section (yellow boxes, images A and B). Images A and B: confocal and SEM images of microglia nodules. Right column: higher-resolution images (20 × 20 × 100 nm) showing degenerated myelin around microglia nodules (orange arrows) and intracellular myelin fragments (blue arrows). Scale bars, 100 μm (overview, immunohistochemistry [IHC]), 100 μm (correlative light and electron microscopy [CLEM] overlay), and 10 μm (high-magnification IHC and SEM).

(E) Confocal image of co-localization of MBP (green) with IBA1^{+} microglia (red) in nodules in the *corpus callosum* of a 24-month-old WT mouse. Clipped 3D images show MBP^{+} myelin particles (green) in a microglia nodule from different angles. Scale bars, 10 μm. The bar plot shows the fraction of IBA1^{+} single cells and IBA1^{+} cells in nodules with internalized myelin fragments in 2- and 24-month-old WT male mice (n = 5 mice per group, each fraction represents the mean value of 5 mice, 2 brain sections were analyzed per mouse).

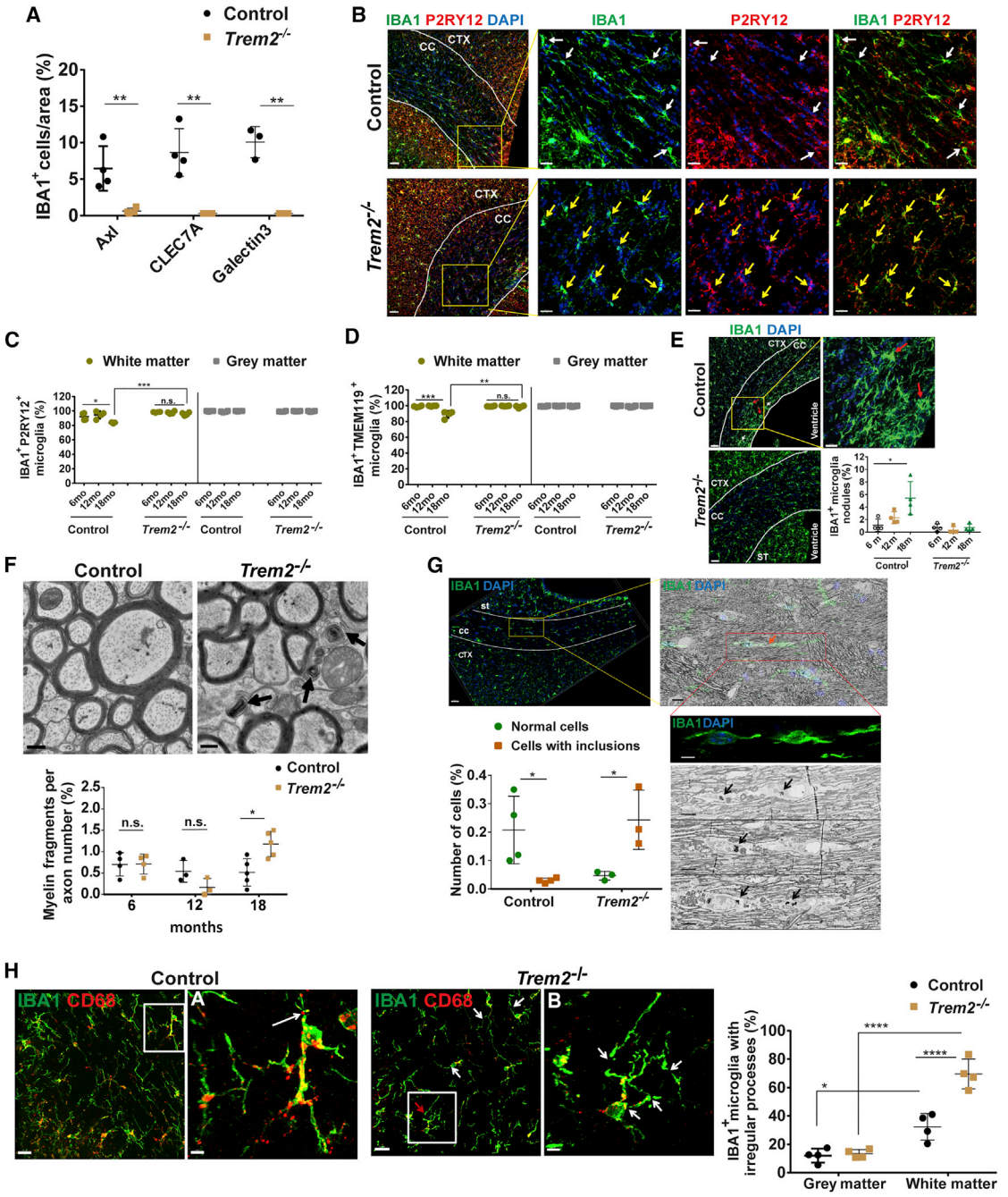

Figure 5. TREM2 is required for WAM states and myelin debris clearance

(A) Quantification of IBA1$^+$ cells also positive for AXL, CLEC7A, and Galectin-3 in the *corpus callosum* of 18-month-old *Trem2*$^{-/-}$ and control mice (n = 4 mice per group, mean ± SD; AXL, **p = 0.009; CLEC7A, **p = 0.0022; Galectin-3, **p = 0.0013; Student's two-tailed t test).

(B) Confocal images showing expression of P2RY12 (red) in IBA1 (green) in 18-month-old *Trem2*$^{-/-}$ and age-matched control mice. The white arrows point to P2RY12$^-$ microglia, and the yellow arrows point to P2RY12$^+$ microglia. Scale bars, 50 μm (overview) and 20 μm (magnification).

(C) Quantification of IBA1$^+$ microglia expressing P2RY12 in WM and GM in 6-, 12-, and 18-month-old *Trem2*$^{-/-}$ and age-matched control mice (n = 4 mice per group, mean ± SD, one-way ANOVA; control, WM, *p = 0.0299; *Trem2*$^{-/-}$, WM, p = 0.1491; 18 months: control versus *Trem2*$^{-/-}$, ***p = 0.0003; Student's two-tailed t test).

(D) Quantification of IBA1$^+$ microglia expressing TMEM119 in WM and GM in 6-, 12-, and 18-month-old *Trem2*$^{-/-}$ and control mice (n = 4 mice, mean ± SD, one way ANOVA; control, WM, ***p = 0.0002; *Trem2*$^{-/-}$, WM, p = 0.1149; 18 months, control versus *Trem2*$^{-/-}$, **p = 0.0058; Student's two-tailed t test).

(E) Confocal image showing abundant microglia nodules in the *corpus callosum* of 18-month-old control compared with age-matched *Trem2*$^{-/-}$ mice. Scale bars, 50 μm (overview) and 20 μm (magnification). Also shown is quantification of the number of microglia nodules in 6-, 12-, and 18-month-old *Trem2*$^{-/-}$ and control male mice (n = 4 mice per group, mean ± SD, one-way ANOVA, *p = 0.0161).

(legend continued on next page)

receptors and to determine their role in mediating myelin debris uptake (Figures S6B and S6C). First we confirmed that expression of TREM2 together with TYROBP (TYRO protein tyrosine kinase-binding protein) induced phagocytosis of myelin debris in HeLa cells (Figure S6D). However, this assay also revealed that a number of different phagocytic receptors were able to mediate myelin debris phagocytosis (Figures S6D–S6F). Notably, all receptors known to depend on direct phosphatidylserine binding or indirect binding using bridging molecules promoted myelin debris uptake. Some of the receptors, such as *Axl*, are part of the WAM response, whereas others, such as *Mertk*, are highly expressed in homeostatic microglia. To confirm that phosphatidylserine is required for myelin debris uptake, we masked phosphatidylserine binding sites by pre-incubating myelin debris with Annexin V, which markedly reduced myelin debris phagocytosis in primary cultures of microglia (Figures S6G and S6H). Thus, binding of myelin debris to multiple receptors that are also expressed in homeostatic microglia suggests that WAMs have an essential function in myelin debris degradation rather than in phagocytotic uptake.

Microglia with WAM and DAM gene signatures co-exist and are generated in an APOE-dependent pathway in models of AD

Next, we explored whether a WAM-like population can be found in mouse models of AD, in which DAMs have been described previously (Keren-Shaul et al., 2017; Krasemann et al., 2017). We generated scRNA-seq data with our optimized protocol from the 6-month-old 5×FAD mouse model of AD. We identified DAM clusters as reported by Keren-Shaul et al. (2017) but also microglia with the WAM gene signature (Figures 7A and 7B). We repeated the same clustering approach on a larger microglial scRNA-seq dataset from Sala Frigerio et al. (2019), which used two mouse models of AD, an *App* knockin mouse model ($App^{NL\text{-}G\text{-}F}$) Masuda et al., 2016; Sasaguri et al., 2017), and transgenic APP/PS1 mice (Borchelt et al., 1997) in combination with an $Apoe^{-/-}$ strain (APP/PS1-$Apoe^{-/-}$) (Sala Frigerio et al., 2019). Our analysis of microglia from AD models distinguishes two microglial subtypes in addition to the four we identified in aged mice. These two additional subtypes match the expression profiles of DAM1 and DAM2 microglia reported previously by Keren-Shaul et al. (2017). In AD models, microglia with the WAM gene expression profile appear very early but with nearly identical signatures compared with the normal aging-induced profiles. DAM1 and DAM2 showed strong gradual upregulation of sets 1–3 and downregulation of the homeostatic genes in set 4 (Figures 1C, 2E, and 7B). Next, we visualized regulation of the DAM program in our aged microglia dataset by plotting the top 500 genes altered in DAMs (Keren-Shaul et al., 2017). Interestingly, we observed that activated microglia and WAMs upregulated distinct parts of the DAM signature (Figure S7A). WAMs appear to represent a microglial state displaying partial activation of the DAM gene signature, suggesting that the DAM program consists of multiple transcriptional modules. WAM and DAM states are likely to be continuous cell identities that can blend with each other. In aging, microglia activation appears to be shifted toward the WAM state, whereas in AD, the shift is toward DAMs.

Thus, in models of AD, microglia with WAM and DAM gene signatures co-exist, raising the question of when and in which temporal sequence they form. In 3-month-old $App^{NL\text{-}G\text{-}F}$ mice, we did not detect DAM2, whereas microglia with the WAM gene signature were present (Figures 7C and 7D). The proportion of cells in DAM and WAM clusters increased with age until 12 months, and then DAMs showed a decrease between 12–21 months.

How do WAM differ from DAM states? To address this question, we took advantage of one main characteristic of WAMs: their involvement in myelin debris clearance in white matter. Although it is well established that activated microglia are distributed throughout the brain and cluster around amyloid plaques (Ulrich et al., 2017), it is not clear whether microglia nodules containing myelin debris are formed. We used immunohistochemistry to determine whether microglia form nodules in white matter of mouse models of AD. We co-stained 6-month-old $App^{NL\text{-}G\text{-}F}$ mice with antibodies against IBA1, MBP, and amyloid and detected nodules with $IBA1^+$ cells containing MBP^+ intracellular particles in the *corpus callosum* that were not associated with amyloid plaques (Figure S7B). Similar findings were obtained in 6-month-old 5×FAD mice, in which nodules containing $IBA1^+$ cells with MBP^+ intracellular particles were detected in the *corpus callosum* (Figures S7C and S7D). A large fraction of $IBA1^+$ cells was also positive for CLEC7A and LGALS3 (Figures S7E and S7F). In 2-month-old 5×FAD mice, only a relatively small number of microglia nodules were detected (Figures S7E and S7F). When $App^{NL\text{-}G\text{-}F}$ mice were crossed with $Trem2^{-/-}$

(F) Representative transmission electron microscopy (TEM) image of the *corpus callosum* in 18-month-old $Trem2^{-/-}$ and control mice, showing myelinated axons and myelin fragments (arrows). Scale bar, 0.2 μm. Also shown is quantification of myelin fragments in 6-, 12-, and 18-month-old $Trem2^{-/-}$ compared with control mice (n = 3–5 mice per group, mean ± SD, two-way ANOVA followed by Bonferroni's post hoc test; 6 months old, $p > 0.9999$; 12 months old, $p > 0.9999$; 18 months old, $^*p = 0.0186$).

(G) CLEM of an 18-month-old $Trem2^{-/-}$ *corpus callosum* region. Top left: confocal image as a guide for correlation. Top right: overlaid confocal image (transparent, IBA1 in green, DAPI in blue) onto the SEM serial section and relocation of an $IBA1^+$ cell on the SEM section (red box). Bottom right: confocal and SEM images of an $IBA1^+$ cell. 3 images of SEM serial sections (10 × 10 × 100 nm) reveal intracellular electron-dense inclusions (black arrows). Scale bars, 50 μm (overview, IHC), 20 μm (CLEM overlay), and 10 μm (high-magnification SEM). Also shown is quantification of the number of cells with electron-dense inclusions (n = 3–4 per group, mean ± SD; control, $^*p = 0.0245$; $Trem2^{-/-}$; $^*p = 0.0371$; Student's two-tailed t test).

(H) Confocal image of microglia co-labeled with IBA1 (green) and CD68 (red), showing microglia with irregular processes in $Trem2^{-/-}$ and microglia in control mice (18 months old). Normal processes are defined by a CD68-positive connection between two IBA1-positive structures (white arrow in image A), whereas fragmented processes have no CD68-positive connection (white arrows in image B). Scale bars, 20 μm (overview) and 5 μm (magnification). Also shown is quantification of the number of microglia with irregular processes in the *corpus callosum* and cortex (layers I–IV) of 18-month-old $Trem2^{-/-}$ and control male mice (n = 4 mice per group, mean ± SD, two-way ANOVA followed by Bonferroni's post hoc test; GM versus WM: control, $^*p = 0.0156$; $Trem2^{-/-}$, $^{****}p < 0.0001$; WM: control versus $Trem2^{-/-}$, $^{****}p < 0.0001$).

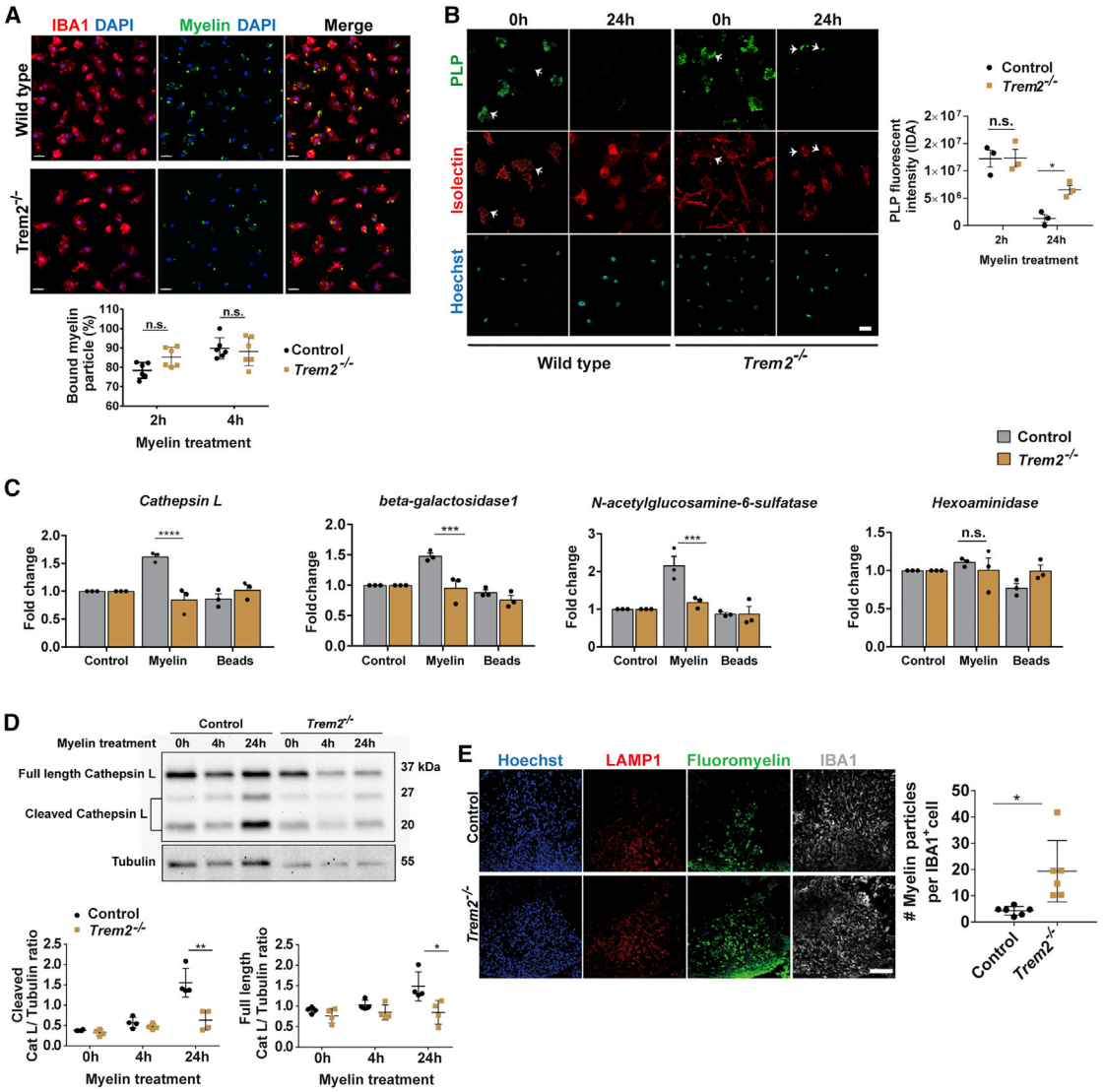

Figure 6. TREM2 is required for lysosomal degradation of internalized myelin debris in microglia

(A) Immunocytochemistry showing PKH67-labeled myelin particles (green) bound to *Trem2*$^{-/-}$ and WT primary microglia (red) in a cell surface binding assay. Scale bar, 20 μm. Also shown is quantification of the number of primary microglia with attached myelin particles 2 and 4 h after myelin treatment (n = 3 independent experiment, mean ± SD; each dot shows the percentage of microglia bound to myelin particles in an area of 0.1 mm^2; two-way ANOVA followed by Bonferroni's post hoc test; control versus *Trem2*$^{-/-}$: 2 h, p = 0.2828; 4 h, p > 0.9999).

(B) Immunocytochemistry showing uptake of PLP-labeled myelin particles (green) by isolectin-labeled microglia (red) isolated from *Trem2*$^{-/-}$ and WT mice. Scale bar, 25 μm. Also shown is quantification of the amount of myelin within microglia cells as measured by the average PLP fluorescence intensity per cell (n = 3 independent experiment, mean ± SD, two-way ANOVA followed by Sidak's post hoc test; control versus *Trem2*$^{-/-}$: 2 h, p = 0.9970; 24 h, *p = 0.0322).

(C) Quantification of expression of the lysosomal enzymes *cathepsinL*, *beta-galactosidase1*, *N-acetylglucosamine-6-sulfatase*, and *hexoaminidase* in *Trem2*$^{-/-}$ and WT microglia treated with myelin or beads (as control) compared with *Trem2*$^{-/-}$ and WT untreated cells. Data are expressed as fold change compared with untreated cells 24 h after myelin debris treatment (two-way ANOVA followed by Sidak's post hoc test; *cathepsinL,* ****p < 0.0001; *beta-galactosidase*, ***p < 0.0004; *acetylglucosamine-6-sulfatase*, ***p = 0.0007; *hexoaminidase*, p = 0.7427).

(D) Western blot analysis of Cathepsin L levels in control and *Trem2*$^{-/-}$ microglia culture lysates 4 and 24 h after myelin treatment. Also shown is quantification of the expression level of full-length and cleaved Cathepsin L compared with tubulin under each condition (mean ± SD, error bar represents 4 independent experiments, Student's two-tailed t test; cleaved CTSL (CatL), **p = 0.0053; full-length CatL, *p = 0.0312).

(E) Confocal images of demyelinating lesions (lysolecithin model) showing myelin debris accumulation (FluoroMyelin in green) in lysosomes (LAMP1 in red) of 3-month-old *Trem2*$^{-/-}$ and control microglia. Scale bar, 100 μm. Also shown is quantification of the number of myelin particles in *Trem2*$^{-/-}$ and control microglia in demyelinating lesions (n = 6 lesion taken from 3 animals per group, mean ± SD, *p = 0.0108, Student's two-tailed t test).

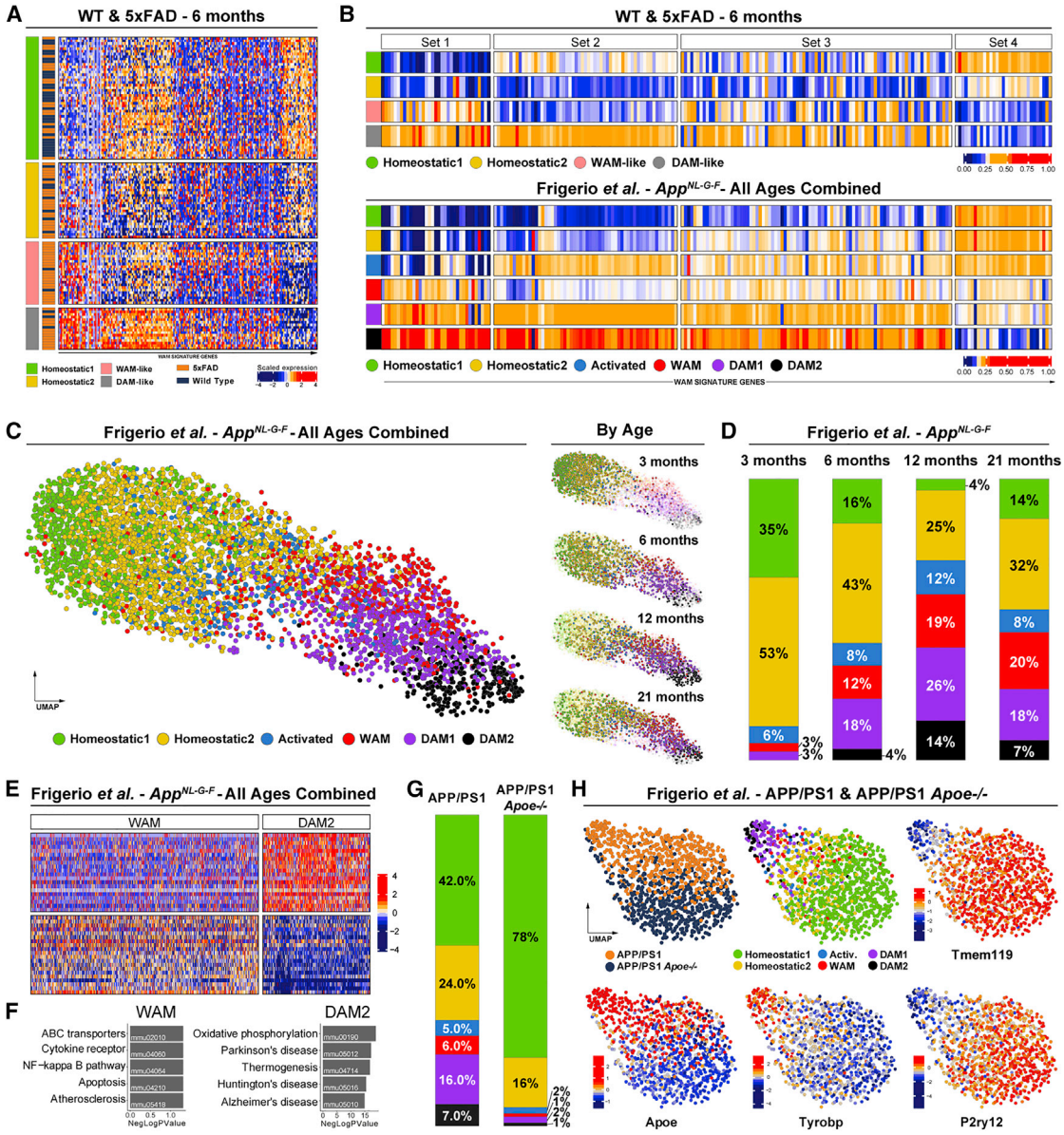

Figure 7. Microglia with a WAM-like signature co-exist with DAMs in AD models

(A) Heatmap of microglia from 5×FAD and wild-type mice, 6 months old. Each row represents a single cell and each column a gene. The bars on the left correspond to the color annotation for population and genotype.

(B) Heatmaps of the average expression of WAM signature gene sets (set 1–4) for each population, along with the six populations of the Sala Frigerio et al., 2019 dataset. Values are normalized per gene.

(C) UMAPs showing the populations identified by the Sala Frigerio et al., 2019 $App^{NL\text{-}G\text{-}F}$ data. Each age group is emphasized separately in the right column.

(D) Cell population ratios by age groups; 3-, 6-, 12-, and 21-month-old $App^{NL\text{-}G\text{-}F}$ mouse data from Sala Frigerio et al., 2019 (Table S1).

(E) WAM and DAM2 populations analyzed separately. Shown is a heatmap with the top 20 DEGs for DAM2 and WAMs. Each row represents a gene and each column a single cell; 947 cells in total, of which 644 are WAMs and 303 DAM2.

(F) KEGG pathway enrichment for WAM and DAM2 upregulated DEGs.

(G) Bar plot showing the relative distribution of each microglia population in APP/PS1 and APP/PS1 $Apoe^{-/-}$.

(H) UMAP of microglia from APP/PS1 and APP/PS1 $Apoe^{-/-}$ combined, using the WAM signature genes.

mice, we found that white matter microglia nodules were completely absent, showing that their formation depends on TREM2 as in normal aging (Figure S7G). These data show that microglia in the white matter of mouse models of AD show a response that is associated with white matter aging, suggesting that myelin degeneration and debris clearance start much earlier in the presence of β-amyloid (Aβ) pathology. To distinguish DAM clustering around amyloid plaques from microglia nodules in

white matter, we determined differentially expressed genes in WAM and DAM2 (Figure 7E). Interestingly, the KEGG pathway enrichment analysis showed that DAM2 upregulated genes involved in multiple disease pathways, including AD, Parkinson's disease, and Huntington's diseases, whereas WAM upregulated genes linked to atherosclerosis, cytokine signaling, and apoptosis (Figure 7F). Next we searched for genes with different expression levels in WAMs compared with DAMs (Figure S7H). *ApoE* and *Tyrobp/Dap12*, which are required for signaling functions in AD (Wang et al., 2015; Krasemann et al., 2017), were found to be upregulated in DAMs. In addition, the inflammatory cytokine macrophage migration inhibitory factor (*Mif*) was expressed at higher levels in DAMs. *Srgap2*, *Cd33*, and *Abca1* are genes that were elevated in WAMs, whereas *Serinc3*, *Lyz2*, and *Clec7a* are examples of genes that were expressed at similar levels in WAMs and DAMs (Figure S7H). Next, we wanted to find out whether we could spatially separate the different microglia states in brain sections of models of AD. We used antibodies against MIF, a gene found to be expressed at higher levels in DAMs compared with WAMs, and found that virtually all microglia associated with amyloid plaques stained positive for MIF, but this was not the case for microglia forming nodules in white matter (Figure S7I). In contrast, antibodies against CLEC7A immunolabeled both populations of microglia (Figure S7J). Next we compared the numbers of CLEC7A and MIF-positive cells in white matter during aging of wild-type mice. We found hardly any MIF-positive cells until 18 months of age; only at 24 months of age were ~4% of IBA^+ cells immunolabeled for MIF. This was in contrast to CLEC7A, which was expressed in cells in white matter earlier and to a much higher extent (20.75% ± 9.67% $CLEC7A^+IBA1^+$ cells/area at 24 months) (Figures S7K and S7L).

Next we determined whether WAM and DAM formation depends on similar signal pathways in the aged brain compared with AD. Because previous work has shown that the APOE-TREM2 pathway triggers DAM conversion in AD models (Krasemann et al., 2017), and because *ApoE* and *Tyrobp/Dap12* were found to be upregulated in DAMs, we tested the requirement of APOE in aging and AD. In the APP/PS1 AD model from Sala Frigerio et al. (2019), we identified an ~8-fold reduction of DAM populations in the $Apoe^{-/-}$ genotype, whereas microglia with the WAM signature were reduced by ~4-fold (Figures 7G and 7H).

To determine whether WAMs are also generated in an APOE-dependent pathway in aged mice, we used droplet-based scRNA-seq on white matter of 18-month-old wild-type and $Apoe^{-/-}$ mice (13,954 high-quality cells from 8 mice used in four independent Drop-seq runs; Figure 8A; Figures S8A–S8C). Tissues were prepared as described above for the Drop-seq dataset, and cells were partitioned into major cell types (Figure 8A). We focused our analysis on microglia using white matter signature genes. These analyses identified a continuous range of microglia that reproduced the four microglial states in the previous scRNA-seq datasets (Figure 8B). Furthermore, wild-type and $Apoe^{-/-}$ mouse white matter had similar ratios of WAMs and activated microglia (Figure 8C). This result suggests that WAM formation is not APOE dependent in aging. To validate the scRNA-seq results, we co-stained $IBA1^+$ microglia with antibodies against CLEC7A, AXL, and LGALS3 in 21-month-old wild-type and $Apoe^{-/-}$ mice. Quantification revealed that similar numbers of $IBA1^+$ cells were positive for CLEC7A, AXL, and LGALS3 (Figure 8D). Notably, nodules containing $IBA1^+$ cells with MBP^+ intracellular particles were observed to the same extent in 21-month-old wild-type and $Apoe^{-/-}$ mice (Figure 8E). Thus, WAMs appear to be generated in an APOE-independent pathway in aged mice, whereas, in models of AD, generation of microglia with the DAM and WAM gene signature require APOE function.

DISCUSSION

In this study, we identified WAMs, which are age dependent, require TREM2 for their formation, and are defined by activation of genes implicated in phagocytic activity and lipid metabolism. WAMs localize in nodules that are engaged in clearing myelin debris in white matter. They display partial activation of the DAM program and form in the absence of APOE in normal aging. WAM identification was possible by performing scRNA-seq on microglia purified from white and gray matter separately and by integrating this spatial information into gene clustering. Using this WAM signature of differentially expressed genes in white and gray matter microglia, we also identified WAMs in previous scRNA-seq datasets (Hammond et al., 2019; Sala Frigerio et al., 2019), providing evidence of the robustness and reproducibility of our findings.

Why does white matter aging specifically shape microglial identity? Although aging is known to result in gray and white matter damage, it is possible that the extent of myelin sheath degeneration and/or the nature of the lipid-rich membrane are responsible for TREM2-dependent microglial responses in white matter. Indeed, when we analyzed microglia in a mouse model for Pelizaeus-Merzbacher disease, in which myelin is gradually broken down because of a mutation in an oligodendrocyte-specific gene, *Plp1*, we observed that microglia nodules containing myelin debris were already formed after a few months in white but not gray matter. Gray matter predominantly consists of neuronal cell bodies and dendrites but is also composed of myelinated axons. It is possible that the extent of myelin degeneration is not sufficient to trigger WAM responses in gray matter. However, our data do not exclude that microglia with the WAM signature can occur outside of white matter; for example, in diseases such as AD, where amyloid plaques trigger cell death in the gray matter. WAM and DAM states are likely to be continuous cell identities that can blend with each other in a continuum. In aging, microglia activation appears to be dominated by the WAM state, whereas it is shifted toward DAMs in AD. Proliferative region-associated microglia (PAM) subsets that share characteristics with DAMs have been identified previously in postnatal white matter at a time point that correlates with oligodendrocyte precursor cell apoptosis (Li et al., 2019). However, in contrast to the cells we identified in this study, PAMs do not require TREM2 for their formation (Li et al., 2019).

TREM2 is a V-type immunoglobulin (Ig) domain-containing receptor that binds to a variety of different ligands, such as various apolipoprotein and anionic lipid species (Ulrich et al., 2017). TREM2 can also function as a receptor for myelin debris uptake (Cantoni et al., 2015; Poliani et al., 2015; Wang et al., 2015), and

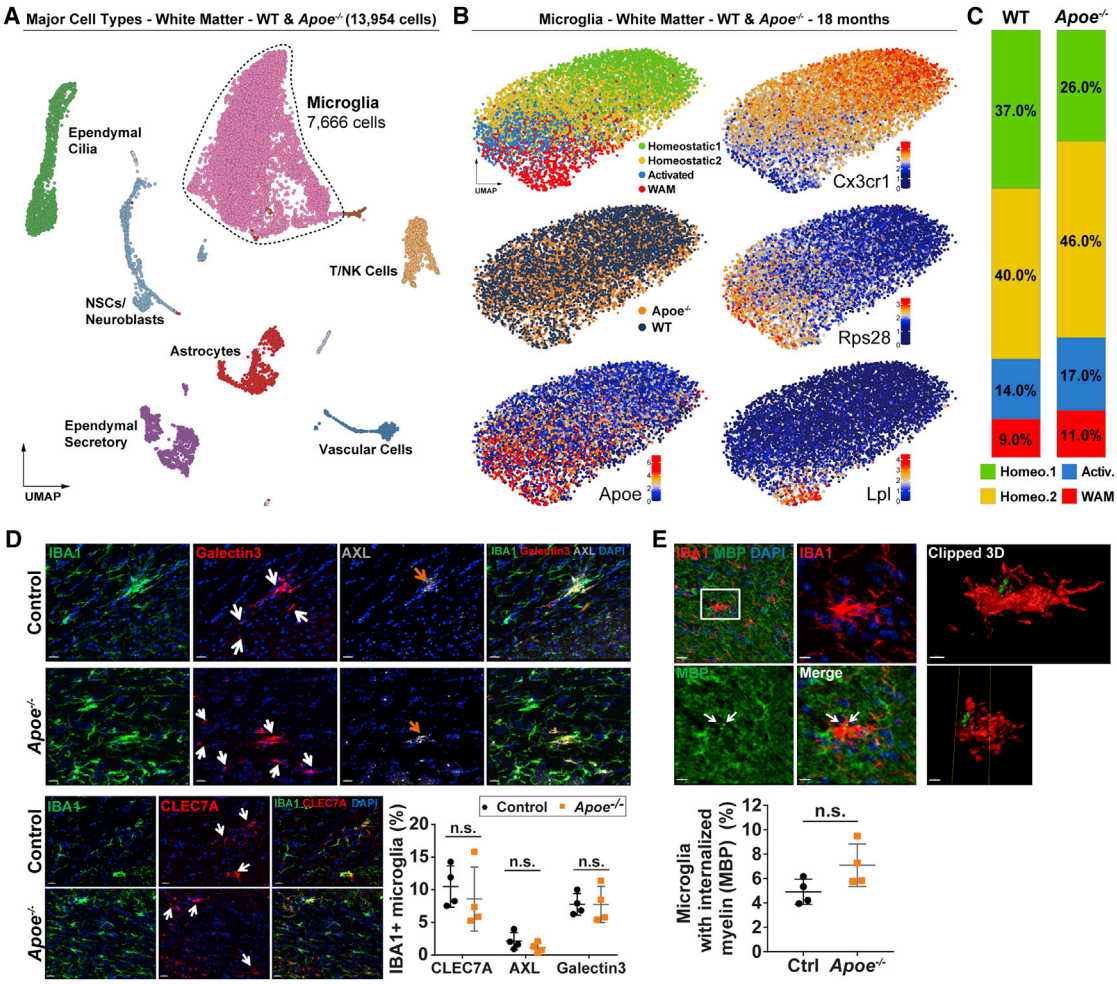

Figure 8. The WAM response is induced in an APOE-independent pathway in aged mice

(A) UMAP of 13,954 single-cell transcriptomes, colored by major cell-type clusters. 18 months old, WM only, WT, and *Apoe*$^{-/-}$.

(B) UMAP of microglia (7,666 cells), depicting the identified populations, genotype annotation, and expression of representative marker genes.

(C) Bar plot showing the relative distribution of each microglia population in WT WM and *Apoe*$^{-/-}$ WM.

(D) Confocal images of CLEC7A, AXL, and Galectin-3 co-localized with IBA1^{+} microglia (green) in the *corpus callosum* in 21-month-old *Apoe*$^{-/-}$ and control mice. Scale bar, 20 μm. Also shown is quantification of the percentage of IBA1^{+} microglia expressing CLEC7A, AXL, and Galectin-3 in 21-month-old *Apoe*$^{-/-}$ and control mice in the WM (*corpus callosum*; n = 4 mice per group, mean ± SD; AXL, p = 0.2348; CLEC7A, p = 0.5373; Galectin-3, p = 0.9962; Student's two-tailed t test).

(E) Confocal images of microglia nodules (red) containing internalized MBP-labeled myelin particles (green) in the *corpus callosum* of a 21-month-old *Apoe*$^{-/-}$ mouse (arrows). The clipped 3D reconstruction shows myelin within microglia. Scale bars, 20 μm (overview), 8 μm (magnification), and 5 μm (clipped 3D). Also shown is quantification of microglia with internalized myelin particles in the *corpus callosum* of 21-month-old *Apoe*$^{-/-}$ and age-matched control mice (*corpus callosum*, n = 4 mice per group, mean ± SD, p = 0.0753, Student's two-tailed t test).

our results concur with these studies but show that TREM2 is dispensable for myelin phagocytosis. We find that myelin debris uptake occurs by a wide range of phosphatidylserine receptors that are most likely able to compensate for the loss of TREM2 receptor activity. Thus, our data provide evidence of an essential function of TREM2 not in phagocytic uptake but in mediating the genetic response required to degrade and metabolize lipid-rich myelin debris when internalization has occurred. For cargos that do not depend on phosphatidylserine interactions, such as beads or bacteria, the function of TREM2 in phagocytosis appears to be more critical (Linnartz-Gerlach et al., 2019).

Complete loss of TREM2 function causes polycystic lipomembranous osteodysplasia with sclerosing leukoencephalopathy (PLOSL or Nasu-Hakola disease), a disease characterized by progressive presenile dementia and bone cysts associated with accumulation of lipomembranous structures in adipose tissue, bone marrow, and the brain (Bianchin et al., 2010). An overarching pathogenic mechanism could be an inability to initiate metabolic pathways required for degradation of lipid-rich membrane structures in tissue-resident macrophages. Loss of TREM2 in mice results in a much more subtle myelin phenotype with only a modest increase in degenerated myelin

profiles in aged mice. It is possible that the short lifespan of mice is not sufficient to induce leukodystrophy as seen in humans. Compensatory functions of astrocytes taking over myelin debris clearance when microglia become dysfunctional is another possible explanation. Rare variants in the *Trem2* gene have also been shown to increase an individual's risk of developing AD, which is associated with misfolded and aggregated proteins (Guerreiro et al., 2013; Jonsson et al., 2013). Several studies have shown that TREM2 is required to induce the DAM program in models of AD (Keren-Shaul et al., 2017; Krasemann et al., 2017; Mathys et al., 2017). DAMs increase with progression of amyloid deposition and accumulate close to amyloid plaques, where they are involved in Aβ phagocytosis and plaque compaction (Condello et al., 2015; Wang et al., 2016; Keren-Shaul et al., 2017). The different functional requirements of microglia in aging and in neurodegenerative diseases raise the question of how these microglial populations differ. In aging, we find that the distinct genetic modules of reactive microglia are segregated in subpopulations, with activated microglia displaying upregulation of translation-associated genes and WAMs exhibiting activation of lysosomal, phagocytic, and lipid metabolism pathways. Although WAMs are the predominant microglial subpopulation induced by aging, our bioinformatics analyses reveal that microglia with WAM and DAM signatures coexist in models of AD. In the context of these disease models, microglia with the WAM signature appear to be generated earlier than DAMs. Interestingly, the proportion of DAMs showed a decrease between 12 and 21 months, possibly because microglial cell death in the DAM populations and repopulation with homeostatic microglia or DAMs returning to the homeostatic state. Previously, we developed methods to distinguish discrete versus continuous heterogeneity in scRNA-seq data (Stanley et al., 2020), and WAM and DAM identities are good examples of continuous cell identities without clear separation. Our data show that microglia in the white matter of mouse models of AD form nodules containing MBP^{+} intracellular particles relatively early in disease, suggesting that myelin degeneration and debris clearance start prematurely in AD. Strikingly, in the Dominantly Inherited Alzheimer's Network (DIAN), white matter alterations were detected by MRI in individuals with autosomal dominant, fully penetrant mutations for AD up to 20 years before the expected onset of symptoms (Lee et al., 2016). The nature of these alterations is not fully resolved but possibly reflects demyelination and axonal damage (Brun and Englund, 1986; Prins and Scheltens, 2015; Nasrabady et al., 2018).

One interesting distinguishing feature of DAM and WAM responses appears to be their differential dependence on APOE. Previous work has shown that the APOE pathway triggers DAM conversion in models of neurodegeneration (Krasemann et al., 2017). Notably, our analyses reveal that, in the absence of APOE, fewer microglia with the WAM gene signature are generated in AD mouse models, whereas microglia with features of WAM are detected in similar numbers in aged white matter of $Apoe^{-/-}$ and wild-type mice, suggesting that the activity of APOE depends on the brain environment. How APOE triggers WAM/DAM conversion in AD models but not in aging is an open question. APOE, which is produced in excess in AD, could act directly on microglia, possibly by binding to TREM2 and activating downstream signaling (Atagi et al., 2015; Bailey et al., 2015; Yeh et al., 2016). Because APOE is critical for Aβ deposition and its subsequent fibrillization into amyloid deposits, amyloid-dependent indirect effects on microglia are another possible explanation for APOE-dependent microglial activation in AD (for a review, see Chen et al., 2021).

It is important to understand the relationship between activated microglia, WAMs, and DAMs. One possibility is that they are generated from homeostatic microglia, but it is also conceivable that they represent progressive activation states. Although such transformations are, in general, regarded as a protective response (Deczkowska et al., 2018), precocious DAM conversion may also cause harm by exhausting DAM function or inducing pro-inflammatory damage. Recently, lipid droplet-accumulating microglia have been identified in the aging brain (Marschallinger et al., 2020). These cells were defective in phagocytosis and produced high levels of reactive oxygen species and pro-inflammatory cytokines, representing a dysfunctional or dystrophic microglial state.

In summary, we identify WAMs as a novel microglial state associated with white matter aging. We propose that WAMs represent a protective metabolic response required to clear the increasing amounts of myelin debris that accumulate during aging. Because the WAM signature is also associated with phagosome as well as antigen processing and presentation, harmful functions, such as immune reactivity, cannot be excluded. In addition, we speculate that attrition of WAM function could contribute to development of neurodegenerative disease by accumulation of toxic protein or lipid species in the brain. If this is the case, then enhancing formation of WAMs could be used therapeutically; for example, to help to combat the age-associated decline of white matter function and possibly also dementia resulting from white matter involvement. Transcriptional signatures differ between mouse and human microglia (Masuda et al., 2019; Zhou et al., 2020), but interesting differences between human gray and white matter microglia have been detected (Sankowski et al., 2019), raising the possibility that WAMs also exist in humans.

STAR★METHODS

Detailed methods are provided in the online version of this paper and include the following:

- KEY RESOURCES TABLE
- RESOURCE AVAILABILITY
  - Lead contact
  - Materials availability
  - Data and code availability
- EXPERIMENTAL MODEL AND SUBJECT DETAILS
  - Mice
- METHOD DETAILS
  - Mice perfusion, cell isolation for Smart-seq2
  - Library preparation for Smart-seq2
  - Processing and analyses of Smart-seq2 data
  - Mice perfusion, cell isolation for Drop-seq
  - Library preparation for Drop-seq
  - Processing and analyses of Drop-seq data

- Processing and analyses of external datasets
- Immunohistochemistry
- RNAscope *in Situ* Hybridization
- Bulk RNA Sequencing
- Transmission Electron Microscopy
- Correlative Light and Scanning Electron Microscopy
- Myelin isolation and purification
- Myelin uptake assay
- Microglia-myelin binding assay
- Myelin clearance assay
- Lysolecithin-induced demyelination
- Gene expression analysis
- Western Blotting
- Image processing and analysis

● QUANTIFICATION AND STATISTICAL ANALYSIS

SUPPLEMENTAL INFORMATION

Supplemental Information can be found online at https://doi.org/10.1016/j.neuron.2021.01.027.

ACKNOWLEDGMENTS

The work was supported by grants from the German Research Foundation (TRR128-2, TRR 274 - ID 408885537, SyNergy Excellence Cluster EXC2145, Projekt ID390857198, and RO 4076/3-2), the ERC (consolidator grant to M.S.), the Dr. Miriam and Sheldon G. Adelson Medical Research Foundation, the Chan Zuckerberg Initiative (CZI), and a NARSAD Young Investigator Award (to O.G.). For the single-cell and sorting studies, we are grateful for support from the Flow Cytometric Cell Sorter Sony SH800 Core Unit run by the Department of Vascular Biology at the Institute for Stroke and Dementia Research (ISD) and SyNergy EXC2145. We thank Christian Haass for providing Trem2 knockout and App^{NL-G-F} transgenic mice and Sabina Tahirovic for providing mouse sections. We thank Jürgen Bernhagen for providing the rabbit anti-MIF antibody. Preclinical PET imaging was supported by the Deutsche Forschungsgemeinschaft (DFG) by dedicated PET imaging grants (BR4580/1-1 and RO5194/1-1). ActiGliA is funded by the DFG under Germany's Excellence Strategy within the framework of the Munich Cluster for Systems Neurology (EXC 2145 SyNergy – ID 390857198, Project D1) and by a Manfred Strohscher Fellowship provided by Hirnliga e.V.

AUTHOR CONTRIBUTIONS

M. Simons and O.G. conceived and supervised the project. S.S., S.B.-G., T.K., M. Schifferer, L.L., N.K., O.G., H.J., F.U., L.C.-C., M.J.R., R.P., G.G., M.B., D.F., and X.X. performed experiments and analyzed the data. S.B.-G. and T.K. developed software and curated and visualized the scRNA-seq data. O.G., M.R., and M. Simons analyzed the data or supervised data acquisition. M. Simons and O.G. wrote the manuscript with input from all authors.

DECLARATION OF INTERESTS

The authors declare no competing interests.

Received: August 31, 2020
Revised: December 8, 2020
Accepted: January 26, 2021
Published: February 18, 2021

REFERENCES

Atagi, Y., Liu, C.C., Painter, M.M., Chen, X.F., Verbeeck, C., Zheng, H., Li, X., Rademakers, R., Kang, S.S., Xu, H., et al. (2015). Apolipoprotein E Is a Ligand for Triggering Receptor Expressed on Myeloid Cells 2 (TREM2). J. Biol. Chem. *290*, 26043–26050.

Ayata, P., Badimon, A., Strasburger, H.J., Duff, M.K., Montgomery, S.E., Loh, Y.E., Ebert, A., Pimenova, A.A., Ramirez, B.R., Chan, A.T., et al. (2018). Epigenetic regulation of brain region-specific microglia clearance activity. Nat. Neurosci. *21*, 1049–1060.

Bailey, C.C., DeVaux, L.B., and Farzan, M. (2015). The Triggering Receptor Expressed on Myeloid Cells 2 Binds Apolipoprotein E. J. Biol. Chem. *290*, 26033–26042.

Bianchin, M.M., Martin, K.C., de Souza, A.C., de Oliveira, M.A., and Rieder, C.R. (2010). Nasu-Hakola disease and primary microglial dysfunction. Nat. Rev. Neurol. *6*, 2 p following 523.

Borchelt, D.R., Ratovitski, T., van Lare, J., Lee, M.K., Gonzales, V., Jenkins, N.A., Copeland, N.G., Price, D.L., and Sisodia, S.S. (1997). Accelerated amyloid deposition in the brains of transgenic mice coexpressing mutant presenilin 1 and amyloid precursor proteins. Neuron *19*, 939–945.

Brun, A., and Englund, E. (1986). A white matter disorder in dementia of the Alzheimer type: a pathoanatomical study. Ann. Neurol. *19*, 253–262.

Butler, A., Hoffman, P., Smibert, P., Papalexi, E., and Satija, R. (2018). Integrating single-cell transcriptomic data across different conditions, technologies, and species. Nat. Biotechnol. *36*, 411–420.

Cantoni, C., Bollman, B., Licastro, D., Xie, M., Mikesell, R., Schmidt, R., Yuede, C.M., Galimberti, D., Olivecrona, G., Klein, R.S., et al. (2015). TREM2 regulates microglial cell activation in response to demyelination in vivo. Acta Neuropathol. *129*, 429–447.

Cantuti-Castelvetri, L., Fitzner, D., Bosch-Queralt, M., Weil, M.T., Su, M., Sen, P., Ruhwedel, T., Mitkovski, M., Trendelenburg, G., Lütjohann, D., et al. (2018). Defective cholesterol clearance limits remyelination in the aged central nervous system. Science *359*, 684–688.

Cardona, A., Saalfeld, S., Schindelin, J., Arganda-Carreras, I., Preibisch, S., Longair, M., Tomancak, P., Hartenstein, V., and Douglas, R.J. (2012). TrakEM2 software for neural circuit reconstruction. PLoS ONE *7*, e38011.

Chen, W.T., Lu, A., Craessaerts, K., Pavie, B., Sala Frigerio, C., Corthout, N., Qian, X., Laláková, J., Kühnemund, M., Voytyuk, I., et al. (2020). Spatial Transcriptomics and In Situ Sequencing to Study Alzheimer's Disease. Cell *182*, 976–991.e19.

Chen, Y., Strickland, M.R., Soranno, A., and Holtzman, D.M. (2021). Apolipoprotein E: Structural Insights and Links to Alzheimer Disease Pathogenesis. Neuron *109*, 205–221.

Condello, C., Yuan, P., Schain, A., and Grutzendler, J. (2015). Microglia constitute a barrier that prevents neurotoxic protofibrillar Aβ42 hotspots around plaques. Nat. Commun. *6*, 6176.

Deczkowska, A., Keren-Shaul, H., Weiner, A., Colonna, M., Schwartz, M., and Amit, I. (2018). Disease-Associated Microglia: A Universal Immune Sensor of Neurodegeneration. Cell *173*, 1073–1081.

Dobin, A., Davis, C.A., Schlesinger, F., Drenkow, J., Zaleski, C., Jha, S., Batut, P., Chaisson, M., and Gingeras, T.R. (2013). STAR: ultrafast universal RNA-seq aligner. Bioinformatics *29*, 15–21.

Fang, T., Lu, X., Berger, D., Gmeiner, C., Cho, J., Schalek, R., Ploegh, H., and Lichtman, J. (2018). Nanobody immunostaining for correlated light and electron microscopy with preservation of ultrastructure. Nat. Methods *15*, 1029–1032.

Finak, G., McDavid, A., Yajima, M., Deng, J., Gersuk, V., Shalek, A.K., Slichter, C.K., Miller, H.W., McElrath, M.J., Prlic, M., et al. (2015). MAST: a flexible statistical framework for assessing transcriptional changes and characterizing heterogeneity in single-cell RNA sequencing data. Genome Biol. *16*, 278.

Friedman, B.A., Srinivasan, K., Ayalon, G., Meilandt, W.J., Lin, H., Huntley, M.A., Cao, Y., Lee, S.H., Haddick, P.C.G., Ngu, H., et al. (2018). Diverse Brain Myeloid Expression Profiles Reveal Distinct Microglial Activation States and Aspects of Alzheimer's Disease Not Evident in Mouse Models. Cell Rep. *22*, 832–847.

Füger, P., Hefendehl, J.K., Veeraraghavalu, K., Wendeln, A.C., Schlosser, C., Obermüller, U., Wegenast-Braun, B.M., Neher, J.J., Martus, P., Kohsaka, S., et al. (2017). Microglia turnover with aging and in an Alzheimer's model via long-term in vivo single-cell imaging. Nat. Neurosci. *20*, 1371–1376.

Gokce, O., Stanley, G.M., Treutlein, B., Neff, N.F., Camp, J.G., Malenka, R.C., Rothwell, P.E., Fuccillo, M.V., Südhof, T.C., and Quake, S.R. (2016). Cellular Taxonomy of the Mouse Striatum as Revealed by Single-Cell RNA-Seq. Cell Rep. *16*, 1126–1137.

Grabert, K., Michoel, T., Karavolos, M.H., Clohisey, S., Baillie, J.K., Stevens, M.P., Freeman, T.C., Summers, K.M., and McColl, B.W. (2016). Microglial brain region-dependent diversity and selective regional sensitivities to aging. Nat. Neurosci. *19*, 504–516.

Guerreiro, R., Wojtas, A., Bras, J., Carrasquillo, M., Rogaeva, E., Majounie, E., Cruchaga, C., Sassi, C., Kauwe, J.S., Younkin, S., et al.; Alzheimer Genetic Analysis Group (2013). TREM2 variants in Alzheimer's disease. N. Engl. J. Med. *368*, 117–127.

Haimon, Z., Volaski, A., Orthgiess, J., Boura-Halfon, S., Varol, D., Shemer, A., Yona, S., Zuckerman, B., David, E., Chappell-Maor, L., et al. (2018). Re-evaluating microglia expression profiles using RiboTag and cell isolation strategies. Nat. Immunol. *19*, 636–644.

Hammond, T.R., Dufort, C., Dissing-Olesen, L., Giera, S., Young, A., Wysoker, A., Walker, A.J., Gergits, F., Segel, M., Nemesh, J., et al. (2019). Single-Cell RNA Sequencing of Microglia throughout the Mouse Lifespan and in the Injured Brain Reveals Complex Cell-State Changes. Immunity *50*, 253–271.e6.

Jonsson, T., Stefansson, H., Steinberg, S., Jonsdottir, I., Jonsson, P.V., Snaedal, J., Bjornsson, S., Huttenlocher, J., Levey, A.I., Lah, J.J., et al. (2013). Variant of TREM2 associated with the risk of Alzheimer's disease. N. Engl. J. Med. *368*, 107–116.

Keren-Shaul, H., Spinrad, A., Weiner, A., Matcovitch-Natan, O., Dvir-Szternfeld, R., Ulland, T.K., David, E., Baruch, K., Lara-Astaiso, D., Toth, B., et al. (2017). A Unique Microglia Type Associated with Restricting Development of Alzheimer's Disease. Cell *169*, 1276–1290.e17.

Kleinberger, G., Brendel, M., Mracsko, E., Wefers, B., Groeneweg, L., Xiang, X., Focke, C., Deußing, M., Suárez-Calvet, M., Mazaheri, F., et al. (2017). The FTD-like syndrome causing TREM2 T66M mutation impairs microglia function, brain perfusion, and glucose metabolism. EMBO J. *36*, 1837–1853.

Krasemann, S., Madore, C., Cialic, R., Baufeld, C., Calcagno, N., El Fatimy, R., Beckers, L., O'Loughlin, E., Xu, Y., Fanek, Z., et al. (2017). The TREM2-APOE Pathway Drives the Transcriptional Phenotype of Dysfunctional Microglia in Neurodegenerative Diseases. Immunity *47*, 566–581.e9.

Kubota, Y., Sohn, J., Hatada, S., Schurr, M., Straehle, J., Gour, A., Neujahr, R., Miki, T., Mikula, S., and Kawaguchi, Y. (2018). A carbon nanotube tape for serial-section electron microscopy of brain ultrastructure. Nat. Commun. *9*, 437.

Lee, S., Viqar, F., Zimmerman, M.E., Narkhede, A., Tosto, G., Benzinger, T.L., Marcus, D.S., Fagan, A.M., Goate, A., Fox, N.C., et al.; Dominantly Inherited Alzheimer Network (2016). White matter hyperintensities are a core feature of Alzheimer's disease: Evidence from the dominantly inherited Alzheimer network. Ann. Neurol. *79*, 929–939.

Leng, L., Metz, C.N., Fang, Y., Xu, J., Donnelly, S., Baugh, J., Delohery, T., Chen, Y., Mitchell, R.A., and Bucala, R. (2003). MIF signal transduction initiated by binding to CD74. J. Exp. Med. *197*, 1467–1476.

Li, Q., Cheng, Z., Zhou, L., Darmanis, S., Neff, N.F., Okamoto, J., Gulati, G., Bennett, M.L., Sun, L.O., Clarke, L.E., et al. (2019). Developmental Heterogeneity of Microglia and Brain Myeloid Cells Revealed by Deep Single-Cell RNA Sequencing. Neuron *101*, 207–223.e10.

Linnartz-Gerlach, B., Bodea, L.G., Klaus, C., Ginolhac, A., Halder, R., Sinkkonen, L., Walter, J., Colonna, M., and Neumann, H. (2019). TREM2 triggers microglial density and age-related neuronal loss. Glia *67*, 539–550.

Lloyd, A.F., Davies, C.L., Holloway, R.K., Labrak, Y., Ireland, G., Carradori, D., Dillenburg, A., Borger, E., Soong, D., Richardson, J.C., et al. (2019). Central nervous system regeneration is driven by microglia necroptosis and repopulation. Nat. Neurosci. *22*, 1046–1052.

Love, M.I., Huber, W., and Anders, S. (2014). Moderated estimation of fold change and dispersion for RNA-seq data with DESeq2. Genome Biol. *15*, 550.

Luckner, M., and Wanner, G. (2018). From Light Microscopy to Analytical Scanning Electron Microscopy (SEM) and Focused Ion Beam (FIB)/SEM in Biology: Fixed Coordinates, Flat Embedding, Absolute References. Microsc. Microanal. *24*, 526–544.

Marschallinger, J., Iram, T., Zardeneta, M., Lee, S.E., Lehallier, B., Haney, M.S., Pluvinage, J.V., Mathur, V., Hahn, O., Morgens, D.W., et al. (2020). Lipid-droplet-accumulating microglia represent a dysfunctional and proinflammatory state in the aging brain. Nat. Neurosci. *23*, 194–208.

Masuda, A., Kobayashi, Y., Kogo, N., Saito, T., Saido, T.C., and Itohara, S. (2016). Cognitive deficits in single App knock-in mouse models. Neurobiol. Learn. Mem. *135*, 73–82.

Masuda, T., Sankowski, R., Staszewski, O., Böttcher, C., Amann, L., Sagar, Scheiwe, C., Nessler, S., Kunz, P., van Loo, G., et al. (2019). Spatial and temporal heterogeneity of mouse and human microglia at single-cell resolution. Nature *566*, 388–392.

Mathys, H., Adaikkan, C., Gao, F., Young, J.Z., Manet, E., Hemberg, M., De Jager, P.L., Ransohoff, R.M., Regev, A., and Tsai, L.H. (2017). Temporal Tracking of Microglia Activation in Neurodegeneration at Single-Cell Resolution. Cell Rep. *21*, 366–380.

Mathys, H., Davila-Velderrain, J., Peng, Z., Gao, F., Mohammadi, S., Young, J.Z., Menon, M., He, L., Abdurrob, F., Jiang, X., et al. (2019). Single-cell transcriptomic analysis of Alzheimer's disease. Nature *570*, 332–337.

McKenzie, I.A., Ohayon, D., Li, H., de Faria, J.P., Emery, B., Tohyama, K., and Richardson, W.D. (2014). Motor skill learning requires active central myelination. Science *346*, 318–322.

Mount, C.W., and Monje, M. (2017). Wrapped to Adapt: Experience-Dependent Myelination. Neuron *95*, 743–756.

Nasrabady, S.E., Rizvi, B., Goldman, J.E., and Brickman, A.M. (2018). White matter changes in Alzheimer's disease: a focus on myelin and oligodendrocytes. Acta Neuropathol. Commun. *6*, 22.

Norton, W.T., and Poduslo, S.E. (1973). Myelination in rat brain: method of myelin isolation. J. Neurochem. *21*, 749–757.

Oakley, H., Cole, S.L., Logan, S., Maus, E., Shao, P., Craft, J., Guillozet-Bongaarts, A., Ohno, M., Disterhoft, J., Van Eldik, L., et al. (2006). Intraneuronal beta-amyloid aggregates, neurodegeneration, and neuron loss in transgenic mice with five familial Alzheimer's disease mutations: potential factors in amyloid plaque formation. J. Neurosci. *26*, 10129–10140.

Pan, S., Mayoral, S.R., Choi, H.S., Chan, J.R., and Kheirbek, M.A. (2020). Preservation of a remote fear memory requires new myelin formation. Nat. Neurosci. *23*, 487–499.

Perry, V.H., and Holmes, C. (2014). Microglial priming in neurodegenerative disease. Nat. Rev. Neurol. *10*, 217–224.

Peters, A. (2002). The effects of normal aging on myelin and nerve fibers: a review. J. Neurocytol. *31*, 581–593.

Picelli, S., Faridani, O.R., Björklund, A.K., Winberg, G., Sagasser, S., and Sandberg, R. (2014). Full-length RNA-seq from single cells using Smart-seq2. Nat. Protoc. *9*, 171–181.

Plemel, J.R., Stratton, J.A., Michaels, N.J., Rawji, K.S., Zhang, E., Sinha, S., Baaklini, C.S., Dong, Y., Ho, M., Thorburn, K., et al. (2020). Microglia response following acute demyelination is heterogeneous and limits infiltrating macrophage dispersion. Sci. Adv. *6*, eaay6324.

Poliani, P.L., Wang, Y., Fontana, E., Robinette, M.L., Yamanishi, Y., Gilfillan, S., and Colonna, M. (2015). TREM2 sustains microglial expansion during aging and response to demyelination. J. Clin. Invest. *125*, 2161–2170.

Prins, N.D., and Scheltens, P. (2015). White matter hyperintensities, cognitive impairment and dementia: an update. Nat. Rev. Neurol. *11*, 157–165.

Prinz, M., Jung, S., and Priller, J. (2019). Microglia Biology: One Century of Evolving Concepts. Cell *179*, 292–311.

Readhead, C., Schneider, A., Griffiths, I., and Nave, K.A. (1994). Premature arrest of myelin formation in transgenic mice with increased proteolipid protein gene dosage. Neuron *12*, 583–595.

Rock, R.B., Gekker, G., Hu, S., Sheng, W.S., Cheeran, M., Lokensgard, J.R., and Peterson, P.K. (2004). Role of microglia in central nervous system infections. Clin. Microbiol. Rev. *17*, 942–964.

Safaiyan, S., Kannaiyan, N., Snaidero, N., Brioschi, S., Biber, K., Yona, S., Edinger, A.L., Jung, S., Rossner, M.J., and Simons, M. (2016). Age-related myelin degradation burdens the clearance function of microglia during aging. Nat. Neurosci. *19*, 995–998.

Sala Frigerio, C., Wolfs, L., Fattorelli, N., Thrupp, N., Voytyuk, I., Schmidt, I., Mancuso, R., Chen, W.T., Woodbury, M.E., Srivastava, G., et al. (2019). The Major Risk Factors for Alzheimer's Disease: Age, Sex, and Genes Modulate the Microglia Response to Aβ Plaques. Cell Rep. *27*, 1293–1306.e6.

Salter, M.W., and Stevens, B. (2017). Microglia emerge as central players in brain disease. Nat. Med. *23*, 1018–1027.

Sankowski, R., Böttcher, C., Masuda, T., Geirsdottir, L., Sagar, Sindram, E., Seredenina, T., Muhs, A., Scheiwe, C., Shah, M.J., et al. (2019). Mapping microglia states in the human brain through the integration of high-dimensional techniques. Nat. Neurosci. *22*, 2098–2110.

Sasaguri, H., Nilsson, P., Hashimoto, S., Nagata, K., Saito, T., De Strooper, B., Hardy, J., Vassar, R., Winblad, B., and Saido, T.C. (2017). APP mouse models for Alzheimer's disease preclinical studies. EMBO J. *36*, 2473–2487.

Sowell, E.R., Peterson, B.S., Thompson, P.M., Welcome, S.E., Henkenius, A.L., and Toga, A.W. (2003). Mapping cortical change across the human life span. Nat. Neurosci. *6*, 309–315.

Stadelmann, C., Timmler, S., Barrantes-Freer, A., and Simons, M. (2019). Myelin in the Central Nervous System: Structure, Function, and Pathology. Physiol. Rev. *99*, 1381–1431.

Stanley, G., Gokce, O., Malenka, R.C., Südhof, T.C., and Quake, S.R. (2020). Continuous and Discrete Neuron Types of the Adult Murine Striatum. Neuron *105*, 688–699.e8.

Steadman, P.E., Xia, F., Ahmed, M., Mocle, A.J., Penning, A.R.A., Geraghty, A.C., Steenland, H.W., Monje, M., Josselyn, S.A., and Frankland, P.W. (2020). Disruption of Oligodendrogenesis Impairs Memory Consolidation in Adult Mice. Neuron *105*, 150–164.e6.

Street, K., Risso, D., Fletcher, R.B., Das, D., Ngai, J., Yosef, N., Purdom, E., and Dudoit, S. (2018). Slingshot: cell lineage and pseudotime inference for single-cell transcriptomics. BMC Genomics *19*, 477.

Streit, W.J., Sammons, N.W., Kuhns, A.J., and Sparks, D.L. (2004). Dystrophic microglia in the aging human brain. Glia *45*, 208–212.

Szklarczyk, D., Gable, A.L., Lyon, D., Junge, A., Wyder, S., Huerta-Cepas, J., Simonovic, M., Doncheva, N.T., Morris, J.H., Bork, P., et al. (2019). STRING v11: protein-protein association networks with increased coverage, supporting functional discovery in genome-wide experimental datasets. Nucleic Acids Res. *47* (D1), D607–D613.

Tapia, J.C., Kasthuri, N., Hayworth, K.J., Schalek, R., Lichtman, J.W., Smith, S.J., and Buchanan, J. (2012). High-contrast en bloc staining of neuronal tissue for field emission scanning electron microscopy. Nat. Protoc. *7*, 193–206.

Tischer, J., Krueger, M., Mueller, W., Staszewski, O., Prinz, M., Streit, W.J., and Bechmann, I. (2016). Inhomogeneous distribution of Iba-1 characterizes microglial pathology in Alzheimer's disease. Glia *64*, 1562–1572.

Turnbull, I.R., Gilfillan, S., Cella, M., Aoshi, T., Miller, M., Piccio, L., Hernandez, M., and Colonna, M. (2006). Cutting edge: TREM-2 attenuates macrophage activation. J. Immunol. *177*, 3520–3524.

Ulrich, J.D., Ulland, T.K., Colonna, M., and Holtzman, D.M. (2017). Elucidating the Role of TREM2 in Alzheimer's Disease. Neuron *94*, 237–248.

Van Hove, H., Martens, L., Scheyltjens, I., De Vlaminck, K., Pombo Antunes, A.R., De Prijck, S., Vandamme, N., De Schepper, S., Van Isterdael, G., Scott, C.L., et al. (2019). A single-cell atlas of mouse brain macrophages reveals unique transcriptional identities shaped by ontogeny and tissue environment. Nat. Neurosci. *22*, 1021–1035.

Wang, Y., Cella, M., Mallinson, K., Ulrich, J.D., Young, K.L., Robinette, M.L., Gilfillan, S., Krishnan, G.M., Sudhakar, S., Zinselmeyer, B.H., et al. (2015). TREM2 lipid sensing sustains the microglial response in an Alzheimer's disease model. Cell *160*, 1061–1071.

Wang, Y., Ulland, T.K., Ulrich, J.D., Song, W., Tzaferis, J.A., Hole, J.T., Yuan, P., Mahan, T.E., Shi, Y., Gilfillan, S., et al. (2016). TREM2-mediated early microglial response limits diffusion and toxicity of amyloid plaques. J. Exp. Med. *213*, 667–675.

Wang, F., Ren, S.Y., Chen, J.F., Liu, K., Li, R.X., Li, Z.F., Hu, B., Niu, J.Q., Xiao, L., Chan, J.R., and Mei, F. (2020). Myelin degeneration and diminished myelin renewal contribute to age-related deficits in memory. Nat. Neurosci. *23*, 481–486.

Wu, Y.E., Pan, L., Zuo, Y., Li, X., and Hong, W. (2017). Detecting Activated Cell Populations Using Single-Cell RNA-Seq. Neuron *96*, 313–329.e6.

Ximerakis, M., Lipnick, S.L., Innes, B.T., Simmons, S.K., Adiconis, X., Dionne, D., Mayweather, B.A., Nguyen, L., Niziolek, Z., Ozek, C., et al. (2019). Single-cell transcriptomic profiling of the aging mouse brain. Nat. Neurosci. *22*, 1696–1708.

Yeh, F.L., Wang, Y., Tom, I., Gonzalez, L.C., and Sheng, M. (2016). TREM2 Binds to Apolipoproteins, Including APOE and CLU/APOJ, and Thereby Facilitates Uptake of Amyloid-Beta by Microglia. Neuron *91*, 328–340.

Zheng, G.X., Terry, J.M., Belgrader, P., Ryvkin, P., Bent, Z.W., Wilson, R., Ziraldo, S.B., Wheeler, T.D., McDermott, G.P., Zhu, J., et al. (2017). Massively parallel digital transcriptional profiling of single cells. Nat. Commun. *8*, 14049.

Zhou, Y., Zhou, B., Pache, L., Chang, M., Khodabakhshi, A.H., Tanaseichuk, O., Benner, C., and Chanda, S.K. (2019). Metascape provides a biologist-oriented resource for the analysis of systems-level datasets. Nat. Commun. *10*, 1523.

Zhou, Y., Song, W.M., Andhey, P.S., Swain, A., Levy, T., Miller, K.R., Poliani, P.L., Cominelli, M., Grover, S., Gilfillan, S., et al. (2020). Human and mouse single-nucleus transcriptomics reveal TREM2-dependent and TREM2-independent cellular responses in Alzheimer's disease. Nat. Med. *26*, 131–142.

STAR★METHODS

KEY RESOURCES TABLE

REAGENT or RESOURCE	SOURCE	IDENTIFIER
Antibodies		
Rabbit anti-IBA1	Wako	Cat#019-19741; RRID: AB_839504
Guinea anti-pig IBA1	Synaptic Systems	Cat#234004; RRID: AB_2493179
Rat anti-MAC2 (Galectin 3)	Biolegend	Cat#125402; RRID: AB_1134238
Rat anti-MBP (Myelin Basic Protein)	Abcam	Cat#ab7349; RRID: AB_305869
Mouse anti-PLP (Proteolipid Protein)	Bio-Rad	Cat#MCA839G; RRID: AB_2237198
Chicken anti-MBP (Myelin Basic Protein)	Thermofisher Scientific	Cat#PA1-10008; RRID: AB_1077024
Rat anti-CD68	Bio Rad	Cat#MCA1957; RRID: AB_322219
Goat anti-AXL (Tyrosine-protein kinase receptor)	R&D Systems	Cat# AF854; RRID: AB_355663
Rat anti CLEC7A (DECTIN1) (Clec7a)	InvivoGen	Cat#mabg-mdect; RRID: AB_2753143
Rabbit anti-TMEM119 (Transmembrane Protein 1119)	Abcam	Cat#ab209064; RRID: AB_2800343
Rat anti-P2RY12 (Purinergic receptor P2Y, G-protein coupled12)	Biolegend	Cat#848002; RRID: AB_2650634
Rat anti-CD45 (eFluor 450, 30-F11)	Thermofisher Scientific	Cat#48-0451-82; RRID: AB_1518806
Rat anti-CD11b (PE/Cy7, M1/70)	Thermofisher Scientific	Cat#25-0112-82; RRID: AB_469588
Mouse anti-PU.1	Santa Cruz	Cat#sc-390405; RRID: N/A
Mouse anti-beta-Amyloid (NAB228)	Santa Cruz	Cat#sc-32277; RRID: AB_626670
Goat anti-Cathepsin L	R&D Systems	Cat#AF1515; RRID: AB_2087690
Rabbit anti-MIF	Prof. Jürgen Bernhagen (Laboratory of Vascular Biology, ISD, Munich).	Leng et al., 2003
Biological samples		
Mouse brain sections: 21 months old ApoE KO	Dr. Dirk Fitzner (Department of Neurology, University of Göttingen)	N/A
Mouse brain sections: 2 and 6 months old 5xFAD	Dr. Sabine Tahirovich (Laboratory of *ex vivo* models, DZNE, Munich	N/A
Mouse brain sections: 6 months old App NL-G-F Knock-in	Dr. Sabine Tahirovich (Laboratory of *ex vivo* models, DZNE, Munich)	N/A
Mouse brain sections: 18 months old *App NL-G-F; Trem2*$^{-/-}$	Prof. Christian Haass (Laboratory of Neurodegenerative Disease Research, DZNE, Munich)	N/A
Chemicals, peptides, and recombinant proteins		
FluoroMyelin, green fluorescent myelin stain	Invitrogen	Cat#F34651
Annexin-V, Alexa Fluor 555 conjugate	Thermofisher Scientific	Cat#A35108
CD11b (Microglia) microbeads, human and mouse	Miltenyi Biotec	Cat#130-093-634
Actinomycin D	Sigma-Aldrich	No. A1410; CAS: 50-76-0
Fc-blocking reagent (CD16/CD32 Monoclonal Antibody (93)	Thermofisher Scientific	Cat#14-0161-82; RRID: AB_467133
Aminoactinomycin D (7AAD)	Thermofisher Scientific	Cat# A1310
Prolong gold antifade reagent	Invitrogen	Cat#P36934
L-α-Lysophosphatidylcholine from egg yolk (L-α-lysolecithin)	Sigma-Aldrich	Cat#L4129; CAS: 9008-30-4
Bafilomycin	InvivoGen	Cat#tlrl-baf1
Leupeptin Hemisulfate	Selleckchem	Cat#S7380; CAS: 103476-89-7
Recombinant ribonuclease inhibitor	Takara Clontech	Cat#2313B
Triton X-100	Sigma-Aldrich	Cat#93443
SMARTScribe Reverse Transcriptase	Takara Clontech	Cat#639538
Betaine solution 5 M, PCR Reagent	Sigma-Aldrich	Cat#B0300

(*Continued on next page*)

Continued

REAGENT or RESOURCE	SOURCE	IDENTIFIER
UltraPure Dithiothreitol	Thermofisher Scientific	Cat#15508013
Magnesium chloride solution for molecular biology, 1.00 M ± 0.01 M	Sigma-Aldrich	Cat#M1028
Lambda Exonuclease	New England Biolabs	Cat#M0262L
AMPure XP Beads	Beckman-Coulter	Cat#A63881
Myelin Removal Beads II	Miltenyi Biotec	Cat#130-096-731
Critical commercial assays		
PKH67 Green Fluorescent Cell Linker Kit for General Cell Membrane Labeling,	Sigma-Aldrich	Cat#PKH67GL-1KT
RNAscope multiplex fluorescent reagent kit v2 assay	Advanced Cell Diagnostics	Cat#323100-USM
Neural Tissue Dissociation Kit (P)	Miltenyi Biotec	Cat#130-092-628
KAPA HiFi HotStart ReadyMix PCR Kit	Roche	Cat#KK2602 07958935001
Agilent High Sensitivity DNA Kit	Agilent	Cat#5067-4626
Qubit dsDNA HS Assay Kit	Thermofisher Scientific	Cat# Q32854
Chromium Next GEM Single Cell 3′ GEM, Library & Gel Bead Kit v3.1	10x Genomics	Cat#1000121
Deposited data		
Raw and analyzed data	This manuscript	SRA/GEO
Experimental models: cell lines		
Human: HeLa cells	ATCC	HeLa (ATCC CCL2)
Experimental models: organisms/strains		
Mouse: C57BL/6J	Janvier Labs	N/A
Mouse: Trem2$^{-/-}$	Prof. Christian Haass (Laboratory of Neurodegenerative Disease Research, DZNE, Munich),	Turnbull et al., 2006
Mouse: B6.129P2-Apoe^{tm1Unc}/J (ApoE KO)	The Jackson Laboratory	Stock#002052
Mouse: B6SJL-Tg (APPSwFILon, PSEN1*M146L*L286V)6799Vas/Mmjax (5xFAD)	The Jackson Laboratory	Stock#034840-JAX; RRID: MMRRC_034840-JAX
Mouse: APP NL-G-F Knock-in	Takaomi Saido	N/A
Mouse: APP NL-G-F; Trem2$^{-/-}$	Prof. Christian Haass (Laboratory of Neurodegenerative Disease Research, DZNE, Munich)	N/A
Mouse: B6.129P-Cx3cr1tm1Litt/J	The JacksonLaboratory	Stock#005582
Oligonucleotides		
qPCR: hexosaminidase (Forward): GCTGCAGAATCCTTTGCTTACGG	This manuscript	N/A
qPCR: hexosaminidase (Reverse): GGGTCACGTGAACGGGAGG	This manuscript	N/A
qPCR: N-acetylglucosamine-6-sulfatase (Forward): GAAAACCAAGGCCCTCATCG	This manuscript	N/A
qPCR: N-acetylglucosamine-6-sulfatase (Reverse): TGTTGTTAACGACGTGGTGG	This manuscript	N/A
qPCR: Galactosidase Beta 1 (Forward): CACTGCCTAACGGAGAGACC	This manuscript	N/A
qPCR: Galactosidase Beta 1 (Reverse): TCCCGAGATGTATCGGAATGG	This manuscript	N/A
qPCR: Cathepsin L (Forward): TCGGATTTCACCTCAGTGTCC	This manuscript	N/A
qPCR: cathepsin L (Reverse): CTTAAAAACTAGTGGGGCTGGC	This manuscript	N/A
ERCC RNA	Ambion – Fisher Scientific	Cat#4456740

(*Continued on next page*)

Continued

REAGENT or RESOURCE	SOURCE	IDENTIFIER
oligo-dT primer (with tag): AAGCAGTGGTATCAACG CAGAGTACTTTTTTTTTTTTTTTTTTTTTTTTTTTTTTVN	Eurogentec	DNA Wobble 200 nmol
dNTP Mix	Thermofisher Scientific	Cat# R0192
Template-switching oligos (TSO): AAGCAGTGGTAT CAACGCAGAGTACrGrG+G	Eurogentec	DNA LNA 200 nmol
ISPCR primers: 5′ AAGCAGTGGTATCAACGCAGAGT-3	Eurogentec	DNA Base 200 nmol scale
qPCR: Ubb77 (Primer1): 5′-GGAGAGTCCATCGTGGTTATTT-3′	This manuscript	N/A
qPCR: Ubb77 (Primer2): 5′-ACCTCTAGGGTGATGGTCTT-3′	This manuscript	N/A
qPCR: Ubb77 (Probe): 5′-/5Cy5/TGCAGATCTTCGTG AAGACCTGAC/3IAbRQSp/-3′	This manuscript	N/A
Recombinant DNA		
Plasmid: Tim4 (Myc-DDK-tagged)	OriGene Technologies	Cat#MR222206; NM_178759
Plasmid: Tim1 (Havcr1) (Myc-DDK-tagged)	OriGene Technologies	Cat#MR227388; NM_134248
Plasmid: Fcgr1 (Myc-DDK-tagged)	OriGene Technologies	Cat#MR225268; NM_010186
Plasmid: Olr1 (Myc-DDK-tagged)	OriGene Technologies	Cat#MR226641; NM_138648
Plasmid: Msr1 (Myc-DDK-tagged)	OriGene Technologies	Cat#MR205384; NM_031195
Plasmid: Siglech (Myc-DDK-tagged)	OriGene Technologies	Cat#MR204374; NM_178706
Plasmid: Cd33 (Myc-DDK-tagged)	OriGene Technologies	Cat#MR219960; NM_021293
Plasmid: Cd68 (Myc-DDK-tagged)	OriGene Technologies	Cat#MR204757; NM_BC021637
Plasmid: Sirpa (Myc-DDK-tagged)	OriGene Technologies	Cat#MR226909; NM_007547
Plasmid: Cd209a (Myc-DDK-tagged)	OriGene Technologies	Cat#MR225861; NM_133238
Plasmid: Cd300a (Myc-DDK-tagged)	OriGene Technologies	Cat#MR224901; NM_170758
Plasmid: Axl (Myc-DDK-tagged)	OriGene Technologies	Cat# MR211073; NM_009465
Plasmid: Jmjd6 (Myc-DDK-tagged)	OriGene Technologies	Cat#MR206341; NM_033398
Plasmid: Itgam (CR3)	Addgene	Cat#8631; RRID:Addgene_8631
Plasmid: Itgav (C-treminal His tag)	Addgene	Cat#27290; RRID:Addgene_27290
Plasmid: Cd36 (EGFP)	Addgene	Cat#21853; RRID: Addgene_21853
Plasmid: Dectin1A (Clec7a, tdTomato tag)	Addgene	Cat#58089; RRID: Addgene_58089
Plasmid: Human Mertk (C-Flag tag)	Sino Biological	Cat., HG10298-CF; NM_006343.2
Plasmid: Trem2-DAP12 (with a HA-tag at N terminus)	Prof. Christian Haass (Laboratory of Neurodegenerative Disease Research, DZNE, Munich)	N/A
Software and algorithms		
ImageJ	https://imagej.net/Welcome	RRID:SCR_003070
Graphpad Prism	https://www.graphpad.com:443/	RRID:SCR_002798
Imaris	Bitplane	RRID:SCR_007370
rnaSTAR	Dobin et al., 2013	https://github.com/alexdobin/STAR
FastQC	Simon Andrews	https://github.com/s-andrews/FastQC
Cutadapt	Marcel Martin	https://github.com/marcelm/cutadapt/
Trimgalore	Felix Krueger	https://github.com/FelixKrueger/TrimGalore
Seurat	Butler et al., 2018	https://github.com/satijalab/seurat
DESeq2	Love et al., 2014	https://github.com/mikelove/DESeq2
MAST	Finak et al., 2015	https://github.com/RGLab/MAST/
Slingshot	Street et al., 2018	https://github.com/kstreet13/slingshot
10x Genomics Cell Ranger	Zheng et al., 2017	https://support.10xgenomics.com/single-cell-gene-expression/software/pipelines/latest/what-is-cell-ranger
Metascape	Zhou et al., 2019	http://metascape.org/
STRING	Szklarczyk et al., 2019	https://string-db.org

(*Continued on next page*)

Continued

REAGENT or RESOURCE	SOURCE	IDENTIFIER
Other		
RNAscope Probe: Mm-ITGAX assigned to channel 1	Advanced Cell Diagnostics	Cat#311501
RNAscope Probe: 3-Plex positive control probe-Mm	Advanced Cell Diagnostics	Cat# 320881
RNAscope Probe: 3-Plex negative control probe (dapB)	Advanced Cell Diagnostics	Cat#320871
RNAscope Probe: Probe diluent	Advanced Cell Diagnostics	Cat#300041

RESOURCE AVAILABILITY

Lead contact

Further information and requests for resources and reagents should be directed to and will be fulfilled by the Lead Contact, Mikael Simons (mikael.simons@dzne.de).

Materials availability

All unique reagents generated in this study are available from the Lead Contact with a completed Material Transfer Agreement.

Data and code availability

Single-cell sequencing data generated during this study are available in the NCBI database through accession number NCBI: GSE166548 and bulk sequencing data generated during this study are available through accession number NCBI: GSE166304. All other data that support findings are available upon request from the authors.

EXPERIMENTAL MODEL AND SUBJECT DETAILS

Mice

All animal experiments were reviewed and overseen by the institutional animal use and care committee in German Center for Neurodegenerative Diseases (DZNE) in Munich. The following mouse lines were used in the study: Wild-type C57BL/6J mice from Janvier Labs; *Trem2*$^{-/-}$ mice in the C57BL/6J background (Turnbull et al., 2006, the mice were provided by Prof. Christian Haass, Laboratory of Neurodegenerative Disease Research, DZNE, Munich), ApoE KO mice (B6.129P2-Apoe^{tm1Unc}/J, Jackson Laboratory, Stock No. 002052, the brain sections were provided by Dr. Dirk Fitzner, Department of Neurology, University of Göttingen); 5xFAD mice (B6SJL-Tg (APPSwFILon, PSEN1*M146L*L286V) 6799 Vas/Mmjax, Jackson Laboratory, stock No. 034840-JAX, the brain sections were provided by Dr. Sabine Tahirovic, Laboratory of *ex vivo* models, DZNE, Munich); APP $^{NL-G-F}$ Knock-in mice (available through Takaomi Saido, Ph.D.Wako-shi, Saitama 351-0198, Japan, the brain sections were provided by Dr. Sabine Tahirovic (Laboratory of *ex vivo* models, DZNE, Munich); APP $^{NL-G-F}$ Trem2$^{-/-}$ mice (the brain sections were provided by Prof. Christian Haass, Laboratory of Neurodegenerative Disease Research, DZNE, Munich); CX3CR1^{GFP} (B6.129P-Cx3cr1^{tm1Litt}/J, Jackson Laboratory, Stock No. 005582). The mice were kept in groups of three in Greenline IVC GM500 plastic cages and were housed in a temperature-controlled environment (21 ± 2°C) on a 12 h light/dark cycle with food and water available *ad libitum* in the animal facility in German Center for Neurodegenerative Diseases (DZNE) in Munich. The ApoE KO mice were kept under the same condition in the animal facility of Max Planck Institute of Experimental Medicine in Göttingen. Pups were bred in-house and kept with the adult female under standard light/dark conditions until P21, then they were weaned. Most of the experiments including immunohistochemistry, scRNA sequencing and electron microscopy were performed on adult mice at the age of 2, 6, 12, 18, 20 and 24 months. The exact age of mice used for each analysis is indicated in the figure legends. Mice were aged either in house or purchased from Janvier Labs. Both males and females were included in all analyses and we did not notice any influence of sex on our analyzed parameters in the study. For microglia isolation, P6-P8 C57BL/6J wild-type or knockout mice and for myelin extraction from brain, 2 months old C57BL/6J wild-type mice were used. lysolecithin injection was done on 9 to 15 weeks old mice. The mice and samples including brain sections were allocated into experimental groups randomly. *Cell line:* HeLa cells were grown in Dulbecco's modified Eagle's medium (DMEM) supplemented by 10% FCS. For maintenance, these cells were re-suspended in the freezing media containing 50% FCS and 10% DMSO at concentration of 5×10^6 to 1×10^7 *cells*/mL. Aliquots in 1.5 mL cryo-tubes were frozen slowly at 1°C/min by placing tubes in a NALGENE cryo freezing container in –80°C freezer, then transferring to liquid nitrogen storage.

METHOD DETAILS

Mice perfusion, cell isolation for Smart-seq2

The mice were deeply anesthetized and perfused with cold HBSS between 9am-11am (to decrease circadian fluctuations). Each brain was removed and under a dissection microscope individually micro-dissected; gray matter was isolated from the frontal cortex and white matter form optic tract, *medial lemniscus* and *corpus callosum* (attached gray matter and choroid plexus were removed

carefully) isolated. We developed and established a microglia isolation protocol that prevents *ex-vivo* transcription and automatizes the mechanical isolation parts using GentleMacs with the Neural Tissue Dissociation Kit (Papain) (Miltenyi Biotec). We added actinomycin D (Act-D, Sigma, No. A1410) to a final concentration of 45 μM into the dissociation solution and enzyme mix to prevent *ex-vivo* transcription. The dissociated cell suspension was passed through a 70 μm cell strainer (Corning, 352350) before labeling. Subsequently, cells were blocked with mouse FcR-blocking reagent (CD16/CD32 Monoclonal Antibody, eBioscience cat:14-0161-82,1100) and then stained for 15 min using 7AAD (Thermo Fisher, A1310, 25 ug/mL) and the antibodies against CD45 (eFluor 450, 30-F11, eBioscience,Cat.:48-0451-82, 1:200) and CD11b (PE/Cy7,M1/70, eBioscience, Cat:48-0451-82,1:200) and after washed with PBS (Sigma, D8537). Viable (7AAD negative) single immune cells (CD45 and CD11b positive cells) were sorted by flow cytometry (SH800; Sony). For GFP positive microglia from CX3CR1$^{GFP/+}$ mice, cells were either dissociated with Act-D or without and labeled with DAPI (4',6-diamidino-2-phenylindole, 1:4000 dilution; Sigma) to label dead cells. After FSC-A/FSC-H selection of single-cells, DAPI negative and GFP positive cells were selected. Single immune cells (CD45 and CD11b positive cells) were sorted by flow cytometry (SH800; Sony). Flow cytometry data were analyzed using FlowJo v10. Single-cells were sorted into 96 well plates filled with 4 μL lysis buffer containing 0.05% Triton X-100 (Sigma) and, ERCC (External RNA Controls Consortium) RNA spike-in Mix (Ambion, Life Technologies) (1:24000000 dilution), 2.5 μM oligo-dT, 2.5 mM dNTP and 2 U/μL of recombinant RNase inhibitor (Clontech) then spun down and frozen at −80°C. Plates were thawed and libraries prepared as described below.

Library preparation for Smart-seq2

The 96-well plates containing the sorted single cells were first thawed and then incubated for 3 min at 72°C and thereafter immediately placed on ice. To perform reverse transcription (RT) we added each well a mix of 0.59 μL H2O, 0.5 μL SMARTScribe Reverse Transcriptase (Clontech), 2 μL 5x First Strand buffer, 0.25 μL Recombinant RNase Inhibitor (Clontech), 2 μL Betaine (5 M Sigma), 0.5 μL DTT (100 mM) 0.06 μL MgCl2 (1 M Sigma), 0.1 μL Template-switching oligos (TSO) (100 μM AAGCAGTGGTATCAAC GCAGAGTACrGrG+G). Next RT reaction mixes were incubated at 42°C for 90 min followed by 70°C for 5 min and 10 cycles of 50°C 2 min, 42°C 2 min; finally ending with 70°C for 5 min for enzyme inactivation. Pre-amplification of cDNA was performed by adding 12.5 μL KAPA HiFi Hotstart 2x (KAPA Biosystems), 2.138 μL H2O, 0.25 μL ISPCR primers (10 μM, 5′ AAGCAGTGGTATCAACG CAGAGT-3), 0.1125 μL Lambda Exonuclease under the following conditions: 37°C for 30 min, 95°C for 3 min, 23 cycles of (98°C for 20 s, 67°C for 15 s, 72°C for 4 min), and a final extension at 72°C for 5 min. Libraries were then cleaned using AMPure bead (Beckman-Coulter) cleanup at a 0.7:1 ratio of beads to PCR product. Libraries were assessed by Bio-analyzer (Agilent 2100), using the High Sensitivity DNA analysis kit, and also fluorometrically using Qubit's DNA HS assay kits and a Qubit 4.0 Fluorometer (Invitrogen, LifeTechnologies) to measure the concentrations. Further selection of samples was performed via qPCR assay against ubiquitin transcripts Ubb77 (primer 1 5′-GGAGAGTCCATCGTGGTTATTT-3′ primer 2 5′-ACCTCTAGGGTGATGGTCTT-3′, probe 5′-/5Cy5/TGCA GATCTTCGTGAAGACCTGAC/3IAbRQSp/-3′) measured on a LightCycler 480 Instrument II (Roche). Samples were normalized to 160 pg/μL. Sequencing libraries were constructed by using in-house produced Tn5 transposase (Picelli et al., 2014). Libraries were barcoded and pooled then underwent three 3 rounds of AMPure bead (Beckman-Coulter) cleanup at a 0.8:1 ratio of beads to library. Libraries were sequenced 2x150 reads base pairs (bp) paired-end on Illumina HiSeq4000 to a depth of 3x10^5–6x10^5 reads/sample.

Processing and analyses of Smart-seq2 data

BCL files were demultiplexed with the bcl2fastq software from Illumina. After quality-control with FastQC, reads were aligned using rnaSTAR (Dobin et al., 2013) to the GRCm38 (mm10) genome with ERCC synthetic RNA added. Read counts were collected using the parameter "quantMode GeneCounts" of rnaSTAR and using the unstranded values. From that point, Seurat R v.2.3.4 package was used (Butler et al., 2018). Low-quality samples were filtered out from the dataset based on a threshold for the number of genes detected (min 1000 unique genes/cell), percentage of mitochondrial genes (max 0.5%), percentage of ERCCs (5% max) and number of reads on a log10 scale (between 4 to 5.5) as shown in Figure S1G and H. 1038 single-cells passed the quality-control. Gene expressions were log normalized to 10,000 using the NormalizeData function of Seurat. Dataset were scaled and depth of sequencing was regressed using ScaleData function and using the percentage of ERCCs. The first 12 principal components were considered for the UMAP of all cell types. Non-microglia cells were removed from analysis using markers and threshold such as performed by Keren-Shaul et al. (2017) and shown in Figures S1I and S1J. The first 8 principal components were used for the UMAP of microglia only. To find the clusters/populations of microglial states, hierarchical clustering (Ward's method) was used on the differentially expressed genes specific to the WAM cluster (FindClusters on first 8 PCs). To refine the WAM signature, differential expression analysis was performed using DESeq2 (Love et al., 2014) using FindAllMarkers. 212 genes were found significant at adjusted p value < 0.05 (Table S2). Gene sets of 1, 2, 3 and 4 were defined using hierarchical clustering (Ward's method) on the genes of the WAM signature. For the DAM signature, the top 500 genes were grouped by set in a similar way as described above. Slingshot analyses are based on the first 2 components of the PCA using the WAM signature genes. The previously described 4 clusters of microglia were used as input for Slingshot (Street et al., 2018). All gene ontology analyses were performed using Metascape (http://metascape.org/).

Mice perfusion, cell isolation for Drop-seq

Briefly, the mice were deeply anesthetized and perfused with cold HBSS between 9am-11am (to decrease circadian fluctuations). Each brain was removed and under a dissection microscope individually micro-dissected and dissociated same as described above.

After dissociation, myelin debris were removed using Myelin Removal Beads II (Miltenyi Biotec). The cells were resuspended in 0.04% BSA+PBS and cells were counted using automated cell counter (TC20 Bio-Rad) before loading to Chromium Controller.

Library preparation for Drop-seq

Single-cell suspensions were loaded onto the Chromium Single Cell Controller using the Chromium Single Cell 3′ Library & Gel Bead Kit v3.1 (10X Genomics) chemistry following the manufacturer's instructions. Sample processing and library preparation was performed according to manufacturer instructions using AMPure beads (Beckman Coulter). Libraries were sequenced on the DNBSEQ Sequencing System (BGI group).

Processing and analyses of Drop-seq data

Fastq files were processed with Cell Ranger v4 and aligned to the mm10 (Ensembl 93) genome. From that point, Seurat R v.3 package was used (Butler et al., 2018). Low-quality samples were filtered out from the dataset based on a threshold for the number of genes detected (min 200 unique genes/cell), percentage of mitochondrial genes (max 10%). 21197 out of 25719 and 13954 out of 17263 single-cells passed the quality-control for the aging and Apoe-KO datasets, respectively. Gene expressions were normalized using SCTransform function of Seurat. The first 30 principal components were considered for the UMAP of all cell types. Non-microglia cells were removed from analysis using markers genes as shown in Figures S2C and S2D. The first 15 principal components were used for the UMAP of microglia only. WAM populations were identified using the WAM signature gene set via hierarchical clustering (Ward's method). All gene ontology analyses were performed using Metascape (http://metascape.org/) and STRING (Szklarczyk et al., 2019). After identification of the novel microglial populations, WAM signature was used for generating the UMAPs, as described previously. For the *Apoe*$^{-/-}$ dataset, Apoe was omitted from the WAM signature while generating the UMAPs.

Processing and analyses of external datasets

External datasets from Hammond et al. and Frigerio et al. were analyzed with the same Seurat pipeline using Seurat 3 and MAST (Finak et al., 2015) for differential gene expression. For Hammond et al. (2019) datasets, raw data was downloaded from GSE121654. 4 samples for wild-type data; two replicates of each 1 month old (GSM3442024, GSM3442025) and 18 months old (GSM3442036, GSM3442037) were quality-controlled and processed as described above. After the QC steps, 9558 cells were kept for downstream analyses (Table S2). For Sala Frigerio et al. (2019) datasets, normalized datasets were available. Wild-Type and *App*$^{NL\text{-}G\text{-}F}$ data were downloaded from GSE127892 and analyzed separately. After filtering, 4856 and 5093 microglia were included in the downstream analyses for *App*$^{NL\text{-}G\text{-}F}$ dataset and WT dataset, respectively. The whole dataset acquired from GSE127892, consists of 32 experimental conditions, 2 mice per conditions as reported by the authors. Data for each condition were pooled (Table S1). Merging the current study and Sala Frigerio et al. (2019) wild-type data (Figure S3B) was established by using the Seurat 3 data integration functions. APP/PS1 and APP/PS1-*Apoe*$^{-/-}$ data were downloaded from GSE127884. After filtering, 1143 microglia were kept for downstream analyses. For the average heatmap (Figure S7A) from Keren-Shaul et al. (2017) data, their Table S2 was used to plot the average gene expression per microglial population for the 500 DAM signature genes.

Immunohistochemistry

Animals were anesthetized by intraperitoneal injection of 14% chloral hydrate, perfused transcardially with 4% paraformaldehyde. Post fixation of brain tissue was done in 4% PFA overnight. Then the brain tissue was further cryo-protected in 30% sucrose in PBS for 24 h. After freezing the tissue on dry ice using Tissue-Tek O.C.T, 30 μm coronal sections were cut by cryostat Leica CM 1900. Free-floating sections were collected in a solution containing 25% glycerol and 25% ethylenglycol in PBS. The sections were rinsed with 1x PBS containing 0.2% Tween-20 and permeabilized in 0.5% Triton X-100 for 10 to 30 min depending on primary antibody. Fab fragment goat anti mouse IgG (1:100) (Dianova) was added for 1 h at room temperature to block endogenous mouse tissue immunoglobulins. After a brief wash the sections were blocked for 1 h at room temperature in a solution containing 2.5% FCS, 2.5% BSA and 2.5% fish gelatin in PBS. Primary antibodies, diluted in 10% blocking solution, were added and incubated overnight at 4°C. On the following day sections were incubated with secondary antibodies, diluted in 10% blocking solution, for 1 h at room temperature. The sections were washed with PBS followed by distilled H_2O and mounted using fluorescence mounting medium (Dako) over superfrost plus slides. For AXL and CLEC7A staining, antigen retrieval protocol using citrate buffer (10 mM, pH 6) was performed on free-floating sections followed by staining protocol as mentioned above. The immunostaining of PU.1 was done as following. The free floating sections were permeabilized with 0.5% Triton X-100 for 30 min at room temperature. Then sections were treated with blocking solution containing 0.3% Triton X-100 for 24 hours at 4C. The primary antibody in blocking solution without Triton X-100 was incubated for 65 hours at 4C. the sections were incubated with secondary antibody in blocking solution at 4C over night.

RNAscope *in Situ* Hybridization

RNAscope *in situ* hybridization assay was applied to detect mRNA of *Itgax* in the brain cryosections prepared from aged and young wild-type mice. The assay was performed using a commercially available kit, RNAscope Multiplex Fluorescent Detection Reagents v2 (Advanced Cell Diagnostics, ACD) and the manufacturer instruction was followed. Briefly, 30 μm cryosections were fixed on superfrost plus slides; they were pretreated with hydrogenproxide for 10 min at room temperature and then with antigen retrieval reagent (5min boiling) to unmask the target RNA. After applying Protease III on the sections for 30 min at 40°C, probe hybridization was done

by incubating sections in mouse *Itgax* probe assigned to channel 1 (Cat. 311501), diluted 1:50 in probe diluent, for 2 h at 40°C. Positive control probes targeting housekeeping genes including *Polr2a*, *Ppib* and *Ubc*. (Advanced Cell Diagnostics, Hayward, CA) and 3-Plex negative control probes targeting the bacterial *DapB* gene (Advanced Cell Diagnostics, Hayward, CA) were used to test mRNA integrity in the tissue. Afterward, signal amplification and detection were performed according to the instruction of the kit. Signal detection was done using Opal dyes (Opal520-green) diluted 1:3000 in TSA buffer. To visualize microglia, after *in situ* hybridization, immunohistochemistry assay was performed using Iba1 antibody (Wako, 1:1000). The nuclei of cells were counterstained with DAPI (4',6-diamidino-2-phenylindole) and then the slides were mounted over superfrost plus slides using prolong gold antifade reagent (Invitrogen).

Bulk RNA Sequencing

The isolated microglia were homogenized in RLT buffer using QIAShredder (QIAGEN) and the total RNA was extracted using RNeasy Micro Kit (QIAGEN) and cDNA was synthesized using Ovation RNA-Seq System V2 (NuGEN). 1 μg of cDNA was used as input for Ion Xpress Plus Fragment Library Kit (ThermoFisher Scientific) to generate barcoded libraries. Barcoded libraries were then quantified using qRT-PCR (KAPA Library Quantification Kit). Barcoded libraries were then pooled and clonally amplified on Ion Spheres (Ion One Touch 200 Template Kit v2, ThermoFisher Scientific) and were sequenced on an Ion Proton sequencer (ThermoFisher Scientific). Raw reads were sorted based on barcodes and were subjected to quality analysis using FASTQC. The sequences were subsequently aligned to the genome of *Mus musculus* (GRCm38/Mm10) using the TMAP aligner with default parameters. The reads mapping to unique locations were quantified using RefSeq Gene Annotations(v73) into genes. Differential gene expression analysis and hypergeometric pathway analysis using KEGG genesets was performed using a commercial platform (Partek). Genes with fold change greater than 2 and p values less than 0.05 were considered for further hypergeometric pathway enrichment analysis.

Transmission Electron Microscopy

Mice brains were fixed in 2.5% glutaraldehyde and 4% paraformaldehyde in 0.1 M sodium cacodylate buffer at pH 7.4 after deep anesthesia (isoflurane) perfusion. Brains were vibratome sectioned and immersion fixed in the same buffer for 24 h at 4°C. After tissue trimming and washes in 0.1 M sodium cacodylate buffer, postfixation in reduced Osmium (2% Osmium, 2.5% potassium ferrocyanide in 0.1 M cacodylate buffer) was followed by en bloc uranyl acetate (1% aqueous uranylacetate) contrasting, graded dehydration in ethanol and embedding in epon resin (Serva). After ultrathin sectioning the grids (Leica UC7 ultramicrotome) were contrasted by 1% uranyl acetate and lead citrate (Ultrostain, Leica). Images were acquired with a JEOL JEM1400 plus TEM equipped with a Ruby 8Mpx CCD camera. For each analysis, randomly selected regions in three to five different animals were imaged. Data analysis was carried out using ImageJ 1.41.

Correlative Light and Scanning Electron Microscopy

The correlated workflow was adapted from Fang et al. (2018). Mice were perfused and brains fixed for 24 h in 4% paraformaldehyde and 3% w/v sucrose in 0.1 M PBS (pH 7.4). The brain tissue was sectioned into 100μm thick vibrotome sections. After 24 h incubation in fixative, smaller regions containing the corpus callosum were trimmed to restrict the correlation area and prevent tissue curving during the en bloc staining. The immunostaining was performed as mentioned before with a slight change. The sections were incubated with Iba1 antibody (Wako, 1:1000) for 48 h and with secondary antibody (Alexa Fluor 488, Invitrogen) overnight. Sections were stained with DAPI (1:2000 in PBS) for 5 min, washed in PBS and mounted on glass slides using secure-seal spacer (13 mm, 0.12 mm thickness, Invitrogen). Tile scans of the whole section with a 20x air objective and regions of interest with a 63x oil objective were acquired on a Leica TCS SP5 confocal microscope. After careful unmounting, sections were post-fixed (2.5% glutaraldehyde in 0.1 M sodium cacodylate buffer) for 24 h. In order to keep a flat orientation corresponding to the confocal imaging plane, the sections were glued onto of Aclar spears (Science Services) using Cell-Tak adhesive (Corning) (Luckner and Wanner, 2018). We applied a rOTO (reduced osmium-thiocarbohydrazide-somium) staining procedure adopted from Tapia et al. (2012). Briefly, the tissue was initially postfixed in 2% osmium tetroxide (EMS), 2% potassium ferricyanide (Sigma) in 0.1 M sodium cacodylate (Science Services) buffer (pH 7.4). After three washing steps in buffer and water the staining was enhanced by reaction with 1% thiocarbohydrazide (Sigma) for 45 min at 50°C. The tissue was washed in water and incubated in 2% aqueous osmium tetroxide. All osmium incubation steps were carried out over 90 min with substitution by fresh reagents after 45 min, respectively. To further intensify the staining, 2% aqueous uranyl acetate was applied overnight at 4°C and subsequently warmed to 50°C for 2 h. The samples were dehydrated in an ascending ethanol series and infiltrated with LX112 (LADD). The sample were flat embedded into gelatin capsules (Science Services) and cured for 48h. For SEM experiments without correlation samples were fixed as mentioned in the TEM protocol and subjected to the rOTO protocol described above. The block was trimmed by 200 μm at a 90° angle on each side using a TRIM90 diamond knife (Diatome) on an ATUMtome (Powertome, RMC). The front face was carefully trimmed to collect all sections beginning at the very surface areas that correspond to the confocal images (depth of 15-20 μm). Consecutive sections were taken with a 35° ultra-diamond knife (Diatome) at a nominal cutting thickness of 100nm and collected on freshly plasma-treated (custom-built, based on Pelco easiGlow, adopted from Mark Terasaki) CNT tape (Kubota et al., 2018). Starting from the block face with the complete tissue exposed we collected 300 ultrathin sections, covering a thickness of 30 μm in depth. Tape strips were mounted with adhesive carbon tape (Science Services) onto 4-inch silicon wafers (Siegert Wafer) and grounded by additional adhesive carbon tape strips (Science Services). EM micrographs were acquired on a Crossbeam Gemini 340 SEM (Zeiss) with a four-quadrant backscatter detector at 8 kV. In

ATLAS5 Array Tomography (Fibics), the whole wafer area was scanned at 2000-4000 nm/pixel to generate an overview map. For correlation, sections were selected and the entire corpus callosum region (1356 × 491 μm^2) of 177 sections (one wafer, 17.7 μm in z) scanned at 200 × 200 nm^2. The images were aligned by a sequence of automatic and manual processing steps in Fiji TrakEM2 (Cardona et al., 2012). The correlation was achieved by using nuclei and further anatomical landmarks (section border morphology, myelinated areas). Based on this correlation we selected an area in xy (544 × 324 × 13.9 μm^3) and the respective sections (corresponding to the ROI in z) for high resolution acquisition at 20 × 20 nm^2. After correlation of this dataset we imaged single images containing IBA1 positive cells at 4 × 4 nm^2.

Myelin isolation and purification

Myelin was isolated from 8-week-old C57BL/6 mice brains by sequential centrifugation on discontinuous sucrose gradient according to a protocol previously described (Norton and Poduslo, 1973) with some modifications. The ultracentrifugation was done using SW41 Ti rotor. The brain tissues were homogenized with a Dounce homogenizer in a solution containing 10 mM HEPES, 5mM EDTA, and 0.32 M sucrose. The homogenized tissue was layered on HEPES/EDTA buffer containing 0.85 M sucrose, centrifuged at 24600 rpm for 30 min with low deceleration and acceleration. The crude myelin fraction was removed from interface, resuspended in ice-cold distilled water, and centrifuged at 9500 rpm for 15 min. The hypo-osmotic shock was applied to the pellet two more times. The pellet from the last step was dissolved in HEPES/EDTA buffer containing 0.3 M sucrose, and placed over the 0.85 M sucrose; all the centrifugation steps and hypo-osmotic shocks were repeated as before. Eventually, the purified myelin pellet was resuspended in 1 mL PBS and stored at −20°C.

Myelin uptake assay

18 mm coverslips were coated with fibronectin in PBS (20 $\mu g/mL$) in the 24-well plates for 1 h in the incubator (37C, 5% CO_2). After changing PBS with the culture medium (DMEM plus 10% fetal calf serum, 1% Glutamax, and 0.5% antibiotics) HeLa Cells were seeded at 4 × 10^4 cells/mL and cultured with 5% CO_2 at 37°C for 18-24 h before transfection. 1 μg of expression plasmids were introduced into HeLa cells by the calcium phosphate precipitation method. The level of gene expression was tested 24-48 h after incubation. Next, transfected cells were treated with myelin as following. Purified myelin isolated from 2-month-old wild-type mouse brains was labeled with PKH67 (Sigma), and then washed in PBS by centrifugation at 15000 g. The final pellet was resuspended in culture medium and sonicated for 20 min in an ultrasound water bath. Transfected HeLa cells were treated with 4 μg PKH76-labeled myelin and incubated at 37°C in the presence of 5% CO_2 for 2 to 5 h. The cells were fixed in 4% PFA for 15 min and myelin uptake was assessed by immunocytochemistry.

Microglia-myelin binding assay

Microglia were isolated from C57BL/6, P6-P8 wild-type mice by MACS Technology. Brain tissue was dissociated using a Neural Tissue Dissociation Kit (Papain) (Miltenyi Biotec). Briefly, brain tissue was removed, cut into small pieces and dissociated by enzymatic digestion provided in the kit. The tissue suspension was applied to a 40 μm cell strainer, and washed twice with DMEM containing 1 mM sodium pyruvate. The final palette was resuspended in 10 volume of DMEM containing 10% FCS, 1 mM sodium pyruvate, 1% antibiotics (DMEM/FCS) plus 1 volume of CD11b microbeads (Miltenyi Biotec) and incubated at 4°C for 15 min. After washing with DMEM/FCS, the pellet was resuspended in 500 μL of the same medium, applied in a MACS column in the magnetic field, following three times wash, CD11b positive cells (microglia) were flushed out of the column, centrifuged at 400 x g for 10 min at 4°C. Isolated microglia were plated over 12 mm coverslips at 7 × 10^4 cell/mL, and incubated for 48-72 h. PKH67-labeled myelin was sonicated in an ultrasound water bath for 20 min. Primary microglia cultures were treated with 4 μg myelin and incubated on the ice for 2-4 h. Purified myelin was conjugated with Annexin V Alexa Fluor 555 (Thermo Fisher) as following. 4 μg of sonicated myelin was incubated with different concentration of Annexin V (13.5 M, 18 M and 22.5 M) in the binding buffer (10 mM HEPES, 140 mM NaCl, 2.5 mM CaCl2, pH 7.4) for 1 h at room temperature.

Myelin clearance assay

To analyze the rate of clearance of myelin debris, microglia cultures were pretreated with serum free DMEM, supplemented with 2 ng/mL TGF-β2 (Peprotech, 100-35B), 20 ng/mL CSF1 (M-CSF, Peprotech, 315-02) and 1.5 $\mu g/mL$ cholesterol (Avanti Polar Lipids (Otto Nordwald), 700000P) (TCC medium). The cells were treated with 10 $\mu g/mL$ myelin (or HEPES control) in the TCC medium for 2 h. After treatment, the cells were washed three times, and incubated with the TCC medium for 2 or 24 h. For the experiment with the inhibitors of lysosomal degradation, 100 nM Bafilomycin (Invivogen) or 10 μM leupeptin (Selleckchem) were administered 30 minutes before myelin administration and kept in the media until the end of the experiment. After fixation, the myelin in cells was stained using anti-PLP antibody; the cells were stained using DyLight 694 labeled tomato lectin (Vector Laboratories, DL-1178) and 2 $\mu g/mL$ Hoechst 33342. The cells were imaged on a Leica SP5 confocal microscope with a 63x objective. For the quantification, the intensity of the PLP staining contained within the cell membrane was measured per cell.

Lysolecithin-induced demyelination

Stereotactic injection of lysolecithin in the spinal cord was performed in wt C57BL/6J and *Trem2*$^{-/-}$ mice that were 9 to 15 weeks old. 1% lysolecithin was prepared by dissolving L-α-Lysophosphatidylcholine from egg yolk (Sigma, L4129) in PBS, pH 7.4 (GIBCO,

10010056). 3% Monastral blue was prepared by dissolving Copper(II) phthalocyanine-tetrasulfonic acid tetrasodium salt (Aldrich, 274011) in milliq water, and the solution was sterilized by filtration through a 0.45-μm filter and autoclaving. Prior to injection, 1μl of 3% Monastral blue was mixed with 25μl of 1% lysolecithin. Glass Capillaries for Nanoliter 2010 (World Precision Instruments, 504949 or 4878) were pulled using the P-1000 Next Generation Micropipette Puller (Sutter Instrument). The program had the following parameters: Heat 530, Pull 0, Vel 60, Time 250, Pressure 500, Ramp 520, Microinjection – BF100.50.10, Tip < 1 μm, Taper 6-8 mm. R ~40-80 Meg, Heat = Ramp, FB255B, 2.5mm Box. Before surgery, the animals were anesthetized by intraperitoneal injection of 0.5 mg/kg body weight medetomidine, 5.0 mg/kg midazolam and 0.05 mg/kg fentanyl (MMF). The anesthetized animals were kept on a heating pad at 37°C, and the anesthetic depth was monitored by checking the reflex between the toes and the corneal reflex. The surgery and intraspinal injection of lysolecithin was conducted using the digital mouse stereotaxic frame and Nanoliter 2010 Injector with MICRO4 controller (World Precision Instruments) as previously described (Cantuti-Castelvetri et al., 2018). After the spinal cord was exposed, the capillary was positioned 0.55 mm lateral to the dorsal artery, and lowered 1.15 mm into the tissue. At each injection site, 1 μl of 1% lysolecithin containing 0.12% monastral blue was injected at a speed of 350 nl/min. 1 minute after the end of the delivery, the capillary was retracted. After injection, the skin was sutured, and the wound was sutured. After the operation, the animals were injected with 250 μl of 0.9% NaCl (normal saline solution) to compensate for the loss of blood and with the analgesic buprenorphine at a dose of 0.1 mg/kg. When MMF was used for anesthesia, 2.5 mg/kg atipamezole, 0.5 mg/kg flumazenil and 1.2 mg/kg naloxone (AFN) was injected IP for the animals to antagonize the anesthesia and awaken the animal. The animals were injected SC with buprenorphine for two days after surgery.

Gene expression analysis

For the preparation of RNA from cell, primary microglia was treated with myelin or fluoresbright beads. At the end of the treatment, the cells were collected in RLT buffer and the RNA was isolated with the RNAeasy isolation kit (QIAGEN, 74104). The RNA was retrotranscribed to cDNA with the Superscript III kit (Thermo Fisher Scientific, 18080051). For the quantitative PCR, the cDNA was quantified with the Power SYBR green PCR Master mix (4367659 Thermo Fisher Scientific) on a Applied Biosystem 7500 Fast Cycler, according to the PCR mix data sheet. The relative quantification of each gene was performed with the ΔΔCt method: each gene was quantified and its expression was normalized to the house keeper gene (Cytochrome C1, cyc1). The primers used for the analysis were:

hexosaminidase forward 5'-GCTGCAGAATCCTTTGCTTACGG-3′;
hexosaminidase reverse 5'-GGGTCACGTGAACGGGAGG-3′;
N-acetylglucosamine-6-sulfatase forward 5'-GAAAACCAAGGCCCTCATCG-3′;
N-acetylglucosamine-6-sulfatase reverse 5'-TGTTGTTAACGACGTGGTGG-3′;
Galactosidase Beta 1 forward 5'-CACTGCCTAACGGAGAGACC-3′;
Galactosidase Beta 1 reverse 5'-TCCCGAGATGTATCGGAATGG-3′;
Cathepsin L forward 5'-TCGGATTTCACCTCAGTGTCC-3′;
cathepsin L reverse 5'-CTTAAAAACTAGTGGGGCTGGC-3′.

Western Blotting

Following separation with SDS-PAGE, the proteins were transferred from the gel onto the nitrocellulose membrane using the mini Trans-Blot Module. The gel sandwich in blotting cassette was placed in the tank of the module containing transfer buffer (0.25 M Tris base, 1.92 M glycine, 20% methanol) with 100 V for 1 hour. The membrane was washed in PBST (0.1% Tween 20 in PBS) for 10 min, immersed in 4% skim milk powder in PBST as a blocking solution for 30 min at room temperature and then incubated with primary antibody in PBST at 4°C overnight. After washing, it was incubated with horse radish peroxidase (HRP)-conjugated secondary antibody in PBST for one hour at room temperature. Then targeted protein was detected with enhanced chemiluminescence method using Luminol enhancer and peroxide solutions (Pierce/Thermo Scientific) and was visualized with an Odyssey Fc imager from LI-COR.

Image processing and analysis

Images were acquired via a Leica TCS SP5 confocal microscope and were processed and analyzed with Imaris (64x version 9.2.0) and ImageJ 1.41 image processing software. For quantification of microglia nodules, a cluster of three or more cells that were identified by their nuclei labeled with DAPI or PU.1 antibody.

QUANTIFICATION AND STATISTICAL ANALYSIS

To compare more than two groups, one-way analysis of variance (ANOVA) followed by Bonferroni post hoc test was applied. A two-tailed Student's t test was performed for comparison of two groups. Two-way ANOVA followed by Bonferroni post hoc test was used for analyzing the interaction of age and brain region or age and genotype. In all tests a p value of < 0.05 was considered as significant. Statistical analyses were done using GraphPad Prism (GraphPad Software, Inc.). The type of statistical test and the exact p value for each experiment are included in the figure legends. All cell culture experiments using cell lines and primary cells were done at least

three times independently to ensure reproducibility. Technical and biological replicates were included. The average of at least 3 technical replicates was counted as one biological replicate which was then used for statistical analysis and comparison within the biological replicates. For all mouse experiments, 4 to 5 mice per genotype were analyzed. For histological analysis, 3 to 4 random region of interest (ROIs) per brain section were taken and three random brain sections per animal were quantified to account for variability within the biological sample. All values obtained from *in vivo* experiments were represented as mean ± sd of 3 brain sections per mouse for immunohistochemistry and 2 brain sections per mouse for RNAScope *in situ* hybridization. The values from *in vitro* experiments were reported as mean ± sd of the number of independent experiments. No power analyses were used to predetermine sample sizes. However, sample sizes were chosen based on prior literature using similar experimental paradigms. The value of n per group and what n represents in each experiment can be found in the figure legends. All data acquisition and analysis for wild-type and knockout samples were done in a blinded manner and no data were excluded from any analysis. For the scRNA-seq statistical data analysis, the n represents a sequencing lane, containing then a defined tissue (GM or WM) for a defined mouse (SS2) or a pool of mice (Drop-seq). Differential expression analysis was performed with DESeq2 (Love et al., 2014) and MAST (Finak et al., 2015) with adjusted p value below 0.05 considered as significant. For pathway enrichment analysis, Metascape (Zhou et al., 2019) and STRING (Szklarczyk et al., 2019) were used with default parameters.

2.2 CD8+ T cells induce interferon-responsive oligodendrocytes and microglia in white matter aging

Abstract

A hallmark of nervous system aging is a decline of white matter volume and function, but the underlying mechanisms leading to white matter pathology are unknown. In the present study, we found age-related alterations of oligodendrocyte cell state with a reduction in total oligodendrocyte density in aging murine white matter. Using single-cell RNA-sequencing, we identified interferon (IFN)-responsive oligodendrocytes, which localize in proximity to CD8+ T cells in aging white matter. Absence of functional lymphocytes decreased the number of IFN-responsive oligodendrocytes and rescued oligodendrocyte loss, whereas T-cell checkpoint inhibition worsened the aging response. In addition, we identified a subpopulation of lymphocyte-dependent, IFN-responsive microglia in the vicinity of the CD8+ T cells in aging white matter. In summary, we provide evidence that CD8+ T-cell-induced, IFN-responsive oligodendrocytes and microglia are important modifiers of white matter aging.

Declaration of Contribution

M. Simons and O.G. conceived and supervised the project. **T.K.**, N.M., L.L., S.B.-G., H.J., S.K., O.G., J.W., L.C. and M. Schifferer performed experiments and analyzed the data. M. Simons and O.G. analyzed the data or supervised data acquisition. A.L. and J.G. provided essential reagents. M. Simons and O.G. wrote the manuscript with input from all authors.

nature neuroscience

Article

https://doi.org/10.1038/s41593-022-01183-6

CD8$^+$ T cells induce interferon-responsive oligodendrocytes and microglia in white matter aging

Received: 8 November 2021

Accepted: 14 September 2022

Published online: 24 October 2022

Check for updates

Tuğberk Kaya[1,2,3,4,7], Nicola Mattugini[2,3,7], Lu Liu[1,7], Hao Ji[1], Ludovico Cantuti-Castelvetri[2,3], Jianping Wu[2,3,4], Martina Schifferer[3,5], Janos Groh[6], Rudolf Martini[6], Simon Besson-Girard[1,4], Seiji Kaji[2,3], Arthur Liesz[1], Ozgun Gokce[1,5,8] ✉ and Mikael Simons[1,2,3,5,8] ✉

A hallmark of nervous system aging is a decline of white matter volume and function, but the underlying mechanisms leading to white matter pathology are unknown. In the present study, we found age-related alterations of oligodendrocyte cell state with a reduction in total oligodendrocyte density in aging murine white matter. Using single-cell RNA-sequencing, we identified interferon (IFN)-responsive oligodendrocytes, which localize in proximity to CD8$^+$ T cells in aging white matter. Absence of functional lymphocytes decreased the number of IFN-responsive oligodendrocytes and rescued oligodendrocyte loss, whereas T-cell checkpoint inhibition worsened the aging response. In addition, we identified a subpopulation of lymphocyte-dependent, IFN-responsive microglia in the vicinity of the CD8$^+$ T cells in aging white matter. In summary, we provide evidence that CD8$^+$ T-cell-induced, IFN-responsive oligodendrocytes and microglia are important modifiers of white matter aging.

Age is the major risk factor for the most prevalent neurodegenerative diseases[1]. A better understanding of age-related alterations is therefore of overarching importance, but relatively little is known about the pathology occurring in the white matter, which is to a large extent composed of myelin, a lipid-rich membrane wrapped around axons by oligodendrocytes[2]. Myelination is not limited to early development but extends into adult life and contributes to brain plasticity. Regulated by neuronal stimuli and various environmental factors, there is a substantial fraction of adult-born oligodendrocytes that is actively engaged in forming new myelin sheaths, a process that declines in aging[3–5]. In humans, white matter volume starts to decline already in mid-life and these global alterations are often associated with focal lesions that appear hyperintense on magnetic resonance images[6–9]. Focal white matter degeneration is related to an increased risk of stroke and dementia[6] and contributes to cognitive decline possibly by disrupting connective pathways in the brain[10–12]. In nonhuman primates and rodents, ultrastructural analyses of aging white matter show pathology of myelinated fibers, consisting of focal areas of degenerated myelin and axonal damage[13,14]. We have previously shown that such age-related myelin pathology results in a distinct white matter-associated microglia state, in which the disease-associated microglia (DAM) or microglia-neurodegenerative phenotype (MGnD) program is partially activated to clear myelin debris in groups of a few closely connected microglia[15–18]. Whereas the microglial responses to

[1]Institute for Stroke and Dementia Research, University Hospital of Munich, Ludwig Maximilian University (LMU) of Munich, Munich, Germany. [2]Institute of Neuronal Cell Biology, Technical University Munich, Munich, Germany. [3]German Center for Neurodegenerative Diseases, Munich, Germany. [4]Graduate School of Systemic Neurosciences, LMU Munich, Munich, Germany. [5]Munich Cluster of Systems Neurology, Munich, Germany. [6]Department of Neurology, Section of Developmental Neurobiology, University Hospital Würzburg, Würzburg, Germany. [7]These authors contributed equally: Tuğberk Kaya, Nicola Mattugini, Lu Liu. [8]These authors jointly supervised this work: Ozgun Gokce, Mikael Simons. ✉e-mail: oezguen.goekce@med.uni-muenchen.de; mikael.simons@dzne.de

aging and disease are more intensely studied[15,17,19–21], less is known about aging-related oligodendrocyte reactions related to myelin pathology. In the present study, we studied aging-induced glial reactivity and identified IFN-responsive oligodendrocyte and microglia in the white matter. We observed that CD8$^+$ T cells increase in aging white matter and localize in close proximity to IFN-responsive cells. Genetic ablation of functional lymphocytes by using *Rag1*$^{-/-}$ mice[22] or *CD8*$^{-/-}$ mice[23] prevented aging-induced oligodendrocyte loss and IFN-responsive oligodendrocyte and microglia formation. Inversely, T-cell-checkpoint inhibition worsened the aging effect. These perturbation experiments support a role of CD8$^+$ T cells in driving white matter aging.

Results

Transcriptomic aging responses of oligodendrocytes

To characterize the oligodendrocyte aging effect at single-cell resolution, we used two different single-cell RNA-sequencing (scRNA-seq) methods. For plate-based scRNA-seq (Smart-seq2), we dissociated gray matter from the frontal cortex and white matter tracts from the corpus callosum as well as the optical tracts, and the medial lemniscus from young (3-month-old) and aged (24-month-old), wild-type male mice (Fig. 1a). The scRNA-seq experimental details and animal information are reported according to guidelines[24,25] (Methods and Supplementary Tables 1 and 2). To avoid isolation artifacts, we used our previously established automated dissociation protocol that inhibits ex vivo transcription[18]. We sorted live nonmyeloid (CD11b$^-$ and SYTOX BLUE$^-$) cells (Extended Data Fig. 1a). Each single-cell library passed through strict quality thresholds filtering out 112 single cells due to low quality and 2,538 single cells from 8 mice remained (Extended Data Fig. 1b). The cell-type composition of these cells was analyzed by unsupervised Uniform Manifold Approximation and Projection (UMAP) analysis (Fig. 1b, Extended Data Fig. 1c,d and Supplementary Table 1). Oligodendrocytes were separated into four different subclusters, of which the most abundant two clusters represent the heterogeneity of oligodendrocytes previously identified in juvenile and adult mouse by Marques et al.[26]. In our analysis, two additional oligodendrocyte clusters appeared in aged mice, which were enriched in white matter. One was characterized by a high expression of the serine (or cysteine) peptidase inhibitor, member 3N (Serpina3n) and the complement component C4b, previously associated with injury responses[27–32]. As this cluster was highly enriched in the aged white matter, we named it aging-related oligodendrocytes (Fig. 1b,c,e). We uncovered a smaller IFN-responsive oligodendrocyte subpopulation (IRO), which was characterized by the expression of genes commonly associated with an IFN response, such as *Stat1*, *Ifi27l2a* and major histocompatibility complex (MHC) class I-related genes (*H2-K1 and H2-D1)* (Fig. 1b,c,f). A related gene expression profile has been detected in oligodendrocyte progenitor cells (OPCs) in the context of multiple sclerosis[28,30]. To validate our results, we performed scRNA-seq using the 10× platform with cells from gray and white matter of 24-month-old mice (8,726 high-quality cells from 8 mice: Fig. 1b and Extended Data Fig. 1e). Tissues were prepared as described for Smart-seq2 and enriched for live cells using flow cytometry (Extended Data Fig. 1a). Major cell types were annotated based on canonical markers upon clustering (Extended Data Fig. 1e–g). We again identified a continuous range of oligodendrocytes that reproduced the major oligodendrocyte clusters of the Smart-seq2 scRNA-seq dataset (Fig. 1b,g). The higher number of oligodendrocytes allowed us to resolve Oligo1 and Oligo2 into five subclusters, but the identity and ratios of all four major clusters remained similar in both aged scRNA-seq datasets (Fig. 1g,h and Extended Data Fig. 1h). Using 20 independent scRNA-seq experiments, we compared changes in ratios of IROs and age-related oligodendrocytes by using the single-cell differential composition analysis (scCODA), which takes account of the compositionality of the scRNA-seq data and reliably controls for false discoveries[33]. Both age-related oligodendrocyte and IRO cluster proportions were significantly increased in the aged white matter samples (Fig. 1e,f). These increases were accompanied by a significant decrease in aged white matter Oligo1 but not in Oligo2 (Extended Data Fig. 2a).

CD8$^+$ T cells induce reactivity and loss of oligodendrocytes

To validate the changes in scRNA-seq cluster ratios and to determine the localization of the age-related and the IFN-responsive oligodendrocytes, we costained anti-adenomatous polyposis coli (APC) clone CC1 (CC1$^+$) oligodendrocytes by using antibodies against C4b, Serpina3n, B2M and STAT1. Consistent with the scRNA-seq data, we found that antibodies against C4b, Serpina3n, B2M and STAT1 labeled oligodendrocytes in the white matter, and only rarely in the gray matter (cortical areas of the brain) of aged (24-month-old) mice (Fig. 2a and Extended Data Fig. 2b,c). Colabeling against STAT1 and Serpina3n did not detect double-positive cells, in agreement with our scRNA-seq data that STAT1$^+$ oligodendrocytes are distinct from Serpina3n$^+$ oligodendrocytes (Extended Data Fig. 2e). Next, we compared the labeling in young (3-month) and old (24-month) gray and white matter and found that CC1$^+$ oligodendrocytes, also immunoreactive for C4b, Serpina3n, STAT1 or B2M, are restricted to the aged brains mostly in the white matter (Fig. 2a and Extended Data Fig. 2b,c). Quantification revealed that about 3–5% of the CC1$^+$ cells within the corpus callosum of 24-month-old mice were positive for the markers STAT1 and B2M. We found that C4b$^+$/Serpina3n$^+$ oligodendrocytes were more abundant (41% of CC1$^+$ cells were Serpina3n$^+$/CC1$^+$ and 30% C4b$^+$/CC1$^+$ in 24-month-old white matter) and also more evenly distributed compared with B2M$^+$/STAT1$^+$ oligodendrocytes (Fig. 2a and Extended Data Fig. 2d,f). Our subregional localization analysis revealed that STAT1$^+$ oligodendrocytes were localized significantly closer to the medial white matter bordering the lateral ventricles compared with the frontal white matter (Extended Data Fig. 3a,b). Previous work has identified infiltrating T cells in the aged brain, close to neurogenic niches and within the optic nerve[34,35]. As T cells are a major source of IFNs, we analyzed T-cell proportions in the mouse aging single-cell transcriptomic atlas[35] and found that the T cells significantly increased in 24-month-old mice compared with 18- and 3-month-old mice (Extended Data Fig. 3f). Using immunohistochemistry, we analyzed the CD3$^+$ T cells in the white and gray matter of the aged brain and observed that the T cells, which were mostly CD8$^+$ T cells, were almost exclusively found in the white matter, where they were enriched in areas close to the lateral ventricles (Fig. 2b and Extended Data Figs. 2d and 3a,b,d). Next, we studied the spatial relationship between the IFN-responsive oligodendrocytes (STAT1$^+$CC1$^+$) and CD8$^+$ T cells in aging white matter. Strikingly, STAT1$^+$CC1$^+$ cells are more frequently localized in close proximity to CD8$^+$ T and vice versa (<20 µm) (Fig. 2c). Moreover, STAT1$^+$CC1$^+$ oligodendrocytes are found significantly more often in close proximity to CD8$^+$ T cells than randomly chosen DAPI$^+$ cells (Fig. 2d), which was not the case for Serpin3n$^+$CC1$^+$ oligodendrocytes (Extended Data Fig. 3e).

To characterize the CD8$^+$ T cells in the aging brain, we analyzed the mouse aging single-cell transcriptomic atlas[36] and the CD8$^+$ T-cell dataset from Groh et al.[34]. Our analysis, which included samples from 4 different organs of 21- and 24-month-old mice, showed that brain-associated CD8$^+$ T cells segregated away from CD8$^+$ T cells from the spleen, kidney and lung in the UMAP presentation (Extended Data Fig. 4a). Genes differentially upregulated in the brain CD8$^+$ T cells were enriched in tissue-resident memory T-cell markers (*Cxcr6*, *Cd69*, *Junb*, *Bhlhe40*), checkpoint molecules (*Pdcd1*) and effector function-associated genes (*Gzmb*, *Ccl4*, *Ccl5*, *Ifng*), but low in genes associated with central memory T cells (*Sell*, *Ccr7*) compared with CD8$^+$ T cells from the spleen, kidney and lung (Extended Data Fig. 4a–d).

Next, we performed immunofluorescence staining for the tissue-resident memory T-cell marker, CD69, which showed that almost all the CD8$^+$ T cells were also positive for CD69 (Extended Data Fig. 5a). We analyzed the expression of the checkpoint molecules, programmed cell death protein 1 (PD-1) and the lymphocyte-activation

https://doi.org/10.1038/s41593-022-01183-6

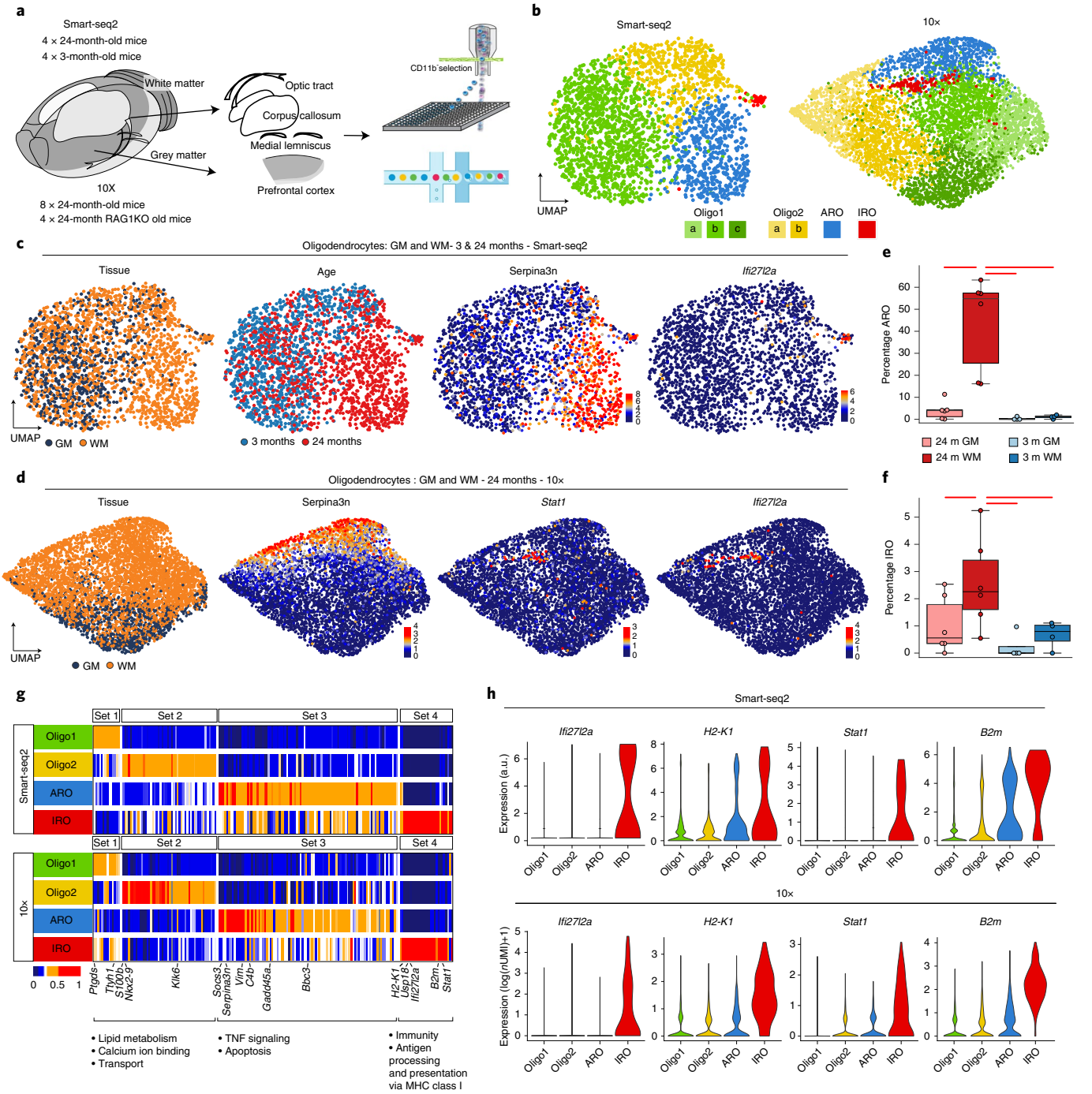

Fig. 1 | Identification of age-related gene expression signatures in oligodendrocytes. a, Experimental design from dissection to cell sorting and cell loading for the plate-based (Smart-seq2 (SS2)) and 10× pipelines, respectively. **b**, UMAP plots of oligodendrocytes in the SS2 and 10× datasets, colored by identified populations. **c**, UMAP plots of oligodendrocytes in the SS2 dataset, colored by tissue, age and expression of selected marker genes. **d**, The 10× dataset oligodendrocyte UMAP plots colored by tissue and expression of selected marker genes. **e**–**f**, Boxplots of the age-related oligodendrocytes (ARO) (**e**) and interferon-responsive oligodendrocytes (IRO) (**f**) cluster proportions per sample, respectively. The central line denotes the median, boxes represent the IQR and whiskers show the distribution except for outliers. Outliers are all points outside 1.5× the IQR. Each dot represents a sample ($n = 20$ independent experiments) and significant results (scCODA model) are indicated with red bars. 24 m, 24-month-old; 3 m, 3-month-old. **g**, Heatmaps of average expression of differentially expressed genes, comparing the four oligodendrocyte populations. Gene sets were identified as differentially expressed markers for each population using the SS2 dataset. Values are normalized per gene, showing the gene expression across populations. Each column represents a gene. GO terms are shown below each set of genes (Supplementary Table 3). TNF, tumor necrosis factor. **h**, Violin plots showing selected IRO-enriched marker genes across SS2 and 10× datasets. a.u., arbitrary units representing the corrected log(1*P*) (counts) value.

gene 3 (*LAG-3*) and found that 40% of CD8$^+$ T cells were immunolabeled by antibodies against PD-1 and 32% of CD8$^+$ T cells by antibodies against *LAG-3* (Extended Data Fig. 5b,c).

As checkpoint molecules are known to control the function of T cells, we treated 18-month-old mice with antibodies against the coinhibitory receptors such as cytotoxic T-lymphocyte-associated protein

https://doi.org/10.1038/s41593-022-01183-6

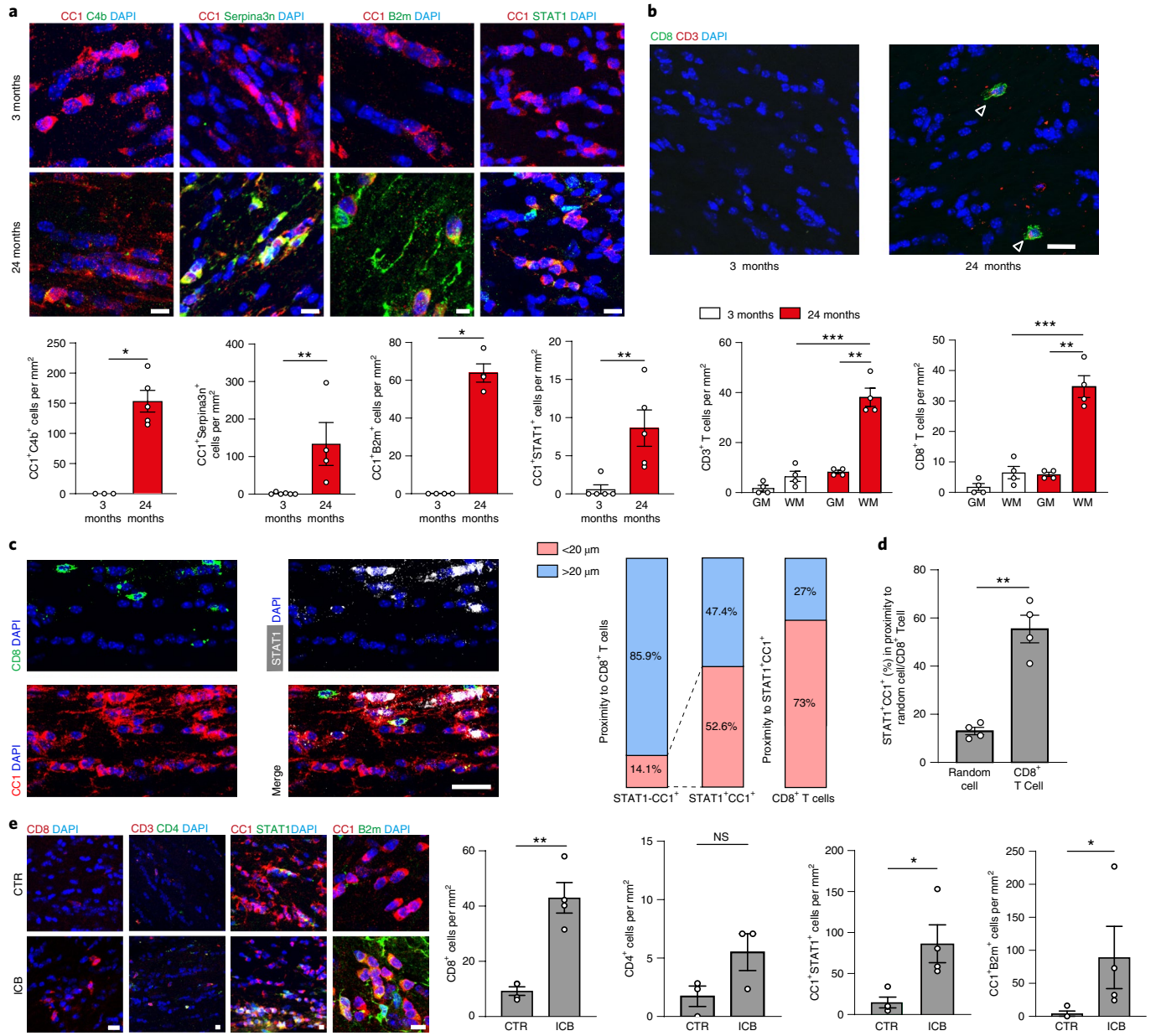

Fig. 2 | IFN-responsive oligodendrocytes localize to aged white matter close to CD8$^+$ T cells. a, Immunofluorescence staining and quantification of C4b, Serpina3n, B2m and STAT1 in CC1$^+$ oligodendrocytes in the white matter of 3- and 24-month-old mice (C4b$^+$CC1$^+$, 3-month, $n = 3$, 24-month, $n = 5$, $^*P = 0.0357$; Serpina3n$^+$CC1$^+$, 3-month, $n = 6$, 24-month, $n = 4$, $^{**}P = 0.0095$; B2m$^+$CC1$^+$, 3-month, $n = 4$, 24-month, $n = 4$, $^*P = 0.0286$; STAT1$^+$CC1$^+$, 3-month, $n = 5$, 24-month, $n = 5$, $^{**}P = 0.0079$; data are mean ± s.e.m.; *P* values are from a two-tailed Mann–Whitney *U*-test). Scale bar, 20 µm; for B2m, 10 µm. **b**, Immunofluorescence showing CD3$^+$CD8$^+$ T cells (indicated by arrowheads). Scale bar, 20 µm. Quantification of CD3$^+$ T cells and CD8$^+$ T cells in the gray (GM) and white (WM) matter of 3- and 24-month-old mice ($n = 4$ mice per group, 3-month WM versus 24-month WM, CD3$^+$, $^{***}P = 0.0003$, CD8$^+$, $^{***}P = 0.0005$; 24-month GM versus 24-month WM, CD3$^+$, $^{**}P = 0.0050$, CD8$^+$, $^{**}P = 0.0032$; data are mean ± s.e.m.; *P* values represent a two-sided Student's *t*-test). **c**, Immunofluorescence of CD8$^+$ T cells and STAT1$^+$CC1$^+$ oligodendrocytes in proximity in the white matter of 24-month-old mice. Scale bars, 20 µm. Bar plots show quantification of STAT1$^+$ and STAT1$^-$CC1$^+$ proximity to CD8$^+$ T cells and vice versa (3 sections per mouse were selected; a total of 134 CD8$^+$ T cells and 272 STAT1$^+$CC1$^+$ oligodendrocytes from 4 mice were analyzed). **d**, Quantification of the percentage of STAT1$^+$CC1$^+$ oligodendrocytes found in proximity to random cells compared with CD8$^+$ T cells ($n = 4$ mice per group, $^{**}P = 0.0052$; data are mean ± s.e.m; *P* value represents a two-sided paried Student's *t*-test). **e**, Immunofluorescence staining and quantification of CD8$^+$ T cells, CD4$^+$ T cells, B2m$^+$ and STAT1$^+$CC1$^+$ oligodendrocytes in the white matter of mice treated with anti-PD-1 and CTLA-4 (ICB) and isotype control antibodies (CTR) for 6 weeks starting at an age of 18 months (CD8$^+$, $n = 4$, $^{**}P = 0.0011$; CD4$^+$, $n = 3$; STAT1$^+$CC1$^+$, $n = 4$, $^*P = 0.0244$; B2m$^+$CC1$^+$, $n = 4$, $^*P = 0.0286$; data are mean ± s.e.m.; *P* values represent a two-sided Student's *t*-test (CD8$^+$, STAT1$^+$CC1$^+$) or two-tailed Mann–Whitney *U*-test (CD4$^+$, B2m$^+$CC1$^+$)). Scale bar, 20 µm. NS, not significant.

4 (CTLA-4) and PD-1 to determine the effect on oligodendrocytes. Immune checkpoint blockage therapy is used to dampen coinhibitory molecules to achieve robust anti-tumor immune response[37]. Treatment of mice with twice-weekly intraperitoneal injections with anti-PD-1 and anti-CTLA-4 antibodies for 6 weeks resulted in an increased number of CD8$^+$ T cells, but not CD4$^+$ T cells, in the white matter (Fig. 2e). In addition, the number of STAT1$^+$CC1$^+$ and B2M$^+$CC1$^+$ oligodendrocytes increased within the corpus callosum by checkpoint blockage

therapy (Fig. 2e). The formation of Serpina3n$^+$ oligodendrocytes was not induced by anti-PD-1/anti-CTLA-4 antibody treatment (Extended Data Fig. 6c).

To continue exploring the link between T cells and white matter aging, we performed three independent scRNA-seq experiments using the 10× platform on 24-month-old *Rag1*$^{-/-}$ mice, which lack functional lymphocytes. The *Rag1*$^{-/-}$ dataset integrated well with our 24-month-old wild-type 10× datasets, showing good batch mixing while still preserving biological variance (Fig. 3a and Extended Data Fig. 6a–c). The unsupervised clustering of T/natural killer (NK) cells showed that the number of *Cd3d*- and *Trbc2*-expressing T cells are significantly higher in the white matter of aged wild-type mice (Fig. 3b,c and Extended Data Fig. 6d). Unsupervised clustering of oligodendrocytes from the combined datasets showed again the same transcriptional clusters with *Stat1* and *H2-D1* expressing IROs and Serpina3n expressing age-related oligodendrocytes (Fig. 3d). The scCODA analysis showed a marked reduction of IROs in *Rag1*$^{-/-}$ mice (Fig. 3e). This finding was consistent with our immunolabeling experiments, which showed a reduction of IROs in *Rag1*$^{-/-}$ mice (Fig. 3f). Together, these data provide evidence that the adaptive immune system promotes IFN responses in oligodendrocytes in the aging white matter, but to what extent these changes contribute to white matter degeneration is unclear.

Next, we used correlated light and electron microscopy to detect areas of high IBA1$^+$ cell density by immunohistochemistry, followed by scanning electron microscopy to determine the ultrastructure of myelinated axons. This analysis uncovered focal areas of hypomyelination in the corpus callosum of 24-month-old mice close to the ventricular area (Extended Data Fig. 6e). To quantify the age-related decay, we determined the number of oligodendrocytes in the aging brain. First, we analyzed oligodendrocyte proportions by using the mouse aging single-cell transcriptomic atlas[36] and found that the oligodendrocyte significantly decreased in 24-month-old compared with 18- and 3-month-old mice (Extended Data Fig. 7d). Next, we used immunohistochemistry to quantify oligodendrocyte cell numbers in 12-, 18- and 24-month-old mice (Fig. 3g). We observed that the density of CC1$^+$ oligodendrocytes declined in the 24-month-old compared with the 12-month-old white matter, whereas no changes were observed in the aged gray matter (Fig. 3g). Similar results were obtained when glutathione *S*-transferase (GST-π) was used as an additional marker to stain for mature oligodendrocytes (Extended Data Fig. 7a,b). In addition, there was a decrease in Olig2$^+$ oligodendroglial cells, but not of Pdgfra$^+$ OPCs (Extended Data Fig. 7c). Next, we analyzed oligodendrocytes in *Rag1*$^{-/-}$ mice and found no differences in oligodendrocyte density compared with controls at 6 months in both gray and white matter (Extended Data Fig. 7e,f). However, when 24-month-old mice were analyzed, we detected a higher density of oligodendrocytes in the white matter of 24-month-old *Rag1*$^{-/-}$ compared with wild-type control mice (Fig. 3g).

As *Rag1*$^{-/-}$ mice lack various populations of mature adaptive immune cells, including CD4, CD8, gamma–delta and B cells, we used mice homozygous for the Cd8a^{tm1Mak}-targeted mutation (CD8$^{-/-}$) that specifically lacks functional CD8$^+$ T cells[23]. When we analyzed 24-month-old CD8$^{-/-}$ mice, we found a reduction of the number of STAT1$^+$CC1$^+$ oligodendrocytes compared with control wild-type mice (Fig. 3h). Next, we determined the density of CC1$^+$ oligodendrocytes and detected higher numbers of oligodendrocytes in 24-month-old CD8$^{-/-}$ mice compared with controls (Fig. 3i), confirming that CD8$^+$ T cells induce IFN responses and loss of oligodendrocytes.

CD8$^+$ T cells induce IFN-responsive microglia

As previous studies have identified IFN-responsive microglia in various models of neurodegenerative disease and during aging[15], we asked whether the adaptive immune system mediates IFN-responsive microglia conversion. Unsupervised clustering of 15,601 microglia from the aged white and gray matter of *Rag1*$^{-/-}$ and wild-type mice revealed distinct populations, including previously described homeostatic microglia, activated microglia, white matter-associated microglia and, in addition, a smaller population of IFN-responsive microglia (Fig. 4a). The IFN-responsive microglia subset was significantly enriched in aged white compared with gray matter and was reduced in aged *Rag1*$^{-/-}$ mice (Fig. 4a,b). INF-responsive microglia are characterized by the upregulation of IFN-stimulated genes *Stat1* and *Ifit3* (Fig. 4c,d). Gene ontology (GO) enrichment analysis showed that IFN-responsive microglia and oligodendrocytes share a transcriptional signature of IFN-induced genes including *Stat1*, *Ifit3*, *Usp18* and *Ifit27l2a* (Fig. 4e). GO enrichment analysis also detected differences with upregulated genes involved in antigen processing and positive regulation of T-cell-mediated cytotoxicity for IFN-responsive oligodendrocytes, lymphocyte chemotaxis and immune responses for IFN-responsive microglia.

To validate the presence of IFN-responsive microglia in the aged white matter, we costained IBA1$^+$ microglia by using antibodies against STAT1 and, in agreement with our scRNA-seq data, we detected STAT1$^+$IBA1$^+$ microglia in the white matter of 24-month-old mice (Fig. 4f). Notably, these cells were almost absent from the white matter of 3-month-old mice. Next, we studied the spatial relationship between STAT1$^+$IBA1$^+$ microglia and CD8$^+$ T cells in aging white matter and found that they were frequently in close proximity (<20 µm) (Fig. 5a). Our analysis showed that STAT1$^+$IBA1$^+$ microglia are significantly more often found in close proximity to CD8$^+$ T cells than randomly chosen DAPI$^+$ cells (Fig. 5b). To determine whether the formation of STAT1$^+$IBA1$^+$ microglia depends on the function of adaptive immune cells, we first analyzed the effect of the treatment of 18-month-old mice with antibodies against the coinhibitory receptors CTLA-4 and PD-1. The number of STAT1$^+$IBA1$^+$ microglia increased within the corpus callosum by checkpoint blockage therapy (Fig. 5c). Next, we analyzed the number of STAT1$^+$IBA1$^+$ microglia in the white matter of 24-month-old *Rag1*$^{-/-}$ mice, which revealed a reduction of STAT1$^+$IBA1$^+$

Fig. 3 | Absence of functional lymphocytes reduces IFN-responsive oligodendrocyte numbers and increases oligodendrocyte cell density in the aged white matter. a, UMAP plot of 44,983 single-cell transcriptomes, colored by major cell types. **b**, UMAP of T cells and NK cells, colored by T-cell identity, genotype and T-cell marker genes. **c**, Bar plot showing the relative distribution of each genotype-tissue experimental group within the T/NK cell population. **d**, UMAP plots of oligodendrocytes in the *Rag1*$^{-/-}$ and wild-type integrated dataset, colored by identified clusters, genotype and tissue annotation, as well as selected marker genes. **e**, Boxplot of the IRO cluster proportion per sample. The central line denotes the median, boxes represent the IQR and whiskers show the distribution except for outliers. Outliers are all points outside 1.5× the IQR. Each dot represents a sample ($n = 8$ independent experiments) and significant results (scCODA model) are indicated with red bars. **f**, Immunofluorescence staining and quantification of STAT1$^+$CC1$^+$ oligodendrocytes in the white matter of 24-month-old wild-type and 24-month-old *Rag1*$^{-/-}$ mice ($n = 5$ mice per group, $^*P = 0.0466$; data are mean ± s.e.m.; *P* values represent a two-sided Student's *t*-test). Scale bar, 20 µm. **g**, Immunofluorescence staining and quantification of CC1$^+$ oligodendrocyte density in the gray (GM) and white matter (WM) of 12-, 18- and 24-month-old wild-type and *Rag1*$^{-/-}$ mice (GM, $n = 3, 3, 5, 4$; WM, $n = 3, 3, 5, 4$; 12 months versus 24 months, $^*P = 0.0185$, 24-month versus 24-month *Rag1*$^{-/-}$, $^{**}P = 0.0083$; data are mean ± s.e.m.; *P* values represent two-sided, one-way ANOVA with post hoc Tukey's test). Scale bar, 20 µm. **h**, Immunofluorescence staining and quantification of CC1$^+$STAT1$^+$ oligodendrocytes in the white matter of 24-month-old wild-type and *CD8*$^{-/-}$ mice ($n = 4$ mice per group, $^{**}P = 0.0035$; data are mean ± s.e.m.; *P* value represents a two-sided Student's *t*-test). Scale bar, 20 µm. **i**, Immunofluorescence staining and quantification of CC1$^+$ oligodendrocyte density (red) in the white matter of 24-month-old wild-type and CD8$^{-/-}$ mice ($n = 4$ mice per group, $^*P = 0.0176$; data are mean ± s.e.m.; *P* value represents a two-sided Student's *t*-test). Scale bar, 20 µm.

https://doi.org/10.1038/s41593-022-01183-6

microglia number compared with control wild-type mice (Fig. 4f). Finally, we stained for STAT1^{+}IBA1^{+} microglia in aged CD8$^{-/-}$ mice. Again, 24-month-old mice deficient in functional CD8^{+} T cells had markedly lower numbers of STAT1^{+}IBA1^{+} microglia compared with control wild-type mice (Fig. 5d). Together, these data show that CD8^{+} T cells not only induce an IFN-responsive oligodendrocyte but also microglia state in the aged white matter.

As our previous work identified the age-dependent formation of white matter-associated microglia, engaged in clearing myelin debris[18], we asked whether these cells are required for lymphocyte-dependent

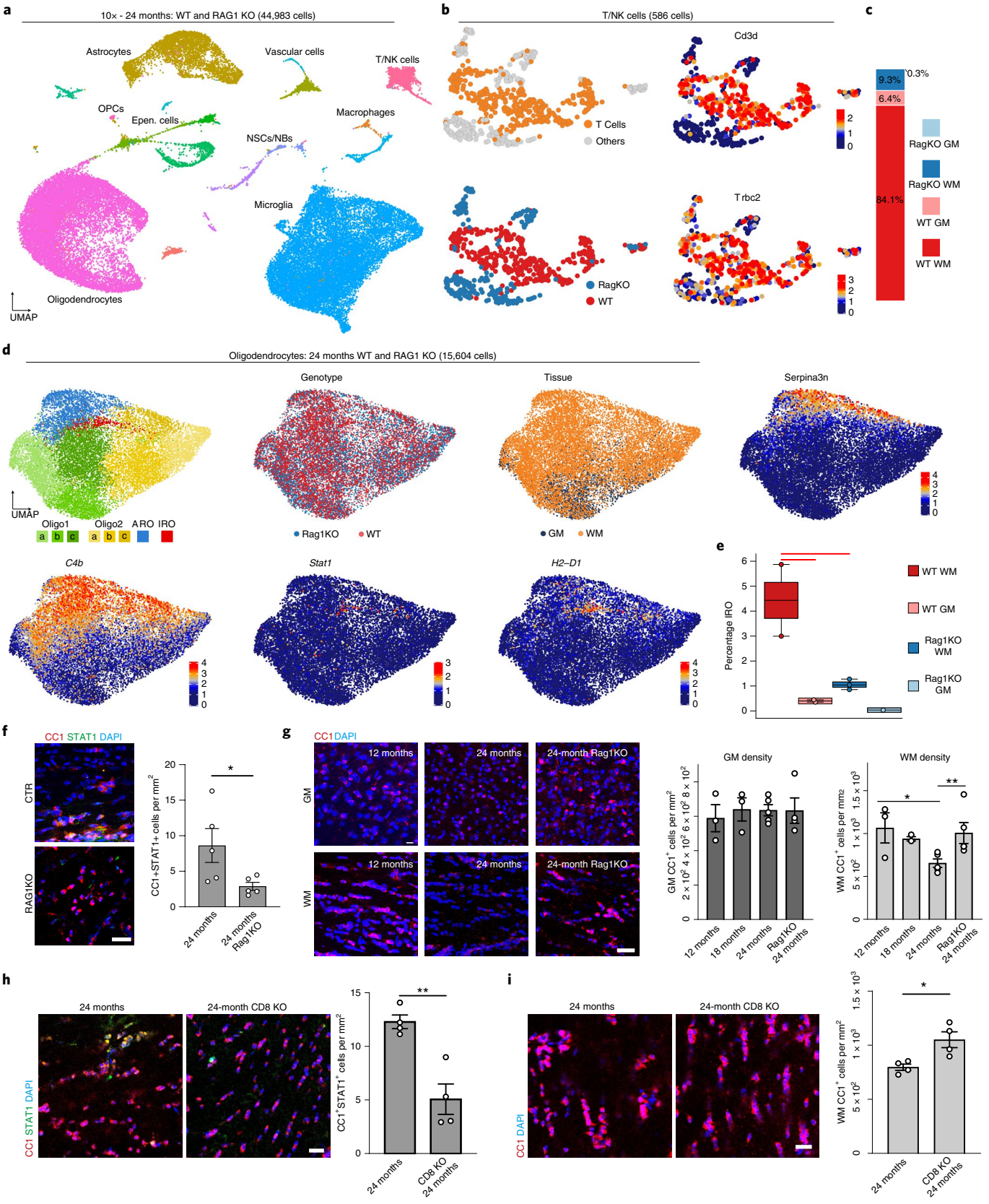

https://doi.org/10.1038/s41593-022-01183-6

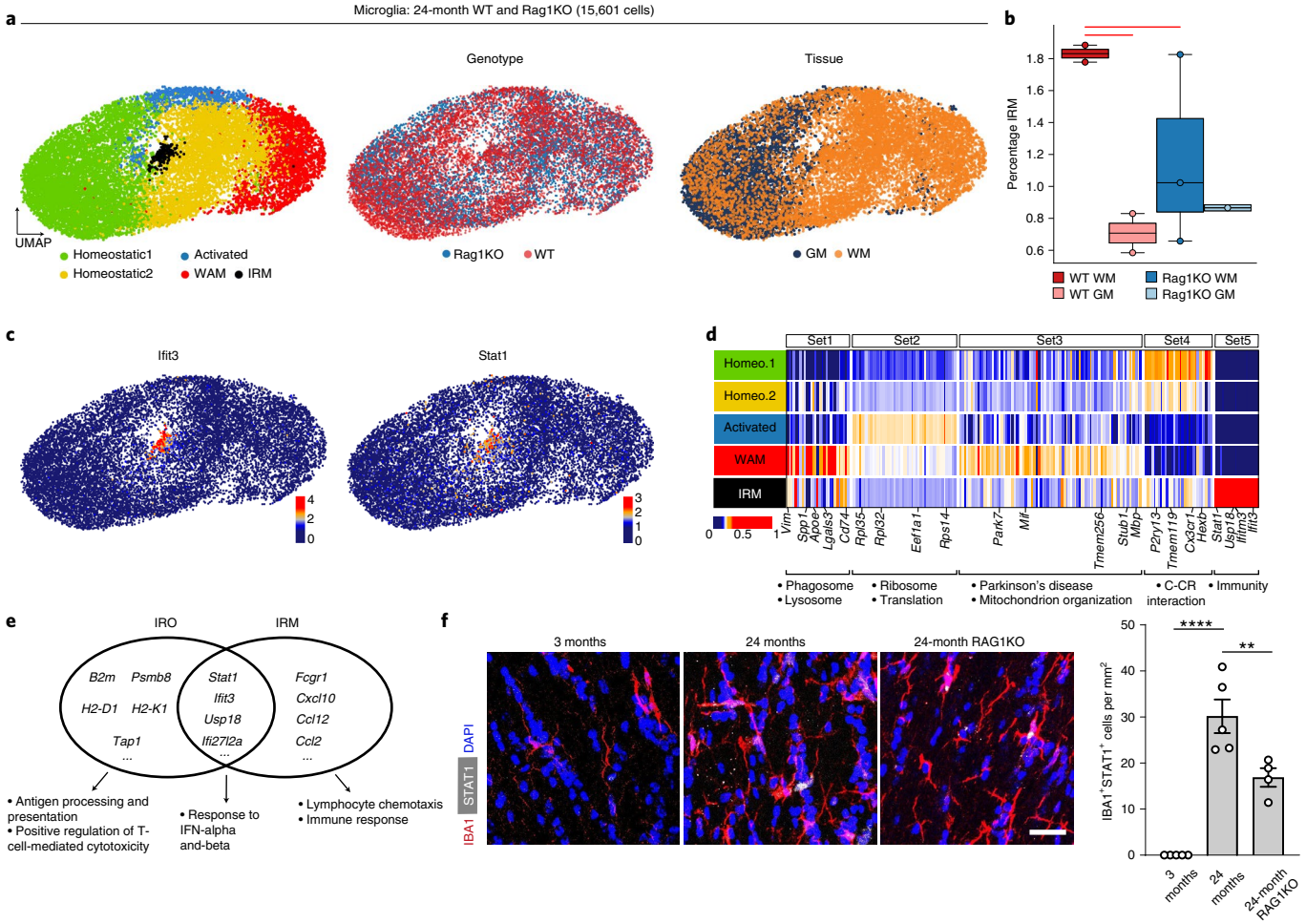

Fig. 4 | Identification of IFN-responsive microglia in aged white matter. a, UMAP plots of microglia colored by identified clusters, genotype and tissue annotation. **b**, Boxplot of the IRM cluster proportion per sample, respectively. WAM, White matter associated microglia; WT, Wild-type. The central line denotes the median, boxes represent the IQR and whiskers show the distribution except for outliers. Outliers are all points outside 1.5× the IQR. Each dot represents a sample ($n = 8$ independent experiments) and significant results (scCODA model) are indicated with red bars. **c**, UMAP plots of selected IRM marker genes. **d**, Heatmaps of average expression of differentially expressed genes, comparing the five microglia populations. Gene sets 1–4 were identified in Safaiyan et al.[18] and set 5 was identified by differential expression analysis of the IRM cluster. Values are normalized per gene, showing the gene expression across populations. Each column represents a gene. GO terms are shown below each set of genes. **e**, Venn diagram of top 50 differentially expressed genes of IRO and IRM clusters with an intersection set of 16 genes. Gene lists are found in Supplementary Table 3. **f**, Immunofluorescence staining and quantification of $STAT1^+IBA1^+$ microglia in the white matter of 3- and 24-month-old wild-type and 24-month-old *Rag1*$^{-/-}$ mice ($IBA1^+STAT1^+$, $n = 5,5,4$; 3 months versus 24 months, $^{***}P = 0.000002$: 24-month versus 24-month *Rag1*$^{-/-}$, $^{**}P = 0.0087$; data are mean ± s.e.m.; P value represents two-sided, one-way ANOVA with post hoc Tukey's test). Scale bar, 20 µm.

IFN responses in aged white matter. This seemed plausible because white matter-associated microglia are defined by the activation of genes implicated in phagocytic activity, antigen processing and presentation, and they also express MHC-I (Extended Data Fig. 8a,b) and are enriched in *Mbp* transcripts (Extended Data Fig. 8c,d), reminiscent of microglia containing myelin transcripts previously detected in the brains of patients with multiple sclerosis[38]. As the triggering receptor expressed on myeloid cell 2 (TREM2) is required for the formation of white matter-associated microglia[18], we analyzed *Trem2*$^{-/-}$ mice to determine possible differences in the formation of IFN-responsive oligodendrocytes and microglia.

However, when aged *Trem2*$^{-/-}$ mice were analyzed, we did not detect any significant differences in the number of $STAT1^+CC1^+$ oligodendrocytes or $STAT1^+IBA1^+$ microglia and also not in the proximity of $STAT1^+IBA1^+$ microglia to $CD8^+$ T cells, even if there was a lower number of $CD8^+$ T cells (Extended Data Fig. 8e–h), pointing to TREM2-independent mechanisms in the formation of IFN-responsive oligodendrocytes and microglia in aged white matter. However, aged *Trem2*$^{-/-}$ mice suffer from slightly degenerating white matter and seizures[18], which can cause innate immune reactions[39], making the interpretation of the data more difficult.

IFN-γ injection induces oligodendrocyte loss

Next, we performed experiments to determine the functional consequences of IFN on oligodendrocytes. Previous work has shown that $CD8^+$ cytotoxic T lymphocytes in the aged brain produce IFN-γ[35]. To assess the impact of IFN-γ on oligodendrocytes, we stereotactically injected 10 ng of IFN-γ into the white matter of 4- and 18-month-old mice, which was sufficient to induce $STAT1^+CC1^+$ oligodendrocytes (Extended Data Fig. 9a). Strikingly, when lesions were analyzed 48 h postinjection in 4- and 18-month-old mice, we found that the aged mice contained more $MAC2^+$ phagocytes loaded with myelin debris, displayed stronger reduction of $CC1^+$ oligodendrocytes and showed more pronounced demyelination with loss of myelin basic protein (MBP) and a reduction of neurofilament labeling (Fig. 6a–e and Extended Data Fig. 9c). Control vehicle injections in 18-month-old mice did not

https://doi.org/10.1038/s41593-022-01183-6

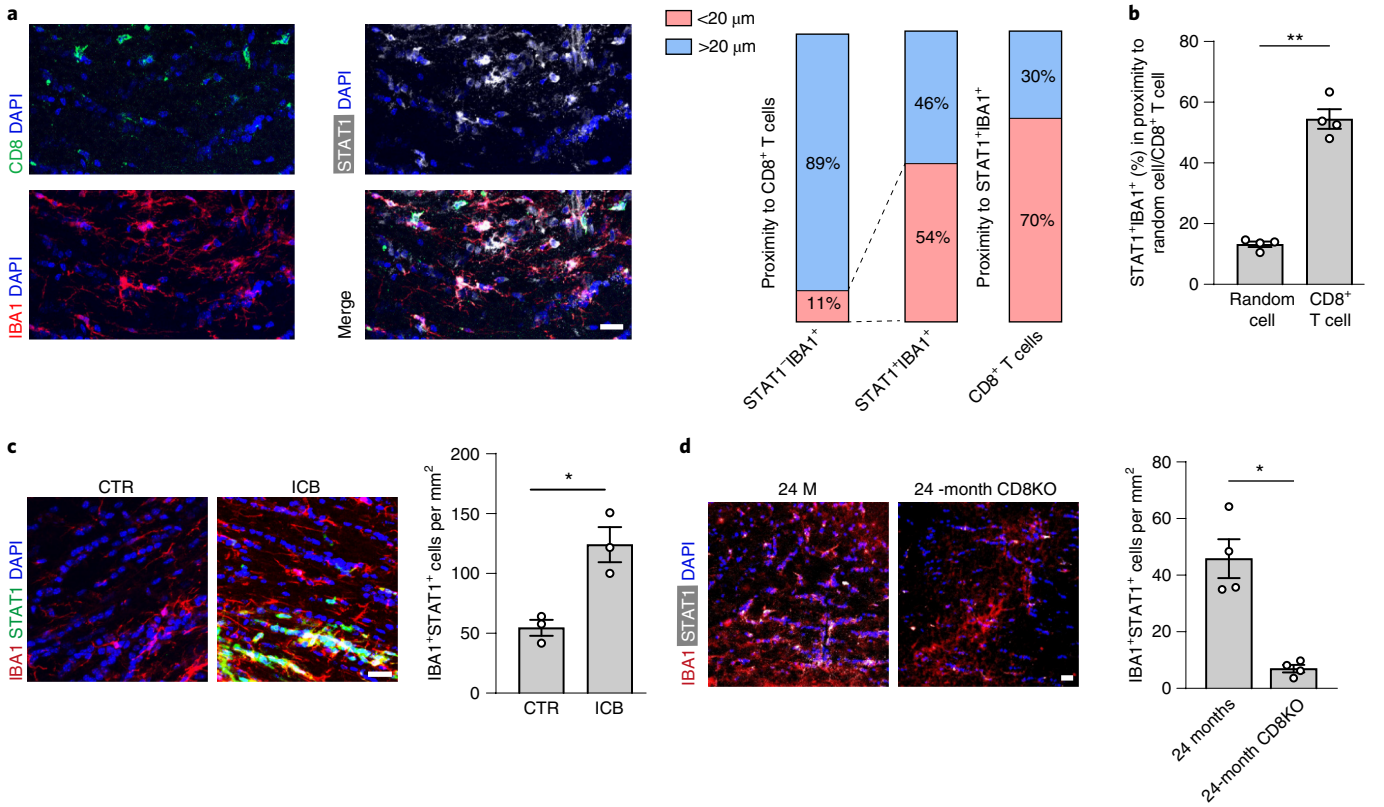

Fig. 5 | CD8$^+$ T cells induce an IFN-responsive microglia state in the aged white matter. a, Immunofluorescence staining and quantification of CD8$^+$ T cells (green) and STAT1$^+$IBA1$^+$ microglia proximity in the white matter of 24-month-old mice. Scale bars, 20 µm. Bar plots show quantification of STAT1$^+$ and STAT1$^-$IBA1$^+$ in proximity to CD8$^+$ T cells and vice versa (3 sections per mouse were selected, and a total of 117 CD8$^+$ T cells and 203 STAT1$^+$IBA1$^+$ microglia from 4 mice were analyzed). **b**, Quantification of the percentage of STAT1$^+$IBA1$^+$ microglia found in proximity to random cells compared with CD8$^+$ T cells ($n = 4$ mice per group, $^{**}P = 0.0052$; data are mean ± s.e.m.; P value represents a two-sided paired Student's t-test). **c**, Immunofluorescence staining and quantification of STAT1$^+$IBA1$^+$ microglia in the white matter of mice treated with anti-PD-1 and CTLA-4 (ICB) and isotype control antibodies (CTR) for 6 weeks starting at the age of 18 months ($n = 3$ mice per group, $^{*}P = 0.0125$; data are mean ± s.e.m.; P value represents a two-sided Student's t-test). Scale bar, 20 µm. **d**, Immunofluorescence staining and quantification of STAT1$^+$IBA1$^+$ microglia in the white matter of 24-month-old wild-type and 24-month-old *CD8*$^{-/-}$ mice ($n = 4$ mice per group, $^{*}P = 0.0223$; data are mean ± s.e.m.; P value represents a two-sided Student's t-test).

induce such lesions (Fig. 6f–h and Extended Data Fig. 9b). Previous studies have shown that IFN-γ can induce oligodendrocyte cell death in vitro and in vivo[40–42]. To directly determine the response of IFN-γ on oligodendrocytes, we treated primary cultures of mouse oligodendrocytes with IFN-γ. We used IFN-γ in concentrations that triggered STAT1 expression, to determine whether the induction was sufficient to induce cell death. Immunofluorescence analysis indicated that the STAT1$^+$ oligodendrocyte state did not affect cell viability in culture at this concentration (Fig. 6i). As IFN-γ is an important activator of microglia, we asked whether the cytotoxic effects of IFN-γ toward oligodendrocytes is mediated by microglia. Indeed, when oligodendrocytes were cocultured with microglia, a marked reduction of oligodendrocyte cell number was observed in the presence. but not in the absence, of IFN-γ (Fig. 6j). Thus, microglia can induce IFN-γ-mediated oligodendrocyte injury in vitro; however, other cells and mechanisms, such as direct CD8$^+$ T-lymphocyte-mediated cytotoxicity, might contribute to oligodendrocyte reactions during aging in vivo.

Discussion

White matter aging causes myelin degeneration, but how oligodendrocytes respond to aging is poorly defined. In the present study, we found that aging was associated with distinct oligodendrocyte responses, shown by the generation of a subpopulations of STAT1$^+$/B2M$^+$ and Serpina3n$^+$/C4b$^+$ oligodendrocytes and a reduction of oligodendrocyte density in aged white matter. We provided evidence that adaptive immune cells contributed to the cellular alterations that were associated with white matter aging. In both *Rag1*$^{-/-}$ and *CD8*$^{-/-}$ aged mice, the number of STAT1$^+$ oligodendrocytes decreased and the total density of oligodendrocytes increased to a similar extent, providing evidence that functional CD8$^+$ T cells are an important modifier of white matter aging. In addition, we identified a subpopulation of lymphocyte-dependent IFN-responsive microglia in aging white matter. These results show that adaptive immunity drives IFN-responsive cell states in aging white matter, but the exact link of CD8$^+$ T cells, microglia and oligodendrocytes remains to be established. Previous work has shown that CD8$^+$ T cells invading the aging brain exhibit high levels of IFN-γ, which drive IFN signaling within the neurogenic niche of the subventricular zone[35]. CD8$^+$ T-cell-derived IFN-γ may also induce IFN responses in oligodendrocytes and microglia, but the contribution of other IFNs cannot be excluded[43]. One possible scenario is the secretion of IFN-γ by CD8$^+$ T cells, which, in turn, polarizes microglia into an injurious phenotype. It is interesting to compare our results with a previous study using a viral model of encephalitis in mice, in which CD8$^+$ T-cell-derived IFN-γ triggers acute loss of axosomatic connections[44]. In this model, phagocytes activated by neurons, which have been stimulated by CD8$^+$ T-cell-derived IFN-γ triggers synapse loss[44]. Accordingly, it is conceivable that IFN-responsive oligodendrocytes actively recruit proinflammatory microglia as effector cells in aged white matter. Alternatively, CD8$^+$ T-lymphocyte cytotoxicity occurs in a cognate T-cell receptor- and granzyme B-dependent manner, as

https://doi.org/10.1038/s41593-022-01183-6

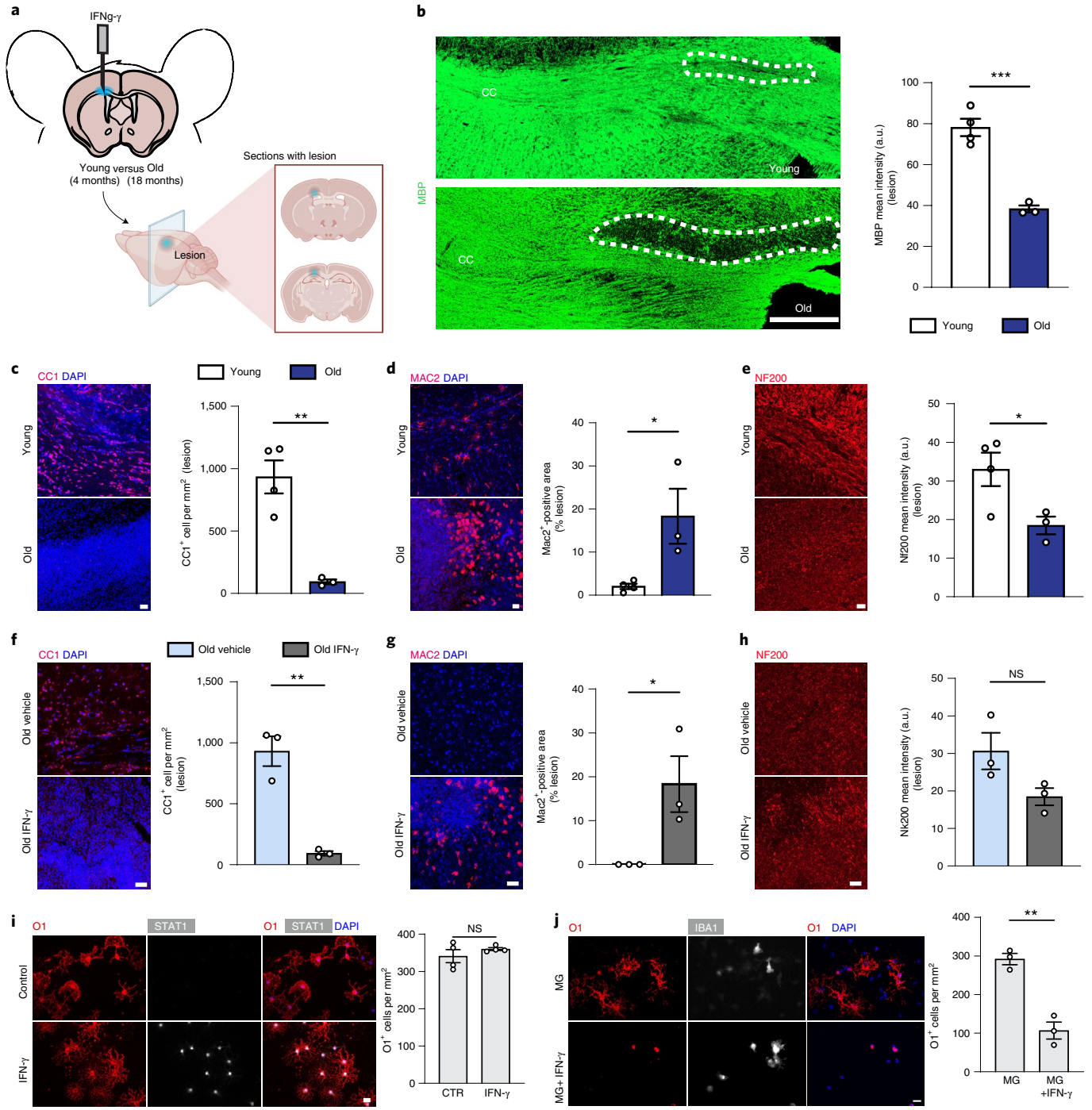

Fig. 6 | IFN-γ injections induce myelin and oligodendrocyte loss in aged mice. **a**, Diagram showing the model of IFN-γ injection in the corpus callosum (CC). The lesion area was identified by the positivity for monastral blue. **b**, Representative pictures of the CC after injection of 1 µl of a solution of 10 ng µl^{-1} of IFN-γ, 48 h postinjection. The intensity of the staining for MBP (green) was used to quantify the extent of demyelination (young, $n = 4$; old, $n = 3$; $^{***}P = 0.0006$; data are mean ± s.e.m.; P value represents a two-sided Student's t-test). a.u., arbitrary units. **c**–**e**, Representative confocal images and quantifications of IFN-γ-mediated lesions in young and old mice, showing CC1$^+$ oligodendrocytes (**c**), MAC2$^+$ microglia (**d**) and NF200$^+$ axons (**e**). The number of oligodendrocytes was expressed as number of cells per mm^2; the amount of phagocytes was expressed as percentage area of the lesion occupied by MAC2$^+$ cells; the extent of axonal damage was expressed as staining intensity of NF200 (young, $n = 4$; old, $n = 3$; CC1$^+$, $^{**}P = 0.0031$; MAC2$^+$, $^{*}P = 0.0291$; NF200$^+$, $^{*}P = 0.0451$; data are mean ± s.e.m.; P values represent a two-sided Student's t-test). Scale bar, 20 µm. **f**–**h**, Representative confocal images and quantifications of IFN-γ-mediated lesions in old mice and of the vehicle control showing CC1$^+$ oligodendrocytes (**f**), MAC2$^+$ cells (**g**) and NF200$^+$ axons (**h**) ($n = 3$ mice per group, CC1$^+$, $^{**}P = 0.0025$; MAC2$^+$, $^{*}P = 0.0451$; data are mean ± s.e.m.; P values represent a two-sided Student's t-test). **i**, Representative images of cultured oligodendrocytes (labeled for O1 in red and STAT1 in white) after treatment with IFN-γ for 24 h compared with control. Quantification of the number of oligodendrocytes after IFN-γ or vehicle treatment, expressed as number of O1$^+$ cells per mm^2 ($n = 4$ biological replicates per group, $^{**}P = 0.0022$; data are mean ± s.e.m.; P values represent a two-sided Student's t-test). **j**, Representative images of oligodendrocytes cultured with microglia alone (MG) or microglia together with IFN-γ (MG+IFN-γ) and stained for O1 (oligodendrocytes) and IBA1 (microglia). Quantification of the number of oligodendrocytes, expressed as number of O1$^+$ cells per mm^2 ($n = 4$ biological replicates per group, $^{**}P = 0.0022$; data are mean ± s.e.m.; P values represent a two-sided Student's t-test).

shown for axons in the optic nerve[34]. In this context, the age-related induction of Serpina3n$^+$ oligodendrocytes is of interest, because Serpina3n is an inhibitor of granzyme B that can dampen axon and myelin damage in autoimmune conditions[45]. Several studies have identified distinct populations of clonally expanded CD8$^+$ T cells expressing the checkpoint inhibitor PD-1 in aged mice and humans[35,46]. We found that treatment of mice with antibodies against the checkpoint receptors, CTLA-4 and PD-1, resulted in an increase in the number of CD8$^+$ T cells and IFN-responsive oligodendrocytes and microglia. These data could possibly explain why immune checkpoint inhibition in cancer causes behavioral and cognitive changes in some patients[47].

The temporal sequence and causality of pathological processes contributing to white matter aging need to be established. As the deep white matter areas lie at the ends of the arterial circulation, they are particularly susceptible to decreases in blood flow and oxygenation, possibly contributing to increased vulnerability of aged white matter to hypoperfusion and aging-induced leaky blood–brain barrier[48,49]. Progressive vascular damage, induced by injury to myelinated fibers, may promote the infiltration of CD8$^+$ T cells, thereby triggering harmful immune reactivity toward microglia and oligodendrocytes. A key question that remains to be established is how CD8$^+$ T cells enter the brain and whether antigen recognition is necessary for this process. The clonal expansion of CD8$^+$ T cells in aging provides evidence that they actively recognize antigen(s)[34,35]. It is unclear why CD8$^+$ T cells migrate specifically to the central nervous system white matter. It is possible that they are attracted by myelin self-antigens, reminiscent of the T cells found in multiple sclerosis. The long-lived myelin proteins and lipids may accumulate oxidation and posttranslational modifications during aging that lead to their recognition as neoantigens when presented to T cells. Proof of principle that oligodendrocyte pathology can trigger adaptive autoimmune responses against myelin has been provided in a model of oligodendrocyte ablation[50]. However, passive mechanisms such as age-related changes in the migration of CD8$^+$ T across a leaky blood–brain barrier, dural sinuses or choroid plexus are also conceivable. In addition, it remains to be clarified whether CD8$^+$ T cells produce IFN-γ in the aging white matter, as has been shown for the stem cell niches of aging mice[35].

Previous work has shown that oligodendrocytes are particularly sensitive to IFN-γ, because it can trigger oligodendroglial cell death and demyelination[40–42]. Strikingly, we find that this effect is highly pronounced in the aged brain, in which IFN-γ potently induces loss of oligodendrocytes and demyelinating injury. Possibly, the aging brain is primed toward IFN-γ due to age-associated, chronic, low-grade inflammation, so-called 'inflammaging'[51]. Notably, OPCs respond to IFN-γ by inducing the antigen presentation pathway to activate T cells, which in turn can kill the OPCs as their target cells[28,30]. Immune responses in the aging brain are not limited to oligodendrocyte-lineage cells and myelinated axons. Previous work has shown T-cell infiltration in the aged brain, where the T cells impair the function of neuronal stem cells within the neurogenic niche[35,52,53]. Intriguingly, proliferation of neural stem cells was inhibited by IFN-γ, which was secreted from CD8$^+$ T cells[35]. This mechanism is likely to be of functional relevance for the oligodendroglial lineage, because aging is not only associated with myelin degeneration but also with insufficient myelin renewal, a result of reduced capacity of OPCs to proliferate and differentiate[3,4,10,54,55]. Indeed, we found that myelin degeneration was not associated with an increase in OPC numbers in the aging brain.

As aging is the biggest factor for the most prevalent neurodegenerative diseases, it will be interesting to understand how the cellular alterations that occur in the white matter intermix with the pathology of these disorders. White matter changes and myelin alterations have been detected in Alzheimer's disease and its mouse models[18,56,57], which may contribute to disease pathology, including TREM2-dependent DAM signaling[16,17]; however, TREM2-independent glial responses have also been described[27,58]. As our previous work identified TREM2- and age-dependent, white matter-associated microglial responses, we analyzed the TREM2 dependence of IFN-responsive microglia but found instead a role of CD8$^+$ T cells.

Our data emphasize the contribution of CD8$^+$ T cells in triggering IFN-responsive cell states in the aging white matter, but it is likely that additional mechanisms contribute. In particular, prolonged exposure of nucleic acids to pattern-recognition, immune-sensing receptors can lead to inappropriate type I IFN release[59]. It is interesting that Aicardi–Goutieres syndrome, a prototype of an inherited disease with abnormal nucleic acid sensing and IFN induction, is associated with white matter pathology[59]. Likewise, deletion of ubiquitin-specific protease 18, a protein that negatively regulates STAT1 signaling, causes fatal activation of white matter microglia and myelin pathology[60,61]. Due to the extensive crosstalk between type 1 and type 2 IFN signaling pathways, future studies need to address their specific contribution within the different cell types during white matter aging.

Although the exact communication across CD8$^+$ T cells, microglia and oligodendrocytes and the link to IFN signaling remain to be established, these results support the hypothesis that cytotoxic CD8$^+$ T cells contribute to age-associated white matter decay.

Online content

Any methods, additional references, Nature Research reporting summaries, source data, extended data, supplementary information, acknowledgements, peer review information; details of author contributions and competing interests; and statements of data and code availability are available at https://doi.org/10.1038/s41593-022-01183-6.

References

1. Hou, Y. et al. Ageing as a risk factor for neurodegenerative disease. *Nat. Rev. Neurol.* **15**, 565–581 (2019).
2. Stadelmann, C., Timmler, S., Barrantes-Freer, A. & Simons, M. Myelin in the central nervous system: structure, function, and pathology. *Physiol. Rev.* **99**, 1381–1431 (2019).
3. Hughes, E. G., Orthmann-Murphy, J. L., Langseth, A. J. & Bergles, D. E. Myelin remodeling through experience-dependent oligodendrogenesis in the adult somatosensory cortex. *Nat. Neurosci.* https://doi.org/10.1038/s41593-018-0121-5 (2018).
4. Hill, R. A., Li, A. M. & Grutzendler, J. Lifelong cortical myelin plasticity and age-related degeneration in the live mammalian brain. *Nat. Neurosci.* https://doi.org/10.1038/s41593-018-0120-6 (2018).
5. Fard, M. K. et al. BCAS1 expression defines a population of early myelinating oligodendrocytes in multiple sclerosis lesions. *Sci. Transl. Med.* https://doi.org/10.1126/scitranslmed.aam7816 (2017).
6. Prins, N. D. & Scheltens, P. White matter hyperintensities, cognitive impairment and dementia: an update. *Nat. Rev. Neurol.* **11**, 157–165 (2015).
7. Sowell, E. R. et al. Mapping cortical change across the human life span. *Nat. Neurosci.* **6**, 309–315 (2003).
8. Bethlehem, R. A. I. et al. Brain charts for the human lifespan. *Nature* **604**, 525–533 (2022).
9. Brouwer, R. M. et al. Genetic variants associated with longitudinal changes in brain structure across the lifespan. *Nat. Neurosci.* **25**, 421–432 (2022).
10. Wang, F. et al. Myelin degeneration and diminished myelin renewal contribute to age-related deficits in memory. *Nat. Neurosci.* https://doi.org/10.1038/s41593-020-0588-8 (2020).
11. Pan, S., Mayoral, S. R., Choi, H. S., Chan, J. R. & Kheirbek, M. A. Preservation of a remote fear memory requires new myelin formation. *Nat. Neurosci.* https://doi.org/10.1038/s41593-019-0582-1 (2020).
12. Steadman, P. E. et al. Disruption of oligodendrogenesis impairs memory consolidation in adult mice. *Neuron* **105**, 150–164.e156 (2020).

13. Safaiyan, S. et al. Age-related myelin degradation burdens the clearance function of microglia during aging. *Nat. Neurosci.* **19**, 995–998 (2016).
14. Peters, A. The effects of normal aging on myelin and nerve fibers: a review. *J. Neurocytol.* **31**, 581–593 (2002).
15. Sala Frigerio, C. et al. The major risk factors for Alzheimer's disease: age, sex, and genes modulate the microglia response to abeta plaques. *Cell Rep.* **27**, 1293–1306.e1296 (2019).
16. Krasemann, S. et al. The TREM2-APOE pathway drives the transcriptional phenotype of dysfunctional microglia in neurodegenerative diseases. *Immunity* **47**, 566–581.e569 (2017).
17. Keren-Shaul, H. et al. A unique microglia type associated with restricting development of Alzheimer's disease. *Cell* **169**, 1276–1290.e1217 (2017).
18. Safaiyan, S. et al. White matter aging drives microglial diversity. *Neuron* **109**, 1100–1117.e1110 (2021).
19. Ximerakis, M. et al. Single-cell transcriptomic profiling of the aging mouse brain. *Nat. Neurosci.* **22**, 1696–1708 (2019).
20. Hammond, T. R. et al. Single-cell RNA sequencing of microglia throughout the mouse lifespan and in the injured brain reveals complex cell-state changes. *Immunity* **50**, 253–271.e256 (2019).
21. Friedman, B. A. et al. Diverse brain myeloid expression profiles reveal distinct microglial activation states and aspects of Alzheimer's disease not evident in mouse models. *Cell Rep.* **22**, 832–847 (2018).
22. Mombaerts, P. et al. RAG-1-deficient mice have no mature B and T lymphocytes. *Cell* **68**, 869–877 (1992).
23. Fung-Leung, W. P. et al. CD8 is needed for development of cytotoxic T cells but not helper T cells. *Cell* **65**, 443–449 (1991).
24. Fullgrabe, A. et al. Guidelines for reporting single-cell RNA-seq experiments. *Nat. Biotechnol.* **38**, 1384–1386 (2020).
25. Percie du Sert, N. et al. The ARRIVE guidelines 2.0: updated guidelines for reporting animal research. *PLoS Biol.* **18**, e3000410 (2020).
26. Marques, S. et al. Oligodendrocyte heterogeneity in the mouse juvenile and adult central nervous system. *Science* **352**, 1326–1329 (2016).
27. Zhou, Y. et al. Human and mouse single-nucleus transcriptomics reveal TREM2-dependent and TREM2-independent cellular responses in Alzheimer's disease. *Nat. Med.* **26**, 131–142 (2020).
28. Kirby, L. et al. Oligodendrocyte precursor cells present antigen and are cytotoxic targets in inflammatory demyelination. *Nat. Commun.* **10**, 3887 (2019).
29. Jakel, S. et al. Altered human oligodendrocyte heterogeneity in multiple sclerosis. *Nature* **566**, 543–547 (2019).
30. Falcao, A. M. et al. Disease-specific oligodendrocyte lineage cells arise in multiple sclerosis. *Nat. Med.* **24**, 1837–1844 (2018).
31. Mathys, H. et al. Single-cell transcriptomic analysis of Alzheimer's disease. *Nature* **570**, 332–337 (2019).
32. Kenigsbuch et al. A shared disease-associated oligodendrocyte signature among multiple CNS pathologies. *Nat. Neurosci*. https://doi.org/10.1038/s41593-022-01104-7 (2022).
33. Buttner, M., Ostner, J., Muller, C. L., Theis, F. J. & Schubert, B. scCODA is a Bayesian model for compositional single-cell data analysis. *Nat. Commun.* **12**, 6876 (2021).
34. Groh, J. et al. Accumulation of cytotoxic T cells in the aged CNS leads to axon degeneration and contributes to cognitive and motor decline. *Nat. Aging* **1**, 357–367 (2021).
35. Dulken, B. W. et al. Single-cell analysis reveals T cell infiltration in old neurogenic niches. *Nature* **571**, 205–210 (2019).
36. Tabula Muris, C. A single-cell transcriptomic atlas characterizes ageing tissues in the mouse. *Nature* **583**, 590–595 (2020).
37. Wei, S. C., Duffy, C. R. & Allison, J. P. Fundamental mechanisms of immune checkpoint blockade therapy. *Cancer Discov.* **8**, 1069–1086 (2018).
38. Schirmer, L. et al. Neuronal vulnerability and multilineage diversity in multiple sclerosis. *Nature* **573**, 75–82 (2019).
39. Turrin, N. P. & Rivest, S. Innate immune reaction in response to seizures: implications for the neuropathology associated with epilepsy. *Neurobiol. Dis.* **16**, 321–334 (2004).
40. Horwitz, M. S., Evans, C. F., McGavern, D. B., Rodriguez, M. & Oldstone, M. B. A. Primary demyelination in transgenic mice expressing interferon-γ. *Nat. Med.* **3**, 1037–1041 (1997).
41. Corbin, J. G. et al. Targeted CNS expression of interferon-gamma in transgenic mice leads to hypomyelination, reactive gliosis, and abnormal cerebellar development. *Mol. Cell Neurosci.* **7**, 354–370 (1996).
42. Vartanian, T., Li, Y., Zhao, M. & Stefansson, K. Interferon-gamma-induced oligodendrocyte cell death: implications for the pathogenesis of multiple sclerosis. *Mol. Med.* **1**, 732–743 (1995).
43. Baruch, K. et al. Aging. Aging-induced type I interferon response at the choroid plexus negatively affects brain function. *Science* **346**, 89–93 (2014).
44. Di Liberto, G. et al. Neurons under t cell attack coordinate phagocyte-mediated synaptic stripping. *Cell* **175**, 458–471.e419 (2018).
45. Haile, Y. et al. Granzyme B-inhibitor serpina3n induces neuroprotection in vitro and in vivo. *J. Neuroinflammation* **12**, 157 (2015).
46. Gate, D. et al. Clonally expanded CD8 T cells patrol the cerebrospinal fluid in Alzheimer's disease. *Nature* **577**, 399–404 (2020).
47. Hottinger, A. F. Neurologic complications of immune checkpoint inhibitors. *Curr. Opin. Neurol.* **29**, 806–812 (2016).
48. Joutel, A. Prospects for diminishing the impact of nonamyloid small-vessel diseases of the brain. *Annu. Rev. Pharmacol. Toxicol.* **60**, 437–456 (2020).
49. Montagne, A. et al. Blood–brain barrier breakdown in the aging human hippocampus. *Neuron* **85**, 296–302 (2015).
50. Traka, M., Podojil, J. R., McCarthy, D. P., Miller, S. D. & Popko, B. Oligodendrocyte death results in immune-mediated CNS demyelination. *Nat. Neurosci.* **19**, 65–74 (2016).
51. Franceschi, C., Garagnani, P., Parini, P., Giuliani, C. & Santoro, A. Inflammaging: a new immune–metabolic viewpoint for age-related diseases. *Nat. Rev. Endocrinol.* **14**, 576–590 (2018).
52. Kalamakis, G. et al. Quiescence modulates stem cell maintenance and regenerative capacity in the aging brain. *Cell* **176**, 1407–1419. e1414 (2019).
53. Buckley, M. T. et al. Cell type-specific aging clocks to quantify aging and rejuvenation in regenerative regions of the brain. Preprint at *bioRxiv* https://doi.org/10.1101/2022.01.10.475747 (2022).
54. Neumann, B. et al. Metformin restores CNS remyelination capacity by rejuvenating aged stem cells. *Cell Stem Cell* **25**, 473–485.e478 (2019).
55. Young, K. M. et al. Oligodendrocyte dynamics in the healthy adult CNS: evidence for myelin remodeling. *Neuron* **77**, 873–885 (2013).
56. Chen, J. F. et al. Enhancing myelin renewal reverses cognitive dysfunction in a murine model of Alzheimer's disease. *Neuron* **109**, 2292–2307.e2295 (2021).
57. Nasrabady, S. E., Rizvi, B., Goldman, J. E. & Brickman, A. M. White matter changes in Alzheimer's disease: a focus on myelin and oligodendrocytes. *Acta Neuropathol. Commun.* **6**, 22 (2018).
58. Lee, S. H. et al. TREM2-independent oligodendrocyte, astrocyte, and T cell responses to tau and amyloid pathology in mouse models of Alzheimer disease. *Cell Rep.* **37**, 110158 (2021).
59. Crow, Y. J. & Manel, N. Aicardi–Goutieres syndrome and the type I interferonopathies. *Nat. Rev. Immunol.* **15**, 429–440 (2015).

60. Goldmann, T. et al. USP18 lack in microglia causes destructive interferonopathy of the mouse brain. *EMBO J.* **34**, 1612–1629 (2015).
61. Schwabenland, M. et al. Loss of USP18 in microglia induces white matter pathology. *Acta Neuropathol. Commun.* **7**, 106 (2019).

Methods

Animals

The mouse lines used in the present study are the following: wild-type C57BL/6J mice were from Janvier Labs; *Trem2*$^{-/-}$ mice[62] on the C57BL/6J background were kindly provided by C. Haass, Laboratory of Neurodegenerative Disease Research, German Center for Neurodegenerative Diseases (DZNE), Munich; *Rag1*$^{-/-}$ (B6.129S7-Rag1tm1Mom/J)[22] and *Cd8*$^{-/-}$ mice (B6.129S2-Cd8atm1Mak/J)[23] and wild-type controls were on the C57BL/6J background. Experiments were performed with young, adult and aged mice (aged 3, 12, 18 and 24 months) as indicated in the figures and legends. Only aged mice that were on inspection healthy were used for experiments. Animals were randomly assigned to the different groups. Treatment with antibodies against PD-1 and CTLA-4 and their respective isotype controls was performed in 18-month-old mice; mice were injected intraperitoneally with a mix of both antibodies of concentration 10 mg kg^{-1} (PD-1) and 20 mg kg^{-1} (CTLA-4) twice a week for 6 weeks in total. All animal experiments were reviewed and overseen by the institutional animal use and care committee of the DZNE in Munich and the University Hospital in Würzburg. All animals were free from the most common mouse viral pathogens, ectoparasites, endoparasites and mouse bacterial pathogens harbored in research animals. The battery of screened infective agents met the standard health profile established in the animal facility in the DZNE animal housing facility. The mice were kept in groups in Greenline IVC GM500 plastic cages and were housed in a temperature-controlled environment (21 ± 2 °C) on a 12 h light:dark cycle with standard chow and water freely available. Water was provided in a water bottle, which was changed weekly. Cages were changed every week.

Mice perfusion and cell isolation for Smart-seq2

Four young (3-month-old) and four old (24-month-old) male C57BL/6J mice were deeply anesthetized and perfused with cold phosphate-buffered saline (PBS; Sigma-Aldrich, catalog no. D8537). Each brain was carefully removed and individually microdissected under a dissection microscope; gray matter was isolated from the frontal cortex and white matter was carefully isolated from the optic tract, medial lemniscus and corpus callosum (attached gray matter and choroid plexus were removed). We used our previously established isolation protocol[63] using gentleMACS with the Neural Tissue Dissociation Kit (Papain; Miltenyi Biotec) and a final concentration of 45 mM actinomycin D (Act-D, Sigma-Aldrich, catalog no. A1410). Subsequently, cells were blocked with mouse FcR-blocking reagent (CD16/CD32 Monoclonal Antibody, eBioscience, catalog no. 14-0161-82,1100), stained with antibodies against CD11b (PE/Cy7, M1/70, eBioscience, catalog no. 48-0451-82, 1:200) and afterward washed with PBS. Before sorting, the cell suspensions were stained by the live/dead marker SYTOX Blue (final concentration 1 µM). Viable (SYTOX Blue-negative) nonmyeloid single cells (CD11b^{-} cells) were sorted by flow cytometry (Sony, catalog no. SH800). Single cells were sorted into 96-well plates filled with 4 ml of lysis buffer containing 0.05% Triton X-100 (Sigma-Aldrich) and ERCC (External RNA Controls Consortium) RNA spike-in Mix (Ambion, Life Technologies; 1:24,000,000 dilution), 2.5 mM oligo(dT), 2.5 mM dNTP and 2 U ml^{-1} of recombinant RNase inhibitor (Clontech), then spun down and frozen at −80 °C. Plates were thawed and libraries prepared as described below.

Library preparation for Smart-seq2

The 96-well plates containing the sorted single cells were first thawed and then incubated for 3 min at 72 °C and thereafter immediately placed on ice. To perform reverse transcription (RT) we added to each well a mix of 0.59 µl of H_2O, 0.5 µl of SMARTScribe Reverse Transcriptase (Clontech), 2 µl of 5× First Strand buffer, 0.25 µl of Recombinant RNase Inhibitor (Clontech), 2 µl of Betaine (5 M Sigma), 0.5 µl of dithiothreitol (100 mM), 0.06 µl of $MgCl_2$ (1 M, Sigma-Aldrich) and 0.1 µl of template-switching oligos (TSOs) (100 µM, AAGCAGTGGTATCAACGCAGAGTACrGrG + G). Next, RT reaction mixes were incubated at 42 °C for 90 min, followed by 70 °C for 5 min and 10 cycles of 50 °C for 2 min and 42 °C for 2 min, finally ending with 70 °C for 5 min for enzyme inactivation. Preamplification of complementary DNA was performed by adding 12.5 µl of KAPA HiFi Hotstart 2× (KAPA Biosystems), 2.138 µl of H_2O, 0.25 µl of ISPCR primers (10 µM, 5′-AAGCAGTGGTATCAACGCAGAGT-3′) and 0.1125 µl of lambda exonuclease under the following conditions: 37 °C for 30 min, 95 °C for 3 min, 23 cycles of 98 °C for 20 s, 67 °C for 15 s and 72 °C for 4 min, and a final extension at 72 °C for 5 min. Libraries were then cleaned using AMPure bead (Beckman-Coulter) clean-up at a 0.7:1 beads:PCR product ratio. Libraries were assessed using Bio-analyzer (Agilent, catalog no. 2100), using the High Sensitivity DNA analysis kit, and also fluorometrically using Qubit's DNA HS assay kits and a Qubit 4.0 Fluorometer (Invitrogen, Life Technologies) to measure the DNA concentrations. Further selection of samples was performed via quantitative PCR assay against ubiquitin transcript Ubb77 (primer 1 5′-GGAGAGTCCATCGTGGTTATTT-3′; primer 2 5′-ACCTCTAGGGTGATGGTCTT-3′; probe 5′-/5Cy5/TGCAGATCTTCGTGAAGACCTGAC/3IAbRQSp/−3′) measured on a LightCycler 480 Instrument II (Roche). Samples were normalized to 160 pg µl^{-1}. Sequencing libraries were constructed using in-house-produced Tn5 transposase33. Libraries were barcoded and pooled then underwent three rounds of AMPure bead (Beckman-Coulter) clean-up at a 0.8:1 ratio beads:library. Libraries were sequenced 2× 150 reads bp paired-end on Illumina HiSeq4000 to a depth of 3 × 105–4 × 105 reads per sample.

Processing, quality control and analyses of Smart-seq2 scRNA-seq data

BCL files were demultiplexed with the bcl2fastq software from Illumina. After quality control with FastQC, reads were aligned using rnaSTAR[64] to the GRCm38 (mm10) genome with ERCC synthetic RNA added. Read counts were collected using the parameter 'quantMode GeneCounts' of rnaSTAR and the unstranded values. Quantitative criteria were used to filter out low-quality cells as shown in Extended Data Fig. 1b. We observed the distribution of all samples for each quality metrics and defined thresholds to remove outliers or samples with abnormal values. In the same order as in Extended Data Fig. 1b, we considered the number of reads per sample (≥20,000 and ≤4 × 10^6), the number of genes per sample (≥1,000 and ≤6,500), the average sequence read length after trimming (≥180 and ≤200), the mismatch rate during alignment (≥0.15 and ≤0.5), the percentage of uniquely mapped reads (≥68 and ≤100), the percentage of multimapped reads (≥2.3 and ≤7.7), the percentage of reads considered too short (≥0 and ≤17), the percentage of ERCCs (≥0 and ≤0.011) and the percentage of mitochondrial genes (≥0 and ≤0.006). From 2,650 single cells, 2,538 passed quality control. From that point, Seurat v.3.2.3R package was utilized[65]. Gene expressions were normalized using the SCTransform function (3,000 variable features) within Seurat. The first eight PCs were selected based on the elbow plot and heatmap of PC embeddings and used for downstream analysis steps. Cell-type clusters were identified using the Louvain algorithm and annotated by canonical cell-type markers (Extended Data Fig. 1c,d). Oligodendrocytes (2,413 single cells) were extracted and analyzed separately. After processing with SCTransform (2,000 variable features), the first 10 PCs were considered for downstream analyses. Unbiased clustering was performed using the Louvain algorithm that led to the identification of the four aforementioned oligodendrocyte populations. Gene sets of clusters 1, 2, 3 and 4 were defined by using the FindMarkers function with a threshold of avg_log$_2$(fold-change) (avg_log$_2$(FC)) > 1 (Fig. 1g). GO analyses were performed with the DAVID annotation tool[66], STRING[67] and Metascape[68].

Mice perfusion and cell isolation for 10× genomic experiments

For 10× genomic experiments, mice were deeply anesthetized and perfused with cold PBS. Each brain was removed, individually

microdissected under a dissection microscope and dissociated in the same way as described above (10× mice information is provided in Supplementary Table 2). To collect enough cells for loading on to the 10× Genomics Chromium chip, two gray matter/white matter tissue samples were combined into one sample. After tissue dissociation, SYTOX Blue-negative cells were sorted into a 2-ml Eppendorf tube with 1 ml of RPMI + 5% fetal bovine serum (FBS). Sorted cells were centrifuged at 300*g* for 10 min at 4 °C. Cell pellets were resuspended in 0.04% bovine serum albumin (BSA) + PBS catching medium at a concentration of 700–900 cells per µl.

Library preparation for 10× genomic experiments

Single-cell suspensions were loaded on to the Chromium Single Cell Controller using the Chromium Single Cell 3′ Library & Gel Bead Kit v.3.1 (10× Genomics) chemistry following the manufacturer's instructions. Sample processing and library preparation were performed according to the manufacturer's instructions using AMPure beads (Beckman-Coulter). Libraries were sequenced on the DNBSEQ Sequencing System (BGI group).

Preprocessing and analyses of 10× data

Fastq files were processed with Cell Ranger v.3.0.2 (wild-type aging), 4.0.0 (Rag1KO 1st batch) and 6.1.2 (Rag1KO 2nd batch). From that point, the Seurat v.3.2.3R package[65] was used for downstream analyses. Unless stated otherwise, all gene expression matrices were filtered with the parameters 'min.cells=3', 'min.genes=200' and 'mitochondrial percentage>0.10' (Extended Data Fig. 6c), removing cells with <200 genes and mitochondrial gene percentage >10% and keeping genes with expression in at least 3 cells. Further sets of filters are explained in detail for each sample.

Wild-type aging datasets. The two batches of libraries (Supplementary Table 2) were processed separately. For the first batch, expression matrices were filtered by number of unique molecular modifiers (UMIs) (<30,000) and genes (<6,000). Processed data were normalized with the SCTransform function (variable.features.rv.th=1.4) and the top 9 PCs were selected for downstream analyses on inspection. Major cell types were identified using Louvain clustering and canonical cell-marker expression. Oligodendrocytes were extracted to be analyzed separately. The oligodendrocyte subset dataset was processed with SCTransform (variable.features.rv.th=1.5), principal component analysis (ten PCs) and Louvain clustering as explained earlier. In addition, *Gm42418* and *AY036118* genes were removed from the expression matrix because they indicate ribosomal RNA contamination[69].

The samples in the second batch were analyzed similarly; by extracting the oligodendrocytes after processing the libraries by quality control (QC) filtering, normalization, dimensionality reduction, clustering and cell-type annotation. QC filtering was done by number of UMIs (<50,000) and genes (<8,000). The filtered expression matrix was normalized by SCTransform (variable.features.rv.th=1.4 and regression by 'mitochondrial percentage'). The top 30 PCs were picked for downstream analyses. The oligodendrocyte subset dataset was again put through the same processing steps: SCTransform (top 750 variable genes) normalization, preceding downstream analyses conducted with the top 10 PCs.

To avoid batch-specific effects while still preserving biological variability, the sequenced libraries (four sequencing runs from eight animals) were integrated using the Seurat 3 CCA integration workflow[70]. Both the dataset with all cell types and the oligodendrocyte subset dataset were integrated using the integration steps tailored for SCTransform-normalized datasets. For the dataset with all cell types, the first 30 PCs were selected for the downstream analyses. Major cell types were identified using Louvain clustering and canonical cell-marker expression (Extended Data Fig. 1e,f).

For the oligodendrocyte dataset integration, the top 750 most variable genes and the top 20 PCs were selected for the 'anchoring'. After the integration, the top 10 PCs were used for downstream steps and unbiased clustering with a resolution of 0.5 identified the aforementioned 7 oligodendrocyte populations.

Rag1KO datasets. Samples from the two batches were analyzed separately, similar to the steps described for the wild-type aging datasets. For the first batch, expression matrices were filtered by number of UMIs (<20,000). Processed data were normalized using the SCTransform function (variable.features.rv.th=1.4 and regression by 'mitochondrial percentage'). The top 30 PCs were selected for downstream analyses and major cell types were identified using Louvain clustering and canonical cell-marker expression. A small cluster with high microglial-marker gene expression was removed. Oligodendrocytes were extracted and analyzed separately before integration. *Gm42418* and *AY036118* genes were removed from the expression matrix to prevent technical artifacts. In addition, a small cluster with high microglial-marker gene expression were removed. The same normalization parameters were applied: variable.features.rv.th=1.4 and regression by 'mitochondrial percentage'. The second batch of samples (both all cell types and oligodendrocyte subsets) were analyzed in the same way with the exception of filtering parameters (number of UMIs <25,000 and genes <8,000).

Integration of wild-type and Rag1KO datasets. The Seurat v.3 RPCA integration method was used to analyze wild-type and Rag1KO samples together. Previously described four batches of oligodendrocytes subsets (eight sequencing runs in total, four per genotype) were integrated (Fig. 3d and Extended Data Fig. 6c). The 500 most variable genes from each batch and the top 20 PCs were used in the 'anchoring' (k.anchor=3) of the Seurat objects. Postintegration, the top 15 PCs were selected for downstream analyses. Unbiased clustering identified the same oligodendrocyte populations as previously described.

To analyze wild-type and Rag1KO microglia, our previously described microglia dataset[18] was integrated together with the microglia from our Rag1KO libraries. Four batches of microglia subsets (eight sequencing runs in total, four per genotype) were integrated (Fig. 4a and Extended Data Fig. 6c). The 750 most variable genes from each batch and the top 15 PCs were used in the 'anchoring' (k.anchor=4, max. features=100) of the Seurat objects. Postintegration, the top 15 PCs were selected for downstream analyses. Unbiased clustering identified the same microglial populations in Safaiyan et al.[18] with addition to IFN-responsive microglia.

Datasets generated in the present study and external datasets (12 sequencing runs, 4 from Safaiyan et al.[18], 8 from the present study) were integrated using RPCA (Fig. 3a). The 3,000 most variable genes and default parameters for other functions were used in the 'anchoring'. The first 30 PCs were selected for clustering analysis and major cell types were identified using canonical marker genes.

Integration of CD8 T-cell datasets. Processed gene expression matrices and metadata of brain (FACS), kidney (droplet), lung (droplet) and spleen (droplet) datasets from the mouse aging single-cell transcriptomic atlas[36] were downloaded. After filtering based on gene expression and age, only $CD8^+$ T cells from 21- and 24-month-old samples were kept. The processed gene expression matrix and metadata were provided on request by the authors for the Groh et al. dataset[34]. These five datasets were integrated with the RPCA workflow for log(normalized datasets); the 500 most variable genes and the top 10 PCs were used in the anchoring steps. The integrated dataset was scaled with default parameters and the top ten PCs were used to calculate the UMAP.

All differential gene expression analyses were conducted using the FindMarkers function with Wilcoxon's rank-sum test. The scCODA v.0.1.6 package was used for compositional analysis of the single-cell data. The

false discovery rate (FDR) value was set to 0.4 to be able to detect subtle yet biologically relevant changes, as described by the authors in their documentation. In all boxplots, the central line denotes the median, boxes represent the interquartile range (IQR) and whiskers show the distribution except for outliers. Outliers are all points outside 1.5× the IQR.

Immunohistochemistry

Animals were anesthetized by 10 mg ml^{-1} of ketamine and 1 mg ml^{-1} of xylazine solution intraperitoneally and perfused transcardially with 4% paraformaldehyde (PFA). Postfixation of brain tissue was done in 4% PFA overnight. Then the brain tissue was further cryoprotected in 30% sucrose in PBS for 24 h. After freezing the tissue on dry ice using Tissue-Tek O.C.T, 30-µm coronal sections were cut using a cryostat Leica CM1900. Free-floating sections were collected in a solution containing 25% glycerol and 25% ethylene glycol in PBS. The sections were rinsed with 1× PBS containing 0.2% Tween-20 and permeabilized in 0.5% Triton X-100 for 30 min. Fab fragment goat anti-mouse immunoglobulin G (1:100, Dianova) was added for 1 h at room temperature to block endogenous mouse tissue immunoglobulins. After a brief wash the sections were blocked for 1 h at room temperature in a solution containing 2.5% fetal calf serum, 2.5% BSA and 2.5% fish gelatin in PBS. Primary antibodies, diluted in 10% blocking solution, were incubated overnight at 4 °C. On the following day, sections were incubated with secondary antibodies, diluted in 10% blocking solution, for 2 h at room temperature. The sections were washed with PBS followed by DAPI incubation in 1× PBS for 10 min and mounted. The following antibodies were used: mouse anti-APC (Millipore, catalog no. OP80-100UG, 1:100), rabbit anti-B2m (abcam, catalog no. ab75853-100ul, 1:100), rabbit anti-STAT1 (Cell Signaling Technology, catalog no. 14994S, 1:250), rat anti-CD8 (Promega, catalog no. 100702, 1:100), rabbit anti-Iba1 (Wako, catalog no. 234 004, 1:250), goat anti-Serpina3n (Bio-Techne, catalog no. AF4709, 1:100), rat anti-C4b (Thermo Fisher Scientific, catalog no. MA1-40047,1:25), rabbit anti-Olig2 (Millipore, catalog no. AB9610, 1:250), mouse anti-Gstp (BD, catalog no. 610719, 1:250), rat anti-Mac2 (BioLegend, catalog no. 125402, 1:250), chicken anti-MBP (Thermo Fisher Scientific, catalog no. PA1-10008, 1:1,000), chicken anti-neurofilament heavy polypeptide (abcam, catalog no. ab4680, 1:400), anti-PDGF-Ralpha (R&D Systems, catalog no. 1:100), goat anti-CD69 (R&D Systems,1:100), goat anti-PD-1 (R&D Systems,1:100), rabbit anti-LAG-3 antibody (Abcam, 1:100), AF1062FM green fluorescent myelin stain (Thermo Fisher Scientific, catalog no. F34651, 1:400), anti-mouse 555 (Thermo Fisher Scientific, catalog no. A-21422, 1:500), anti-mouse 647 (Thermo Fisher Scientific, catalog no. A-21235, 1:500), anti-mouse 488 (Thermo Fisher Scientific, catalog no. A-21202, 1:500), anti-rabbit 555 (Thermo Fisher Scientific, catalog no. A-21428, 1:500), anti-rabbit 488 (Thermo Fisher Scientific, catalog no. A-11008,1:500), anti-rat 555 (Thermo Fisher Scientific, catalog no. A-21434, 1:5600), anti-goat 555 (Thermo Fisher Scientific, catalog no. A-32116, 1:500), donkey anti-rat 488 (Thermo Fisher Scientific, 1:500), donkey anti-goat 555 (Thermo Fisher Scientific, 1:500) and donkey anti-rabbit 647 (Thermo Fisher Scientific, 1:500). For CC1, B2m, Gstp, OLIG2, STAT1 and Serpina3n staining, antigen retrieval protocol using citrate buffer (10 mM, pH 6) was performed on free-floating sections, followed by a staining protocol as mentioned above. For CD8, STAT1 and CC1/IBA1 combined staining, the sections were permeabilized with 0.5% Triton X-100 for 30 min at room temperature and blocked in 5% goat serum, and primary antibodies, diluted in 10% blocking solution, were added and incubated overnight at 4 °C with 0.5% Triton X-100 for 30 min at room temperature and blocked in 5% goat serum; secondary antibodies include goat anti-rabbit IgG antibody (H + L), biotinylated (Vector Laboratories, 1:200), goat anti-rat 488 and goat anti-mouse 647 (Invitrogen, 1:500) for 1 h at room temperature. Sections were then washed with PBS and incubated with streptavidin 555 (Invitrogen, 1:500). To determine the proximity of $CD8^+$ T cells to $STAT1^+CC1^+$ oligodendrocytes (IROs), $CD8^+$ T cells (or random $DAPI^+$ cells) were selected manually, from which a circle with a 20-µm radius was drawn from the center of the cell via ImageJ automatically. We then quantified the percentage of $STAT1^+CC1^+$ oligodendrocytes located within that circle. Conversely, we proceeded similarly but took oligodendrocytes as a reference and quantified the T cells within a circle with a 20-µm radius. The same quantification method was applied to determine the proximity of $CD8^+$ T cells to $STAT1^+IBA1^+$ microglia (IRM). Images were acquired via a Leica TCS SP5 confocal microscope or with an LSM900 Zeiss microscope and were processed and analyzed with ImageJ 1.41 image-processing software.

Correlated light and electron microscopy

Mice were perfused by 4% PFA (electron microscope (EM) grade, Science Services) in PBS (pH 7.4), the brain dissected and vibratome sectioned coronally at 100-µm thickness. Every second section was subjected to immunohistochemistry, whereas the remaining sections were postfixed with 2.5% glutaraldehyde in 0.1 M cacodylate buffer (Science Services) for potential EM. The method of immunohistochemistry for Iba1 staining was described as above. Sections were assessed by fluorescence imaging for sites of Iba1 enrichment in the corpus callosum, indicative of microglial nodules. The adjacent EM section was selected and subjected to a standard rOTO contrasting procedure. After postfixation in 2% osmium tetroxide (Electron Microscope Services), 1.5% potassium ferricyanide (Sigma-Aldrich) in 0.1 M sodium cacodylate, staining was enhanced by reaction with 1% thiocarbohydrazide (Sigma-Aldrich) for 45 min at 40 °C. The tissue was washed in water and incubated in 2% aqueous osmium tetroxide, washed and further contrasted by overnight incubation in 1% aqueous uranyl acetate at 4 °C and 2 h at 50 °C. Samples were dehydrated in an ascending ethanol series and infiltration with LX112 (LADD). We serially sectioned the tissue at 200-nm thickness on to carbon nanotube (CNT) tape (Science Services) on an ATUMtome (Powertome, RMC) using a 35° ultra-diamond knife (Diatome). CNT tape stripes were assembled on to adhesive carbon tape (Science Services) attached to 4-inch silicon wafers (Siegert Wafer) and grounded by adhesive carbon tape strips (Science Services). EM micrographs were acquired on a Crossbeam Gemini 340 SEM (Zeiss) with a four-quadrant backscatter detector at 8 kV. Overview scans were taken at 200-nm lateral and higher resolution scans at 20-nm lateral resolution. Serial section data were aligned by a sequence of automatic and manual processing steps in Fiji TrakEM2 (ref. [71]) and relevant regions selected.

Subregional localization analysis

To compare the difference between frontal white matter and medial white matter, coronal sections with corpus callosum were divided into two groups following the *Allen Mouse Brain Atlas*: the white matter in the front of the brain, which does not contain lateral ventricles, was defined as 'frontal white matter' and white matter from sections that have lateral ventricles is defined as 'medial white matter'. For each quantification, two brain sections were selected from each group of three to four mice. For statistical analysis the paired Student's *t*-test was used.

RNAscope in situ hybridization

RNAscope in situ hybridization assay was applied to detect *Mbp* mRNA in the brain cryosections prepared from aged wild-type mice as performed previously[18]. The assay was performed using a commercially available RNAscope Multiplex Fluorescent Detection Reagent v.2 (Advanced Cell Diagnostics) kit and the manufacturer's instructions were followed. Briefly, 30-µm cryosections were fixed on superfrost plus slides; they were pretreated with hydrogen peroxide for 10 min at room temperature and then with antigen retrieval reagent (5 min of boiling) to unmask the target RNA. After applying Protease III on the sections for 30 min at 40 °C, probe hybridization was done by incubating sections in mouse *Mbp* probe assigned to channel 3, diluted 1:50 in probe diluent, for 2 h at 40 °C. Afterwards, signal amplification and detection were performed according to the kit's instruction. Signal

detection was done using Opal dyes (Opal520-green) diluted 1:3,000 in tyramide signal amplification (TSA) buffer. To visualize microglia, after in situ hybridization, an immunohistochemistry assay was performed using Iba1 antibody (Wako, 1:1,000). After washing with 1× PBS, sections were incubated for 30 s with 1× TrueBlack to remove autofluorescence background. The nuclei of cells were counterstained with DAPI and mounted. Images were acquired via a Leica TCS SP5 confocal microscope or with an LSM900 Zeiss microscope and were processed and analyzed with ImageJ 1.41 image-processing software.

Cell culture

OPCs were prepared from P8 C57BL/6J mouse brains by immunopanning[72]. Briefly, brains were dissociated to single-cell suspension, which was passed through two negative-selection plates coated with BSL1 to remove microglia. The remaining cell suspension was then incubated in a positive-selection plate coated with anti-CD140a antibodies. The attached cells were collected by accutase and cultured on poly(L-lysine)-coated coverslips in proliferation medium containing Dulbecco's modified Eagle's medium (DMEM; Thermo Fisher Scientific, catalog no. 41965), Sato Supplement, B-27 Supplement, GlutaMAX, Trace Elements B, penicillin–streptomycin, sodium pyruvate, insulin, *N*-acetyl-L-cysteine, D-biotin, forskolin, ciliary neurotrophic factor (CNTF), platelet-derived growth factor (PDGF) and neurotrophin-3 (NT-3). Primary microglia cultures were prepared from p11 C57BL/6J mouse brains. The brains were homogenized to a single-cell suspension using the neural tissue dissociation kit (Miltenyi Biotech, catalog no. 130-092-628) and by filtering the homogenate through a 70-µm cell strainer to remove tissue debris. Then, the cells were incubated with magnetic beads against CD11b and the solution was passed through a magnetic column. Microglia were flushed and plated in DMEM supplemented with 10% bovine calf serum, 10 ng ml^{-1} of monocytic colony-stimulating factor, 1% penicillin–streptomycin and 1% glutamate for 4–7 d before using them for experiments. For the coculture experiments, OPCs were cultured in differentiation medium containing DMEM (Thermo Fisher Scientific), Sato Supplement, B-27 Supplement, GlutaMAX, Trace Elements B, penicillin–streptomycin, sodium pyruvate, insulin, *N*-acetyl-l-cysteine, D-biotin, forskolin, CNTF and NT-3. After 1.5 d, when OPCs had differentiated into oligodendrocytes, microglia were collected after scraping, counted and plated with oligodendrocytes. After 6 h, IFN-γ (Millipore, catalog no. IF005) in 5 mM phosphate buffer, pH 8.0 containing 0.1% BSA was diluted 1:5,000 in the coculture to a final concentration of 0.1 ng µl^{-1}. For the control, phosphate buffer containing BSA was diluted in the same way. After 2 d, the coculture was fixed and analyzed by immunocytochemistry. Briefly, the cells were permeabilized with 0.1% Triton X-100 for 1 min and blocked in 10% blocking solution for 1 h. The cells were then incubated with primary antibodies overnight at 4 °C, washed twice in PBS and incubated for 1 h at room temperature with secondary antibodies. Oligodendrocytes were stained for O1 (mouse hybridoma, 1:5), microglia for IBA1 (Wako, catalog no. 234 004, 1:250) and nuclei were stained with DAPI. After mounting, the cells were imaged on a Leica DMI6000 widefield microscope (×20, 0.4 numerical aperture, air objective) and analyzed using Fiji.

Stereotactic injection in the corpus callosum

A solution of 10 ng µl^{-1} of IFN-γ was prepared by mixing IFN-γ with sterile 1× PBS. Monastral blue (Sigma-Aldrich, catalog no. 274011; autoclaved and sterile filtered) was added to a final concentration of 0.03% just before injection to identify the lesion area during tissue processing. Mice were anesthetized with an intraperitoneal injection of MMF solution (0.5 mg medetomidin per kg (body weight), 5 mg midazolam per kg (body weight) and 0.05 mg fentanyl per kg (body weight)). Then the head was shaved and the eyes were protected with bepanthene cream (Bayer, catalog no. 1578847). A small incision was performed in the skin to expose the skull. The mouse was positioned into a stereotactic injection apparatus and a small hole was drilled at the injection coordinates: *X*, ±0.55 mm; *Y*, −1.22 mm (from the bregma). The glass capillary containing the IFN-γ solution or the control solution (PBS) was then lowered to *Z* of −1.25 mm from bregma, and 1 µl was injected at a rate of 100 nl min^{-1}. Then, 3 min after the delivery of the solution, the capillary was slowly retracted. The mouse was then injected with 0.05 mg of buprenorphin per kg (body weight) and the skin wound was sutured. Anesthesia was terminated by the injection of the antagonist solution, containing 2.5 mg kg^{-1} of atipamezol, 1.2 mg kg^{-1} of naloxone and 0.5 mg kg^{-1} of flumazenil. After 48 h, the animals were perfused transcardially with 4% PFA. Postfixation of brain tissue was done in 4% PFA overnight. Then the brain tissue was further cryoprotected in 30% sucrose and PBS for 24 h. The brain lesions were sectioned and stained using the same method as used in Immunohistochemistry.

Statistical analysis

For immunohistochemistry analysis three to six sections from each animal were analyzed. Data are shown as mean ± s.e.m. No statistical methods were used to predetermine sample sizes, but our sample sizes are similar to those generally employed in the field[16–20]. Each dot represents one animal. Normal distribution of the samples was tested using the Shapiro–Wilk test. For statistical analysis, paired or unpaired Student's *t*-test, or the Mann–Whitney *U*-test, was used to compare two groups. Two-sided, one-way analysis of variance (ANOVA) followed by post hoc Tukey's test was used for multiple comparisons. Test were chosen according to their distribution. In all tests a P value <0.05 was considered significant with $^{*}P < 0.05$, $^{**}P < 0.01$ and $^{***}P < 0.001$. Statistical analyses were done using GraphPad Prism (GraphPad Software, Inc.). Data acquisition and analysis were performed in a blinded manner. No animals were excluded from the analyses.

Reporting summary

Further information on research design is available in the Nature Research Reporting Summary linked to this article.

Data availability

The datasets we used (scRNA-seq) are deposited at the Gene Expression Omnibus (National Center for Biotechnology Information) under accession no. GSE202579. External datasets used in the present study include data from accession nos. GSE166548, GSE138891 and GSE132042. Source data are provided with this paper.

Code availability

The R code used for the analyses can be found at the github web-page: https://github.com/ISD-SystemsNeuroscience/Aging_Oligos_Microglia.

References

62. Turnbull, I. R. et al. Cutting edge: TREM-2 attenuates macrophage activation. *J. Immunol.* **177**, 3520–3524 (2006).
63. Liu, L. et al. Dissociation of microdissected mouse brain tissue for artifact free single-cell RNA sequencing. *STAR Protoc.* **2**, 100590 (2021).
64. Dobin, A. et al. STAR: ultrafast universal RNA-seq aligner. *Bioinformatics* **29**, 15–21 (2013).
65. Butler, A., Hoffman, P., Smibert, P., Papalexi, E. & Satija, R. Integrating single-cell transcriptomic data across different conditions, technologies, and species. *Nat. Biotechnol.* **36**, 411–420 (2018).
66. Huang, D. W., Sherman, B. T. & Lempicki, R. A. Systematic and integrative analysis of large gene lists using DAVID bioinformatics resources. *Nat. Protoc.* **4**, 44–57 (2009).
67. Szklarczyk, D. et al. STRING v11: protein–protein association networks with increased coverage, supporting functional discovery in genome-wide experimental datasets. *Nucleic Acids Res.* **47**, D607–D613 (2019).

68. Zhou, Y. et al. Metascape provides a biologist-oriented resource for the analysis of systems-level datasets. *Nat. Commun.* **10**, 1523 (2019).
69. Akama-Garren, E. H. et al. Follicular T cells are clonally and transcriptionally distinct in B cell-driven mouse autoimmune disease. *Nat. Commun.* **12**, 6687 (2021).
70. Stuart, T. et al. Comprehensive integration of single-cell data. *Cell* **177**, 1888–1902.e1821 2019).
71. Schindelin, J. et al. Fiji: an open-source platform for biological-image analysis. *Nat. Methods* **9**, 676–682 (2012).
72. Emery, B. & Dugas, J. C. Purification of oligodendrocyte lineage cells from mouse cortices by immunopanning. *Cold Spring Harb. Protoc.* **2013**, 854–868 (2013).

Acknowledgements

The work was supported by grants from the German Research Foundation (DFG, grant no. SI/746 15-1 to M.S.), TRR 128-2 (to M.S.), project no. 408885537-TRR 274 and SyNergy Excellence Cluster, EXC2145, project no. ID390857198 (to M.S. and O.G.), the Human Frontier Science Program (to M.S.), the ERC-ADG (grant no. 101019594 to M.S.), and the Dr. Miriam and Sheldon G. Adelson Medical Research Foundation (to M.S.), Chan-Zuckerberg Initiative grant (to M.S. and O.G.), the China Scholarship Council (CSC) fellowship program (to L.L. and H.J.) and Else Kröner-Fresenius-Stiftung grant (to O.G.). For the single-cell and sorting studies, we thank the 'Flow Cytometric Cell Sorter Sony SH800 Core Unit' run by the Department of Vascular Biology at the Institute for Stroke and Dementia Research and SyNergy EXC2145 for their support. The funders had no role in study design, data collection and analysis, decision to publish or preparation of the manuscript. We thank C. Haass for providing TREM2 knockout (KO) mice.

Author contributions

M. Simons and O.G. conceived and supervised the project. T.K., N.M., L.L., S.B.-G., H.J., S.K., O.G., J.W., L.C. and M. Schifferer performed experiments and analyzed the data. M. Simons and O.G. analyzed the data or supervised data acquisition. A.L. and J.G. provided essential reagents. M. Simons and O.G. wrote the manuscript with input from all authors.

Funding

Open access funding provided by Deutsches Zentrum für Neurodegenerative Erkrankungen e.V. (DZNE) in der Helmholtz-Gemeinschaft.

Competing interests

The authors declare no competing interests.

Additional information

Extended data is available for this paper at https://doi.org/10.1038/s41593-022-01183-6.

Supplementary information The online version contains supplementary material available at https://doi.org/10.1038/s41593-022-01183-6.

Correspondence and requests for materials should be addressed to Ozgun Gokce or Mikael Simons.

Peer review information *Nature Neuroscience* thanks Goncalo Castelo-Branco, Akiko Nishiyama, and the other, anonymous, reviewer(s) for their contribution to the peer review of this work.

https://doi.org/10.1038/s41593-022-01183-6

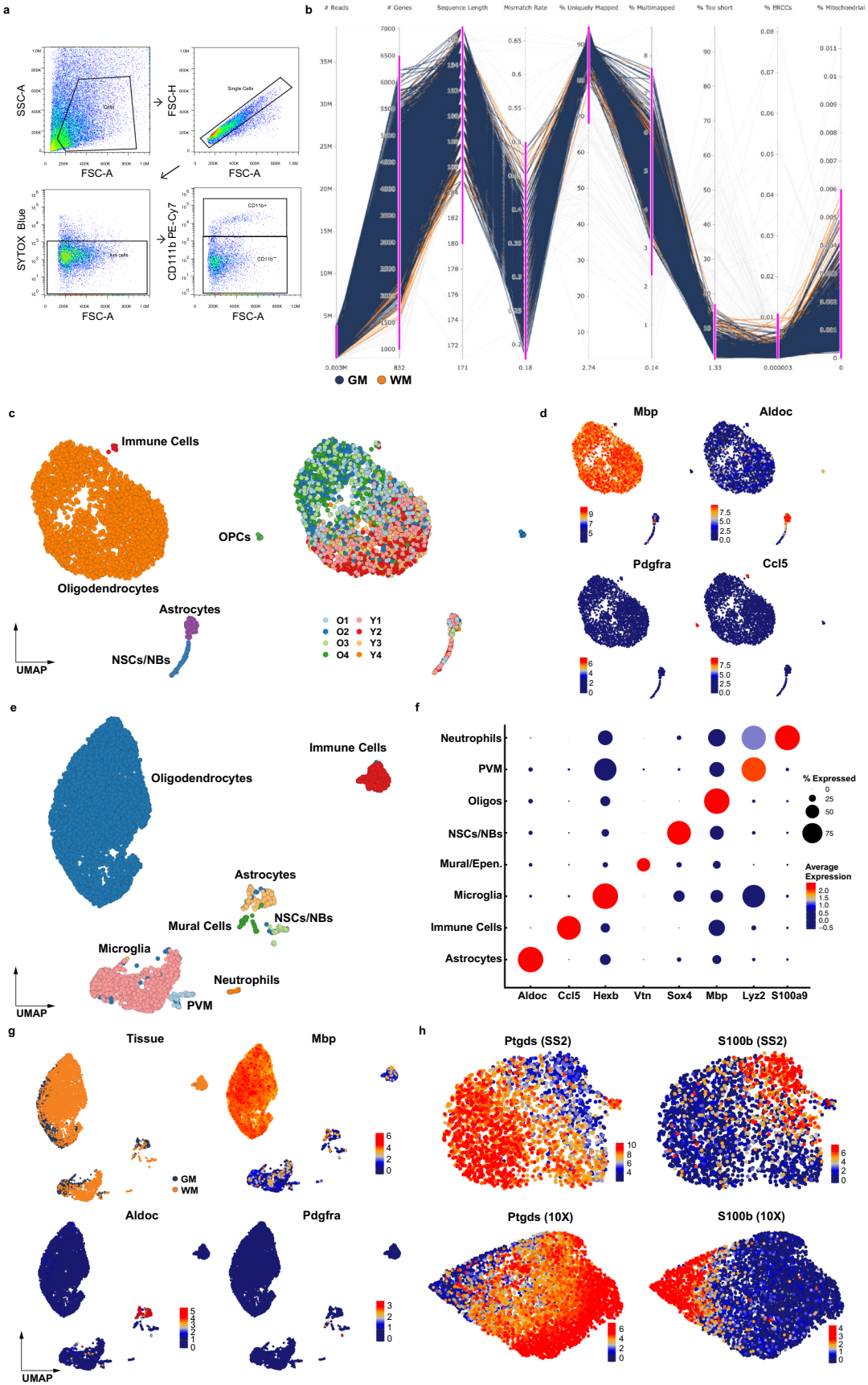

Extended Data Fig. 1 | See next page for caption.

https://doi.org/10.1038/s41593-022-01183-6

Extended Data Fig. 1 | Sorting strategy and quality control of scRNA-seq data. a, Sorting strategy for the SS2 libraries. Flow cytometry gating of CD11b negative cells to enrich for oligodendrocytes and astrocytes. **b**, Parallel coordinates trace for Smart-seq2 dataset quality metrics. Distribution of 9 quantitative quality control metrics reported by fastqc or from early gene expression matrix analysis. Each line, continuously going through all metrics is a sample (single cell). Light grey samples were discarded based on windows of inclusion (depicted in fuchsia for each metric). Selected samples for the grey matter are in blue, white matter are in orange. From left to right, the metrics are: number of reads, number of genes, average length of sequence after trimming, mismatch rate during alignment, % of uniquely mapped reads, % of multimapped reads, % of reads considered too short, % of ERCCs, % of mitochondrial genes. 2538 single-cells passed the quality-control thresholds. **c**, UMAP plots of 2538 single-cell transcriptomes. Cell type clusters and samples from different animals are colour coded. O1-2-3-4 and Y1-2-3-4 correspond to samples from 24-month old and 3-month old animals, respectively. **d**, UMAP plots of selected cell type-specific marker genes in the SS2 dataset; *Mbp* (Oligodendrocyte), *Aldoc* (Astrocyte), *Pdgfra* (OPC), *Ccl5* (Immune cells). **e**, UMAP plot of 8726 single-cell transcriptomes in the 10x dataset. Different cell type clusters are color coded. **f**, Dot plot showing cell-type marker gene expression by clusters. **g**, UMAP plots of tissue annotation and cell-type specific marker genes in the 10x dataset. **h**, UMAP plots of the oligodendrocyte populations depicting the expression of Oligo1 and Oligo2 marker genes (*Ptgds* and *S100*b, respectively), in the SS2 and 10x dataset.

https://doi.org/10.1038/s41593-022-01183-6

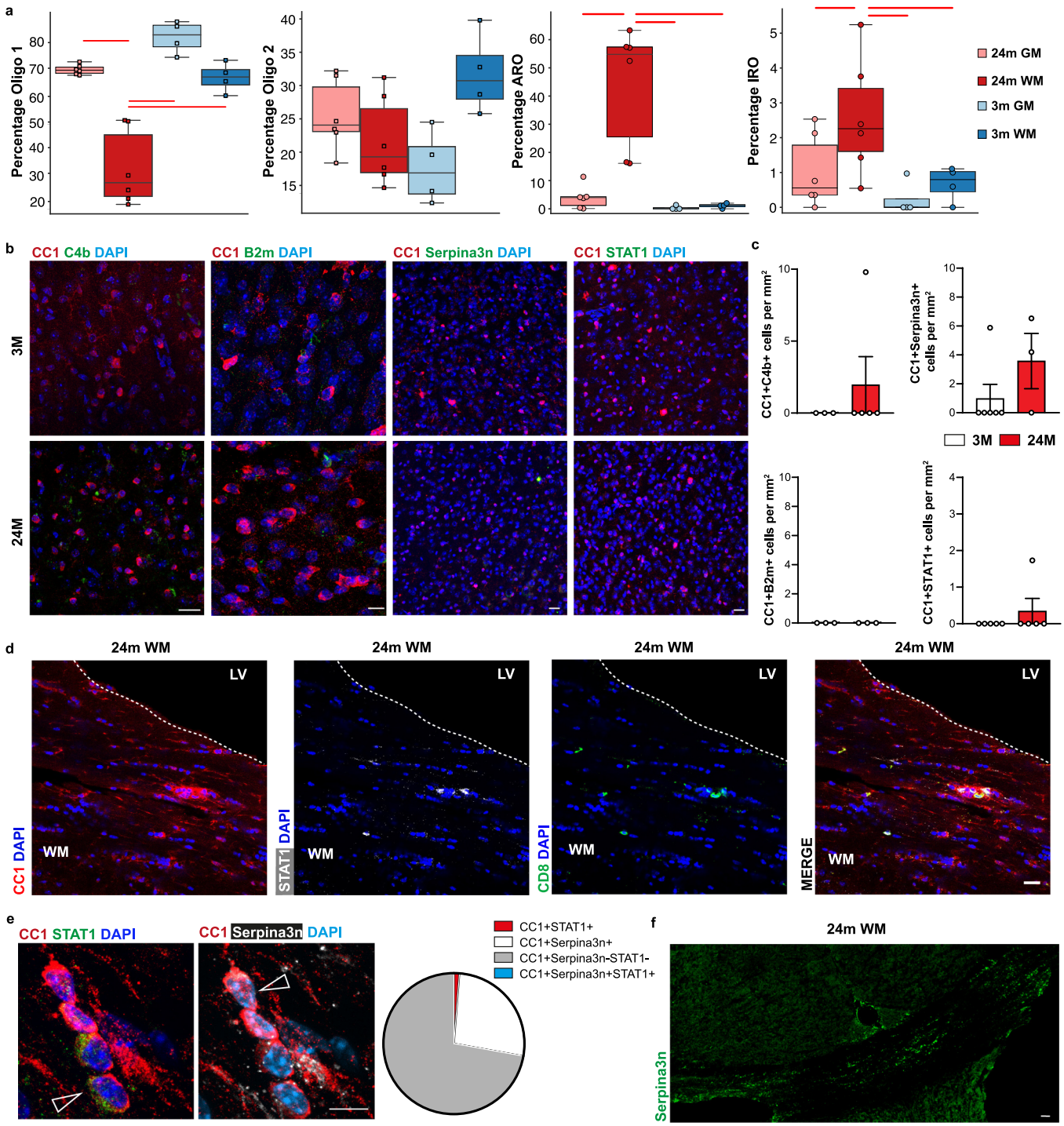

Extended Data Fig. 2 | Characterization of age-related and interferon-responsive oligodendrocytes. a, Boxplots of the Oligo1, Oligo2, ARO and IRO cluster proportions per sample (n = 20 independent experiments). The central line denotes the median, boxes represent the interquartile range (IQR), and whiskers show the distribution except for outliers. Outliers are all points outside 1.5 times of the IQR. Each dot represents a sample and significant results (scCODA model) are indicated with red bars. **b**, Immunofluorescence showing expression of C4b, B2m, Serpina3n and STAT1 (green) in $CC1^+$ oligodendrocytes (red) in the grey matter of 3- and 24- month old mice. Scale bar for C4b, Serpina3n and STAT1 20 µm, for B2m 10 µm. **c**, Quantification of $CC1^+$ oligodendrocytes expressing C4b, B2m, Serpina3n and STAT1 at 3- and 24-month old mice in the grey matter ($C4b^+CC1^+$, 3 M, n = 3, 24 M, n = 5; $Serpina3n^+CC1^+$, 3 M, n = 6, 24 M, n = 3; $B2m^+CC1^+$, 3 M, n = 4, 24 M, n = 4; $STAT1^+CC1^+$, 3 M, n = 5, 24 M, n = 5; data are means±s.e.m.; *P* values from two-tailed Mann–Whitney test). **d**, Representative confocal images showing $CD8^+$ T cells (green) and $STAT1^+CC1^+$ (white and red, respectively) oligodendrocytes in the white matter of 24-month old mice. **e**, Immunofluorescence showing expression Serpina3n (white) and STAT1 (green) in $CC1^+$ oligodendrocytes (red) in 24-month old mice in the white matter. Scale bar, 10 µm. Arrows indicate cells positive for $STAT1^+CC1^+$ and $Serpina3n^+CC1^+$. Pie chart of percentage of different subpopulations. **f**, Representative confocal overview image of large showing Serpina3n distribution in the white matter of 24-month old mice. The experiment was repeated three times independently with similar results. Scale bar, 50 µm.

https://doi.org/10.1038/s41593-022-01183-6

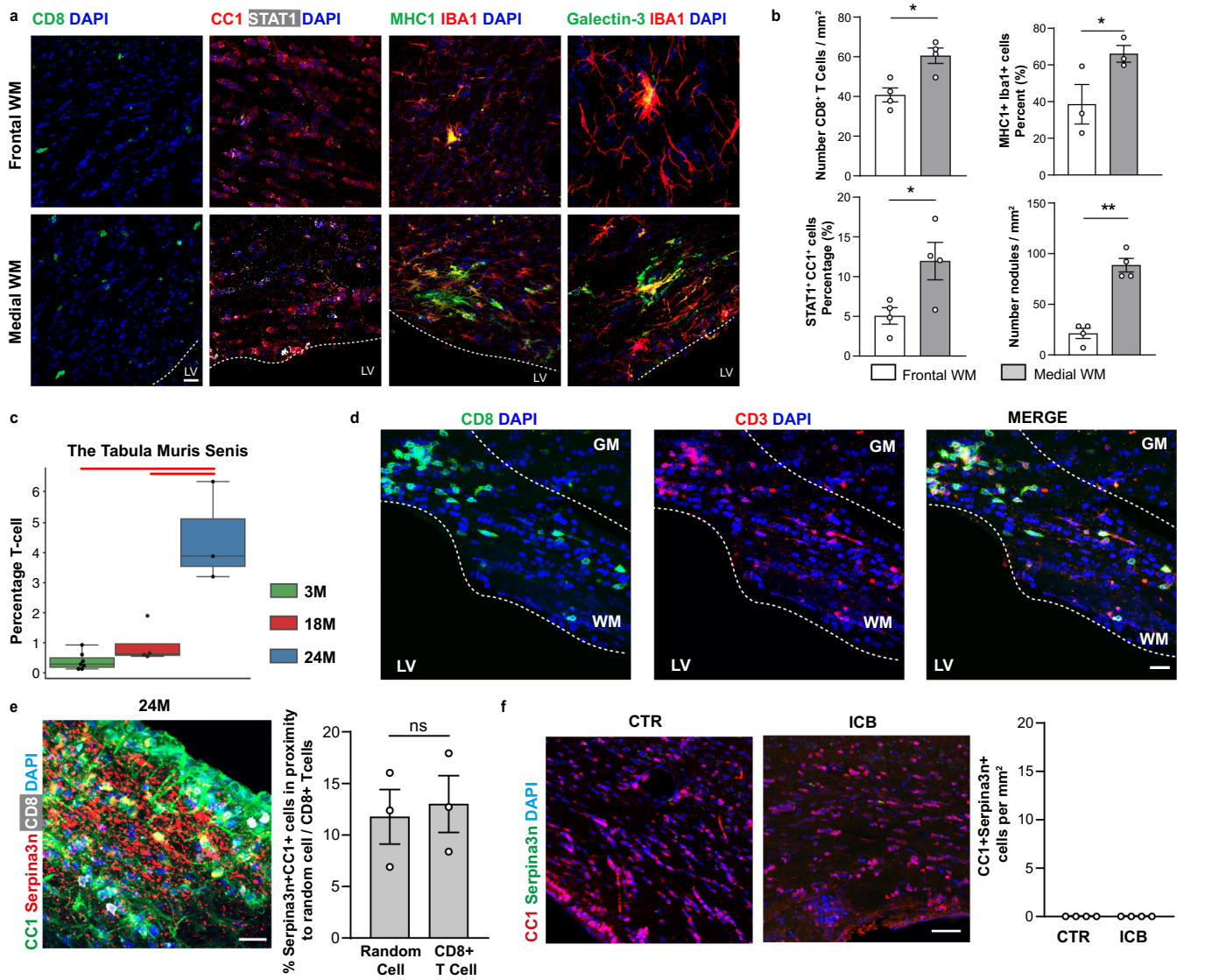

Extended Data Fig. 3 | Characterization of CD8 + T cells in the aging white matter. a, Immunofluorescence staining showing the different densities of $CD8^+$ T cells, $STAT1^+CC1^+$ cells, $MHC1^+IBA1^+$ cells and nodules (Galectin-3^+Iba1^+ cell clusters) between frontal white matter away from lateral ventricles and medial white matter close to lateral ventricles. Scale bar 20 µm. **b**, Quantification of $CD8^+$ T cells, $STAT1^+CC1^+$ cells, $MHC1^+IBA1^+$ cells, and nodules (Galectin-3^+IBA1^+ cells cluster) density difference between frontal white matter and medial white matter of 24-month old mice (for $CD8^+$, $STAT1^+CC1^+$, and nodules, n = 4 mice per group; $CD8^+$, $^*P = 0.0438$; $STAT1^+CC1^+$, $^*P = 0.0148$; nodules, $^{**}P = 0.0088$; for $MHC1^+IBA1^+$, n = 3 mice per group; $^*P = 0.0479$; data are means±s.e.m. *P* values represent a two-sided paried Student's t-test). **c**, T cells proportion per (n = 14 independent experiments) in the Tabula Muris Senis dataset. The central line denotes the median, boxes represent the interquartile range (IQR), and whiskers show the distribution except for outliers. Outliers are all points outside 1.5 times of the IQR. **d**, Representative confocal images of aged white matter stained for CD3 (red) and CD8 (green). The experiment was repeated three times independently with similar results. Scale bar, 20 µm. **e**, Immunofluorescence image showing $CD8^+$ T cells (white) and $Serpina3n^+$ (red) in $CC1^+$ oligodendrocytes (green) in the white matter of 24-month old mice. Scale bars, 20 µm. Quantification of the percentage of $Serpina3n^+CC1^+$ oligodendrocytes found around random cells (<20 µm) compared to the percentage of $Serpina3n^+CC1^+$ oligodendrocytes found around $CD8^+$ T cells (n = 3 mice per group; data are means±s.e.m.; *P* value represents a two-sided paried Student's t-test). **f**, Immunofluorescence showing expression of Serpina3n (green) in $CC1^+$ oligodendrocytes (red) in the white matter of mice treated with antibodies anti PD-1 and CTLA-4 and isotype control for 6 weeks starting at an age of 18 months. Scale bar 20 µm. Quantification of $CC1^+$ oligodendrocytes expressing Serpina3n in the white matter of mice treated with antibodies anti PD-1 and CTLA-4 and isotype control antibodies (n = 4 mice per group; data are means±s.e.m).

https://doi.org/10.1038/s41593-022-01183-6

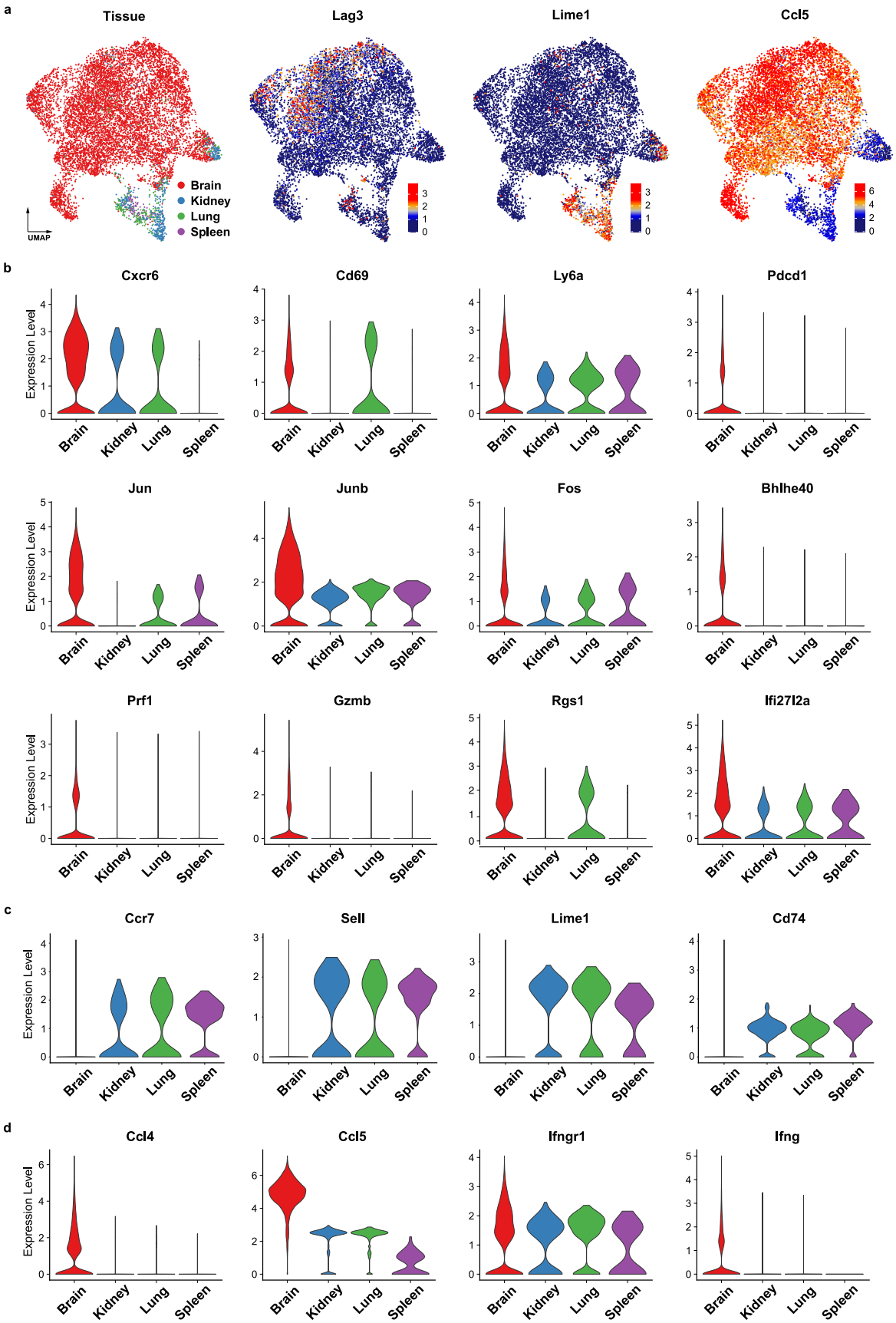

Extended Data Fig. 4 | Comparison of transcriptome prolife of CD8 + T cells within the brain compared to other organs. a, UMAP plots of 9732 CD8$^+$ T cells isolated from published aged mouse scRNA-seq datasets; Brain CD8$^+$ T cells (3 independent experiments taken from the Groh et al[34] and the Tabula Muris Senis datasets[36]), Kidney, Lung and spleen CD8$^+$ T cells (2-4 independent experiments taken from the Tabula Muris Senis 21- and 24-months old datasets), colored by tissue annotation and the expression of selected marker genes. **b**–**c**, Violin plots of up-regulated (b) and down-regulated (c) genes in the brain compared to kidney, lung and spleen. **d**, Violin plots of differentially expressed cytokine and cytokine receptor genes in the brain.

https://doi.org/10.1038/s41593-022-01183-6

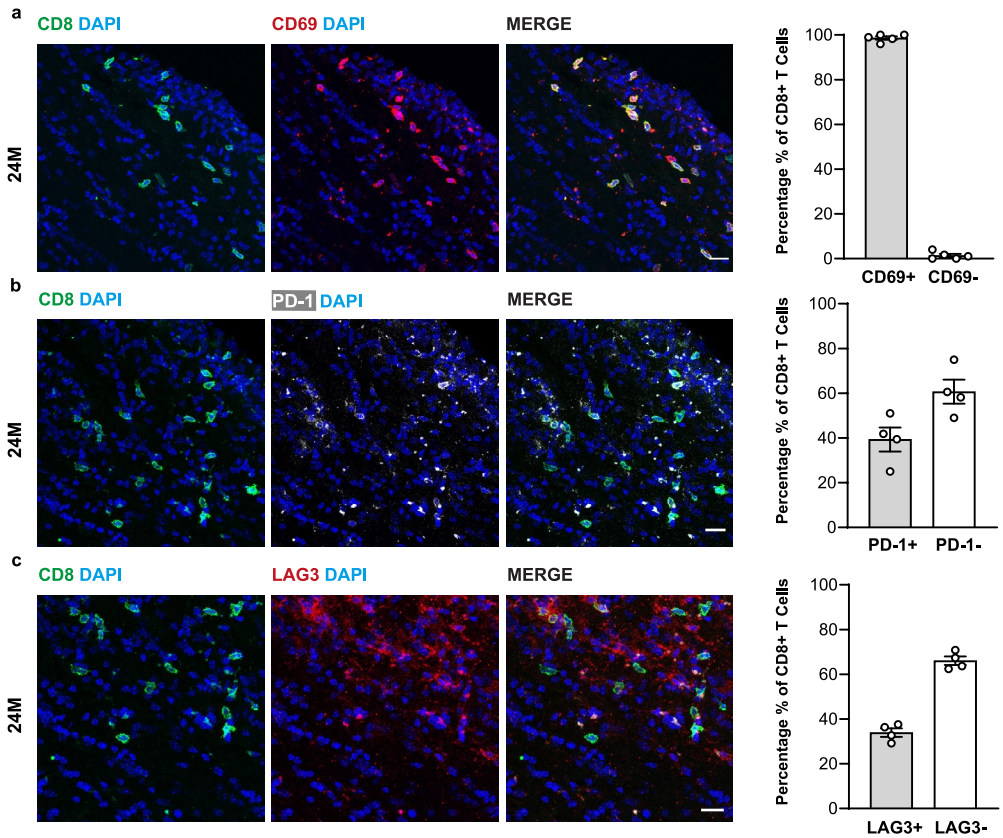

Extended Data Fig. 5 | CD8 + T cells within the aged white matter express tissue-resident memory and checkpoint markers. a, Representative confocal images of aged white matter stained for CD8 (green) with CD69 (red). Scale bar, 20 µm. Quantification of the percentage of $CD8^+$ and $CD69^+$ T cells in the aged white matter (three sections per mouse; 256 $CD8^+$ T cells were analyzed from 4 mice; data are means±s.e.m). **b**, Representative confocal images of aged white matter stained for CD8 (green) with PD-1 (white). Scale bar, 20 µm. Quantification of the percentage of $CD8^+$ and $PD\text{-}1^+$ cells in the aged white matter (three sections per mouse; 237 $CD8^+$ T cells were analyzed from 4 mice; data are means±s.e.m). **c**, Representative confocal images of aged white matter stained for CD8 (green) with LAG3 (red). Scale bar, 20 µm. Quantification of the percentage of $CD8^+$ and $LAG3^+$ cells in the aged white matter (three sections per mouse; 237 $CD8^+$ T cells were analyzed from 4 mice; data are means±s.e.m).

https://doi.org/10.1038/s41593-022-01183-6

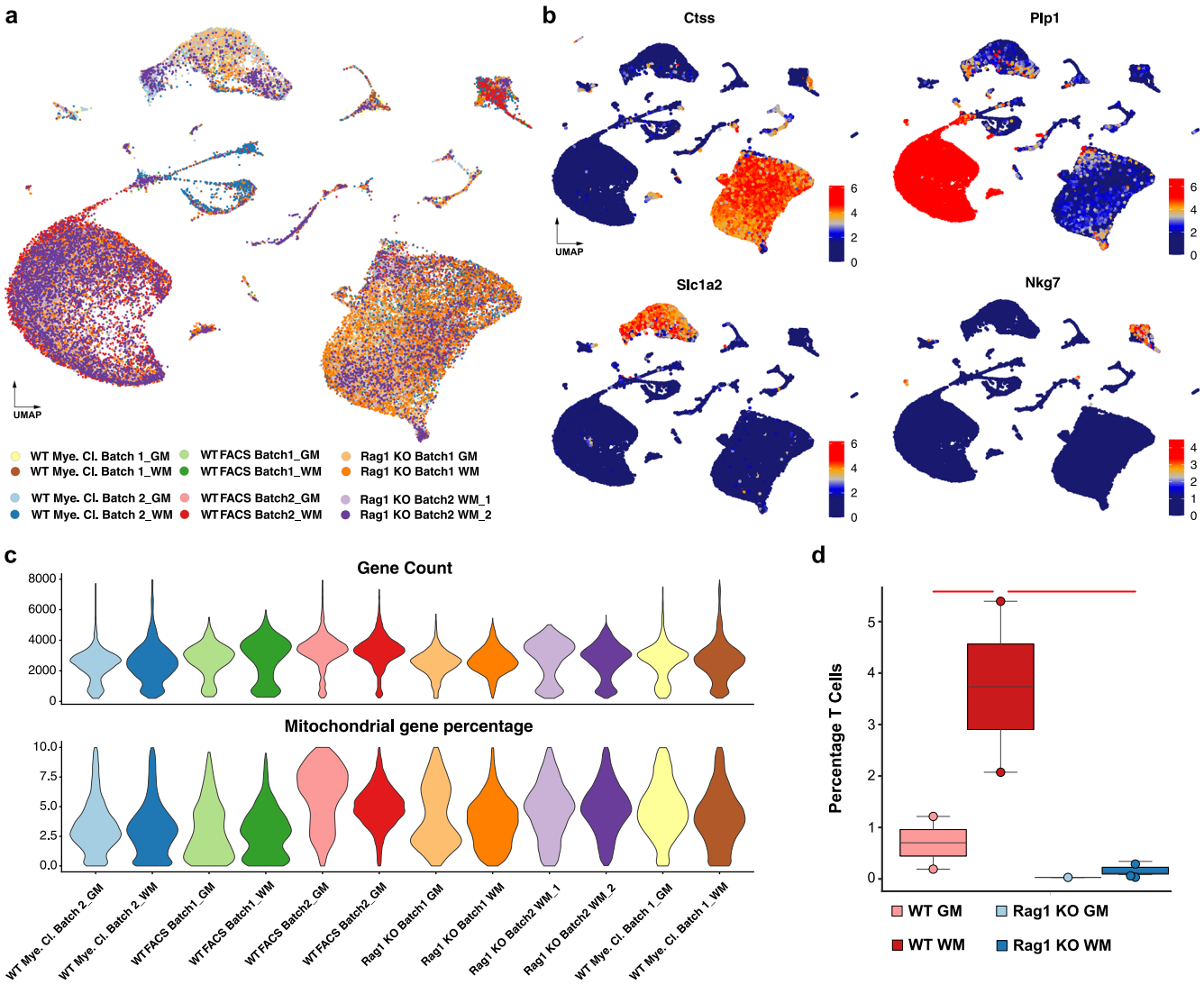

Extended Data Fig. 6 | T cell characterization and evidence of focal areas of hypomyelination in the aged white matter. a, UMAP plot of 44938 single-cell transcriptomes. Sequencing runs are color-coded. **b**, UMAP plots selected cell-type specific marker genes. **c**, Violin plots of gene count and mitochondrial gene percentage per cell in each sample. **d**, Boxplot of the T cells (Fig. 3a,b) proportion per sample (n = 8 independent experiments), respectively. The central line denotes the median, boxes represent the interquartile range (IQR), and whiskers show the distribution except for outliers. Outliers are all points outside 1.5 times of the IQR. Each dot represents a sample and significant results (scCODA model) are indicated with red bars. **e**, Confocal microscopy image of a vibratome brain section from 24-month old wild type mice stained for Iba1 (red) and DAPI (blue). Scale bar 100 µm. Correlative Light and Electron Microscopy of the corpus callosum in the aged mice with two boxed regions labeled as 1 and 2. Scanning electron micrograph of the same region on the adjacent vibratome section showing normal myelination next to areas with hypomyelination. Scale bar 50 µm. Boxed regions of thinner myelin with myelin fragments (1) and normal myelin (2) are shown at higher resolution. The experiment was repeated three times independently with similar results.

https://doi.org/10.1038/s41593-022-01183-6

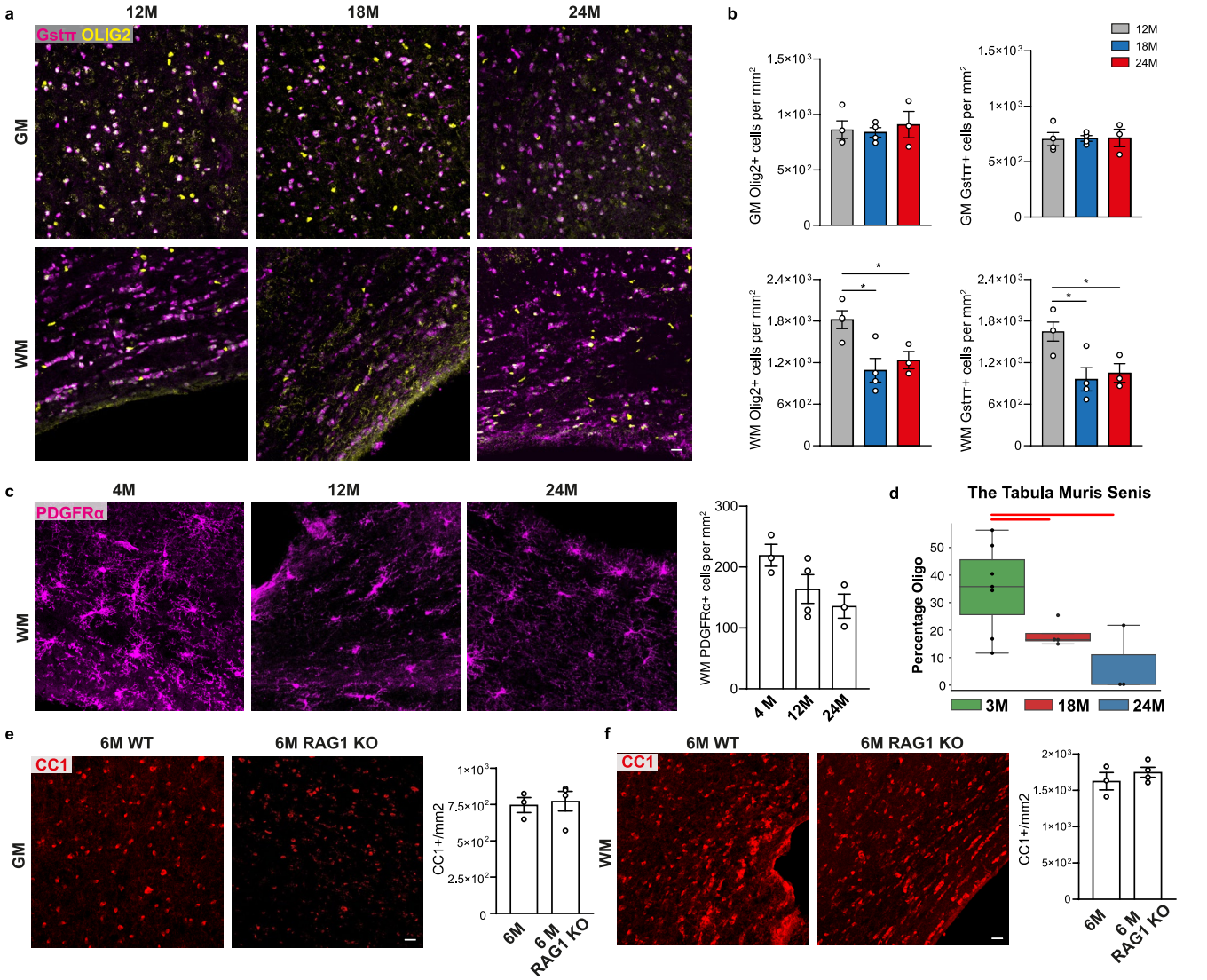

Extended Data Fig. 7 | Evidence of oligodendrocyte loss in the aged white matter. a, Immunofluorescence showing OLIG2$^+$ oligodendrocytes lineage cells (yellow) and oligodendrocytes GSTπ$^+$ (magenta) and in the grey and white matter of 12-, 18-, 24-month old mice. Scale bar 20 µm. **b**, Quantification OLIG2$^+$ and GSTπ$^+$ cells in the grey and white matter of 12-, 18-, 24-month old mice (for all the graphs in b, n = 4,4,3 mice per group; Olig2$^+$ cells in WM, 12 M versus 24 M, *P = 0.0493, 12 M versus 18 M, *P = 0.0123; GSTπ$^+$ cells in WM, 12 M versus 24 M, *P = 0.0481, 12 M versus 18 M, *P = 0.0180; data are mean±s.e.m.; P values represent two sided one-way ANOVA with post hoc Tukey test). **c**, Immunofluorescence showing and PDGFRα$^+$ cells (magenta) in the white matter of 4-, 12-, 24-month old mice. Scale bar 20 µm. Quantification PDGFRα$^+$ OPCs (magenta) in the white matter of 4-, 12-, 24-month old mice (PDGFRα$^+$, n = 3,4,3; data are mean ± s.e.m.; P value represents two sided, one-way ANOVA with post hoc Tukey test). **d**, Oligodendrocytes proportion per sample (n = 14 independent experiments) in the Tabula Muris Senis dataset. The central line denotes the median, boxes represent the interquartile range (IQR), and whiskers show the distribution except for outliers. Outliers are all points outside 1.5 times of the IQR. **e-f**, Immunofluorescence showing CC1$^+$ oligodendrocytes (red) in the grey matter and white matter of 6-month old wild type and *Rag1*$^{-/-}$ mice. Scale bar, 20 µm. Quantification of CC1$^+$ oligodendrocytes in the grey matter and white matter of 6-month old wild type and *Rag1*$^{-/-}$ mice (n = 3,4 mice per group, mean ± s.e.m.).

https://doi.org/10.1038/s41593-022-01183-6

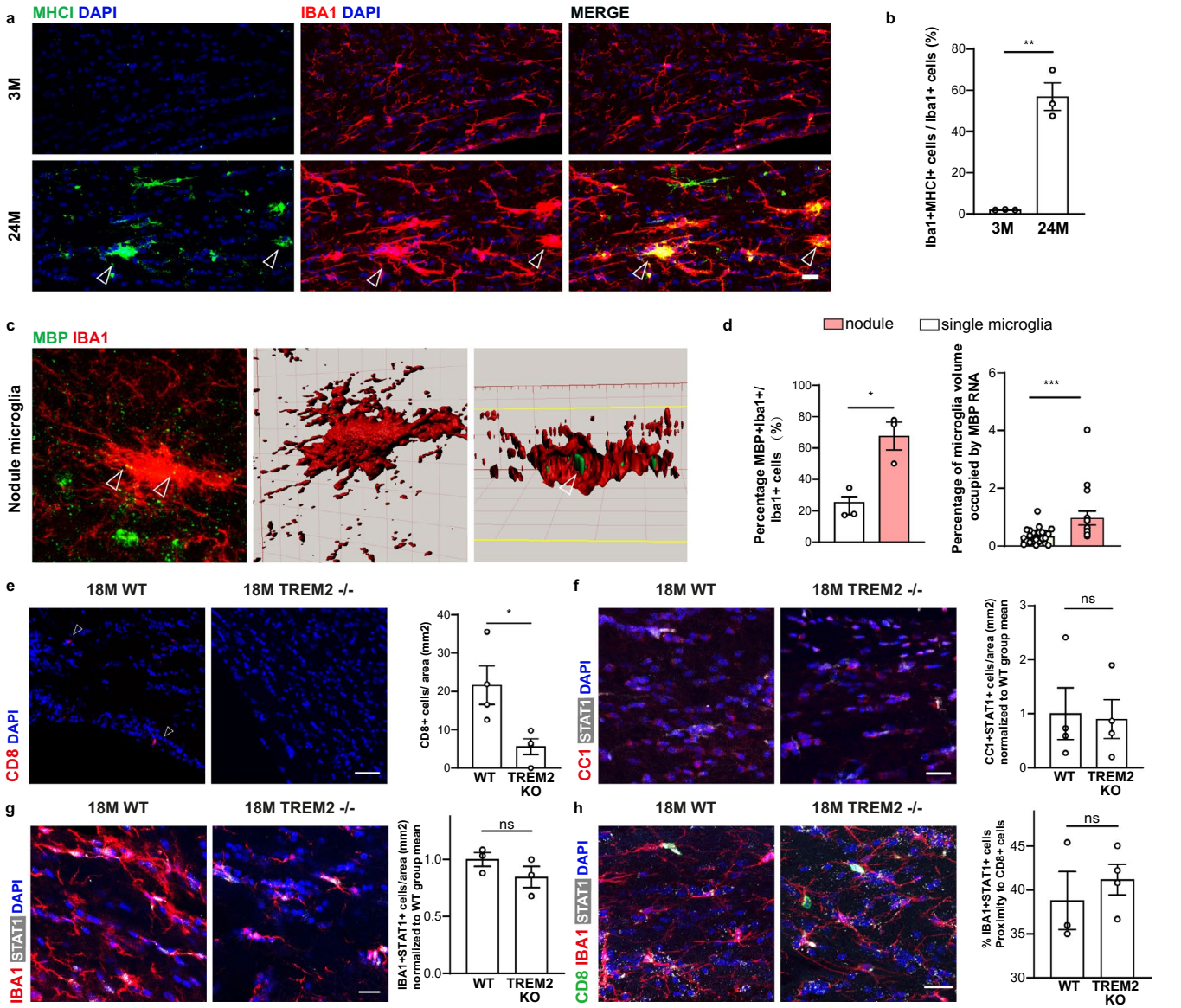

Extended Data Fig. 8 | TREM2-independent formation of interferon-responsive oligodendrocytes and microglia in the aged white matter. a, Immunofluorescence staining and **b**, quantification of MHC1$^+$IBA1$^+$ microglia in the white matter of 3-month old and 24-month old mice. Arrow marks MHC1$^+$ nodules (n = 3 mice per group, $^{**}P = 0.0012$; data are means±s.e.m; *P* value represents a two-sided Student's t-test). Arrows mark double positive microglia nodulces. **c**, Immunofluorescence combined with RNAscope of MBP mRNA (green) within IBA1$^+$ microglia nodule (red). Clipped 3D images show MBP mRNA in a microglia nodule. Arrow mark MBP mRNA inside microglia. Scale bar, 20 µm, 3D rendering 10 µm. **d**, Quantification of percentage of IBA1$^+$ single microglia and IBA1$^+$ nodule with MBP mRNA inside (n = 3 mice per group, $^{*}P = 0.0160$; data are means±s.e.m; *P* values represent a two-sided Student's t-test). Quantification of percentage of IBA1$^+$ volume occupied by MBP mRNA (single microglia, n = 26 cells, IBA1$^+$ nodules, n = 30; $^{***}P = 0.0004$; data are means±s.e.m.; *P* value represents two-tailed Mann-Whitney test). **e**, Immunofluorescence staining and quantification of CD8$^+$ T (red) cells in the white matter of 18-month old wild type and *Trem2*$^{-/-}$ (n = 4 mice per group, $^{*}P = 0.0252$; data are means±s.e.m; *P* value represents a two-sided Student's t-test). Arrows indicate CD8$^+$ T cells. Scale bar 20 µm. **f**, Immunofluorescence staining and quantification of STAT1$^+$CC1$^+$ oligodendrocytes in the white matter of 18-month old wild type and 18-month old *Trem2*$^{-/-}$ mice (n = 4 mice per group; data are means±s.e.m; *P* value represents a two-sided Student's t-test). Scale bar, 20 µm. **g**, Immunofluorescence staining and quantification of STAT1$^+$IBA1$^+$ microglia in the white matter of 18-month old wild type and 18-month old *Trem2*$^{-/-}$ mice (n = 3 mice per group; data are means±s.e.m; *P* value represents a two-sided Student's t-test). Scale bar, 20 µm. **h**, Immunofluorescence staining of CD8$^+$ T cells and STAT1$^+$IBA1$^+$ microglia in the white matter of 18-month old wild type and 18-month old *Trem2*$^{-/-}$ mice. Scale bars, 20 µm. Quantification of STAT1$^+$IBA1$^+$ microglia and CD8$^+$ T cells proximity (<20 µm) in 18-month old wild type and *Trem2*$^{-/-}$ mice (WT, n = 3; *Trem2*$^{-/-}$, n = 4 mice; data are means ± s.e.m. *P* value represents a two-sided Student's t-test).

https://doi.org/10.1038/s41593-022-01183-6

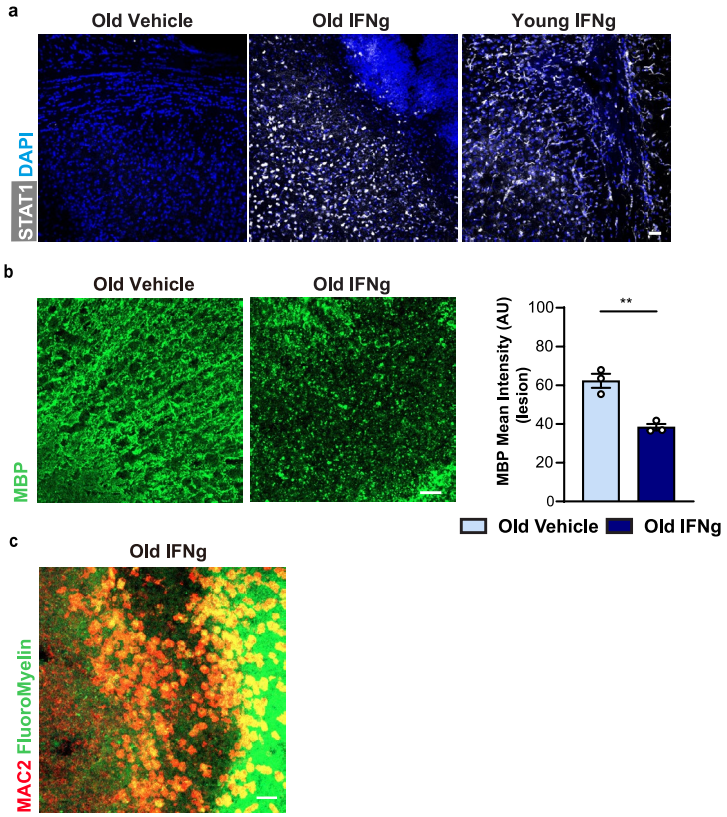

Extended Data Fig. 9 | Characterization of IFN-γ-mediated lesions in the white matter of young and old mice. a, Representative confocal images of IFN-γ-mediated lesions in young and old mice and of the vehicle control stained for STAT1 (white) and DAPI (nuclei, blue). **b**, The data shown in Fig. 5 for IFN-γ-mediated lesions in 18-months old mice is shown here in comparison to vehicle control injections in 18-months old mice. Representative confocal images and quantifications of IFN-γ-mediated lesions in old mice and of the vehicle control showing MBP. The intensity of the staining for MBP was used to quantify the extent of demyelination (n = 3 mice per group, $^{**}P = 0.0040$; data are means±s.e.m.; *P* value represents a two-sided Student's t-test). **c**, Representative confocal images of IFN-γ-mediated lesions in old mice showing $MAC2^{+}$ cells (red) with myelin (green) stained by FluoroMyelin. All scale bars, 20 µm. The experiments were repeated three times independently with similar results.

nature portfolio

Corresponding author(s): Mikael Simons, Ozgun Gokce

Last updated by author(s): Sep 9, 2022

Reporting Summary

Nature Portfolio wishes to improve the reproducibility of the work that we publish. This form provides structure for consistency and transparency in reporting. For further information on Nature Portfolio policies, see our Editorial Policies and the Editorial Policy Checklist.

Statistics

For all statistical analyses, confirm that the following items are present in the figure legend, table legend, main text, or Methods section.

n/a	Confirmed	
☐	☒	The exact sample size (*n*) for each experimental group/condition, given as a discrete number and unit of measurement
☐	☒	A statement on whether measurements were taken from distinct samples or whether the same sample was measured repeatedly
☐	☒	The statistical test(s) used AND whether they are one- or two-sided *Only common tests should be described solely by name; describe more complex techniques in the Methods section.*
☒	☐	A description of all covariates tested
☐	☒	A description of any assumptions or corrections, such as tests of normality and adjustment for multiple comparisons
☐	☒	A full description of the statistical parameters including central tendency (e.g. means) or other basic estimates (e.g. regression coefficient) AND variation (e.g. standard deviation) or associated estimates of uncertainty (e.g. confidence intervals)
☐	☒	For null hypothesis testing, the test statistic (e.g. *F*, *t*, *r*) with confidence intervals, effect sizes, degrees of freedom and *P* value noted *Give P values as exact values whenever suitable.*
☒	☐	For Bayesian analysis, information on the choice of priors and Markov chain Monte Carlo settings
☒	☐	For hierarchical and complex designs, identification of the appropriate level for tests and full reporting of outcomes
☐	☒	Estimates of effect sizes (e.g. Cohen's *d*, Pearson's *r*), indicating how they were calculated

Our web collection on statistics for biologists contains articles on many of the points above.

Software and code

Policy information about availability of computer code

Data collection	1. Confocal images: all images of mouse brain sections were acquired using a Leica TCS SP5 or Zeiss LSM900 confocal microscope and were processed with Imaris (64x version 9.2.0) and ImageJ 1.41 image processing softwares. A Leica DMI6000 widefield microscope was used for cell culture experiments 2. Single-cell RNA-seq data collection for the Smart-seq2 dataset: BCL files were demultiplexed with the bcl2fastq software from Illumina. After quality-control with FastQC, reads were aligned using rnaSTAR to the GRCm38 (mm10) genome with ERCC synthetic RNA added. Read counts were collected using the parameter "quantMode GeneCounts" of rnaSTAR and using the unstranded values.
Data analysis	1. Confocal images: all the image analysis and image processing were done using Imaris (64x version 9.2.0) and ImageJ 1.41 or Fiji image processing softwares. 2. Single-cell RNA-seq data analysis software and packages: BiocManager: 1.30.10, Cell Ranger: 3.0.2 (wild-type aging), 4.0.0 (Rag1KO 1st Batch) and 6.1.2 (Rag1KO 2nd Batch), Seurat: 3.2.3, SeuratObject: 4.0.2, gplots: 3.1.1, ggplot2: 3.3.2, magrittr: 2.0.2, reticulate: 1.16, RColorBrewer: 1.1-2, tidyverse: 1.3.0, scCODA: 0.1.6, pandas: 1.3.5, tensorflow: 2.5.2, sci-kit learn: 1.0.2, matplotlib: 3.5.1, seaborn: 0.11.2, Metascape: 3.5, DAVID 2021, STRING: 11.0-11.5 4. Statistical analyses were done using GraphPad Prism (GraphPad Software, Inc.).

For manuscripts utilizing custom algorithms or software that are central to the research but not yet described in published literature, software must be made available to editors and reviewers. We strongly encourage code deposition in a community repository (e.g. GitHub). See the Nature Portfolio guidelines for submitting code & software for further information.

Data

Policy information about availability of data

All manuscripts must include a data availability statement. This statement should provide the following information, where applicable:

- Accession codes, unique identifiers, or web links for publicly available datasets
- A description of any restrictions on data availability
- For clinical datasets or third party data, please ensure that the statement adheres to our policy

The datasets we use (scRNA-seq) are deposited at GEO (NCBI) under accession number GSE202579. Datasets re-analyzed in this study include data from GSE166548, GSE138891 and GSE132042. The rest of the data included in this study are available within the paper as data source files in the supplementary information.

Field-specific reporting

Please select the one below that is the best fit for your research. If you are not sure, read the appropriate sections before making your selection.

☒ Life sciences ☐ Behavioural & social sciences ☐ Ecological, evolutionary & environmental sciences

For a reference copy of the document with all sections, see nature.com/documents/nr-reporting-summary-flat.pdf

Life sciences study design

All studies must disclose on these points even when the disclosure is negative.

Sample size	No power analyses were used to predetermine sample sizes. However, sample sizes were chosen based on prior literature using similar experimental paradigms (for example doi:10.1016/j.celrep.2019.03.099; doi:10.1016/j.immuni.2017.08.008; doi:10.1016/j.cell.2017.05.018; doi:10.1016/j.neuron.2021.01.027
Data exclusions	No data were excluded from analysis.
Replication	For all mouse experiments, 3-6 mice per genotype were analyzed. For histological analysis, 3-6 random region of interest (ROIs) per each brain section were taken and three random brain sections per animal were quantified to account for variability within the biological sample. Replicaion was succesful for all conditions reported.
Randomization	The allocation of samples including brain sections was random.
Blinding	All data acquisition and analysis fwere done in a blinded manner. The experimentor was unblinded when preparing samples from IFNg because of the obvious differences in the phenotype.

Reporting for specific materials, systems and methods

We require information from authors about some types of materials, experimental systems and methods used in many studies. Here, indicate whether each material, system or method listed is relevant to your study. If you are not sure if a list item applies to your research, read the appropriate section before selecting a response.

Materials & experimental systems

n/a	Involved in the study
☐	☒ Antibodies
☒	☐ Eukaryotic cell lines
☒	☐ Palaeontology and archaeology
☐	☒ Animals and other organisms
☒	☐ Human research participants
☒	☐ Clinical data
☒	☐ Dual use research of concern

Methods

n/a	Involved in the study
☒	☐ ChIP-seq
☐	☒ Flow cytometry
☒	☐ MRI-based neuroimaging

Antibodies

Antibodies used	1.mouse anti APC (1:100) Millipore cat OP80-100UG 2.rabbit anti B2m (1:100) Abcam cat ab75853 3.rabbit anti STAT1 (1:250) Cell Signalling cat 14994S 4.rat anti CD8a (1:100) BioLegend cat 100702 5.rabbit anti Iba1 (1:500) Wako cat 234 004 6.goat anti Serpina3n (1:100) Bio-techne cat AF4709

7.rat anti C4b (1:25) Thermo fisher scientific cat MA1-40047
8.rabbit anti Olig2 (1:250) Millipore cat AB9610
9.mouse anti-Gstp (1:250) BD cat 610719
10.rabbit anti CD3e (1:200) Novus Biologicals cat NB600-1441
11.rat anti MHC class I (ER-HR52) (1:100) Santa Cruz cat sc-59199
12.goat anti-Rabbit IgG Antibody (H+L) Biotinylated (1:200) Vector cat BA-1000-1.5
13. Mouse anti galactocerebroside (O1) (1:5) raised in mouse hybridoma.
14.rat anti Mac2 (1:250) Biolegend cat 125402
15.chicken anti MBP (1:1000) thermo fisher scientific cat PA1-10008
16.chicken anti-Neurofilament heavy polypeptide(1:400) abcam cat ab4680
17. goat anti PDGFR alpha (1:100) R&D Systems cat AF1062
18. goat anti CD69 (1:100) R&D Systems cat AF2386
19. goat anti PD-1 (1:100) R&D Systems cat AF1021
20. rabbit anti-LAG-3 antibody (1:100) Abcam cat ab209238
21.CD16/CD32 Monoclonal Antibody (1:100) eBioscience cat 14-0161-82
22.CD11b (PE/Cy7, M1/70, 1:200) eBioscience Cat:48-0451-82

anti mouse 555 thermo fisher scientific (1:500) cat A-21422
anti mouse 647 thermo fisher scientific (1:500) cat A-21235
anti mouse 488 thermo fisher scientific (1:500) cat A-21202
anti rabbit 555 thermo fisher scientific (1:500) cat A-21428
anti rabbit 488 thermo fisher scientific (1:500) cat A-11008
anti rat 555 thermo fisher scientific (1:500) cat A-21434
anti goat 555 thermo fisher scientific (1:500) cat A-32116
anti rat 488 thermo fisher scientific (1:500) cat A-11006
anti chicken 488 thermo fisher scientific (1:500) cat A-11039
anti chicken 555 thermo fisher scientific (1:500)cat A-32932
Streptavidin, Alexa Fluor ™ 555 conjugate thermo fisher scientific (1:500) cat S32355
AF1062FM green fluorescent myelin stain (thermo fisher scientific F34651,1:400)
Donkey anti-Rat 488 thermo fisher scientific (1:500) cat A-21432
Donkey anti-Goat 555 thermo fisher scientific (1:500) cat A32816
Donkey anti-Rabbit 647 thermo fisher scientific (1:500) cat A-31573

Rat anti PD-1 bxcell cat BE0146
Rat isotype control bxcell cat BE0089
Hamster anti CTLA-4 bxcell cat BP0131
Hamster isotype control bxcell cat BP0087

Validation

All the primary antibodies were validated by extensive previous studies and by the manufacturers.
1. https://www.merckmillipore.com/DE/de/product/Anti-APC-Ab-7-Mouse-mAb-CC-1,EMD_BIO-OP80?ReferrerURL=https%3A%2F%2Fwww.google.com%2F
2.https://www.abcam.com/beta-2-microglobulin-antibody-ep2978y-ab75853.html
3. https://www.cellsignal.com/products/primary-antibodies/stat1-d1k9y-rabbit-mab/14994?site-search-type=Products&N=4294956287&Ntt=+14994s&fromPage=plp&_requestid=2125717
4.https://www.biolegend.com/en-ie/products/purified-anti-mouse-cd8a-antibody-157
5. https://labchem-wako.fujifilm.com/europe/product/detail/W01W0101-1974.html
6. https://www.rndsystems.com/products/mouse-serpin-a3n-antibody_af4709
7. https://www.thermofisher.com/antibody/product/Complement-C4-Antibody-clone-16D2-Monoclonal/MA1-40047
8. https://www.merckmillipore.com/DE/de/product/Anti-Olig-2-Antibody,MM_NF-AB9610?ReferrerURL=https%3A%2F%2Fwww.google.com%2F
9. https://www.bdbiosciences.com/en-us/products/reagents/microscopy-imaging-reagents/immunofluorescence-reagents/purified-mouse-anti-gst.610719
10.https://www.novusbio.com/products/cd3-antibody-sp7_nb600-1441
11.https://www.scbt.com/p/mhc-class-i-antibody-er-hr52?requestFrom=search
12.https://vectorlabs.com/biotinylated-goat-anti-rabbit-igg-antibody.html
14. https://www.biolegend.com/en-us/products/purified-anti-mouse-human-mac-2-galectin-3-antibody-4935
15.https://www.thermofisher.com/antibody/product/MBP-Antibody-Polyclonal/PA1-10008
16.https://www.abcam.com/neurofilament-heavy-polypeptide-antibody-ab4680.html
17.https://www.rndsystems.com/products/mouse-pdgf-ralpha-antibody_af1062
18.https://www.rndsystems.com/products/mouse-cd69-antibody_af2386
19.https://www.rndsystems.com/products/mouse-pd-1-antibody_af1021
20.https://www.abcam.com/lag-3-antibody-epr20294-77-ab209238.html
21.https://www.thermofisher.com/antibody/product/CD16-CD32-Antibody-clone-93-Monoclonal/14-0161-82
22.https://www.thermofisher.com/antibody/product/CD11b-Antibody-clone-M1-70-Monoclonal/25-0112-82

Secondary

https://www.thermofisher.com/antibody/product/Goat-anti-Mouse-IgG-H-L-Cross-Adsorbed-Secondary-Antibody-Polyclonal/A-21422
https://www.thermofisher.com/antibody/product/Goat-anti-Mouse-IgG-H-L-Cross-Adsorbed-Secondary-Antibody-Polyclonal/A-21235
https://www.thermofisher.com/antibody/product/Donkey-anti-Mouse-IgG-H-L-Highly-Cross-Adsorbed-Secondary-Antibody-

Polyclonal/A-21202
https://www.thermofisher.com/antibody/secondary/query/goat+anti-rabbit/filter/species/Rabbit?gclid=EAIaIQobChMIzYLDl8mL9AIVzEaRBR1esQ3fEAAYASAAEgKj4PD_BwE&ef_id=EAIaIQobChMIzYLDl8mL9AIVzEaRBR1esQ3fEAAYASAAEgKj4PD_BwE:G:s&s_kwcid=AL!3652!3!393949267183!b!!g!!%2Bthermo%20%2Banti%20%2Brabbit&cid=bid_pca_aus_r01_co_cp1359_pjt0000_bid00000_0se_gaw_bt_pur_con
https://www.thermofisher.com/antibody/product/Goat-anti-Rabbit-IgG-H-L-Cross-Adsorbed-Secondary-Antibody-Polyclonal/A-11008
https://www.thermofisher.com/antibody/product/Goat-anti-Rat-IgG-H-L-Cross-Adsorbed-Secondary-Antibody-Polyclonal/A-21434
https://www.thermofisher.com/antibody/product/Rabbit-anti-Goat-IgG-H-L-Cross-Adsorbed-Secondary-Antibody-Polyclonal/A-21431
https://www.thermofisher.com/antibody/product/Goat-anti-Rat-IgG-H-L-Cross-Adsorbed-Secondary-Antibody-Polyclonal/A-11006
https://www.thermofisher.com/order/catalog/product/S21381#/S21381
https://www.thermofisher.com/antibody/product/Goat-anti-Chicken-IgY-H-L-Secondary-Antibody-Polyclonal/A-11039
https://www.thermofisher.com/antibody/product/Goat-anti-Chicken-IgY-H-L-Cross-Adsorbed-Secondary-Antibody-Polyclonal/A32932
https://www.thermofisher.com/antibody/product/Donkey-anti-Goat-IgG-H-L-Cross-Adsorbed-Secondary-Antibody-Polyclonal/A-21432
https://www.thermofisher.com/antibody/product/Donkey-anti-Rat-IgG-H-L-Highly-Cross-Adsorbed-Secondary-Antibody-Polyclonal/A-21208
https://www.thermofisher.com/antibody/product/Donkey-anti-Rabbit-IgG-H-L-Highly-Cross-Adsorbed-Secondary-Antibody-Polyclonal/A-31573

in vivo treatment

https://bxcell.com/product/invivomab-anti-m-pd-1/
https://bxcell.com/product/rat-igg2a-isotype-control/
https://bxcell.com/product/m-cd152-m-ctla-4-2/
https://bxcell.com/product/invivoplus-polyclonal-syrian-hamster-igg/

Animals and other organisms

Policy information about studies involving animals; ARRIVE guidelines recommended for reporting animal research

Laboratory animals	Mouse: C57BL/6J Janvier Labs, CSD animal facility, University Hospital animal facility. Age 3,12,18,24 months,male Mouse: Trem2 KO Prof. Christian Haass (Laboratory of Neurodegenerative Disease Research, DZNE, Munich), Turnbull et al., 2006. Age 18 months,male Mouse : RAG1 KO (B6.129S7-Rag1tm1Mom/J), Prof. Arthur Liesz, laboratory of stroke immunology of Insitute of Stroke and dementia, LMU, Munich. Age 24 months ,male Mouse : CD8 KO mice (B6.129S2-Cd8atm1Mak/J) Prof. Rudolf Martini, University Hospital Würzburg, Germany. Age 24 months old,male
Wild animals	No wild animals were used
Field-collected samples	No field collection samples were used in the study
Ethics oversight	All animal experiments performed in this work were in agreement with the German animal welfare law and state specific regulations for animal experiments

Note that full information on the approval of the study protocol must also be provided in the manuscript.

Flow Cytometry

Plots

Confirm that:

☒ The axis labels state the marker and fluorochrome used (e.g. CD4-FITC).

☒ The axis scales are clearly visible. Include numbers along axes only for bottom left plot of group (a 'group' is an analysis of identical markers).

☒ All plots are contour plots with outliers or pseudocolor plots.

☐ A numerical value for number of cells or percentage (with statistics) is provided.

Methodology

Sample preparation	Four young (3-month-old), and four old (24-month-old) male C57BL/6 mice were deeply anesthetized and perfused with cold PBS (Sigma, D8537). Each brain was carefully removed and individually micro-dissected under a dissection microscope; grey matter was isolated from the frontal cortex and white matter was carefully isolated from the optic tract, medial lemniscus and corpus callosum (attached grey matter and choroid plexus were removed). We used our previous established isolation protocol37 using gentleMACS™ with the Neural Tissue Dissociation Kit (Papain) (Miltenyi Biotec) and a final concentration of 45 mM actinomycin D (Act-D, Sigma, No.A1410). Subsequently, cells were blocked with mouse FcR-blocking reagent (CD16/CD32 Monoclonal Antibody, eBioscience cat:14-0161-82, 1:100), stained with antibodies against CD11b (PE/Cy7, M1/70,

	eBioscience, Cat:48-0451-82,1:200) and afterwards washed with PBS. Before sorting, the cell suspensions were stained by the live/dead marker SYTOX Blue (Thermo Fisher, s34857, final concentration 1μM).
Instrument	Sony SH800S Cell Sorter
Software	The SH800S software for the data collection. FlowJo was used for the flow cytometry data analysis.
Cell population abundance	During single-cell library preparation we have confirmed the quality of the single-cells via qPCR assay (more details in methods section).
Gating strategy	CNS cells were gated for singlets by using FSC-A and FSC-H, followed by gating for living cell (SYTOX Blue negative population, fixable viability dye), then CD11b- cells were sorted.

☒ Tick this box to confirm that a figure exemplifying the gating strategy is provided in the Supplementary Information.

3. DISCUSSION

The immune and nervous systems, despite their distinct functionalities, exhibit striking parallels. Both systems are intricately designed to perform complex tasks, including continuous environmental surveillance, signal transmission, and dynamic adjustments to preserve homeostasis (Rustenhoven & Kipnis, 2022). Reflecting the interdisciplinary nature of contemporary science, these systems engage in multilingual communication, both intra-systemically and inter-systemically.

A quintessential illustration of immunological communication involves the secretion of cytokines from one cell, which subsequently influences another cell in a paracrine manner to direct its function and coordinate a specific response. Analogously, in the neurological context, neurotransmitters released from presynaptic terminals interact with corresponding receptors or ligand-binding domains in the postsynaptic density of another neuron, thereby modulating their firing activity.

Intriguingly, neurons in the central nervous system (CNS) and peripheral nervous system (PNS) express cytokine receptors, enabling a variety of responses to cytokines originating from immune cells. In a reciprocal manner, immune cells express receptors for neurotransmitters and neuropeptides—neuron-derived signaling molecules—and immune responses can be altered by neuronal signaling (Habibi et al., 2009).

This understanding is continually evolving, with recent findings indicating that neurons can express cytokines, such as interleukin 13 (IL-13), at presynaptic vesicles and corresponding cytokine receptors at the postsynaptic density. This suggests a form of neuronal communication that utilizes "immunological molecules", even in the absence of actual immune cells (S. Li et al., 2023).

Moreover, neurons can employ communication strategies used by the immune system to regulate neuronal connectivity. This includes the expression of major histocompatibility complex (MHCI) and complement proteins C1q and C3b, which facilitate direct neuronal pruning7 or synapse elimination via microglial engulfment (C. Wang et al., 2020). Similarly, immune cells—like B cells—can produce the neurotransmitter gamma-aminobutyric acid (GABA), which can stimulate the differentiation of anti-inflammatory macrophages. This underscores an immune-immune interaction mediated by traditionally neuron-derived signals (Zhang et al., 2021).

In summary, a myriad of interactions underpin the intricate communication between the nervous and immune systems.

3.1 White-Matter Associated Microglia

In manuscript 2.1, we discovered a new microglial state, termed White Matter Associated Microglia (WAMs), which are characterized by the activation of genes involved in phagocytic activity and lipid metabolism (Frigerio et al., 2019; Hammond et al., 2019). The formation of WAMs is age-dependent and requires the presence of the triggering receptor expressed on myeloid cells 2 (TREM2). Interestingly, WAMs form even in the absence of Apolipoprotein E (APOE) during normal aging, indicating a distinct pathway for their formation.

WAMs localize in nodules within the white matter, where they are engaged in the clearance of myelin debris. This led us to question why microglia states are specifically altered in white matter. The extent of myelin sheath degeneration and/or the nature of the lipid-rich membrane may be responsible for TREM2-dependent microglial responses in white matter. This hypothesis is supported by our observations in a mouse model for Pelizaeus-Merzbacher disease, where microglia nodules containing myelin debris were formed in white matter but not in gray matter (Q. Li et al., 2019).

TREM2, a V-type immunoglobulin (Ig) domain-containing receptor, binds to a variety of different ligands, including various apolipoprotein and anionic lipid species (Ulrich et al., 2017). While TREM2 can function as a receptor for myelin debris uptake (Cantoni et al., 2015), our results indicate that TREM2 is not essential for myelin phagocytosis. Instead, we propose that TREM2 mediates the genetic response required to degrade and metabolize lipid-rich myelin debris once internalization has occurred.

Loss of TREM2 function results in a disease known as polycystic lipomembranous osteodysplasia with sclerosing leukoencephalopathy (PLOSL or Nasu-Hakola disease), characterized by progressive presenile dementia and bone cysts (Bianchin et al., 2010). This disease is associated with the accumulation of lipomembranous structures in various tissues, suggesting an inability to initiate metabolic pathways required for degradation of lipid-rich membrane structures.

In the context of Alzheimer's disease (AD), rare variants in the TREM2 gene have been shown to increase an individual's risk of developing the disease (Guerreiro et al., 2013). Several studies have shown that TREM2 is required to induce the disease-associated microglia (DAM) program in models of AD (Frigerio et al., 2019; Keren-Shaul et al., 2017). DAMs increase with progression of amyloid deposition and accumulate close to amyloid plaques, where they are involved in Aβ phagocytosis and plaque compaction.

In aging, microglial activation appears to be dominated by the WAM state, whereas it is shifted toward DAMs in AD. Interestingly, the proportion of DAMs showed a decrease between 12 and 21 months, possibly because of microglial cell death in the DAM populations and repopulation with homeostatic microglia or DAMs returning to the homeostatic state.

One distinguishing feature of DAM and WAM responses appears to be their differential dependence on APOE. In the absence of APOE, fewer microglia with the WAM gene signature are generated in AD mouse models, whereas microglia with features of

WAM are detected in similar numbers in aged white matter of Apoe–/– and wild-type mice. This suggests that the activity of APOE depends on the brain environment (Y. Chen et al., 2021).

We propose that WAMs represent a protective metabolic response required to clear the increasing amounts of myelin debris that accumulate during aging. However, harmful functions, such as immune reactivity, cannot be excluded. We speculate that attrition of WAM function could contribute to the development of neurodegenerative disease by accumulation of toxic protein or lipid species in the brain. If this is the case, then enhancing the formation of WAMs could be used therapeutically to combat the age-associated decline of white matter function and possibly also dementia resulting from white matter involvement. Future research should explore whether WAMs also exist in humans, as transcriptional signatures differ between mouse and human microglia (Masuda et al., 2019).

3.2 IFN-Responsive Glia

The degeneration of myelin in white matter is a known consequence of aging, yet the response of oligodendrocytes to this process is not well understood. Our recent investigation has provided new insights, revealing unique oligodendrocyte reactions to aging, as evidenced by the emergence of STAT1+/B2M+ and Serpina3n+/C4b+ oligodendrocyte subgroups and a decline in the overall density of oligodendrocytes in aged white matter. Furthermore, our findings suggest that adaptive immune cells play a role in these cellular transformations associated with white matter aging.

In both Rag1–/– and CD8–/– aged mice, we noted a reduction in the number of STAT1+ oligodendrocytes and a comparable increase in the total oligodendrocyte density. This evidence suggests that operational CD8+ T cells significantly influence the aging process of white matter (Dulken et al., 2019). We also discovered a subset of

lymphocyte-dependent IFN-responsive microglia in aging white matter. These findings suggest that adaptive immunity propels IFN-responsive cellular states in aging white matter, but the precise interplay between CD8+ T cells, microglia, and oligodendrocytes is yet to be determined.

Previous studies have demonstrated that CD8+ T cells infiltrating the aging brain exhibit elevated levels of IFN-γ, which stimulate IFN signaling within the neurogenic niche of the subventricular zone (Dulken et al., 2019). It is possible that IFN-γ produced by CD8+ T cells also triggers IFN responses in oligodendrocytes and microglia, but the involvement of other IFNs cannot be dismissed (Baruch et al., 2014). One potential scenario is that CD8+ T cells secrete IFN-γ, which subsequently polarizes microglia into a harmful phenotype. This is reminiscent of a previous study using a viral model of encephalitis in mice, where CD8+ T-cell-derived IFN-γ triggered acute loss of axosomatic connections (Liberto et al., 2018).

When mice were treated with antibodies against the checkpoint receptors, CTLA-4 and PD-1, we observed an increase in the number of CD8+ T cells and IFN-responsive oligodendrocytes and microglia. This could potentially explain why immune checkpoint inhibition in cancer causes behavioral and cognitive changes in some patients.

Our research extends beyond mere observational correlation of CD8+ T cells in close proximity to IFN-responsive oligodendrocytes and microglia. Through rigorous experimentation involving Rag1–/– and CD8–/– aged mice, as well as the application of checkpoint inhibitor drugs, we have established a causal relationship between white matter loss and the influence exerted by the adaptive immune system. However, the chronological sequence and causality of pathological processes contributing to white matter aging need to be established. Progressive vascular damage, induced by injury to myelinated fibers, may promote the infiltration of CD8+ T cells, thereby triggering

harmful immune reactivity toward microglia and oligodendrocytes (Montagne et al., 2015). A key question that remains to be established is how CD8+ T cells enter the brain and whether antigen recognition is necessary for this process.

Previous work has shown that oligodendrocytes are particularly sensitive to IFN-γ, as it can trigger oligodendroglial cell death and demyelination (Horwitz et al., 1997). Strikingly, we find that this effect is highly pronounced in the aged brain, in which IFN-γ potently induces loss of oligodendrocytes and demyelinating injury. Possibly, the aging brain is primed toward IFN-γ due to age-associated, chronic, low-grade inflammation, so-called 'inflammaging' (Mundt et al., 2019).Our data emphasize the contribution of CD8+ T cells in triggering IFN-responsive cell states in the aging white matter, but it is likely that additional mechanisms contribute. In particular, prolonged exposure of nucleic acids to pattern-recognition, immune-sensing receptors can lead to inappropriate type I IFN release (Crow & Manel, 2015). It is interesting that Aicardi–Goutieres syndrome, a prototype of an inherited disease with abnormal nucleic acid sensing and IFN induction, is associated with white matter pathology.

In the context of aging, the IFN pathway's outcomes present a fascinating scenario, suggesting that what appears to be a pathological response may actually be a maladaptive initiation of a pathway that is otherwise crucial for neurological rewiring. While neuronal atrophy is undoubtedly harmful in older individuals, it is important to recognize that programmed neuronal atrophy plays a beneficial role in learning and plasticity among younger subjects by eliminating axonal connections and neuronal clusters that have become functionally redundant.

In the specific instance of the mouse whisker-plucking model of neuronal atrophy, where neuronal clusters that respond to a particular whisker are eradicated following an extended lack of stimuli from that whisker, the activation of type 1 IFN within microglia is an essential process (Escoubas et al., 2023). This activation of type 1 IFN may serve as a central signaling mechanism, facilitating the restructuring of neuronal and glial formations to form more advantageous networks. However, it is worth noting that

an excessive activation of type 1 IFN signaling can lead to severe encephalopathy in Aicardi–Goutieres syndrome, and other prevalent neurodegenerative diseases have been linked to improper type 1 IFN responses within glia (Roy et al., 2020).

Within the aging framework, two potential pathways might erroneously instigate this remodeling, culminating in cognitive impairment. The first, referred to as the 'inflammation-first' model, involves an excessive accumulation of TRM CD8+ T cells in the aged brain, reflecting analogous effects in other tissues. This accumulation may reach a critical threshold, at which point IFNγ production initiates the remodeling process. The second pathway, termed the 'neuron-first model,' posits that an extended lack of stimulation in selected brain regions might wrongly activate the type of remodeling seen in whisker-removed neuronal bundles. In this scenario, type 1 IFN would initiate the remodeling events and enhance the antigen-presentation abilities of microglia, leading to the accumulation of TRM CD8+ T cells and the production of IFNγ.

While this model remains speculative, it aligns with the established protective effects of cognitive engagement during aging. This alignment raises the intriguing possibility of a synergistic approach between cognitive engagement and anti-inflammatory treatments as preventive measures against cognitive decline in the aging population.

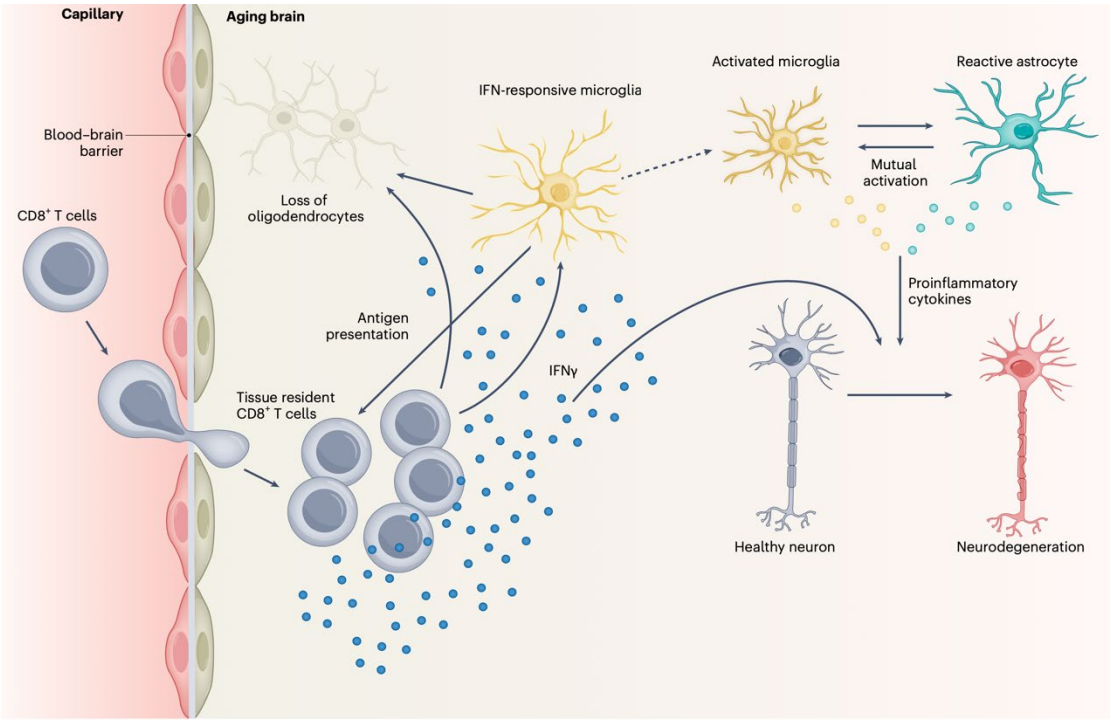

Figure 6: The IFN-CD8 axis.

Our discoveries in Manuscript 2.2 (Kaya et al., 2022) elucidate a novel mechanism associating TRM CD8+ T cells with neurodegeneration during aging (Figure 5) and underscore the potential for numerous therapeutic interventions. The immunological compartment, unlike the neuronal one, is replete with a wealth of validated biologics and small molecule drugs that target various facets of CD8+ T cell biology. Immediate targets, such as the IFN pathway, can be directly interfered with through Janus kinase inhibitors. Additionally, the broad blockade of CD8+ T cell activation can be achieved with a range of therapeutics currently in use for autoimmune and inflammatory conditions. Although the exact communication across CD8+ T cells, microglia and oligodendrocytes and the link to IFN signaling remain to be established, these results support the hypothesis that cytotoxic CD8+ T cells contribute to age-associated white matter decay (Goldmann et al., 2015).

3.3 CD8+ T cells in Neurodegeneration

There has been a growing body of work drawing the connection between CD8+ T cells and neurodegeneration in the context of different conditions such as AD (X. Chen et al., 2023) and ALS (Campisi et al., 2022). Several months after the publication of Manuscript 2.2, a study investigating the role of immunity in response to taupathy came out. Our work focused on normal aging and the cellular responses related to aging, but Chen et al. instead focused on Alzheimer's disease and the role of T-cells in AD patients and models.

Alzheimer's disease is marked by the accumulation of amyloid-β (Aβ) protein and tau protein in the brain. However, brain atrophy is more closely associated with tau accumulation than with Aβ deposition (Giannakopoulos et al., 2003). The researchers used mice models with either Aβ deposition or tauopathy to investigate whether tau triggers a specific cellular response that leads to atrophy.

Previous studies have indicated an inflammatory immune response in mouse models of neurodegeneration (Keren-Shaul et al., 2017) and in humans with Alzheimer's disease (Campisi et al., 2022). Chen et al. focused on immune cells as potential drivers of tau-specific neurodegeneration. They isolated immune cells from the brains of mice with Aβ deposition and tauopathy and used single-cell RNA sequencing to identify cell types based on gene expression. The analysis revealed 12 immune-cell populations in both models, with a significantly higher number of T cells in the brains of tauopathy mice.

The researchers validated these findings by examining brain tissue from mice and humans who had died from Alzheimer's disease. They found that T cells had accumulated in areas of the brain associated with learning, memory, and tau accumulation, suggesting that T cells respond to tau and may contribute to neuronal damage and cognitive defects associated with Alzheimer's.

T cells are activated when their receptor binds to an antigen presented by another cell. The researchers found that many microglia in tauopathy mice had adopted a disease-associated state (Keren-Shaul et al., 2017) or activated immune response-triggering signaling pathways (Kaya et al., 2022). These microglia expressed MHC II molecules, essential for antigen presentation, and were in close proximity to CD8+ T cells in brain slices from tauopathy mice. In vitro experiments showed that culturing microglia and T cells together with a foreign antigen resulted in T-cell proliferation.

Based on these findings, Chen et al. hypothesized that microglia and T cells work together to drive brain atrophy in response to tau. They tested this hypothesis by administering a drug or an antibody to tauopathy mice that resulted in the death of microglia or T cells, respectively. Both treatments led to a significant decrease in brain atrophy and reduced signs of tau's harmful effects when given during neurodegeneration development. Furthermore, T-cell depletion led to near-normal performance in various memory and learning tests. The interaction between T cells and microglia was further supported by the observation that depletion of microglia reduced T-cell numbers in the brain, and T-cell depletion reverted microglia to a state more like that seen in disease-free brains.

The researchers injected tauopathy mice with an anti-PD-1 antibody, used in cancer immunotherapy, which triggers a chain reaction resulting in T-cell activation. Short-term anti-PD-1 treatment increased the proportion of regulatory T cells, which can inhibit activated T cells, and long-term anti-PD-1 treatment reduced neurodegeneration and tau accumulation, as shown in other studies8,9.

Overall, both the approach and the outcomes from Chen et al.'s research align with our results, offering invaluable insight into the interaction between CD8+ T cells and neurodegeneration.

3.4 Antigen Recognition and Presentation

There are still critical questions that are left unanswered. For instance, what is the exact mechanism of antigen presentation in the brain? Normally, the process of antigen presentation and T-cell activation takes place in lymph nodes, and it involves specialized antigen-presenting cells. Ours and results from other studies suggest a role for microglia – a cell type that is not as effective as some other cell types as an antigen-presenting cell (Mundt et al., 2019). It's possible that a specific group or condition of microglia possess strong antigen-presentation capabilities. Another possibility is that specialized immune cells known as macrophages, located at the border of the brain, could assist in presenting antigens. A third alternative could be that other types of cells are responsible for presenting antigens to regulatory and CD8+ T cells.

Another vital question is; Which antigens are being recognized by T cells during the process of aging and neurodegeneration? T cells possess the unique ability to recognize specific antigens via their T-cell receptors (TCRs). This recognition is facilitated by a complex genetic recombination process during T cell development, leading to a diverse array of TCRs. The diversity of these TCRs enables T cells to recognize a broad range of antigens. Upon recognizing a specific antigen, T cells undergo clonal expansion, thereby increasing the number of T cells capable of identifying that particular antigen. This clonal expansion is a crucial element of adaptive immunity, facilitating a rapid and specific immune response against a specific pathogen (Buggert et al., 2023).

TCR sequences can serve as molecular 'barcodes' for T cells. Advanced sequencing technologies, such as next-generation sequencing (NGS), can provide a comprehensive view of the TCR repertoire, enabling the identification and tracking of specific T cell clones. Interestingly, research has shown that some T cell clones from Alzheimer's Disease (AD) patients react to antigens derived from the Epstein-Barr Virus (EBV) (Gate et al., 2020; Piehl et al., 2022). This observation is significant as it suggests a po-

tential role of EBV, or cross-reactive antigens, in the pathogenesis of AD. However, EBV is a ubiquitous infection, making it challenging to definitively establish its role in neurodegeneration.

Epidemiological studies have strongly highlighted a link between EBV and neurodegeneration, particularly in the case of multiple sclerosis (MS). One large-scale study involving over ten million US army personnel showed that individuals who became EBV positive had a 32-fold increase in the risk of MS diagnosis compared to those who remained EBV negative (Soldan & Lieberman, 2023). Another study established a significant correlation between multiple viral exposures, including EBV, and an increased risk of various neurodegenerative diseases (Levine et al., 2023).

Despite these correlations, understanding the exact mechanisms by which EBV or similar infections contribute to the development of neurodegenerative diseases remains a complex task. This complexity is due to inconsistencies in the detection of antigens, viruses, or neoantigens in brains affected by neurodegeneration or MS lesions. Furthermore, these foreign entities activate specific T-cell clones, which may also recognize brain-specific antigens, adding another layer of complexity to the issue.

3.5 New Horizons

As new technologies arise, we are able to resolve information from distinct modalities within a cell type of interest. On top of the transcriptomics data using scRNA-seq platforms, we, now, have the capability of extracting information from many other branches of biological information. For instance, an integrated platform of multi-OMICS and machine learning could be utilized. The platform described in (Vazquez-Lombardi et al., 2022) provides a good foundation to build upon and improve. The method in question provides a novel approach to understanding the complex relationship between T cell biology and neurodegeneration. It combines the power of machine

learning with multi-OMICs data to predict specific T cell clones associated with neurodegeneration and their corresponding targets.

The process begins with the use of a CRISPR/Cas9-mediated immune cell reprogramming platform. This platform employs oligonucleotides with degenerate codons to generate site-directed mutagenesis libraries in mammalian cells. Essentially, this strategy reprograms the immune cells, which is a crucial step in controlling and engineering immunity. This reprogramming allows for the creation of a diverse array of T cell clones, which can then be studied in relation to neurodegenerative processes.

Building on this foundation, a directed evolution platform is used to amplify the T cell clones linked to neurodegeneration. This amplification process allows for the validation and expansion of targets, providing a richer, more detailed dataset for analysis.

The data collected from these processes is then processed through robust machine learning models. These models are capable of handling the complex, multi-dimensional data and can identify patterns and relationships that may not be immediately apparent to human researchers. This allows for a comprehensive understanding of both mouse and human T cell clones and their connection to neurodegeneration.

The proposed platform presents an innovative approach to understanding neurodegeneration through the lens of T cell biology. The T cell receptor (TCR) can serve as a unique identifier for T cell clones, given the low probability of identical V(D)J rearrangements in individual T cells undergoing VDJ recombination. This means that an increase in specific TCR frequency could be indicative of antigen-specific immune responses.

To facilitate extensive analysis, both bulk and single-cell sequencing strategies could be employed to delineate the TCR repertoire. Machine learning can then be used to identify complex patterns in TCR sequencing data, which would help assess the diversity of the adaptive immune system and model TCR sequence determinants of antigen specificity. Deep unsupervised clustering techniques could further improve the classi-

fication of antigen-specific TCRs and extraction of these from noisy single-cell RNA-Seq data.

One of the potential applications of machine learning in this context is the estimation of the likelihood of a T cell clone targeting diseased CNS tissue. Furthermore, machine learning approaches can be applied to multi-omics training data, including single-cell TCR repertoire and transcriptome sequencing. This could help identify clonal and transcriptional phenotypes potentially associated with neurodegeneration and functional decline.

Published TCR repertoires could be used to guide the selection of clones already correlated with CNS, which would allow for the pre-training of machine learning models from the start of the project. This multi-omics trained machine learning model could then identify TCR repertoires targeting the CNS, potentially paving the way for novel drug targets and pharmacological interventions.

The ultimate goal of this approach could be the machine learning-guided discovery of a novel TCR-based biomarker for neurodegeneration in mice. Such a biomarker could serve as a diagnostic tool, refine disease definitions, improve patient stratification, and enhance diagnostic accuracy, thereby setting the stage for future biomarker validation.

Spatial transcriptomics is a revolutionary technique that has seen rapid improvement lately and could be used to understand the spatial distribution and subtype of T-cells within the brain. This could be achieved by using the multiplexed error-robust fluorescence in situ hybridization (MERFISH) technique in conjunction with single-nuclear RNA sequencing (snRNA-seq). MERFISH is a powerful tool that can simultaneously measure hundreds to thousands of transcripts with subcellular resolution, offering a detailed view of cellular activity.

The potential of MERFISH in investigating T-cells and their impact within the brain has been demonstrated in a study published by our lab (Androvic et al., 2023). This study not only identified T-cell types but also interferon-responsive (IR) glial states, which have been implicated in CNS pathology. Importantly, the study showcased the co-localization of IR glia with T-cells in the brain, highlighting the potential of MERFISH in characterizing T-cells and their impact on the CNS.

Building on this groundwork, there is an opportunity to deepen our understanding of cell state identities to potentially suppress the transcriptional signatures of the identified IR glia states. This could provide further insights into the role of T-cells and IR glia in the brain, and their implications for neurodegenerative diseases.

3.6 Other Publications

I have also contributed to research articles not included in this dissertation, focusing on a distinct subject: the mechanisms of SARS-CoV-2 cell entry (Cantuti-Castelvetri et al., 2020; Jocher et al., 2022). As the severity of the pandemic escalated in early 2020, there was an urgent need for the scientific community to respond quickly. More research was required to understand precisely how the virus functioned. Fortunately, my specific skillset allowed me to make valuable contributions to this essential area of research.

A related coronavirus, SARS-CoV caused a smaller outbreak in 2003, possibly due to its infection mainly in the lower respiratory system, unlike SARS-CoV-2, which spreads quickly through the throat. Both viruses use the same cellular receptor, ACE2. Our hypothesis was that SARS-CoV-2's enhanced spreading may be due to a specific cleavage site in its spike protein, absent in SARS-CoV, and found in other viruses like Ebola and HIV. This site increases pathogenicity by priming fusion activity and might create additional binding sites. The cleavage of this site exposes a sequence that can bind to and activate neuropilin (NRP1 and NRP2) receptors at the cell surface.

My specific contribution to the study was the acquisition and the analysis of published scRNA-seq datasets. First, I analyzed whether NRP1 expression was linked to virus RNA detection in single-cell transcriptomes using published data from infected human bronchial cells and cells from severely affected COVID-19 patients (Liao et al., 2020). We found that NRP1, FURIN, and TMPRSS11A were more prevalent in SARS-CoV-2-infected cells compared to noninfected ones, with increased protein expression after infection. Additionally, RNA expression of NRP1 and its homolog NRP2 was higher in SARS-CoV-2-positive cells compared to adjacent cells in the samples from severely affected COVID-19 patients. Next, I analyzed the expression patterns of ACE2, NRP1, and NRP2 in published datasets of human lung tissue (Han et al., 2020) and olfactory epithelium (Durante et al., 2020), since the presence of virus receptors and entry cofactors on host cells' surface influences infectivity. While ACE2 was found at minimal levels, both NRP1 and NRP2 were extensively expressed in nearly all pulmonary and olfactory cells, with endothelial cells showing the highest expression levels. Through comprehensive experiments and analyses, we showed NRP1 potentiates SARS-CoV-2 infectivity (Cantuti-Castelvetri et al., 2020).

I participated in another study focused on SARS-CoV-2 cell entry (Jocher et al., 2022), where my role mirrored my contributions to the Science paper mentioned earlier. Specifically, I analyzed publicly available scRNA-seq datasets, examining the expression patterns of ADAM10, ADAM17, and other proposed cell entry factors. Overall, I have utilized my expertise in acquiring and handling scRNA-seq datasets to contribute to these significant studies.

BIBLIOGRAPHY

Alber, J., Alladi, S., Bae, H.-J., Barton, D. A., Beckett, L. A., Bell, J. M., Berman, S. E., Biessels, G. J., Black, S. E., Bos, I., Bowman, G. L., Brai, E., Brickman, A. M., Callahan, B. L., Corriveau, R. A., Fossati, S., Gottesman, R. F., Gustafson, D. R., Hachinski, V., … Hainsworth, A. H. (2019). White matter hyperintensities in vascular contributions to cognitive impairment and dementia (VCID): Knowledge gaps and opportunities. *Alzheimer's & Dementia : Translational Research & Clinical Interventions*, *5*, 107. https://doi.org/10.1016/j.trci.2019.02.001

Allfrey, V. G., Faulkner, R., & Mirsky, A. E. (1964). ACETYLATION AND METHYLATION OF HISTONES AND THEIR POSSIBLE ROLE IN THE REGULATION OF RNA SYNTHESIS. *Proceedings of the National Academy of Sciences of the United States of America*, *51*(5), 786–794. https://doi.org/10.1073/pnas.51.5.786

Alspach, E., Lussier, D. M., & Schreiber, R. D. (2019). Interferon γ and Its Important Roles in Promoting and Inhibiting Spontaneous and Therapeutic Cancer Immunity. *Cold Spring Harbor Perspectives in Biology*, *11*(3), a028480. https://doi.org/10.1101/cshperspect.a028480

Alves de Lima, K., Rustenhoven, J., & Kipnis, J. (2020). Meningeal Immunity and Its Function in Maintenance of the Central Nervous System in Health and Disease. *Annual Review of Immunology*, *38*(1), 597–620. https://doi.org/10.1146/annurev-immunol-102319-103410

Alwine, J. C., Kemp, D. J., & Stark, G. R. (1977). Method for detection of specific RNAs in agarose gels by transfer to diazobenzyloxymethyl-paper and hybridization with DNA probes. *Proceedings of the National Academy of Sciences of the United States of America*, *74*(12), 5350–5354. https://doi.org/10.1073/pnas.74.12.5350

Androvic, P., Schifferer, M., Perez Anderson, K., Cantuti-Castelvetri, L., Jiang, H., Ji, H., Liu, L., Gouna, G., Berghoff, S. A., Besson-Girard, S., Knoferle, J., Simons, M., & Gokce, O. (2023). Spatial Transcriptomics-correlated Electron Microscopy maps transcriptional and ultrastructural responses to brain injury. *Nature Communications*, *14*(1), Article 1. https://doi.org/10.1038/s41467-023-39447-9

Ayub, M., & Bae, H. K. J. & J. (2021). The blood cerebrospinal fluid barrier orchestrates immunosurveillance, immunoprotection, and immunopathology in the central nervous system. *BMB Reports*, *54*(4), 196–202. https://doi.org/10.5483/BMBRep.2021.54.4.205

Baruch, K., Deczkowska, A., David, E., Castellano, J. M., Miller, O., Kertser, A., Berkutzki, T., Barnett-Itzhaki, Z., Bezalel, D., Wyss-Coray, T., Amit, I., & Schwartz, M. (2014). Aging-induced type I

interferon response at the choroid plexus negatively affects brain function. *Science*, *346*(6205), 89–93. https://doi.org/10.1126/science.1252945

Bethlehem, R. a. I., Seidlitz, J., White, S. R., Vogel, J. W., Anderson, K. M., Adamson, C., Adler, S., Alexopoulos, G. S., Anagnostou, E., Areces-Gonzalez, A., Astle, D. E., Auyeung, B., Ayub, M., Bae, J., Ball, G., Baron-Cohen, S., Beare, R., Bedford, S. A., Benegal, V., … Alexander-Bloch, A. F. (2022). Brain charts for the human lifespan. *Nature*, *604*(7906), Article 7906. https://doi.org/10.1038/s41586-022-04554-y

Bianchin, M. M., Martin, K. C., de Souza, A. C., de Oliveira, M. A., & Rieder, C. R. de M. (2010). Nasu-Hakola disease and primary microglial dysfunction. *Nature Reviews. Neurology*, *6*(9), 2 p following 523. https://doi.org/10.1038/nrneurol.2010.17-c1

Bradl, M., & Lassmann, H. (2010). Oligodendrocytes: Biology and pathology. *Acta Neuropathologica*, *119*(1), 37–53. https://doi.org/10.1007/s00401-009-0601-5

Brent, L. (2016). Transplantation tolerance – a historical introduction. *Immunology*, *147*(3), 267–268. https://doi.org/10.1111/imm.12567

Buggert, M., Price, D. A., Mackay, L. K., & Betts, M. R. (2023). Human circulating and tissue-resident memory CD8+ T cells. *Nature Immunology*, *24*(7), Article 7. https://doi.org/10.1038/s41590-023-01538-6

Burnet, F. M. (1970). The concept of immunological surveillance. *Progress in Experimental Tumor Research*, *13*, 1–27. https://doi.org/10.1159/000386035

Campisi, L., Chizari, S., Ho, J. S. Y., Gromova, A., Arnold, F. J., Mosca, L., Mei, X., Fstkchyan, Y., Torre, D., Beharry, C., Garcia-Forn, M., Jiménez-Alcázar, M., Korobeynikov, V. A., Prazich, J., Fayad, Z. A., Seldin, M. M., De Rubeis, S., Bennett, C. L., Ostrow, L. W., … Marazzi, I. (2022). Clonally expanded CD8 T cells characterize amyotrophic lateral sclerosis-4. *Nature*, *606*(7916), Article 7916. https://doi.org/10.1038/s41586-022-04844-5

Cantell, K., Hirvonen, S., Kauppinen, H.-L., & Myllylä, G. (1981). *[4] Production of interferon in human leukocytes from normal donors with the use of Sendai virus*. *78*, 29–38. https://doi.org/10.1016/0076-6879(81)78094-7

Cantell, K., Hirvonen, S., & Koistinen, V. (1981). Partial purification of human leukocyte interferon on a large scale. *Methods in Enzymology*, *78*(Pt A), 499–505. https://doi.org/10.1016/0076-6879(81)78161-8

Cantoni, C., Bollman, B., Licastro, D., Xie, M., Mikesell, R., Schmidt, R., Yuede, C. M., Galimberti, D., Olivecrona, G., Klein, R. S., Cross, A. H., Otero, K., & Piccio, L. (2015). TREM2 regulates

microglial cell activation in response to demyelination in vivo. *Acta Neuropathologica*, *129*(3), 429–447. https://doi.org/10.1007/s00401-015-1388-1

Cantuti-Castelvetri, L., Ojha, R., Pedro, L. D., Djannatian, M., Franz, J., Kuivanen, S., van der Meer, F., Kallio, K., Kaya, T., Anastasina, M., Smura, T., Levanov, L., Szirovicza, L., Tobi, A., Kallio-Kokko, H., Österlund, P., Joensuu, M., Meunier, F. A., Butcher, S. J., … Simons, M. (2020). Neuropilin-1 facilitates SARS-CoV-2 cell entry and infectivity. *Science*, *370*(6518), 856–860. https://doi.org/10.1126/science.abd2985

Carmona, J. J., & Michan, S. (2016). Biology of Healthy Aging and Longevity. *Revista De Investigacion Clinica; Organo Del Hospital De Enfermedades De La Nutricion*, *68*(1), 7–16.

Carson, M. J., Doose, J. M., Melchior, B., Schmid, C. D., & Ploix, C. C. (2006). CNS immune privilege: Hiding in plain sight. *Immunological Reviews*, *213*, 48–65. https://doi.org/10.1111/j.1600-065X.2006.00441.x

Chakrabarty, P., Ceballos-Diaz, C., Beccard, A., Janus, C., Dickson, D., Golde, T. E., & Das, P. (2010). IFN-γ Promotes Complement Expression and Attenuates Amyloid Plaque Deposition in Amyloid β Precursor Protein Transgenic Mice. *The Journal of Immunology*, *184*(9), 5333–5343. https://doi.org/10.4049/jimmunol.0903382

Chausse, B., Lewen, A., Poschet, G., & Kann, O. (2020). Selective inhibition of mitochondrial respiratory complexes controls the transition of microglia into a neurotoxic phenotype in situ. *Brain, Behavior, and Immunity*, *88*, 802–814. https://doi.org/10.1016/j.bbi.2020.05.052

Chen, X., Firulyova, M., Manis, M., Herz, J., Smirnov, I., Aladyeva, E., Wang, C., Bao, X., Finn, M. B., Hu, H., Shchukina, I., Kim, M. W., Yuede, C. M., Kipnis, J., Artyomov, M. N., Ulrich, J. D., & Holtzman, D. M. (2023). Microglia-mediated T cell infiltration drives neurodegeneration in tauopathy. *Nature*, *615*(7953), Article 7953. https://doi.org/10.1038/s41586-023-05788-0

Chen, Y., Strickland, M. R., Soranno, A., & Holtzman, D. M. (2021). Apolipoprotein E: Structural Insights and Links to Alzheimer Disease Pathogenesis. *Neuron*, *109*(2), 205–221. https://doi.org/10.1016/j.neuron.2020.10.008

Clark, R., & Kupper, T. (2005). Old Meets New: The Interaction Between Innate and Adaptive Immunity. *Journal of Investigative Dermatology*, *125*(4), 629–637. https://doi.org/10.1111/j.0022-202X.2005.23856.x

Correale, J., & Ysrraelit, M. C. (2022). Multiple Sclerosis and Aging: The Dynamics of Demyelination and Remyelination. *ASN Neuro*, *14*, 17590914221118502. https://doi.org/10.1177/17590914221118502

Crick, F. H. (1958). On protein synthesis. *Symposia of the Society for Experimental Biology*, *12*, 138–163.

Crow, Y. J., & Manel, N. (2015). Aicardi–Goutières syndrome and the type I interferonopathies. *Nature Reviews Immunology*, *15*(7), Article 7. https://doi.org/10.1038/nri3850

Cserr, H. F., Harling-Berg, C. J., & Knopf, P. M. (1992). Drainage of brain extracellular fluid into blood and deep cervical lymph and its immunological significance. *Brain Pathology (Zurich, Switzerland)*, *2*(4), 269–276. https://doi.org/10.1111/j.1750-3639.1992.tb00703.x

Dean, D. C., Jerskey, B. A., Chen, K., Protas, H., Thiyyagura, P., Roontiva, A., O'Muircheartaigh, J., Dirks, H., Waskiewicz, N., Lehman, K., Siniard, A. L., Turk, M. N., Hua, X., Madsen, S. K., Thompson, P. M., Fleisher, A. S., Huentelman, M. J., Deoni, S. C. L., & Reiman, E. M. (2014). Brain differences in infants at differential genetic risk for late-onset Alzheimer disease: A cross-sectional imaging study. *JAMA Neurology*, *71*(1), 11–22. https://doi.org/10.1001/jamaneurol.2013.4544

Dobin, A., Davis, C. A., Schlesinger, F., Drenkow, J., Zaleski, C., Jha, S., Batut, P., Chaisson, M., & Gingeras, T. R. (2013). STAR: Ultrafast universal RNA-seq aligner. *Bioinformatics*, *29*(1), 15–21. https://doi.org/10.1093/bioinformatics/bts635

Dobin, A., & Gingeras, T. R. (2015). Mapping RNA-seq Reads with STAR. *Current Protocols in Bioinformatics*, *51*, 11.14.1-11.14.19. https://doi.org/10.1002/0471250953.bi1114s51

Dogariu, O. A., Dogariu, I., Vasile, C. M., Berceanu, M. C., Raicea, V. C., Albu, C. V., & Gheonea, I. A. (2023). Diagnosis and treatment of Watershed strokes: A narrative review. *Journal of Medicine and Life*, *16*(6), 842–850. https://doi.org/10.25122/jml-2023-0127

Dulken, B. W., Buckley, M. T., Navarro Negredo, P., Saligrama, N., Cayrol, R., Leeman, D. S., George, B. M., Boutet, S. C., Hebestreit, K., Pluvinage, J. V., Wyss-Coray, T., Weissman, I. L., Vogel, H., Davis, M. M., & Brunet, A. (2019). Single-cell analysis reveals T cell infiltration in old neurogenic niches. *Nature*, *571*(7764), Article 7764. https://doi.org/10.1038/s41586-019-1362-5

Durante, M. A., Kurtenbach, S., Sargi, Z. B., Harbour, J. W., Choi, R., Kurtenbach, S., Goss, G. M., Matsunami, H., & Goldstein, B. J. (2020). Single-cell analysis of olfactory neurogenesis and differentiation in adult humans. *Nature Neuroscience*, *23*(3), 323–326. https://doi.org/10.1038/s41593-020-0587-9

Elobeid, A., Libard, S., Leino, M., Popova, S. N., & Alafuzoff, I. (2016). Altered proteins in the aging brain. *Journal of Neuropathology and Experimental Neurology*, *75*(4), Article 4. https://doi.org/10.1093/jnen/nlw002

Engelhardt, B., & Coisne, C. (2011). Fluids and barriers of the CNS establish immune privilege by confining immune surveillance to a two-walled castle moat surrounding the CNS castle. *Fluids and Barriers of the CNS*, *8*(1), 4. https://doi.org/10.1186/2045-8118-8-4

Escoubas, C. C., Dorman, L. C., Nguyen, P. T., Lagares-Linares, C., Nakajo, H., Anderson, S. R., Cuevas, B., Vainchtein, I. D., Silva, N. J., Xiao, Y., Lidsky, P. V., Wang, E. Y., Taloma, S. E., Nakao-Inoue, H., Schwer, B., Andino, R., Nowakowski, T. J., & Molofsky, A. V. (2023). *Type I interferon responsive microglia shape cortical development and behavior* (p. 2021.04.29.441889). bioRxiv. https://doi.org/10.1101/2021.04.29.441889

Filiano, A. J., Xu, Y., Tustison, N. J., Marsh, R. L., Baker, W., Smirnov, I., Overall, C. C., Gadani, S. P., Turner, S. D., Weng, Z., Peerzade, S. N., Chen, H., Lee, K. S., Scott, M. M., Beenhakker, M. P., Litvak, V., & Kipnis, J. (2016). Unexpected role of interferon-γ in regulating neuronal connectivity and social behaviour. *Nature*, *535*(7612), Article 7612. https://doi.org/10.1038/nature18626

Frigerio, C. S., Wolfs, L., Fattorelli, N., Thrupp, N., Voytyuk, I., Schmidt, I., Mancuso, R., Chen, W.-T., Woodbury, M. E., Srivastava, G., Möller, T., Hudry, E., Das, S., Saido, T., Karran, E., Hyman, B., Perry, V. H., Fiers, M., & Strooper, B. D. (2019). The Major Risk Factors for Alzheimer's Disease: Age, Sex, and Genes Modulate the Microglia Response to Aβ Plaques. *Cell Reports*, *27*(4), 1293-1306.e6. https://doi.org/10.1016/j.celrep.2019.03.099

Fujimoto, M., & Naka, T. (2010). SOCS1, a Negative Regulator of Cytokine Signals and TLR Responses, in Human Liver Diseases. *Gastroenterology Research and Practice*, *2010*, 470468. https://doi.org/10.1155/2010/470468

Galea, I., Bechmann, I., & Perry, V. H. (2007). What is immune privilege (not)? *Trends in Immunology*, *28*(1), 12–18. https://doi.org/10.1016/j.it.2006.11.004

Garber, C., Soung, A., Vollmer, L. L., Kanmogne, M., Last, A., Brown, J., & Klein, R. S. (2019). T cells promote microglia-mediated synaptic elimination and cognitive dysfunction during recovery from neuropathogenic flaviviruses. *Nature Neuroscience*, *22*(8), Article 8. https://doi.org/10.1038/s41593-019-0427-y

Gate, D., Saligrama, N., Leventhal, O., Yang, A. C., Unger, M. S., Middeldorp, J., Chen, K., Lehallier, B., Channappa, D., De Los Santos, M. B., McBride, A., Pluvinage, J., Elahi, F., Tam, G. K.-Y., Kim, Y., Greicius, M., Wagner, A. D., Aigner, L., Galasko, D. R., … Wyss-Coray, T. (2020). Clonally expanded CD8 T cells patrol the cerebrospinal fluid in Alzheimer's disease. *Nature*, *577*(7790), Article 7790. https://doi.org/10.1038/s41586-019-1895-7

Giannakopoulos, P., Herrmann, F. R., Bussière, T., Bouras, C., Kövari, E., Perl, D. P., Morrison, J. H., Gold, G., & Hof, P. R. (2003). Tangle and neuron numbers, but not amyloid load, predict cognitive status in Alzheimer's disease. *Neurology*, *60*(9), 1495–1500. https://doi.org/10.1212/01.WNL.0000063311.58879.01

Giroux, M., Schmidt, M., & Descoteaux, A. (2003). IFN-γ-Induced MHC Class II Expression: Transactivation of Class II Transactivator Promoter IV by IFN Regulatory Factor-1 is Regulated by Protein Kinase C-α 1. *The Journal of Immunology*, *171*(8), 4187–4194. https://doi.org/10.4049/jimmunol.171.8.4187

Goldmann, T., Zeller, N., Raasch, J., Kierdorf, K., Frenzel, K., Ketscher, L., Basters, A., Staszewski, O., Brendecke, S. M., Spiess, A., Tay, T. L., Kreutz, C., Timmer, J., Mancini, G. M., Blank, T., Fritz, G., Biber, K., Lang, R., Malo, D., … Prinz, M. (2015). USP18 lack in microglia causes destructive interferonopathy of the mouse brain. *The EMBO Journal*, *34*(12), 1612–1629. https://doi.org/10.15252/embj.201490791

Gross, A., Schoendube, J., Zimmermann, S., Steeb, M., Zengerle, R., & Koltay, P. (2015). Technologies for Single-Cell Isolation. *International Journal of Molecular Sciences*, *16*(8), Article 8. https://doi.org/10.3390/ijms160816897

Grunberger, D., Weinstein, I. B., & Jacobson, K. B. (1969). Codon recognition by enzymatically mischarged valine transfer ribonucleic acid. *Science (New York, N.Y.)*, *166*(3913), 1635–1637. https://doi.org/10.1126/science.166.3913.1635

Guan, T., & Kong, J. (2015). Functional regeneration of the brain: White matter matters. *Neural Regeneration Research*, *10*(3), 355–356. https://doi.org/10.4103/1673-5374.153675

Guerreiro, R., Wojtas, A., Bras, J., Carrasquillo, M., Rogaeva, E., Majounie, E., Cruchaga, C., Sassi, C., Kauwe, J. S. K., Younkin, S., Hazrati, L., Collinge, J., Pocock, J., Lashley, T., Williams, J., Lambert, J.-C., Amouyel, P., Goate, A., Rademakers, R., … Alzheimer Genetic Analysis Group. (2013). TREM2 variants in Alzheimer's disease. *The New England Journal of Medicine*, *368*(2), 117–127. https://doi.org/10.1056/NEJMoa1211851

Haan, C., Kreis, S., Margue, C., & Behrmann, I. (2006). Jaks and cytokine receptors—An intimate relationship. *Biochemical Pharmacology*, *72*(11), 1538–1546. https://doi.org/10.1016/j.bcp.2006.04.013

Habibi, L., Ebtekar, M., & Jameie, S. B. (2009). Immune and Nervous Systems Share Molecular and Functional Similarities: Memory Storage Mechanism. *Scandinavian Journal of Immunology*, *69*(4), 291–301. https://doi.org/10.1111/j.1365-3083.2008.02215.x

Hammond, T. R., Dufort, C., Dissing-Olesen, L., Giera, S., Young, A., Wysoker, A., Walker, A. J., Gergits, F., Segel, M., Nemesh, J., Marsh, S. E., Saunders, A., Macosko, E., Ginhoux, F., Chen, J., Franklin, R. J. M., Piao, X., McCarroll, S. A., & Stevens, B. (2019). Single-Cell RNA Sequencing of Microglia throughout the Mouse Lifespan and in the Injured Brain Reveals Complex Cell-State Changes. *Immunity*, *50*(1), 253-271.e6. https://doi.org/10.1016/j.immuni.2018.11.004

Han, X., Zhou, Z., Fei, L., Sun, H., Wang, R., Chen, Y., Chen, H., Wang, J., Tang, H., Ge, W., Zhou, Y., Ye, F., Jiang, M., Wu, J., Xiao, Y., Jia, X., Zhang, T., Ma, X., Zhang, Q., … Guo, G. (2020). Construction of a human cell landscape at single-cell level. *Nature*, *581*(7808), 303–309. https://doi.org/10.1038/s41586-020-2157-4

Harling-Berg, C., Knopf, P. M., Merriam, J., & Cserr, H. F. (1989). Role of cervical lymph nodes in the systemic humoral immune response to human serum albumin microinfused into rat cerebrospinal fluid. *Journal of Neuroimmunology*, *25*(2–3), 185–193. https://doi.org/10.1016/0165-5728(89)90136-7

Hase, Y., Horsburgh, K., Ihara, M., & Kalaria, R. N. (2018). White matter degeneration in vascular and other ageing-related dementias. *Journal of Neurochemistry*, *144*(5), 617–633. https://doi.org/10.1111/jnc.14271

He, Z., Yang, Y., Xing, Z., Zuo, Z., Wang, R., Gu, H., Qi, F., & Yao, Z. (2020). Intraperitoneal injection of IFN-γ restores microglial autophagy, promotes amyloid-β clearance and improves cognition in APP/PS1 mice. *Cell Death & Disease*, *11*(6), Article 6. https://doi.org/10.1038/s41419-020-2644-4

Head, S. R., Komori, H. K., LaMere, S. A., Whisenant, T., Van Nieuwerburgh, F., Salomon, D. R., & Ordoukhanian, P. (2014). Library construction for next-generation sequencing: Overviews and challenges. *BioTechniques*, *56*(2), 61–64, 66, 68, passim. https://doi.org/10.2144/000114133

Henle, W. (1950). Interference Phenomena Between Animal Viruses: A Review. *The Journal of Immunology*, *64*(3), 203–236. https://doi.org/10.4049/jimmunol.64.3.203

Holliday, R., & Pugh, J. E. (1975). DNA modification mechanisms and gene activity during development. *Science (New York, N.Y.)*, *187*(4173), 226–232.

Horwitz, M. S., Evans, C. F., Mcgavern, D. B., Rodriguez, M., & Oldstone, M. B. A. (1997). Primary demyelination in transgenic mice expressing interferon-γ. *Nature Medicine*, *3*(9), Article 9. https://doi.org/10.1038/nm0997-1037

Hotchkiss, R. D. (1948). The quantitative separation of purines, pyrimidines, and nucleosides by paper chromatography. *The Journal of Biological Chemistry*, *175*(1), 315–332.

Hou, Y., Dan, X., Babbar, M., Wei, Y., Hasselbalch, S. G., Croteau, D. L., & Bohr, V. A. (2019). Ageing as a risk factor for neurodegenerative disease. *Nature Reviews. Neurology*, *15*(10), 565–581. https://doi.org/10.1038/s41582-019-0244-7

Isaacs, A., & Lindenmann, J. (1957). Virus interference. I. The interferon. *Proceedings of the Royal Society of London. Series B, Biological Sciences*, *147*(927), 258–267. https://doi.org/10.1098/rspb.1957.0048

Isaacs, A., Lindenmann, J., & Valentine, R. C. (1957). Virus Interference. II. Some Properties of Interferon. *Proceedings of the Royal Society of London. Series B, Biological Sciences*, *147*(927), 268–273.

Ivashkiv, L. B. (2018). IFNγ: Signalling, epigenetics and roles in immunity, metabolism, disease and cancer immunotherapy. *Nature Reviews Immunology*, *18*(9), Article 9. https://doi.org/10.1038/s41577-018-0029-z

Jaitin, D. A., Roisman, L. C., Jaks, E., Gavutis, M., Piehler, J., Van der Heyden, J., Uze, G., & Schreiber, G. (2006). Inquiring into the Differential Action of Interferons (IFNs): An IFN-α2 Mutant with Enhanced Affinity to IFNAR1 Is Functionally Similar to IFN-β. *Molecular and Cellular Biology*, *26*(5), 1888–1897. https://doi.org/10.1128/MCB.26.5.1888-1897.2006

Jocher, G., Grass, V., Tschirner, S. K., Riepler, L., Breimann, S., Kaya, T., Oelsner, M., Hamad, M. S., Hofmann, L. I., Blobel, C. P., Schmidt-Weber, C. B., Gokce, O., Jakwerth, C. A., Trimpert, J., Kimpel, J., Pichlmair, A., & Lichtenthaler, S. F. (2022). ADAM10 and ADAM17 promote SARS-CoV-2 cell entry and spike protein-mediated lung cell fusion. *EMBO Reports*, *23*(6), e54305. https://doi.org/10.15252/embr.202154305

Kalaria, R. N., & Hase, Y. (2019). Neurovascular Ageing and Age-Related Diseases. *Sub-Cellular Biochemistry*, *91*, 477–499. https://doi.org/10.1007/978-981-13-3681-2_17

Kasahara, T., Hooks, J. J., Dougherty, S. F., & Oppenheim, J. J. (1983). Interleukin 2-mediated immune interferon (IFN-gamma) production by human T cells and T cell subsets. *The Journal of Immunology*, *130*(4), 1784–1789. https://doi.org/10.4049/jimmunol.130.4.1784

Kato, D., & Wake, H. (2019). Activity-Dependent Myelination. *Advances in Experimental Medicine and Biology*, *1190*, 43–51. https://doi.org/10.1007/978-981-32-9636-7_4

Kawamura, M., McVicar, D. W., Johnston, J. A., Blake, T. B., Chen, Y. Q., Lal, B. K., Lloyd, A. R., Kelvin, D. J., Staples, J. E., & Ortaldo, J. R. (1994). Molecular cloning of L-JAK, a Janus family protein-tyrosine kinase expressed in natural killer cells and activated leukocytes. *Proceedings of the National Academy of Sciences*, *91*(14), 6374–6378. https://doi.org/10.1073/pnas.91.14.6374

Kaya, T., Mattugini, N., Liu, L., Ji, H., Cantuti-Castelvetri, L., Wu, J., Schifferer, M., Groh, J., Martini, R., Besson-Girard, S., Kaji, S., Liesz, A., Gokce, O., & Simons, M. (2022). CD8+ T cells induce interferon-responsive oligodendrocytes and microglia in white matter aging. *Nature Neuroscience*, *25*(11), Article 11. https://doi.org/10.1038/s41593-022-01183-6

Keren-Shaul, H., Spinrad, A., Weiner, A., Matcovitch-Natan, O., Dvir-Szternfeld, R., Ulland, T. K., David, E., Baruch, K., Lara-Astaiso, D., Toth, B., Itzkovitz, S., Colonna, M., Schwartz, M., & Amit, I. (2017). A Unique Microglia Type Associated with Restricting Development of Alzheimer's Disease. *Cell*, *169*(7), 1276-1290.e17. https://doi.org/10.1016/j.cell.2017.05.018

Knight, E. (1975). Heterogeneity of purified mouse interferons. *Journal of Biological Chemistry*, *250*(11), 4139–4144. https://doi.org/10.1016/S0021-9258(19)41397-5

Köhler, A., & Hurt, E. (2007). Exporting RNA from the nucleus to the cytoplasm. *Nature Reviews. Molecular Cell Biology*, *8*(10), 761–773. https://doi.org/10.1038/nrm2255

Kornberg, R. D. (1974). Chromatin structure: A repeating unit of histones and DNA. *Science (New York, N.Y.)*, *184*(4139), 868–871. https://doi.org/10.1126/science.184.4139.868

Lafzi, A., Moutinho, C., Picelli, S., & Heyn, H. (2018). Tutorial: Guidelines for the experimental design of single-cell RNA sequencing studies. *Nature Protocols*, *13*(12), Article 12. https://doi.org/10.1038/s41596-018-0073-y

Laman, J. D., & Weller, R. O. (2013). Drainage of cells and soluble antigen from the CNS to regional lymph nodes. *Journal of Neuroimmune Pharmacology: The Official Journal of the Society on NeuroImmune Pharmacology*, *8*(4), 840–856. https://doi.org/10.1007/s11481-013-9470-8

Larner, A. C., Chaudhuri, A., & Darnell, J. E. (1986). Transcriptional induction by interferon. New protein(s) determine the extent and length of the induction. *The Journal of Biological Chemistry*, *261*(1), 453–459.

Larner, A. C., Jonak, G., Cheng, Y. S., Korant, B., Knight, E., & Darnell, J. E. (1984). Transcriptional induction of two genes in human cells by beta interferon. *Proceedings of the National Academy of Sciences*, *81*(21), 6733–6737. https://doi.org/10.1073/pnas.81.21.6733

Lee, A. J., & Ashkar, A. A. (2018). The Dual Nature of Type I and Type II Interferons. *Frontiers in Immunology*, *9*. https://www.frontiersin.org/articles/10.3389/fimmu.2018.02061

Lee-Kirsch, M. A. (2017). The Type I Interferonopathies. *Annual Review of Medicine*, *68*(1), 297–315. https://doi.org/10.1146/annurev-med-050715-104506

Levine, K. S., Leonard, H. L., Blauwendraat, C., Iwaki, H., Johnson, N., Bandres-Ciga, S., Ferrucci, L., Faghri, F., Singleton, A. B., & Nalls, M. A. (2023). Virus exposure and neurodegenerative

disease risk across national biobanks. *Neuron*, *111*(7), 1086-1093.e2. https://doi.org/10.1016/j.neuron.2022.12.029

Levy, D. E., Lew, D. J., Decker, T., Kessler, D. S., & Darnell, J. E. (1990). Synergistic interaction between interferon-alpha and interferon-gamma through induced synthesis of one subunit of the transcription factor ISGF3. *The EMBO Journal*, *9*(4), 1105–1111. https://doi.org/10.1002/j.1460-2075.1990.tb08216.x

Lew, D. J., Decker, T., & Darnell, J. E. (1989). Alpha interferon and gamma interferon stimulate transcription of a single gene through different signal transduction pathways. *Molecular and Cellular Biology*, *9*(12), 5404–5411. https://doi.org/10.1128/mcb.9.12.5404-5411.1989

Li, Q., Cheng, Z., Zhou, L., Darmanis, S., Neff, N. F., Okamoto, J., Gulati, G., Bennett, M. L., Sun, L. O., Clarke, L. E., Marschallinger, J., Yu, G., Quake, S. R., Wyss-Coray, T., & Barres, B. A. (2019). Developmental Heterogeneity of Microglia and Brain Myeloid Cells Revealed by Deep Single-Cell RNA Sequencing. *Neuron*, *101*(2), 207-223.e10. https://doi.org/10.1016/j.neuron.2018.12.006

Li, S., olde Heuvel, F., Rehman, R., Aousji, O., Froehlich, A., Li, Z., Jark, R., Zhang, W., Conquest, A., Woelfle, S., Schoen, M., O´Meara, C. C., Reinhardt, R. L., Voehringer, D., Kassubek, J., Ludolph, A., Huber-Lang, M., Knöll, B., Morganti-Kossmann, M. C., … Roselli, F. (2023). Interleukin-13 and its receptor are synaptic proteins involved in plasticity and neuroprotection. *Nature Communications*, *14*, 200. https://doi.org/10.1038/s41467-023-35806-8

Li, X., & Wang, C.-Y. (2021). From bulk, single-cell to spatial RNA sequencing. *International Journal of Oral Science*, *13*(1), 1–6. https://doi.org/10.1038/s41368-021-00146-0

Liao, M., Liu, Y., Yuan, J., Wen, Y., Xu, G., Zhao, J., Cheng, L., Li, J., Wang, X., Wang, F., Liu, L., Amit, I., Zhang, S., & Zhang, Z. (2020). Single-cell landscape of bronchoalveolar immune cells in patients with COVID-19. *Nature Medicine*, *26*(6), 842–844. https://doi.org/10.1038/s41591-020-0901-9

Liberto, G. D., Pantelyushin, S., Kreutzfeldt, M., Page, N., Musardo, S., Coras, R., Steinbach, K., Vincenti, I., Klimek, B., Lingner, T., Salinas, G., Lin-Marq, N., Staszewski, O., Jordão, M. J. C., Wagner, I., Egervari, K., Mack, M., Bellone, C., Blümcke, I., … Merkler, D. (2018). Neurons under T Cell Attack Coordinate Phagocyte-Mediated Synaptic Stripping. *Cell*, *175*(2), 458-471.e19. https://doi.org/10.1016/j.cell.2018.07.049

Linossi, E. M., Babon, J. J., Hilton, D. J., & Nicholson, S. E. (2013). Suppression of Cytokine Signaling: The SOCS perspective. *Cytokine & Growth Factor Reviews*, *24*(3), 10.1016/j.cytogfr.2013.03.005. https://doi.org/10.1016/j.cytogfr.2013.03.005

Louveau, A., Harris, T. H., & Kipnis, J. (2015). Revisiting the concept of CNS immune privilege. *Trends in Immunology*, *36*(10), 569–577. https://doi.org/10.1016/j.it.2015.08.006

Louveau, A., Smirnov, I., Keyes, T. J., Eccles, J. D., Rouhani, S. J., Peske, J. D., Derecki, N. C., Castle, D., Mandell, J. W., Lee, K. S., Harris, T. H., & Kipnis, J. (2015). Structural and functional features of central nervous system lymphatic vessels. *Nature*, *523*(7560), 337–341. https://doi.org/10.1038/nature14432

Luger, K., Mäder, A. W., Richmond, R. K., Sargent, D. F., & Richmond, T. J. (1997). Crystal structure of the nucleosome core particle at 2.8 A resolution. *Nature*, *389*(6648), 251–260. https://doi.org/10.1038/38444

Marschallinger, J., Iram, T., Zardeneta, M., Lee, S. E., Lehallier, B., Haney, M. S., Pluvinage, J. V., Mathur, V., Hahn, O., Morgens, D. W., Kim, J., Tevini, J., Felder, T. K., Wolinski, H., Bertozzi, C. R., Bassik, M. C., Aigner, L., & Wyss-Coray, T. (2020). Lipid-droplet-accumulating microglia represent a dysfunctional and proinflammatory state in the aging brain. *Nature Neuroscience*, *23*(2), 194–208. https://doi.org/10.1038/s41593-019-0566-1

Martinez Sosa, S., & Smith, K. J. (2017). Understanding a role for hypoxia in lesion formation and location in the deep and periventricular white matter in small vessel disease and multiple sclerosis. *Clinical Science (London, England: 1979)*, *131*(20), 2503–2524. https://doi.org/10.1042/CS20170981

Masuda, T., Sankowski, R., Staszewski, O., Böttcher, C., Amann, L., Sagar, null, Scheiwe, C., Nessler, S., Kunz, P., van Loo, G., Coenen, V. A., Reinacher, P. C., Michel, A., Sure, U., Gold, R., Grün, D., Priller, J., Stadelmann, C., & Prinz, M. (2019). Spatial and temporal heterogeneity of mouse and human microglia at single-cell resolution. *Nature*, *566*(7744), 388–392. https://doi.org/10.1038/s41586-019-0924-x

McKenzie, I. A., Ohayon, D., Li, H., Paes de Faria, J., Emery, B., Tohyama, K., & Richardson, W. D. (2014). Motor skill learning requires active central myelination. *Science*, *346*(6207), 318–322. https://doi.org/10.1126/science.1254960

Medawar, P. B. (1948). Immunity to homologous grafted skin; the fate of skin homografts transplanted to the brain, to subcutaneous tissue, and to the anterior chamber of the eye. *British Journal of Experimental Pathology*, *29*(1), 58–69.

Medawar, P. B. (1996). A biological analysis of individuality. *Clinical Orthopaedics and Related Research*, *326*, 5–10. https://doi.org/10.1097/00003086-199605000-00002

Medzhitov, R. (2001). Toll-like receptors and innate immunity. *Nature Reviews Immunology*, *1*(2), Article 2. https://doi.org/10.1038/35100529

Mereu, E., Lafzi, A., Moutinho, C., Ziegenhain, C., McCarthy, D. J., Álvarez-Varela, A., Batlle, E., Sagar, Grün, D., Lau, J. K., Boutet, S. C., Sanada, C., Ooi, A., Jones, R. C., Kaihara, K., Brampton, C., Talaga, Y., Sasagawa, Y., Tanaka, K., … Heyn, H. (2020). Benchmarking single-cell RNA-sequencing protocols for cell atlas projects. *Nature Biotechnology*, *38*(6), Article 6. https://doi.org/10.1038/s41587-020-0469-4

Montagne, A., Barnes, S. R., Sweeney, M. D., Halliday, M. R., Sagare, A. P., Zhao, Z., Toga, A. W., Jacobs, R. E., Liu, C. Y., Amezcua, L., Harrington, M. G., Chui, H. C., Law, M., & Zlokovic, B. V. (2015). Blood-Brain Barrier Breakdown in the Aging Human Hippocampus. *Neuron*, *85*(2), 296–302. https://doi.org/10.1016/j.neuron.2014.12.032

Monteiro, S., Roque, S., Marques, F., Correia-Neves, M., & Cerqueira, J. J. (2017). Brain interference: Revisiting the role of IFNγ in the central nervous system. *Progress in Neurobiology*, *156*, 149–163. https://doi.org/10.1016/j.pneurobio.2017.05.003

Moraga, I., Harari, D., Schreiber, G., Uzé, G., & Pellegrini, S. (2009). Receptor density is key to the alpha2/beta interferon differential activities. *Molecular and Cellular Biology*, *29*(17), 4778–4787. https://doi.org/10.1128/mcb.01808-08

Mortazavi, A., Williams, B. A., McCue, K., Schaeffer, L., & Wold, B. (2008). Mapping and quantifying mammalian transcriptomes by RNA-Seq. *Nature Methods*, *5*(7), 621–628. https://doi.org/10.1038/nmeth.1226

Mundt, S., Mrdjen, D., Utz, S. G., Greter, M., Schreiner, B., & Becher, B. (2019). Conventional DCs sample and present myelin antigens in the healthy CNS and allow parenchymal T cell entry to initiate neuroinflammation. *Science Immunology*, *4*(31), eaau8380. https://doi.org/10.1126/sciimmunol.aau8380

Murphy, J. B., & Sturm, E. (1923). CONDITIONS DETERMINING THE TRANSPLANTABILITY OF TISSUES IN THE BRAIN. *The Journal of Experimental Medicine*, *38*(2), 183–197.

Nagalakshmi, U., Waern, K., & Snyder, M. (2010). RNA-Seq: A Method for Comprehensive Transcriptome Analysis. *Current Protocols in Molecular Biology*, *89*(1), 4.11.1-4.11.13. https://doi.org/10.1002/0471142727.mb0411s89

Nave, K.-A., & Ehrenreich, H. (2014). Myelination and Oligodendrocyte Functions in Psychiatric Diseases. *JAMA Psychiatry*, *71*(5), 582–584. https://doi.org/10.1001/jamapsychiatry.2014.189

Nave, K.-A., & Werner, H. B. (2014). Myelination of the nervous system: Mechanisms and functions. *Annual Review of Cell and Developmental Biology*, *30*, 503–533. https://doi.org/10.1146/annurev-cellbio-100913-013101

Nguyen, Q. H., Pervolarakis, N., Nee, K., & Kessenbrock, K. (2018). Experimental Considerations for Single-Cell RNA Sequencing Approaches. *Frontiers in Cell and Developmental Biology*, *6*. https://doi.org/10.3389/fcell.2018.00108

Ousman, S. S., & Kubes, P. (2012). Immune surveillance in the central nervous system. *Nature Neuroscience*, *15*(8), 1096–1101. https://doi.org/10.1038/nn.3161

Ozsolak, F., & Milos, P. M. (2011). RNA sequencing: Advances, challenges and opportunities. *Nature Reviews. Genetics*, *12*(2), 87–98. https://doi.org/10.1038/nrg2934

Pachter, J. S., de Vries, H. E., & Fabry, Z. (2003). The blood-brain barrier and its role in immune privilege in the central nervous system. *Journal of Neuropathology and Experimental Neurology*, *62*(6), 593–604. https://doi.org/10.1093/jnen/62.6.593

Papadopoulos, Z., Herz, J., & Kipnis, J. (2020). Meningeal Lymphatics: From Anatomy to Central Nervous System Immune Surveillance. *The Journal of Immunology*, *204*(2), 286–293. https://doi.org/10.4049/jimmunol.1900838

Papageorgiou, I. E., Lewen, A., Galow, L. V., Cesetti, T., Scheffel, J., Regen, T., Hanisch, U.-K., & Kann, O. (2016). TLR4-activated microglia require IFN-γ to induce severe neuronal dysfunction and death in situ. *Proceedings of the National Academy of Sciences*, *113*(1), 212–217. https://doi.org/10.1073/pnas.1513853113

Pestka, S. (2007). The interferons: 50 years after their discovery, there is much more to learn. *The Journal of Biological Chemistry*, *282*(28), 20047–20051. https://doi.org/10.1074/jbc.R700004200

Peters, A. (2002). The effects of normal aging on myelin and nerve fibers: A review. *Journal of Neurocytology*, *31*(8–9), 581–593. https://doi.org/10.1023/a:1025731309829

Peters, A., Moss, M. B., & Sethares, C. (2000). Effects of aging on myelinated nerve fibers in monkey primary visual cortex. *The Journal of Comparative Neurology*, *419*(3), 364–376. https://doi.org/10.1002/(sici)1096-9861(20000410)419:3<364::aid-cne8>3.0.co;2-r

Picelli, S., Björklund, Å. K., Faridani, O. R., Sagasser, S., Winberg, G., & Sandberg, R. (2013). Smart-seq2 for sensitive full-length transcriptome profiling in single cells. *Nature Methods*, *10*(11), Article 11. https://doi.org/10.1038/nmeth.2639

Piehl, N., van Olst, L., Ramakrishnan, A., Teregulova, V., Simonton, B., Zhang, Z., Tapp, E., Channappa, D., Oh, H., Losada, P. M., Rutledge, J., Trelle, A. N., Mormino, E. C., Elahi, F., Galasko, D. R., Henderson, V. W., Wagner, A. D., Wyss-Coray, T., & Gate, D. (2022). Cerebrospinal fluid immune dysregulation during healthy brain aging and cognitive impairment. *Cell*, *185*(26), 5028-5039.e13. https://doi.org/10.1016/j.cell.2022.11.019

Platanias, L. C. (2005). Mechanisms of type-I- and type-II-interferon-mediated signalling. *Nature Reviews Immunology*, *5*(5), Article 5. https://doi.org/10.1038/nri1604

Pluvinage, J. V., Haney, M. S., Smith, B. A. H., Sun, J., Iram, T., Bonanno, L., Li, L., Lee, D. P., Morgens, D. W., Yang, A. C., Shuken, S. R., Gate, D., Scott, M., Khatri, P., Luo, J., Bertozzi, C. R., Bassik, M. C., & Wyss-Coray, T. (2019). CD22 blockade restores homeostatic microglial phagocytosis in ageing brains. *Nature*, *568*(7751), 187–192. https://doi.org/10.1038/s41586-019-1088-4

Prins, N. D., & Scheltens, P. (2015). White matter hyperintensities, cognitive impairment and dementia: An update. *Nature Reviews. Neurology*, *11*(3), 157–165. https://doi.org/10.1038/nrneurol.2015.10

Prinz, M., & Priller, J. (2017). The role of peripheral immune cells in the CNS in steady state and disease. *Nature Neuroscience*, *20*(2), Article 2. https://doi.org/10.1038/nn.4475

Regev, A., Teichmann, S. A., Lander, E. S., Amit, I., Benoist, C., Birney, E., Bodenmiller, B., Campbell, P., Carninci, P., Clatworthy, M., Clevers, H., Deplancke, B., Dunham, I., Eberwine, J., Eils, R., Enard, W., Farmer, A., Fugger, L., Göttgens, B., … Yosef, N. (2017). The Human Cell Atlas. *eLife*, *6*, e27041. https://doi.org/10.7554/eLife.27041

Rockland, K. S., & Defelipe, J. (2011). Cortical white matter: Beyond the pale. *Frontiers in Neuroanatomy*, *5*, 67. https://doi.org/10.3389/fnana.2011.00067

Roeder, R. G., & Rutter, W. J. (1969). Multiple Forms of DNA-dependent RNA Polymerase in Eukaryotic Organisms. *Nature*, *224*(5216), Article 5216. https://doi.org/10.1038/224234a0

Rose, M. R. (2009). Adaptation, aging, and genomic information. *Aging*, *1*(5), 444–450. https://doi.org/10.18632/aging.100053

Roy, E. R., Wang, B., Wan, Y.-W., Chiu, G., Cole, A., Yin, Z., Propson, N. E., Xu, Y., Jankowsky, J. L., Liu, Z., Lee, V. M.-Y., Trojanowski, J. Q., Ginsberg, S. D., Butovsky, O., Zheng, H., & Cao, W. (2020). Type I interferon response drives neuroinflammation and synapse loss in Alzheimer disease. *The Journal of Clinical Investigation*, *130*(4), 1912–1930. https://doi.org/10.1172/JCI133737

Rubinstein, M., Levy, W. P., Moschera, J. A., Lai, C.-Y., Hershberg, R. D., Bartlett, R. T., & Pestka, S. (1981). Human leukocyte interferon: Isolation and characterization of several molecular forms. *Archives of Biochemistry and Biophysics*, *210*(1), 307–318. https://doi.org/10.1016/0003-9861(81)90194-6

Rustenhoven, J., & Kipnis, J. (2022). Brain borders at the central stage of neuroimmunology. *Nature*, *612*(7940), 417–429. https://doi.org/10.1038/s41586-022-05474-7

Safaiyan, S., Besson-Girard, S., Kaya, T., Cantuti-Castelvetri, L., Liu, L., Ji, H., Schifferer, M., Gouna, G., Usifo, F., Kannaiyan, N., Fitzner, D., Xiang, X., Rossner, M. J., Brendel, M., Gokce, O., & Simons, M. (2021). White matter aging drives microglial diversity. *Neuron*, *109*(7), 1100-1117.e10. https://doi.org/10.1016/j.neuron.2021.01.027

Safaiyan, S., Kannaiyan, N., Snaidero, N., Brioschi, S., Biber, K., Yona, S., Edinger, A. L., Jung, S., Rossner, M. J., & Simons, M. (2016). Age-related myelin degradation burdens the clearance function of microglia during aging. *Nature Neuroscience*, *19*(8), 995–998. https://doi.org/10.1038/nn.4325

Salat, D. H., Tuch, D. S., Greve, D. N., van der Kouwe, A. J. W., Hevelone, N. D., Zaleta, A. K., Rosen, B. R., Fischl, B., Corkin, S., Rosas, H. D., & Dale, A. M. (2005). Age-related alterations in white matter microstructure measured by diffusion tensor imaging. *Neurobiology of Aging*, *26*(8), 1215–1227. https://doi.org/10.1016/j.neurobiolaging.2004.09.017

Schena, M., Shalon, D., Davis, R. W., & Brown, P. O. (1995). Quantitative Monitoring of Gene Expression Patterns with a Complementary DNA Microarray. *Science*, *270*(5235), 467–470. https://doi.org/10.1126/science.270.5235.467

Schindler, C., Levy, D. E., & Decker, T. (2007). JAK-STAT signaling: From interferons to cytokines. *The Journal of Biological Chemistry*, *282*(28), 20059–20063. https://doi.org/10.1074/jbc.R700016200

Schindler, C., Shuai, K., Prezioso, V. R., & Darnell, J. E. (1992). Interferon-dependent tyrosine phosphorylation of a latent cytoplasmic transcription factor. *Science (New York, N.Y.)*, *257*(5071), 809–813. https://doi.org/10.1126/science.1496401

Schoenborn, J. R., & Wilson, C. B. (2007). Regulation of interferon-gamma during innate and adaptive immune responses. *Advances in Immunology*, *96*, 41–101. https://doi.org/10.1016/S0065-2776(07)96002-2

Shatkin, A. J., & Manley, J. L. (2000). The ends of the affair: Capping and polyadenylation. *Nature Structural Biology*, *7*(10), 838–842. https://doi.org/10.1038/79583

Siegal, F. P., Kadowaki, N., Shodell, M., Fitzgerald-Bocarsly, P. A., Shah, K., Ho, S., Antonenko, S., & Liu, Y. J. (1999). The nature of the principal type 1 interferon-producing cells in human blood. *Science (New York, N.Y.)*, *284*(5421), 1835–1837. https://doi.org/10.1126/science.284.5421.1835

Simons, M., & Nave, K.-A. (2016). Oligodendrocytes: Myelination and Axonal Support. *Cold Spring Harbor Perspectives in Biology*, *8*(1), a020479. https://doi.org/10.1101/cshperspect.a020479

Simpson, E. (2004). Reminiscences of Sir Peter Medawar: In Hope of Antigen-Specific Transplantation Tolerance. *American Journal of Transplantation*, *4*(12), 1937–1940. https://doi.org/10.1111/j.1600-6143.2004.00687.x

Soldan, S. S., & Lieberman, P. M. (2023). Epstein-Barr virus and multiple sclerosis. *Nature Reviews. Microbiology*, *21*(1), 51–64. https://doi.org/10.1038/s41579-022-00770-5

Stark, G. R., & Darnell, J. E. (2012). The JAK-STAT pathway at twenty. *Immunity*, *36*(4), 503–514. https://doi.org/10.1016/j.immuni.2012.03.013

Ta, T.-T., Dikmen, H. O., Schilling, S., Chausse, B., Lewen, A., Hollnagel, J.-O., & Kann, O. (2019). Priming of microglia with IFN-γ slows neuronal gamma oscillations in situ. *Proceedings of the National Academy of Sciences*, *116*(10), 4637–4642. https://doi.org/10.1073/pnas.1813562116

Takeuchi, H., Wang, J., Kawanokuchi, J., Mitsuma, N., Mizuno, T., & Suzumura, A. (2006). Interferon-γ induces microglial-activation-induced cell death: A hypothetical mechanism of relapse and remission in multiple sclerosis. *Neurobiology of Disease*, *22*(1), 33–39. https://doi.org/10.1016/j.nbd.2005.09.014

Thériault, P., & Rivest, S. (2016). Microglia: Senescence Impairs Clearance of Myelin Debris. *Current Biology*, *26*(16), R772–R775. https://doi.org/10.1016/j.cub.2016.06.066

Trapnell, C., Pachter, L., & Salzberg, S. L. (2009). TopHat: Discovering splice junctions with RNA-Seq. *Bioinformatics*, *25*(9), 1105–1111. https://doi.org/10.1093/bioinformatics/btp120

Ulrich, J. D., Ulland, T. K., Colonna, M., & Holtzman, D. M. (2017). Elucidating the Role of TREM2 in Alzheimer's Disease. *Neuron*, *94*(2), 237–248. https://doi.org/10.1016/j.neuron.2017.02.042

Unger, M. S., Li, E., Scharnagl, L., Poupardin, R., Altendorfer, B., Mrowetz, H., Hutter-Paier, B., Weiger, T. M., Heneka, M. T., Attems, J., & Aigner, L. (2020). CD8+ T-cells infiltrate Alzheimer's disease brains and regulate neuronal- and synapse-related gene expression in APP-PS1 transgenic mice. *Brain, Behavior, and Immunity*, *89*, 67–86. https://doi.org/10.1016/j.bbi.2020.05.070

Valente, G., Ozmen, L., Novelli, F., Geuna, M., Palestro, G., Forni, G., & Garotta, G. (1992). Distribution of interferon-gamma receptor in human tissues. *European Journal of Immunology*, *22*(9), 2403–2412. https://doi.org/10.1002/eji.1830220933

Vazquez-Lombardi, R., Jung, J. S., Schlatter, F. S., Mei, A., Mantuano, N. R., Bieberich, F., Hong, K.-L., Kucharczyk, J., Kapetanovic, E., Aznauryan, E., Weber, C. R., Zippelius, A., Läubli, H., & Reddy, S. T. (2022). High-throughput T cell receptor engineering by functional screening identifies candidates with enhanced potency and specificity. *Immunity*, *55*(10), 1953-1966.e10. https://doi.org/10.1016/j.immuni.2022.09.004

Vivier, E., & Malissen, B. (2005). Innate and adaptive immunity: Specificities and signaling hierarchies revisited. *Nature Immunology*, *6*(1), Article 1. https://doi.org/10.1038/ni1153

Walsh, J. T., Zheng, J., Smirnov, I., Lorenz, U., Tung, K., & Kipnis, J. (2014). Regulatory T cells in central nervous system injury: A double-edged sword. *Journal of Immunology (Baltimore, Md.: 1950)*, *193*(10), 5013–5022. https://doi.org/10.4049/jimmunol.1302401

Walter, M. R., Windsor, W. T., Nagabhushan, T. L., Lundell, D. J., Lunn, C. A., Zauodny, P. J., & Narula, S. K. (1995). Crystal structure of a complex between interferon-γ and its soluble high-affinity receptor. *Nature*, *376*(6537), Article 6537. https://doi.org/10.1038/376230a0

Waltl, I., & Kalinke, U. (2022). Beneficial and detrimental functions of microglia during viral encephalitis. *Trends in Neurosciences*, *45*(2), 158–170. https://doi.org/10.1016/j.tins.2021.11.004

Wang, A. M., Doyle, M. V., & Mark, D. F. (1989). Quantitation of mRNA by the polymerase chain reaction. *Proceedings of the National Academy of Sciences of the United States of America*, *86*(24), 9717–9721. https://doi.org/10.1073/pnas.86.24.9717

Wang, C., Yue, H., Hu, Z., Shen, Y., Ma, J., Li, J., Wang, X.-D., Wang, L., Sun, B., Shi, P., Wang, L., & Gu, Y. (2020). Microglia mediate forgetting via complement-dependent synaptic elimination. *Science (New York, N.Y.)*, *367*(6478), 688–694. https://doi.org/10.1126/science.aaz2288

Wang, E. T., Sandberg, R., Luo, S., Khrebtukova, I., Zhang, L., Mayr, C., Kingsmore, S. F., Schroth, G. P., & Burge, C. B. (2008). Alternative isoform regulation in human tissue transcriptomes. *Nature*, *456*(7221), 470–476. https://doi.org/10.1038/nature07509

Wang, X., He, Y., Zhang, Q., Ren, X., & Zhang, Z. (2021). Direct Comparative Analyses of 10X Genomics Chromium and Smart-seq2. *Genomics, Proteomics & Bioinformatics*, *19*(2), 253–266. https://doi.org/10.1016/j.gpb.2020.02.005

Wang, Z., Gerstein, M., & Snyder, M. (2009). RNA-Seq: A revolutionary tool for transcriptomics. *Nature Reviews. Genetics*, *10*(1), 57–63. https://doi.org/10.1038/nrg2484

Wardlaw, J. M., Valdés Hernández, M. C., & Muñoz-Maniega, S. (2015). What are White Matter Hyperintensities Made of? *Journal of the American Heart Association: Cardiovascular and Cerebrovascular Disease*, *4*(6), e001140. https://doi.org/10.1161/JAHA.114.001140

Weller, R. O., Galea, I., Carare, R. O., & Minagar, A. (2010). Pathophysiology of the lymphatic drainage of the central nervous system: Implications for pathogenesis and therapy of multiple sclerosis. *Pathophysiology: The Official Journal of the International Society for Pathophysiology*, *17*(4), 295–306. https://doi.org/10.1016/j.pathophys.2009.10.007

Wilhelm, B. T., & Landry, J.-R. (2009). RNA-Seq—Quantitative measurement of expression through massively parallel RNA-sequencing. *Methods*, *48*(3), 249–257. https://doi.org/10.1016/j.ymeth.2009.03.016

Willis, R. A., & Keith, A. (1935). Experiments on the intracerebral implantation of embryo tissues in rats. *Proceedings of the Royal Society of London. Series B - Biological Sciences*, *117*(805), 400–412. https://doi.org/10.1098/rspb.1935.0036

Wu, A. R., Neff, N. F., Kalisky, T., Dalerba, P., Treutlein, B., Rothenberg, M. E., Mburu, F. M., Mantalas, G. L., Sim, S., Clarke, M. F., & Quake, S. R. (2014). Quantitative assessment of single-cell RNA-sequencing methods. *Nature Methods*, *11*(1), 41–46. https://doi.org/10.1038/nmeth.2694

Wu, J., & Chen, Z. J. (2014). Innate immune sensing and signaling of cytosolic nucleic acids. *Annual Review of Immunology*, *32*, 461–488. https://doi.org/10.1146/annurev-immunol-032713-120156

Wyss-Coray, T. (2016). Ageing, neurodegeneration and brain rejuvenation. *Nature*, *539*(7628), Article 7628. https://doi.org/10.1038/nature20411

Ye, J., Ortaido, J. R., Conlon, K., Winkler-Pickett, R., & Young, H. A. (1995). Cellular and molecular mechanisms of IFN-γ production induced by IL-2 and IL-12 in a human NK cell line. *Journal of Leukocyte Biology*, *58*(2), 225–233. https://doi.org/10.1002/jlb.58.2.225

Zhang, B., Vogelzang, A., Miyajima, M., Sugiura, Y., Wu, Y., Chamoto, K., Nakano, R., Hatae, R., Menzies, R. J., Sonomura, K., Hojo, N., Ogawa, T., Kobayashi, W., Tsutsui, Y., Yamamoto, S., Maruya, M., Narushima, S., Suzuki, K., Sugiya, H., … Fagarasan, S. (2021). B cell-derived GABA elicits IL-10+ macrophages to limit anti-tumour immunity. *Nature*, *599*(7885), 471–476. https://doi.org/10.1038/s41586-021-04082-1

Zheng, G. X. Y., Terry, J. M., Belgrader, P., Ryvkin, P., Bent, Z. W., Wilson, R., Ziraldo, S. B., Wheeler, T. D., McDermott, G. P., Zhu, J., Gregory, M. T., Shuga, J., Montesclaros, L., Underwood, J. G., Masquelier, D. A., Nishimura, S. Y., Schnall-Levin, M., Wyatt, P. W., Hindson, C. M., … Bielas,

J. H. (2017). Massively parallel digital transcriptional profiling of single cells. *Nature Communications*, *8*(1), Article 1. https://doi.org/10.1038/ncomms14049

Ziegenhain, C., Vieth, B., Parekh, S., Reinius, B., Guillaumet-Adkins, A., Smets, M., Leonhardt, H., Heyn, H., Hellmann, I., & Enard, W. (2017). Comparative Analysis of Single-Cell RNA Sequencing Methods. *Molecular Cell*, *65*(4), 631-643.e4. https://doi.org/10.1016/j.molcel.2017.01.023

COPYRIGHTS OF REUSED FIGURES

SPRINGER NATURE LICENSE TERMS AND CONDITIONS

Apr 17, 2024

This Agreement between Mr. Tugberk Kaya ("You") and Springer Nature ("Springer Nature") consists of your license details and the terms and conditions provided by Springer Nature and Copyright Clearance Center.

License Number	5771370091258
License date	Apr 17, 2024
Licensed Content Publisher	Springer Nature
Licensed Content Publication	Nature Reviews Neurology
Licensed Content Title	Ageing as a risk factor for neurodegenerative disease
Licensed Content Author	Yujun Hou et al
Licensed Content Date	Sep 9, 2019
Type of Use	Thesis/Dissertation
Requestor type	non-commercial (non-profit)
Format	print and electronic
Portion	figures/tables/illustrations
Number of figures/tables/illustrations	1
Would you like a high resolution image with your order?	no
Will you be translating?	no
Circulation/distribution	1 - 29
Author of this Springer Nature content	no
Title of new work	NEURO-IMMUNE AXIS IN WHITE MATTER AGING
Institution name	GSN
Expected presentation date	Jun 2024
Portions	Figure 2
Requestor Location	Mr. Tugberk Kaya Heiterwanger Str 4 Munich, 81373 Germany Attn: Mr. Tugberk Kaya
Total	**0.00 EUR**

Terms and Conditions

Springer Nature Customer Service Centre GmbH Terms and Conditions

The following terms and conditions ("Terms and Conditions") together with the terms specified in your [RightsLink] constitute the License ("License") between you as Licensee and Springer Nature Customer Service Centre GmbH as Licensor. By clicking 'accept' and completing the transaction for your use of the material ("Licensed Material"), you confirm your acceptance of and obligation to be bound by these Terms and Conditions.

1. Grant and Scope of License

1. 1. The Licensor grants you a personal, non-exclusive, non-transferable, non-sublicensable, revocable, world-wide License to reproduce, distribute, communicate to the public, make available, broadcast, electronically transmit or create derivative works using the Licensed Material for the purpose(s) specified in your RightsLink Licence Details only. Licenses are granted for the specific use requested in the order and for no other use, subject to these Terms

and Conditions. You acknowledge and agree that the rights granted to you under this License do not include the right to modify, edit, translate, include in collective works, or create derivative works of the Licensed Material in whole or in part unless expressly stated in your RightsLink Licence Details. You may use the Licensed Material only as permitted under this Agreement and will not reproduce, distribute, display, perform, or otherwise use or exploit any Licensed Material in any way, in whole or in part, except as expressly permitted by this License.

1. 2. You may only use the Licensed Content in the manner and to the extent permitted by these Terms and Conditions, by your RightsLink Licence Details and by any applicable laws.

1. 3. A separate license may be required for any additional use of the Licensed Material, e.g. where a license has been purchased for print use only, separate permission must be obtained for electronic re-use. Similarly, a License is only valid in the language selected and does not apply for editions in other languages unless additional translation rights have been granted separately in the License.

1. 4. Any content within the Licensed Material that is owned by third parties is expressly excluded from the License.

1. 5. Rights for additional reuses such as custom editions, computer/mobile applications, film or TV reuses and/or any other derivative rights requests require additional permission and may be subject to an additional fee. Please apply to journalpermissions@springernature.com or bookpermissions@springernature.com for these rights.

2. Reservation of Rights

Licensor reserves all rights not expressly granted to you under this License. You acknowledge and agree that nothing in this License limits or restricts Licensor's rights in or use of the Licensed Material in any way. Neither this License, nor any act, omission, or statement by Licensor or you, conveys any ownership right to you in any Licensed Material, or to any element or portion thereof. As between Licensor and you, Licensor owns and retains all right, title, and interest in and to the Licensed Material subject to the license granted in Section 1.1. Your permission to use the Licensed Material is expressly conditioned on you not impairing Licensor's or the applicable copyright owner's rights in the Licensed Material in any way.

3. Restrictions on use

3. 1. Minor editing privileges are allowed for adaptations for stylistic purposes or formatting purposes provided such alterations do not alter the original meaning or intention of the Licensed Material and the new figure(s) are still accurate and representative of the Licensed Material. Any other changes including but not limited to, cropping, adapting, and/or omitting material that affect the meaning, intention or moral rights of the author(s) are strictly prohibited.

3. 2. You must not use any Licensed Material as part of any design or trademark.

3. 3. Licensed Material may be used in Open Access Publications (OAP), but any such reuse must include a clear acknowledgment of this permission visible at the same time as the figures/tables/illustration or abstract and which must indicate that the Licensed Material is not part of the governing OA license but has been reproduced with permission. This may be indicated according to any standard referencing system but must include at a minimum 'Book/Journal title, Author, Journal Name (if applicable), Volume (if applicable), Publisher, Year, reproduced with permission from SNCSC'.

4. STM Permission Guidelines

4. 1. An alternative scope of license may apply to signatories of the STM Permissions Guidelines ("STM PG") as amended from time to time and made available at https://www.stm-assoc.org/intellectual-property/permissions/permissions-guidelines/.

4. 2. For content reuse requests that qualify for permission under the STM PG, and which may be updated from time to time, the STM PG supersede the terms and conditions contained in this License.

4. 3. If a License has been granted under the STM PG, but the STM PG no longer apply at the time of publication, further permission must be sought from the Rightsholder. Contact journalpermissions@springernature.com or bookpermissions@springernature.com for these rights.

5. Duration of License

5. 1. Unless otherwise indicated on your License, a License is valid from the date of purchase ("License Date") until the end of the relevant period in the below table:

Reuse in a medical communications project	Reuse up to distribution or time period indicated in License
Reuse in a dissertation/thesis	Lifetime of thesis
Reuse in a journal/magazine	Lifetime of journal/magazine
Reuse in a book/textbook	Lifetime of edition
Reuse on a website	1 year unless otherwise specified in the License
Reuse in a presentation/slide kit/poster	Lifetime of presentation/slide kit/poster. Note: publication whether electronic or in print of presentation/slide kit/poster may require further permission.
Reuse in conference proceedings	Lifetime of conference proceedings
Reuse in an annual report	Lifetime of annual report
Reuse in training/CME materials	Reuse up to distribution or time period indicated in License
Reuse in newsmedia	Lifetime of newsmedia
Reuse in coursepack/classroom materials	Reuse up to distribution and/or time period indicated in license

6. Acknowledgement

6. 1. The Licensor's permission must be acknowledged next to the Licensed Material in print. In electronic form, this acknowledgement must be visible at the same time as the figures/tables/illustrations or abstract and must be hyperlinked to the journal/book's homepage.

6. 2. Acknowledgement may be provided according to any standard referencing system and at a minimum should include "Author, Article/Book Title, Journal name/Book imprint, volume, page number, year, Springer Nature".

7. Reuse in a dissertation or thesis

7. 1. Where 'reuse in a dissertation/thesis' has been selected, the following terms apply: Print rights of the Version of Record are provided for; electronic rights for use only on institutional repository as defined by the Sherpa guideline (www.sherpa.ac.uk/romeo/) and only up to what is required by the awarding institution.

7. 2. For theses published under an ISBN or ISSN, separate permission is required. Please contact journalpermissions@springernature.com or bookpermissions@springernature.com for these rights.

7. 3. Authors must properly cite the published manuscript in their thesis according to current citation standards and include the following acknowledgement: '*Reproduced with permission from Springer Nature*'.

8. License Fee

You must pay the fee set forth in the License Agreement (the "License Fees"). All amounts payable by you under this License are exclusive of any sales, use, withholding, value added or similar taxes, government fees or levies or other assessments. Collection and/or remittance of such taxes to the relevant tax authority shall be the responsibility of the party who has the legal obligation to do so.

9. Warranty

9. 1. The Licensor warrants that it has, to the best of its knowledge, the rights to license reuse of the Licensed Material. **You are solely responsible for ensuring that the material you wish to license is original to the Licensor and does not carry the copyright of another entity or third party (as credited in the published version).** If the credit line on any part of the Licensed Material indicates that it was reprinted or adapted with permission from another source, then you should seek additional permission from that source to reuse the material.

9. 2. EXCEPT FOR THE EXPRESS WARRANTY STATED HEREIN AND TO THE EXTENT PERMITTED BY APPLICABLE LAW, LICENSOR PROVIDES THE LICENSED MATERIAL "AS IS" AND MAKES NO OTHER REPRESENTATION OR WARRANTY. LICENSOR EXPRESSLY DISCLAIMS ANY LIABILITY FOR ANY CLAIM ARISING FROM OR OUT OF THE CONTENT, INCLUDING BUT NOT LIMITED TO ANY ERRORS, INACCURACIES, OMISSIONS, OR DEFECTS CONTAINED THEREIN, AND ANY IMPLIED OR EXPRESS WARRANTY AS TO MERCHANTABILITY OR FITNESS FOR A PARTICULAR PURPOSE. IN NO EVENT SHALL LICENSOR BE LIABLE TO YOU OR ANY OTHER PARTY OR ANY OTHER PERSON OR FOR ANY SPECIAL, CONSEQUENTIAL, INCIDENTAL, INDIRECT, PUNITIVE, OR EXEMPLARY DAMAGES, HOWEVER CAUSED,

ARISING OUT OF OR IN CONNECTION WITH THE DOWNLOADING, VIEWING OR USE OF THE LICENSED MATERIAL REGARDLESS OF THE FORM OF ACTION, WHETHER FOR BREACH OF CONTRACT, BREACH OF WARRANTY, TORT, NEGLIGENCE, INFRINGEMENT OR OTHERWISE (INCLUDING, WITHOUT LIMITATION, DAMAGES BASED ON LOSS OF PROFITS, DATA, FILES, USE, BUSINESS OPPORTUNITY OR CLAIMS OF THIRD PARTIES), AND WHETHER OR NOT THE PARTY HAS BEEN ADVISED OF THE POSSIBILITY OF SUCH DAMAGES. THIS LIMITATION APPLIES NOTWITHSTANDING ANY FAILURE OF ESSENTIAL PURPOSE OF ANY LIMITED REMEDY PROVIDED HEREIN.

10. Termination and Cancellation

10. 1. The License and all rights granted hereunder will continue until the end of the applicable period shown in Clause 5.1 above. Thereafter, this license will be terminated and all rights granted hereunder will cease.

10. 2. Licensor reserves the right to terminate the License in the event that payment is not received in full or if you breach the terms of this License.

11. General

11. 1. The License and the rights and obligations of the parties hereto shall be construed, interpreted and determined in accordance with the laws of the Federal Republic of Germany without reference to the stipulations of the CISG (United Nations Convention on Contracts for the International Sale of Goods) or to Germany´s choice-of-law principle.

11. 2. The parties acknowledge and agree that any controversies and disputes arising out of this License shall be decided exclusively by the courts of or having jurisdiction for Heidelberg, Germany, as far as legally permissible.

11. 3. This License is solely for Licensor's and Licensee's benefit. It is not for the benefit of any other person or entity.

Questions? For questions on Copyright Clearance Center accounts or website issues please contact springernaturesupport@copyright.com or +1-855-239-3415 (toll free in the US) or +1-978-646-2777. For questions on Springer Nature licensing please visit https://www.springernature.com/gp/partners/rights-permissions-third-party-distribution

Other Conditions:

Version 1.4 - Dec 2022

SPRINGER NATURE LICENSE TERMS AND CONDITIONS

Apr 17, 2024

This Agreement between Mr. Tugberk Kaya ("You") and Springer Nature ("Springer Nature") consists of your license details and the terms and conditions provided by Springer Nature and Copyright Clearance Center.

License Number	5771370700436
License date	Apr 17, 2024
Licensed Content Publisher	Springer Nature
Licensed Content Publication	Nature Immunology
Licensed Content Title	T cells drive aging of the brain
Licensed Content Author	Adrian Liston et al
Licensed Content Date	Jan 3, 2023
Type of Use	Thesis/Dissertation
Requestor type	non-commercial (non-profit)
Format	print and electronic
Portion	figures/tables/illustrations
Number of figures/tables/illustrations	1
Would you like a high resolution image with your order?	no
Will you be translating?	no
Circulation/distribution	1 - 29
Author of this Springer Nature content	no
Title of new work	NEURO-IMMUNE AXIS IN WHITE MATTER AGING
Institution name	GSN
Expected presentation date	Jun 2024
Portions	Figure 1
Requestor Location	Mr. Tugberk Kaya Heiterwanger Str 4 Munich, 81373 Germany Attn: Mr. Tugberk Kaya
Total	**0.00 EUR**

Terms and Conditions

Springer Nature Customer Service Centre GmbH Terms and Conditions

The following terms and conditions ("Terms and Conditions") together with the terms specified in your [RightsLink] constitute the License ("License") between you as Licensee and Springer Nature Customer Service Centre GmbH as Licensor. By clicking 'accept' and completing the transaction for your use of the material ("Licensed Material"), you confirm your acceptance of and obligation to be bound by these Terms and Conditions.

1. Grant and Scope of License

1. 1. The Licensor grants you a personal, non-exclusive, non-transferable, non-sublicensable, revocable, world-wide License to reproduce, distribute, communicate to the public, make available, broadcast, electronically transmit or create derivative works using the Licensed Material for the purpose(s) specified in your RightsLink Licence Details only. Licenses are granted for the specific use requested in the order and for no other use, subject to these Terms

and Conditions. You acknowledge and agree that the rights granted to you under this License do not include the right to modify, edit, translate, include in collective works, or create derivative works of the Licensed Material in whole or in part unless expressly stated in your RightsLink Licence Details. You may use the Licensed Material only as permitted under this Agreement and will not reproduce, distribute, display, perform, or otherwise use or exploit any Licensed Material in any way, in whole or in part, except as expressly permitted by this License.

1. 2. You may only use the Licensed Content in the manner and to the extent permitted by these Terms and Conditions, by your RightsLink Licence Details and by any applicable laws.

1. 3. A separate license may be required for any additional use of the Licensed Material, e.g. where a license has been purchased for print use only, separate permission must be obtained for electronic re-use. Similarly, a License is only valid in the language selected and does not apply for editions in other languages unless additional translation rights have been granted separately in the License.

1. 4. Any content within the Licensed Material that is owned by third parties is expressly excluded from the License.

1. 5. Rights for additional reuses such as custom editions, computer/mobile applications, film or TV reuses and/or any other derivative rights requests require additional permission and may be subject to an additional fee. Please apply to journalpermissions@springernature.com or bookpermissions@springernature.com for these rights.

2. Reservation of Rights

Licensor reserves all rights not expressly granted to you under this License. You acknowledge and agree that nothing in this License limits or restricts Licensor's rights in or use of the Licensed Material in any way. Neither this License, nor any act, omission, or statement by Licensor or you, conveys any ownership right to you in any Licensed Material, or to any element or portion thereof. As between Licensor and you, Licensor owns and retains all right, title, and interest in and to the Licensed Material subject to the license granted in Section 1.1. Your permission to use the Licensed Material is expressly conditioned on you not impairing Licensor's or the applicable copyright owner's rights in the Licensed Material in any way.

3. Restrictions on use

3. 1. Minor editing privileges are allowed for adaptations for stylistic purposes or formatting purposes provided such alterations do not alter the original meaning or intention of the Licensed Material and the new figure(s) are still accurate and representative of the Licensed Material. Any other changes including but not limited to, cropping, adapting, and/or omitting material that affect the meaning, intention or moral rights of the author(s) are strictly prohibited.

3. 2. You must not use any Licensed Material as part of any design or trademark.

3. 3. Licensed Material may be used in Open Access Publications (OAP), but any such reuse must include a clear acknowledgment of this permission visible at the same time as the figures/tables/illustration or abstract and which must indicate that the Licensed Material is not part of the governing OA license but has been reproduced with permission. This may be indicated according to any standard referencing system but must include at a minimum 'Book/Journal title, Author, Journal Name (if applicable), Volume (if applicable), Publisher, Year, reproduced with permission from SNCSC'.

4. STM Permission Guidelines

4. 1. An alternative scope of license may apply to signatories of the STM Permissions Guidelines ("STM PG") as amended from time to time and made available at https://www.stm-assoc.org/intellectual-property/permissions/permissions-guidelines/.

4. 2. For content reuse requests that qualify for permission under the STM PG, and which may be updated from time to time, the STM PG supersede the terms and conditions contained in this License.

4. 3. If a License has been granted under the STM PG, but the STM PG no longer apply at the time of publication, further permission must be sought from the Rightsholder. Contact journalpermissions@springernature.com or bookpermissions@springernature.com for these rights.

5. Duration of License

5. 1. Unless otherwise indicated on your License, a License is valid from the date of purchase ("License Date") until the end of the relevant period in the below table:

Reuse in a medical communications project	Reuse up to distribution or time period indicated in License
Reuse in a dissertation/thesis	Lifetime of thesis
Reuse in a journal/magazine	Lifetime of journal/magazine
Reuse in a book/textbook	Lifetime of edition
Reuse on a website	1 year unless otherwise specified in the License
Reuse in a presentation/slide kit/poster	Lifetime of presentation/slide kit/poster. Note: publication whether electronic or in print of presentation/slide kit/poster may require further permission.
Reuse in conference proceedings	Lifetime of conference proceedings
Reuse in an annual report	Lifetime of annual report
Reuse in training/CME materials	Reuse up to distribution or time period indicated in License
Reuse in newsmedia	Lifetime of newsmedia
Reuse in coursepack/classroom materials	Reuse up to distribution and/or time period indicated in license

6. Acknowledgement

6. 1. The Licensor's permission must be acknowledged next to the Licensed Material in print. In electronic form, this acknowledgement must be visible at the same time as the figures/tables/illustrations or abstract and must be hyperlinked to the journal/book's homepage.

6. 2. Acknowledgement may be provided according to any standard referencing system and at a minimum should include "Author, Article/Book Title, Journal name/Book imprint, volume, page number, year, Springer Nature".

7. Reuse in a dissertation or thesis

7. 1. Where 'reuse in a dissertation/thesis' has been selected, the following terms apply: Print rights of the Version of Record are provided for; electronic rights for use only on institutional repository as defined by the Sherpa guideline (www.sherpa.ac.uk/romeo/) and only up to what is required by the awarding institution.

7. 2. For theses published under an ISBN or ISSN, separate permission is required. Please contact journalpermissions@springernature.com or bookpermissions@springernature.com for these rights.

7. 3. Authors must properly cite the published manuscript in their thesis according to current citation standards and include the following acknowledgement: '*Reproduced with permission from Springer Nature*'.

8. License Fee

You must pay the fee set forth in the License Agreement (the "License Fees"). All amounts payable by you under this License are exclusive of any sales, use, withholding, value added or similar taxes, government fees or levies or other assessments. Collection and/or remittance of such taxes to the relevant tax authority shall be the responsibility of the party who has the legal obligation to do so.

9. Warranty

9. 1. The Licensor warrants that it has, to the best of its knowledge, the rights to license reuse of the Licensed Material. **You are solely responsible for ensuring that the material you wish to license is original to the Licensor and does not carry the copyright of another entity or third party (as credited in the published version).** If the credit line on any part of the Licensed Material indicates that it was reprinted or adapted with permission from another source, then you should seek additional permission from that source to reuse the material.

9. 2. EXCEPT FOR THE EXPRESS WARRANTY STATED HEREIN AND TO THE EXTENT PERMITTED BY APPLICABLE LAW, LICENSOR PROVIDES THE LICENSED MATERIAL "AS IS" AND MAKES NO OTHER REPRESENTATION OR WARRANTY. LICENSOR EXPRESSLY DISCLAIMS ANY LIABILITY FOR ANY CLAIM ARISING FROM OR OUT OF THE CONTENT, INCLUDING BUT NOT LIMITED TO ANY ERRORS, INACCURACIES, OMISSIONS, OR DEFECTS CONTAINED THEREIN, AND ANY IMPLIED OR EXPRESS WARRANTY AS TO MERCHANTABILITY OR FITNESS FOR A PARTICULAR PURPOSE. IN NO EVENT SHALL LICENSOR BE LIABLE TO YOU OR ANY OTHER PARTY OR ANY OTHER PERSON OR FOR ANY SPECIAL, CONSEQUENTIAL, INCIDENTAL, INDIRECT, PUNITIVE, OR EXEMPLARY DAMAGES, HOWEVER CAUSED,

ARISING OUT OF OR IN CONNECTION WITH THE DOWNLOADING, VIEWING OR USE OF THE LICENSED MATERIAL REGARDLESS OF THE FORM OF ACTION, WHETHER FOR BREACH OF CONTRACT, BREACH OF WARRANTY, TORT, NEGLIGENCE, INFRINGEMENT OR OTHERWISE (INCLUDING, WITHOUT LIMITATION, DAMAGES BASED ON LOSS OF PROFITS, DATA, FILES, USE, BUSINESS OPPORTUNITY OR CLAIMS OF THIRD PARTIES), AND WHETHER OR NOT THE PARTY HAS BEEN ADVISED OF THE POSSIBILITY OF SUCH DAMAGES. THIS LIMITATION APPLIES NOTWITHSTANDING ANY FAILURE OF ESSENTIAL PURPOSE OF ANY LIMITED REMEDY PROVIDED HEREIN.

10. Termination and Cancellation

10. 1. The License and all rights granted hereunder will continue until the end of the applicable period shown in Clause 5.1 above. Thereafter, this license will be terminated and all rights granted hereunder will cease.

10. 2. Licensor reserves the right to terminate the License in the event that payment is not received in full or if you breach the terms of this License.

11. General

11. 1. The License and the rights and obligations of the parties hereto shall be construed, interpreted and determined in accordance with the laws of the Federal Republic of Germany without reference to the stipulations of the CISG (United Nations Convention on Contracts for the International Sale of Goods) or to Germany´s choice-of-law principle.

11. 2. The parties acknowledge and agree that any controversies and disputes arising out of this License shall be decided exclusively by the courts of or having jurisdiction for Heidelberg, Germany, as far as legally permissible.

11. 3. This License is solely for Licensor's and Licensee's benefit. It is not for the benefit of any other person or entity.

Questions? For questions on Copyright Clearance Center accounts or website issues please contact springernaturesupport@copyright.com or +1-855-239-3415 (toll free in the US) or +1-978-646-2777. For questions on Springer Nature licensing please visit https://www.springernature.com/gp/partners/rights-permissions-third-party-distribution

Other Conditions:

Version 1.4 - Dec 2022

PUBLICATIONS

Included in This Dissertation

Safaiyan, S.*, Besson-Girard, S.*, **Kaya, T.**, Cantuti-Castelvetri, L., Liu, L., Ji, H., Schifferer, M., Gouna, G., Usifo, F., Kannaiyan, N., Fitzner, D., Xiang, X., Rossner, M. J., Brendel, M., Gokce, O., & Simons, M. (2021). White matter aging drives microglial diversity. *Neuron*, *109*(7), 1100-1117.e10. https://doi.org/10.1016/j.neuron.2021.01.027

Kaya, T.*, Mattugini, N*., Liu, L*., Ji, H., Cantuti-Castelvetri, L., Wu, J., Schifferer, M., Groh, J., Martini, R., Besson-Girard, S., Kaji, S., Liesz, A., Gokce, O., & Simons, M. (2022). CD8+ T cells induce interferon-responsive oligodendrocytes and microglia in white matter aging. *Nature Neuroscience*, *25*(11), Article 11. https://doi.org/10.1038/s41593-022-01183-6

*contributed equally

Not Included in This Dissertation

Cantuti-Castelvetri, L., Ojha, R., Pedro, L. D., Djannatian, M., Franz, J., Kuivanen, S., van der Meer, F., Kallio, K., **Kaya, T.**, Anastasina, M., Smura, T., Levanov, L., Szirovicza, L., Tobi, A., Kallio-Kokko, H., Österlund, P., Joensuu, M., Meunier, F. A., Butcher, S. J., … Simons, M. (2020). Neuropilin-1 facilitates SARS-CoV-2 cell entry and infectivity. *Science*, *370*(6518), 856–860. https://doi.org/10.1126/science.abd2985

Liu, L., Besson-Girard, S., Ji, H., Gehring, K., Bulut, B., **Kaya, T.**, Usifo, F., Simons, M., & Gokce, O. (2021). Dissociation of microdissected mouse brain tissue for artifact free single-cell RNA sequencing. *STAR Protocols*, *2*(2), 100590. https://doi.org/10.1016/j.xpro.2021.100590

Jocher, G., Grass, V., Tschirner, S. K., Riepler, L., Breimann, S., **Kaya, T.**, Oelsner, M., Hamad, M. S., Hofmann, L. I., Blobel, C. P., Schmidt-Weber, C. B., Gokce, O.,

Jakwerth, C. A., Trimpert, J., Kimpel, J., Pichlmair, A., & Lichtenthaler, S. F. (2022). ADAM10 and ADAM17 promote SARS-CoV-2 cell entry and spike protein-mediated lung cell fusion. *EMBO Reports*, *23*(6), e54305. https://doi.org/10.15252/embr.202154305

AUTHOR CONTRIBUTIONS

Manuscript 1:

Safaiyan, S.*, Besson-Girard, S.*, **Kaya, T.**, Cantuti-Castelvetri, L., Liu, L., Ji, H., Schifferer, M., Gouna, G., Usifo, F., Kannaiyan, N., Fitzner, D., Xiang, X., Rossner, M. J., Brendel, M., Gokce, O., & Simons, M. (2021). White matter aging drives microglial diversity. *Neuron*, *109*(7), 1100-1117.e10. https://doi.org/10.1016/j.neuron.2021.01.027

Contributions: M. Simons and O.G. conceived and supervised the project. S.S., S.B.-G., **T.K.**, M. Schifferer, L.L., N.K., O.G., H.J., F.U., L.C.-C., M.J.R., R.P., G.G., M.B., D.F., and X.X. performed experiments and analyzed the data. S.B.-G. and **T.K.** developed software and curated and visualized the scRNA-seq data. O.G., M.R., and M. Simons analyzed the data or supervised data acquisition. M. Simons and O.G. wrote the manuscript with input from all authors.

I contributed to the development and expansion of the scRNA-seq data analysis pipeline that was already in place for Smart-seq2 pipeline when I joined the lab. I was responsible for acquiring and analyzing the external datasets generated in Strooper lab (Frigerio et al., 2019)and Stevens lab (Hammond et al., 2019). After the establishment of the 10X pipeline in the lab, S.B.-G. and I developed the analysis workflow for 10X generated single-cell datasets. I characterized the microglial states in both external datasets and our internal 10X datasets using the WAM signature that S.B.-G identified in the SS2 datasets. The addition of the 10X and external datasets has greatly enhanced the scope and validity of the study's results.

Manuscript 2:

Kaya, T.*, Mattugini, N*., Liu, L*., Ji, H., Cantuti-Castelvetri, L., Wu, J., Schifferer, M., Groh, J., Martini, R., Besson-Girard, S., Kaji, S., Liesz, A., Gokce, O., & Simons, M. (2022). CD8+ T cells induce interferon-responsive oligodendrocytes and microglia in white matter aging. *Nature Neuroscience*, *25*(11), Article 11. https://doi.org/10.1038/s41593-022-01183-6

*contributed equally

Contributions: M. Simons and O.G. conceived and supervised the project. **T.K.**, N.M., L.L., S.B.-G., H.J., S.K., O.G., J.W., L.C. and M. Schifferer performed experiments and analyzed the data. M. Simons and O.G. analyzed the data or supervised data acquisition. A.L. and J.G. provided essential reagents. M. Simons and O.G. wrote the manuscript with input from all authors.

I further expanded our scRNA-seq analysis arsenal by adding methods essential for compositional analysis and normalization/transformation. Thanks to the new normalization methods and rigorous quality control, I identified a novel state of oligodendrocytes that could be easily missed with conventional methods. I characterized the responses of oligodendrocytes and microglia in aged WT and Rag1-deficient animals using datasets generated from both the SS2 and 10X pipelines. For immunohistochemistry validations of our results, I provided potential marker genes throughout the study. Additionally, I offered continuous assistance in writing the manuscript and creating the figures.